

FLORIDA STATE UNIVERSITY  
COLLEGE OF ARTS & SCIENCES

CONVECTION IN COUPLED FLUID-POROUS MEDIA SYSTEMS:  
A TALE OF TWO FLUIDS

By

MATTHEW MCCURDY

A Dissertation submitted to the  
Department of Mathematics  
in partial fulfillment of the  
requirements for the degree of  
Doctor of Philosophy

2020

Matthew McCurdy defended this dissertation on June 25, 2020.  
The members of the supervisory committee were:

M. Nick J. Moore  
Professor Co-directing Dissertation

Xiaoming Wang  
Professor Co-directing Dissertation

Ming Ye  
University Representative

Nick Cogan  
Committee Member

Aseel Farhat  
Committee Member

The Graduate School has verified and approved the above-named committee members, and certifies that the dissertation has been approved in accordance with university requirements.

*It was the best of times, it was the worst of times,  
it was the age of wisdom, it was the age of foolishness, . . .*

-Charles Dickens, *A Tale of Two Cities*

To my people—  
you have truly helped make this ‘the best of times.’

# ACKNOWLEDGMENTS

The completion of this dissertation and my graduate studies at FSU would not have been possible without the support and encouragement from numerous people:

- To my advisors, Dr. Nick Moore and Dr. Xiaoming Wang: thank you for your patience, knowledge, and enthusiasm for math. You both have been such great role-models for me as researchers, professors, and mentors. While navigating video calls and timezones hasn't been easy throughout our time together, I'm extremely grateful for your support.
- To my colleagues and friends, Patrick, Alee, Julia, Jenny, Angie, and Kyle: thank you for believing in me, putting up with me, and helping me along the way. You all have been instrumental in my success, and I cannot imagine how I could have finished this without you.
- To the (many) advisors of the math department over the past five years, Elizabeth, Jennifer, Kari, Lisa, Pamela: thank you for your friendship and assistance with everything university-related. You made navigating the administration not only bearable, but fun. The math department would not run without you.
- To my friends and professors from Centre, especially Nick, Victor, Cristin, Josh, and Dr. Swanson: thank you for being my support system over the last nine years. You pushed me to be better, and for that, I am eternally grateful.
- And to my family: words cannot adequately express my gratitude and gratefulness towards you all. So, thank you, and I love you.

# CONTENTS

List of Tables . . . . .	vii
List of Figures . . . . .	viii
Abstract . . . . .	xiii
<b>1 Introduction</b>	<b>1</b>
1.1 Stability . . . . .	3
1.2 Introduction to Rayleigh-Bénard convection . . . . .	4
1.2.1 Early work . . . . .	5
1.2.2 The mid-1950s . . . . .	6
1.2.3 From one layer to two layers . . . . .	6
1.3 Coupled system: stability analysis review . . . . .	7
<b>2 Nonlinear Stability Analysis for the Navier-Stokes-Darcy-Boussinesq System</b>	<b>10</b>
2.1 Introduction . . . . .	10
2.2 Formulation of the problem . . . . .	12
2.2.1 Governing equations . . . . .	12
2.2.2 Boundary and interface conditions . . . . .	14
2.2.3 Steady-state and perturbed system . . . . .	16
2.2.4 Nondimensionalization . . . . .	17
2.3 Linear stability . . . . .	19
2.3.1 Solving the linear system . . . . .	20
2.4 Nonlinear stability . . . . .	23
2.5 Results and discussion . . . . .	28
2.5.1 Marginal stability results . . . . .	28
2.5.2 Influence of interface conditions . . . . .	29
2.5.3 Fluid-dominated versus full convection . . . . .	32
2.6 Conclusions . . . . .	37
<b>3 Numerics</b>	<b>38</b>
3.1 Single layer of fluid . . . . .	38
3.1.1 Equations, and linear stability analysis . . . . .	38
3.1.2 Principle of exchange of stabilities . . . . .	42
3.1.3 Marginal stability curves . . . . .	44
3.1.4 Numerics . . . . .	47
3.1.5 Quantifying convection . . . . .	54
3.1.6 Results . . . . .	56
3.2 Single layer of a porous medium saturated with fluid . . . . .	63
3.2.1 Equations, and linear stability analysis . . . . .	63
3.2.2 Principle of exchange of stabilities . . . . .	65
3.2.3 Marginal stability curves . . . . .	67
3.2.4 Numerics . . . . .	69

3.2.5	Quantifying convection . . . . .	74
3.2.6	Results . . . . .	76
3.3	Coupled numerics . . . . .	80
3.3.1	Heat . . . . .	81
3.3.2	Fluid region . . . . .	82
3.3.3	Porous region . . . . .	83
3.3.4	Simulations with the Finite Element Method . . . . .	83
3.3.5	Verifying numerics . . . . .	87
3.4	Results . . . . .	90
3.4.1	Influence of boundary conditions . . . . .	95
3.5	Conclusions . . . . .	104
3.5.1	Remark . . . . .	105
<b>4</b>	<b>Heuristic Phase Transition Theory</b>	<b>106</b>
4.1	Simple theory, revisited . . . . .	106
4.2	Heuristic theory . . . . .	107
4.2.1	Choosing $\epsilon_T$ values . . . . .	111
<b>5</b>	<b>Conclusions</b>	<b>112</b>
<b>Appendices</b>		
<b>A</b>	<b>Small Darcy Asymptotics</b>	<b>114</b>
<b>B</b>	<b>Implementing the Finite Element Method</b>	<b>118</b>
	References . . . . .	131
	Biographical Sketch . . . . .	140

# LIST OF TABLES

2.1	Transformations from the nondimensional domain to the Chebyshev domain. . . . .	21
2.2	Relative error between predicted and actual $\hat{d}^*$ values for <i>original</i> simple theory. Fixed parameters: $\chi = .3$ , $\alpha = 1.0$ . . . . .	35
3.1	Critical Rayleigh numbers for the single fluid layer with different combinations of boundary conditions. The marginal stability curves for 6 of these cases are shown in Figure 3.2. . . . .	45
3.2	Critical Rayleigh numbers for the single porous layer with different combinations of boundary conditions. . . . .	68
4.1	With $\epsilon_T = 0.5$ , actual $\hat{d}^*$ values from the marginal stability curves along with the two minima of the curve and their associated wavenumbers, Rayleigh numbers. Additionally, predicted $\hat{d}^*$ values from the heuristic theory, and the relative error between the heuristic $\hat{d}^*$ values and those from the linear stability. . . . .	110
4.2	With $\epsilon_T = 0.7$ , actual $\hat{d}^*$ values from the marginal stability curves along with the two minima of the curve and their associated wavenumbers, Rayleigh numbers. Additionally, predicted $\hat{d}^*$ values from the heuristic theory, and the relative error between the heuristic $\hat{d}^*$ values and those from the linear stability. . . . .	110
4.3	With $\epsilon_T = 1.0$ , actual $\hat{d}^*$ values from the marginal stability curves along with the two minima of the curve and their associated wavenumbers, Rayleigh numbers. Additionally, predicted $\hat{d}^*$ values from the heuristic theory, and the relative error between the heuristic $\hat{d}^*$ values and those from the linear stability. . . . .	110
4.4	Thermal conductivity values of materials found in geophysical applications taken at 25°C/77°F, taken from [92]. . . . .	111

# LIST OF FIGURES

1.1	Cherokee Sink, outside of Wakulla Springs, FL. . . . .	2
1.2	Illustrating the concept of stability. . . . .	3
2.1	Schematic of the domain $\Omega = \{(x, y) \in \mathbb{R}^2 \times z \in (-d_m, d_f)\}$ , comprised of a free-flow region $\Omega_f$ and a porous medium $\Omega_m$ . The two subdomains meet at an interface $\Gamma_i$ . The upper and lower boundaries are impermeable and held at constant temperatures $T_U$ and $T_L$ , respectively, with $T_L > T_U$ . . . . .	14
2.2	Eigenvalues for linear stability, with parameters $\hat{d} = .2$ , $a_m = 10.0$ , $\sqrt{\text{Da}} = 5.0 \times 10^{-3}$ , $\epsilon_T = .7$ , $\alpha = 1.0$ , and the BJSJ condition is used ( $\Psi_J = 1, \Psi_S = 0$ ). . . . .	23
2.3	Marginal stability curves for different values of $\text{Da}$ and $\alpha$ , with $\epsilon_T = .7$ in all cases. Both linear (solid) and nonlinear (dashed) stability results are shown. The two results agree closely with one another in all cases, indicating that the region of potential subcritical instability is very small. . . . .	30
2.4	Relative differences between marginal stability curves for various cases. Parameters: $\hat{d} = .1$ , $a_m = 25.0$ , $\epsilon_T = .7$ , $\alpha = 1.0$ . Both comparison lines have slope of 1. . . . .	31
2.5	Marginally stable flow configurations and temperature profiles (color) for two values of $\hat{d}$ . (a) $\hat{d} = .18$ produces convection cells that extend throughout the entire domain, while (b) $\hat{d} = .19$ produces cells that are confined to the free-flow region. In both cases, $\sqrt{\text{Da}} = 5.0 \times 10^{-3}$ , $\epsilon_T = .7$ , $\alpha = 1.0$ , and the BJSJ condition is used ( $\Psi_J = 1, \Psi_S = 0$ ). . . . .	33
2.6	Color map of the Nusselt number with streamlines in black for the same two cases shown in Fig. 2.5. In the first case (a), the greatest variations of $\text{Nu}$ occur in the porous medium, while in the second case (b) the extrema of $\text{Nu}$ are confined to the free-flow region. . . . .	33
2.7	Marginal stability curves for varying $\epsilon_T$ , with $\sqrt{\text{Da}} = 5.0 \times 10^{-3}$ and $\alpha = 1.0$ fixed. Linear stability results with the BJSJ interface condition used ( $\Psi_J = 1, \Psi_S = 0$ ). . . . .	36
3.1	Schematic of the domain $\Omega = \{(x, y) \in \mathbb{R}^2 \times z \in (0, d_f)\}$ . The upper and lower boundaries are impermeable and held at constant temperatures $T_U$ and $T_L$ , respectively, with $T_L > T_U$ . . . . .	39
3.2	Marginal stability curves for a single layer of fluid with various boundary conditions, noted beneath each plot. The conditions are for the velocity at $z = 0$ and $z = 1$ , respectively, followed by the conditions on $\theta_f$ at $z = 0$ and $z = 1$ . . . . .	46
3.3	Schematic of the discretized domain for a single layer of fluid. For simulations, more elements are used. . . . .	47

3.4	Approximate velocity and vorticity from solving the steady Stokes equation (3.8). . .	51
3.5	Convergence for the steady Stokes problem with $\mathcal{P}_1$ and $\mathcal{P}_2$ elements with UMFPACK and GMRES linear solvers. The $L^2$ error of velocity is plotted as the max edge size, $\Delta x$ on the mesh, is varied. The comparison lines in each plot have slopes of 2 for the blue line ( $\mathcal{P}_1$ elts.) and 3 for the red line ( $\mathcal{P}_2$ elts.). . . . .	53
3.6	Time per solve for the steady Stokes problem with $\mathcal{P}_1$ and $\mathcal{P}_2$ elements with UMFPACK and GMRES linear solvers. The green comparison line has a slope of 1, the blue line has a slope of 3/2. . . . .	53
3.7	Convergence with $L^2$ errors of $\mathbf{u}_f$ and $p_f$ with the steady Stokes problem using the Taylor-Hood $\mathcal{P}_2$ - $\mathcal{P}_1$ elements with UMFPACK as the linear solver. The red comparison line has a slope of 2, and the blue has a slope of 3. . . . .	54
3.8	Energy of the systems and the change in energy for various $\text{Ra}_f$ values. The mesh is on $(x, z) \in [-2.5, 2.5] \times [0, 1]$ with 20 elements/unit distance on the mesh, and $\Delta t = .01$ , $\text{Pr}_f = .7$ . . . . .	58
3.9	Scaled energy and scaled Nusselt number of the systems for various $\text{Ra}_f$ values. The solid lines represent the scaled Nusselt number, the dashed are the scaled energy. The mesh is on $(x, z) \in [-2.5, 2.5] \times [0, 1]$ with 20 elements/unit distance on the mesh, and $\Delta t = .01$ , $\text{Pr}_f = .7$ . . . . .	59
3.10	Simulation with $\text{Ra}_f = 2500$ . The mesh is on $(x, z) \in [-2.5, 2.5] \times [0, 1]$ with 20 elements/unit distance on the mesh, and $\Delta t = .01$ , $\text{Pr}_f = .7$ . . . . .	60
3.11	Simulation with $\text{Ra}_f = 10000$ . The mesh is on $(x, z) \in [-2.5, 2.5] \times [0, 1]$ with 20 elements/unit distance on the mesh, and $\Delta t = .01$ , $\text{Pr}_f = .7$ . . . . .	61
3.12	$\text{Ra}_f$ versus saturation energy for a single layer of fluid. . . . .	62
3.13	Energy and the change in energy for $\text{Ra}_f = 10^6$ , in a ‘turbulent’ system. The mesh is on $(x, z) \in [-2.5, 2.5] \times [0, 1]$ with 20 elements/unit distance on the mesh, and $\Delta t = .01$ , $\text{Pr}_f = .7$ . . . . .	62
3.14	Schematic of the domain $\Omega = \{(x, y) \in \mathbb{R}^2 \times z \in (-d_m, 0)\}$ . The upper and lower boundaries are impermeable and held at constant temperatures $T_U$ and $T_L$ , respectively, with $T_L > T_U$ . . . . .	64
3.15	Marginal stability curves for a single layer of a porous medium with various boundary conditions, noted beneath each plot. The conditions are for the velocity at $z = -1$ and $z = 0$ , followed by the conditions on $\theta_m$ at $z = -1$ and $z = 0$ . . . . .	70
3.16	Convergence for the steady Darcy problem with $\mathcal{P}_2$ elements for pressure, $\mathcal{P}_1$ and $\mathcal{P}_2$ for the velocity, and UMFPACK as the linear solver. The $L^2$ errors are plotted as the max edge size, $\Delta x$ on the mesh, is varied. The comparison lines in each plot have slopes of 2 for the red and black lines (for velocity) and 3 for the blue line (for pressure). . . . .	75

3.17	Energy of the systems and the change in energy for various $Ra_m$ values. The mesh is on $(x, z) \in [-2.5, 2.5] \times [-1, 0]$ with 20 elements/unit distance on the mesh, and $Da = 10^{-5}$ , $\Delta t = .01$ , $Pr_m = .7$ , $\chi = .3$ . . . . .	77
3.18	Scaled energy and scaled Nusselt number of the systems for various $Ra_m$ values. The solid lines represent the scaled Nusselt number, the dashed are the scaled energy. The mesh is on $(x, z) \in [-2.5, 2.5] \times [-1, 0]$ with 20 elements/unit distance on the mesh, and $Da = 10^{-5}$ , $\Delta t = .01$ , $Pr_m = .7$ , $\chi = .3$ . . . . .	77
3.19	Simulation with $Ra_m = 50$ . The mesh is on $(x, z) \in [-2.5, 2.5] \times [-1, 0]$ with 20 elements/unit distance on the mesh, and $Da = 10^{-5}$ , $\Delta t = .01$ , $Pr_m = .7$ , $\chi = .3$ . . . .	78
3.20	Simulation with $Ra_m = 75$ . The mesh is on $(x, z) \in [-2.5, 2.5] \times [-1, 0]$ with 20 elements/unit distance on the mesh, and $Da = 10^{-5}$ , $\Delta t = .01$ , $Pr_m = .7$ , $\chi = .3$ . . . .	79
3.21	Schematic of the domain $\Omega = \{(x, y) \in \mathbb{R}^2 \times z \in (-1, d_f/d_m)\}$ . The upper and lower boundaries are impermeable and held at constant temperatures $T_U = 0$ and $T_L = 1$ . . . .	84
3.22	Temperature fields for various values of $\epsilon_T$ in solving the steady ADE (3.32). . . . .	89
3.23	$L^2$ error of the temperature field over the entire domain, $\Omega$ , for various $\epsilon_T$ values. The blue comparison line has a slope of 3. . . . .	89
3.24	Simulation with $Ra_m = 120$ at $t = 10$ . The mesh is on $(x, z) \in [-1.55, 1.55] \times [-1, .3]$ with 25 elements/unit distance on the mesh, and $Da = 10^{-3}$ , $\Delta t = 1.25 \times 10^{-3}$ , $\hat{d} = .3$ , $Pr_m = \epsilon_T = \varrho = .7$ , $\chi = .3$ . . . . .	91
3.25	Full- versus fluid-dominated convection at $Da = 10^{-3}$ and $Da = 10^{-4}$ with $Ra_m = 50$ . All other parameters held constant: $\hat{d} = .3$ , $Pr_m = \epsilon_T = \varrho = .7$ , $\chi = .3$ . . . . .	92
3.26	Energy and change in energy for simulation with $Ra_m = 50$ , $Da = 10^{-4}$ and periodic left/right boundaries. The mesh is on $(x, z) \in [-1.55, 1.55] \times [-1, .3]$ with 25 elements/unit distance on the mesh, and $\Delta t = 2.5 \times 10^{-4}$ , $\hat{d} = .3$ , $Pr_m = \epsilon_T = \varrho = .7$ , $\chi = .3$ . . . . .	93
3.27	Streamlines for $Ra_m = 50$ , $Da = 10^{-4}$ and periodic left/right boundaries. The mesh is on $(x, z) \in [-1.55, 1.55] \times [-1, .3]$ with 25 elements/unit distance on the mesh, and $\Delta t = 2.5 \times 10^{-4}$ , $\hat{d} = .3$ , $Pr_m = \epsilon_T = \varrho = .7$ , $\chi = .3$ . . . . .	94
3.28	Streamlines and temperature profiles at $t = 10$ with $Ra_m = 80$ in (a) and $Ra_m = 90$ in (b) with solid left/right boundaries. The mesh is on $(x, z) \in [-1.55, 1.55] \times [-1, .3]$ with 25 elements/unit distance on the mesh, and $Da = 10^{-3}$ , $\Delta t = 1.25 \times 10^{-3}$ , $\hat{d} = .3$ , $Pr_m = \epsilon_T = \varrho = .7$ , $\chi = .3$ . . . . .	96
3.29	Energy of the coupled system with various Rayleigh numbers and solid left/right boundaries. The mesh is on $(x, z) \in [-1.55, 1.55] \times [-1, .3]$ with 25 elements/unit distance on the mesh, and $Da = 10^{-3}$ , $\Delta t = 1.25 \times 10^{-3}$ , $\hat{d} = .3$ , $Pr_m = \epsilon_T = \varrho = .7$ , $\chi = .3$ . . . . .	97

3.30	(Left) Energy profiles of various Rayleigh numbers ( $Ra_m = 55$ to $Ra_m = 110$ , by increments of 5) and solid left/right boundaries. (Right) The relationship between $Ra_m$ and saturation energy, where the data points come from the simulated energy profiles. The mesh is on $(x, z) \in [-1.55, 1.55] \times [-1, .3]$ with 25 elements/unit distance on the mesh, and $Da = 10^{-3}$ , $\hat{d} = .3$ , $Pr_m = \epsilon_T = \varrho = .7$ , $\chi = .3$ . . . . .	98
3.31	Schematic for metastability, showing two stable solutions. Position 2 is the ‘preferred’ solution, as it has a lower energy than position 1. . . . .	100
3.32	Energy and change in energy of the coupled system with $Ra_m = 120$ and solid left/right boundaries. The mesh is on $(x, z) \in [-1.55, 1.55] \times [-1, .3]$ with 25 elements/unit distance on the mesh, and $Da = 10^{-3}$ , $\hat{d} = .3$ , $Pr_m = \epsilon_T = \varrho = .7$ , $\chi = .3$ . . . . .	100
3.33	Simulation with solid left and right boundaries and the parameters: $Ra_m = 120$ , $Da = 10^{-3}$ , $\hat{d} = .3$ , $Pr_m = \epsilon_T = \varrho = .7$ , $\chi = .3$ , $\Delta t = 1.25 \times 10^{-3}$ . Velocity is shown with the vector field, temperature is with color. From top to bottom, the panels are at $t = 1.0, 5.5, 6.0$ . . . . .	102
3.34	Continued results from Figure 3.33. Simulation with solid left and right boundaries and the parameters: $Ra_m = 120$ , $Da = 10^{-3}$ , $\hat{d} = .3$ , $Pr_m = \epsilon_T = \varrho = .7$ , $\chi = .3$ , $\Delta t = 1.25 \times 10^{-3}$ . Velocity is shown with the vector field, temperature is with color. From top to bottom, the panels are at $t = 6.5, 7.0, 10.0$ . . . . .	103
3.35	(Left) Energy profiles of various Rayleigh numbers ( $Ra_m = 120$ to $Ra_m = 150$ , by increments of 5) and solid left/right boundaries. (Right) The mesh is on $(x, z) \in [-1.55, 1.55] \times [-1, .3]$ with 25 elements/unit distance on the mesh, and $Da = 10^{-3}$ , $\hat{d} = .3$ , $Pr_m = \epsilon_T = \varrho = .7$ , $\chi = .3$ . . . . .	104
4.1	Critical depth ratios for various values of $\epsilon_T$ . The blue line represents the predicted critical depth ratio $\hat{d}^*$ from the heuristic theory, and the red squares are the $\hat{d}^*$ from the marginal stability curves from the linear stability analysis. The yellow circles and purple diamonds are points from our numerical simulations. . . . .	109
B.1	Schematic of $\mathcal{P}_1$ and $\mathcal{P}_2$ reference elements, labelled $\omega^k$ , in the reference $(s, t)$ -domain. . . . .	121
B.2	Basis functions for $\mathcal{P}_1$ elements in the reference $(s, t)$ -domain. . . . .	121
B.3	Quadratic basis functions for $\mathcal{P}_2$ elements in the reference $(s, t)$ -domain. The color corresponds to the value of $\phi_i(x)$ . . . . .	122
B.4	Schematic showing effect of mesh refinement with 1D quadrature points for various orders of quadrature formulas with one, two, and three elements along the reference line. In each plot, the second-order formula is shown on top in blue, fourth-order in the middle with red, and sixth-order at the bottom in green. Colored squares denote the edges of the element while black circles show the quadrature points. . . . .	125
B.5	Log-log plot of the relative error versus $\Delta x$ for various orders of quadrature formulas (with line-integrals) to approximate (B.1). . . . .	125

B.6	Mapping from an element $\omega$ in the original domain to the reference element $\tilde{\omega}$ in the transformed domain. . . . .	126
B.7	Second-, third-, and sixth-order quadrature points from the example element shown in the first graph of Figure B.6. . . . .	127
B.8	Log-log plot of the relative error versus $\Delta x$ for various orders of quadrature formulas for surface-integrals in approximating (B.2). Here, $D = \pi\sqrt{2}$ is the max edge length of the least refined mesh, with the mesh refinements are shown in Figure B.9. . . . .	128
B.9	Mesh refinements used to approximate (B.2). Figure B.8 shows the convergence rates for quadrature formulas of different orders with the mesh refinements shown here. . . . .	128
B.10	Theory for implementing periodic boundary conditions. The purple nodes at the right boundary of the top mesh are removed. The left and right boundaries are then connected, using the green nodes to join the edges. The new mesh resembles the surface of a cylinder. . . . .	130

# ABSTRACT

We perform linear and nonlinear stability analyses for thermal convection in a fluid overlying a saturated porous medium, in addition to conducting novel numerical simulations. We use a coupled system, with the Navier-Stokes equations and Darcy's equation governing the free-flow and the porous regions, respectively. Incorporating a dynamic pressure term in the Lions interface condition (which specifies the normal force balance across the fluid-medium interface) permits an energy bound on the typically uncooperative nonlinear advection term, enabling new nonlinear stability results. Within certain regimes, the nonlinear stability thresholds agree closely with the linear ones, and we quantify the differences that exist. We then compare stability thresholds produced by several common variants of the tangential interface conditions, using both numerics and asymptotics in the small Darcy number limit. Furthermore, we investigate the transition between full convection and fluid-dominated convection using both numerics and a heuristic theory. This heuristic theory is based on comparing the ratio of the Rayleigh number in each domain to its corresponding critical value, and it is shown to agree well with the numerics regarding how the transition depends on the depth ratio, the Darcy number, and the thermal-diffusivity ratio. Finally, we detail the numerical methods used to simulate the coupled system. Our analyses and the heuristic theory are then verified with our numerical results.

# CHAPTER 1

## INTRODUCTION

Water is one of the most ubiquitous and important resources on Earth; humans and most organisms are composed of it, a majority of our planet is covered in it, and humanity's survival depends on it. Despite our dependence on water, there are still many unanswered questions surrounding it, many of which concern fresh water. While fresh water is a renewable resource, this 'renewable' status is contingent upon proper management, and unfortunately, water is one of the most poorly managed and regulated resources on Earth. To exacerbate this problem, humanity is depleting our water supplies at unprecedented rates. As we begin to exhaust these resources more and more rapidly, understanding and studying water resources becomes increasingly crucial.

Roughly 2.5% of the world's water is freshwater, and about 30% of that freshwater comes in the form of surface- or groundwater [45]. A large portion of this drinkable water resides in karst aquifers, which are extremely prevalent throughout the southeastern US, especially Florida. In fact, aquifers lie underneath a majority of Florida: Miami lies above the Biscayne aquifer, and Jacksonville is over the Floridian aquifer. To use these aquifers, companies drill down and pump out water which is almost immediately drinkable. Water made its way through limestone over thousands of years, naturally removing impurities. Companies then aerate the water to remove iron, and add fluoride and a phosphate for dental health and preventing pipe corrosion, respectively. This process in Florida is much less involved than other purification processes and produces some of the cheapest water rates in the country. The water quality also attracts companies from other industries, like breweries, which rely on high-quality water to be successful.

While not providing drinkable water or substantial economic benefits to the region, sinkholes and springs connected to aquifers are extremely common around Florida and Tallahassee. In Figure 1.1, we show one of these sinkholes, Cherokee Sink, outside of Wakulla, FL. For the formation of this sinkhole, ground- and rainwater eroded away limestone to create an underground cavity. As the cavity became too large, the roof collapsed and left a large hole in the ground. Rainwater, in addition to water from the water table, then filtered through the limestone to fill the sinkhole. The

result is a 77 foot deep sinkhole, mainly used for swimming and cave-diving. However, Cherokee Sink is not an anomaly for the area; it is part of the Wakulla-Leon Sinks cave system, the longest underwater cave system in the United States which spans over 31 continuous miles of underground caves.



(a) The sinkhole.



(b) The author doing research on sinkholes.

Figure 1.1: Cherokee Sink, outside of Wakulla Springs, FL.

Sinkhole formation highlights the interplay of surface- and groundwater and provides the main theme of this dissertation: fluid flow in coupled fluid-porous media systems. The phenomenon of fluid flowing over a porous medium has been observed, studied, and scrutinized for more than a century in a variety of settings. This coupling is dominant in geophysical applications as discussed above, with the mixing of surface water and groundwater [13, 15, 19, 39, 40], contaminant transport and bioremediation efforts [25, 88], and flow within oil reservoirs [2, 3]. However, coupled fluid-porous systems have other applications as well, with alloy solidification and industrial settings with heat-sinks. But, given the urgent need to understand water resources more fully, investigating the interaction between surface- and groundwater is particularly timely [98].

In this dissertation, we focus on the interaction between surface- and groundwater by investigating how fluid flows between a free-flow region and a porous medium. We also consider variable temperature since temperature profiles in fluids can vary drastically with depth. With a system of equations governing how fluids behave coupled with an equation detailing how temperature evolves, the novel work conducted in this dissertation centers on determining the stability criteria needed for convection cells to arise as well as simulating the system numerically.

## 1.1 Stability

One of the dominant motifs in this dissertation is stability. Stability describes how a system reacts to a perturbation. For example, consider a ball at the bottom of a valley and a ball perched precariously at the top of a hill, shown in Figure 1.2. If we ‘perturb’ the ball at the bottom of the hill, it will return to its original position; therefore, we say that this system is stable to perturbations. In contrast, if we perturb the ball atop the hill *at all*, it will roll away from its original position. This system would be described as unstable to perturbations since any change to the ball’s position results in it rolling away. So, in layman’s terms, stability can be described as perturbing a system and seeing how the system reacts.

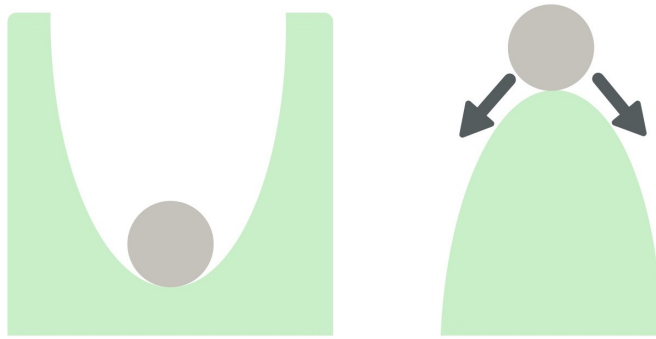


Figure 1.2: Illustrating the concept of stability.

Mathematically, stability can be described in a more quantitative sense. To illustrate this concept, consider the diffusion equation with the solution  $u(x, t)$ :

$$\frac{\partial u}{\partial t} = \frac{\partial^2 u}{\partial x^2} \quad \text{for } x \in \mathbb{R}, t > 0.$$

An obvious steady-state solution to this system is the trivial solution  $\bar{u}(x, t) \equiv 0$ , denoted with an overbar. To determine if this steady-state solution is stable or unstable to perturbations, we perturb the solution and see what happens to it as time goes on. With the perturbation  $e^{\sigma t} e^{ikx}$  (where  $k > 0$  signifies the wavenumber of the perturbation), we substitute

$$u(x, t) = \bar{u} + e^{\sigma t} e^{ikx}$$

into the diffusion equation. This yields

$$\sigma = -k^2 < 0.$$

With  $\sigma < 0$ , the perturbation  $e^{\sigma t} e^{ikx}$  does not grow in time (as  $t \rightarrow \infty$ ) since the magnitude of the perturbation is dictated by the  $e^{\sigma t}$  term. Since the perturbed steady-state solution returns to the trivial solution as time goes on, we say the steady-state solution is stable with respect to perturbations:

$$u(x, t) = \bar{u} + e^{\sigma t} e^{ikx} \rightarrow \bar{u} \quad \text{as } t \rightarrow \infty.$$

Throughout this dissertation, we will be using the concept of stability to describe flow patterns and fluid behavior while heating fluids. Specifically, we are interested in stability with convection geophysical fluids, such as with groundwater that has some temperature difference throughout the fluid. In the following sections, we describe previous work with convection in fluids to help motivate our problem.

## 1.2 Introduction to Rayleigh-Bénard convection

In the late-1800s, Henri Bénard, a physics student at the Collège de France, began performing experiments on thermal convection in a thin layer of fluid heated from below. In his experiments, the liquid layer was usually less than a millimeter deep with a horizontal, heated metal plate below and a free surface atop. The free surface at the top of the liquid (in contact with air) was at a lower temperature than the bottom plate and with the resulting temperature gradient, patterns began to appear in the form of hexagonal cells. Bénard speculated that this was due to buoyancy-driven flow brought about by the temperature differences in the fluid layer. Additionally, he noticed that these cellular instabilities did not arise if the temperature difference between the bottom surface and the top surface was not above some threshold. Bénard hypothesized that there was some critical

temperature necessary for these instabilities to occur. These experiments were the first organized (and published) experiments of their kind.

In 1900, armed with these experimental observations, Bénard published a series of four papers based on his experimental findings regarding convective cells [6, 7, 8, 10]. A year later, he defended his thesis titled “Les Tourbillons cellulaires dans une nappe liquide propageant de la chaleur par convection: en régime permanent” (“Cellular vortices in a liquid layer propagating heat by convection: in a steady state”) [9]. His four papers and thesis became seminal works in the developing field of hydrodynamic instabilities, eventually laying the groundwork for Rayleigh-Bénard convection and Bénard-Marangoni flow (surface-tension-driven flow of a fluid confined between horizontal conducting surfaces). Bénard’s observations and theories would go undisputed until the mid-1950’s.

### 1.2.1 Early work

In 1916, Lord Rayleigh aimed to explain Bénard’s results theoretically in his paper, “On Convection Currents in a Horizontal Layer of Fluid, when the Higher Temperature is on the Under Side” [76]. With the Boussinesq equations, but neglecting viscosity, Lord Rayleigh conducted a linear stability analysis to determine the wavelength of maximum instability for the case where the top and bottom surfaces are fixed. Next, viscosity was included in the governing equations and a similar linear stability analysis was conducted. While Lord Rayleigh’s work was mainly theoretical, he did find the critical temperature difference for a specific case which was in agreement with Bénard’s work. This work was pivotal to the research of later mathematicians.

Almost 25 years later, Pellew and Southwell revisited Bénard’s experimental observations and used Rayleigh’s theoretical results to generalize the stability argument to cases with rigid surfaces or free surfaces [73]. With the Boussinesq equations as the governing system, Pellew and Southwell determined appropriate boundary conditions for the following cases where the top and bottom surfaces of the fluid are: both free, both rigid, and lastly, one surface is free while the other is rigid. Then, with a linear stability argument, they considered the case of marginal stability (where the time component of the perturbations,  $e^{\sigma t}$ , has  $\sigma = 0$ ), derived exact solutions, and determined critical thresholds for instabilities to occur. Pellew and Southwell did not refer to the Rayleigh number by name (since the term ‘Rayleigh number’ had not been popularized yet). However, their

results for the critical threshold revolved around criteria concerning the number:

$$\frac{\beta\gamma h^4}{k\nu},$$

where  $\beta$  is the mean temperature gradient,  $\gamma = g\alpha$  is gravity times the coefficient of thermal expansion,  $h$  is the height of the fluid,  $k$  is the coefficient of thermal diffusivity, and  $\nu$  is kinematic viscosity (all following their notation). They stated if this number was above a critical value, instabilities would begin to occur in the fluid. Their paper detailed the approximate critical value for each of the three cases of boundary conditions. To obtain this stability criterion, a sixth-order differential equation was (non-trivially) solved.

In [77], Reid and Harris presented several methods to approximate the solution to the differential equation used to determine the critical Rayleigh number as well as the eigenfunctions of the spatial- and temperature-components of the perturbations. They compared the critical Rayleigh numbers attained by their approximations to the exact solutions, citing nice agreement for each of their methods. Like a majority of the work conducted in [73], Reid and Harris only considered the case of marginal stability.

### 1.2.2 The mid-1950s

In 1956 and 1958, Block and Pearson showed physically and theoretically that the convection cells Bénard observed in his experiments were, in fact, not due to a thermal instability associated with the heated fluid rising to the top of the fluid layer due to density differences [12, 72]. The convection cells had developed by the variation of surface tension due to the temperature gradient. With thin layers of fluid (like in Bénard's experiments), the density variations were much less dominant than differences in surface tension. In Bénard's observations, he noticed that the middle of the hexagonal cells was slightly depressed in comparison to the cellular boundaries. However, Bénard never spoke of the role of surface tension in the instabilities. As Drazin and Reid so cleverly stated in [37]: "In spite of this ironic discovery, the convection in a horizontal layer of fluid heated from below is still called Bénard convection."

### 1.2.3 From one layer to two layers

In the mid-1960s, Beavers and Joseph proposed their eponymous slip condition at a permeable boundary. While their research was mainly experimental, it allowed others to consider a fluid layer

overlying a porous medium saturated with the same fluid. About a decade later, Nield investigated a fluid overlying a porous medium with the addition of heat [66]. Using steady Navier-Stokes and steady Darcy with the steady advection-diffusion equations, Nield presented the first linear stability analysis of the coupled system. This spurred a multitude of related papers regarding stability in coupled, two-layer systems.

### 1.3 Coupled system: stability analysis review

In [54], Straughan and Hill, advisor and advisee, analyzed a similar situation for thermal convection in a fluid over a porous medium. Based on several assumptions they made about their system, the equations they used are not appropriate for geophysical applications. First, they considered a highly porous medium, necessitating the use of the Brinkman equation to govern the fluid flow in the porous medium instead of the Darcy equation. And second, the Stokes equation was used to model the fluid in the free flow since the nonlinear advection term  $\mathbf{u} \cdot \nabla \mathbf{u}$  in Navier-Stokes creates several issues associated with nonlinear stability arguments. They then performed linear and nonlinear stability analyses for the Stokes-Brinkman system and asserted that the linear and nonlinear stability results system agree well. The centerpiece of this work was the conclusion that “the linear theory accurately encapsulates the physics of the onset of convection.”

Shortly after [54], Hill and Carr (another student of Straughan) considered the same system in [52]: thermal convection in a fluid over a porous medium. This time though, the nonlinear term  $\mathbf{u} \cdot \nabla \mathbf{u}$  was included, as Navier-Stokes was used for the free flow zone. The Brinkman equation was used in the porous medium though with the assumption it has a high porosity ( $\chi > .75$ ). While the ‘high porosity’ assumption is realistic with industrial applications, like foametals which are widely used in applications like lightweight structures, biomedical implants, heat exchangers, and chemical reactors [60, 83], assuming a high porosity is not appropriate for general geophysical settings. For their analysis, Hill and Carr adopted a one-domain approach to the problem. That is, instead of separate systems of equations for the fluid in the free flow and the fluid in the porous medium, a single equation is used to model the fluid in the entirety of the domain. This method avoids having to explicitly formulate interface conditions between the free flow zone and the porous medium. With the one-domain approach, the authors determined unconditional nonlinear energy stability thresholds and compared those thresholds to linear counterparts of one- and two-domain

approaches. The main result of this paper was that the linear and nonlinear stability thresholds “show good agreement, demonstrating that the [one-domain] approach captures the behavior as modelled by the more widely used two-domain model” and the onset of convection is well-captured in both approaches

In [53], Hill and Carr conducted a similar analysis for a fluid over a saturated porous medium with a high porosity; however, the nonlinear advection term was included in this argument. Instead of the Navier-Stokes equation for the fluid in the free flow, the authors used a model proposed by Ladyzhenskaya in the late 1960’s, which is used as an alternative to Navier-Stokes. The model by Ladyzhenskaya is “a well-known model in viscoelasticity,” used and discussed in detail throughout many of Straughan’s works [84, 86, 87]. To model the fluid in the free flow, Hill and Carr used:

$$\rho_0 \left( \frac{\partial \mathbf{u}_f}{\partial t} + \mathbf{u}_f \cdot \nabla \mathbf{u}_f \right) = -\nabla p_f + 2\nabla \cdot [(\mu(T_f) + \mu_1 |\mathbf{D}_f|) \mathbb{D}(\mathbf{u}_f)] - g\rho_0 \mathbf{k} (1 - \alpha (T - T_0))$$

where  $\mu(T_f)$  is the temperature-dependent dynamics viscosity,  $\mu_1 > 0$  is a constant parameter, and  $|\mathbf{D}_f| = (\mathbb{D}(\mathbf{u}_f)\mathbb{D}(\mathbf{u}_f))^{1/2}$  where  $\mathbb{D}(\mathbf{u}_f) = \frac{1}{2} (\nabla \mathbf{u}_f + \nabla \mathbf{u}_f^T)$  is the rate of strain tensor. We note that the viscous term of the equation,

$$\mu(T_f) + \mu_1 |\mathbf{D}_f|,$$

includes temperature dependency and also the magnitude of the rate of strain tensor; this allows two factors to determine the role of viscosity. The temperature effects could dominate, or the  $\mathbb{D}(\mathbf{u}_f)$  term could be the main influence on the viscosity’s role in the equation. The last term of Ladyzhenskaya’s model above is the Boussinesq approximation, describing temperature-dependent density where the density is determined by a linear profile in temperature. Like their works detailed above, this paper shows that “the linear instability and nonlinear stability results clearly show excellent agreement,” and Hill and Carr conclude that “the linear theory accurately encapsulates the physics of the onset of convection.”

With their work in [21], Carr and Straughan analyzed the coupled system of a fluid layer overlying a porous medium. This time, however, the Beavers-Joseph-Saffman-Jones (BJSJ) condition was used for the interface. Using the BJSJ interface condition in this work and not their other papers on the coupled fluid-porous medium system is a result of the assumption that the porosity in the porous medium is small enough so that there will be a jump in the tangential velocity across the interface. With their previous papers [52, 53, 54], the porosity of the porous medium was

high enough (usually, they assumed  $\chi > .75$ ) so that the governing equation was Brinkman and there was no jump in the velocity across the interface. As they lost the ‘high-porosity assumption’ though, the continuity of tangential stresses across the interface was lost as well which necessitated the use of the BJSJ interface condition. Additionally, a quadratic equation of state specific to water between 0° and 4°C was used for the buoyancy terms in the free flow and porous medium since the authors applied their analysis of penetrative convection to the geophysical problem of patterned ground formation.

Before Straughan, Carr, and Hill performed their analyses, a separate group of Chen, Hsu, and Lu studied the effects of different fluid and medium characteristics on the resulting streamline and isotherm patterns associated with the onset of thermal convection in the coupled fluid-porous medium system in [27, 28]. With their work in [28], variable viscosity was considered and analyzed. For the governing equations, the steady-state Navier-Stokes and Darcy equations were used with the steady state advection-diffusion equation to govern heat. The work conducted in [27] investigated the coupled system with the assumption that the porous medium was anisotropic and inhomogeneous. For both works, results were shown regarding the influence of variable viscosity, permeability, and thermal diffusivity each have on convection in the system of a fluid layer overlying a porous medium.

The work of the two groups above (Straughan et al., and Chen et al.) laid the foundations for the analyses presented in this dissertation, specifically the nonlinear analysis conducted in the next chapter.

This dissertation is organized into the following chapters: Chapter 2 presents the novel nonlinear stability arguments and results, Chapter 3 details numerical methods and our algorithms to simulate convection in single layers- a fluid region, and a porous medium- as well the coupled system, Chapter 4 outlines our (improved) heuristic theory for predicting parameter regimes necessary for a transition from full- to fluid-dominated convection, and our conclusions are summarized in Chapter 5. The two appendices contain our asymptotic results for small Darcy numbers, and a discussion about the finite element method along with how it is implemented.

## CHAPTER 2

# NONLINEAR STABILITY ANALYSIS FOR THE NAVIER-STOKES-DARCY-BOUSSINESQ SYSTEM

### 2.1 Introduction

To gain useful insight into the nature of coupled fluid-porous systems, both linear and nonlinear stability arguments have been conducted and analyzed [52, 53, 54]. However, the presence of nonlinear advection  $(\mathbf{u} \cdot \nabla) \mathbf{u}$  can hinder nonlinear stability analysis since, when coupled to non-trivial interface conditions, it produces a sign-indefinite term in the energy bound. As a result, the nonlinear stability of the coupled Navier-Stokes-Darcy system—the most well-accepted model for fluid-porous systems in geophysical applications—remains unresolved. Building upon previous work [52, 53, 54, 71], the primary goal of the current study is to analyze nonlinear stability of this coupled system and to examine the associated convection patterns.

To overcome the indefinite term in the energy analysis, researchers have adopted various approaches. Several works forgo the nonlinear term altogether by exploring *linear* stability of the Navier-Stokes-Darcy-Boussinesq system. Many of these works also include additional physical effects, such as variable viscosity or permeability, quadratic equations of state for thermal expansion, and anisotropic or heterogeneous porous media [20, 21, 26, 27, 28, 66, 83]. Other strategies to treat or avoid the nonlinear term include using Stokes in lieu of Navier-Stokes in the free-flow zone [52], or considering the Navier-Stokes-Brinkman system so that the convective term of the free-flow has a corresponding term in the porous medium [54]. The Brinkman equations apply to highly porous media (e.g. porosity greater than .75), which is a common and physically realistic assumption for many industrial applications such as lightweight structures, biomedical implants, heat exchangers, and chemical reactors [60, 83]. However, for many flows of geophysical interest (e.g. karst aquifers, sinkholes, hyporheic flow, contaminant transport), the porosity is very small and Darcy is the most appropriate equation to model its fluid flow.

A fundamental assumption made in linear stability analyses is that perturbations to the steady-state are small and consequently, the effects of quadratic and higher order terms are lost. As a

result, there is limited information about the behavior of the nonlinear system and a possibility for subcritical instabilities—those that occur prior to the threshold predicted by the linear theory. Nonlinear stability analyses take higher order and nonlinear terms into account, thereby providing a more holistic understanding of the mechanisms that create convection and the interplay between them.

In this chapter, we investigate thermal convection in a fluid overlying a saturated porous medium within the Navier-Stokes-Darcy-Boussinesq model via the energy method. To overcome the difficulty associated with the nonlinear term, we employ the *Lions interface condition*, which incorporates a dynamic pressure term into the normal-force balance<sup>1</sup>. When the Lions interface condition is used in tandem with the Beavers-Joseph-Saffman-Jones (BJSJ) condition, the Navier-Stokes system satisfies an energy law. That is, the energy associated with the nonlinear term of Navier-Stokes can be bounded. We outline the linear argument for the coupled system and then conduct the nonlinear stability analysis, followed by a comparison of marginal stability curves produced by each approach. In addition, while a considerable amount of effort has been placed on determining the appropriate models for fluid flow in surface- and groundwater regions, there is less of a consensus on choosing a condition for the shear-stress balance. Many works specify that the shear stress must balance with a jump in tangential velocity, or some variant thereof. Popular choices for this interface condition are the Beavers-Joseph condition (BJ), the Beavers-Joseph-Jones condition (BJJ), and the BJSJ condition. We show the relative difference between curves produced by the BJSJ condition versus those produced by either BJ or BJJ scales like the Darcy number,  $Da$ , while the absolute differences scale like  $Da^2$ . Thus, differences between these choices are small in the physically relevant regime of small Darcy number.

Convection in a fluid overlying porous media is much more complex than its single layer counterparts, with more physical parameters affecting the heat transport. One physically important phenomenon is the transition from full convection, where convection cells envelope the entire domain, to fluid-dominated convection, where the cells are confined to the free-flow region. Parameters that influence this transition include the Darcy number, the ratio of free-flow to medium depth, and the ratio of the thermal diffusivities. We propose a simple theory, based on comparing the

---

<sup>1</sup>A formal asymptotic analysis justifying the smallness of this dynamic pressure at the physically important small Darcy number regime is included in Appendix A.

critical Rayleigh numbers of the two layers, to predict this transition. Numerical tests confirm that this theory indeed predicts the transition with reasonable accuracy.

The rest of the chapter is organized as follows. We introduce the mathematical formulation of the problem, including the governing equations, the boundary and interface conditions, and the nondimensionalization, in section 2.2. We summarize the linear stability analysis in section 2.3 while section 2.4 is devoted to the nonlinear stability analysis. Main results are outlined and discussed in section 2.5. We offer our conclusions in section 2.6. Formal small Darcy number asymptotic expansions are included in Appendix A.

## 2.2 Formulation of the problem

In this section, we describe the governing equations along with the boundary and interface conditions. We then find steady-state solutions, which serve as reference states for the stability analyses, and we nondimensionalize the resulting system.

### 2.2.1 Governing equations

In the free-flow zone, we use the incompressible Navier-Stokes equations with constant viscosity and the Boussinesq approximation, coupled with the advection-diffusion equations for heat:

$$\left\{ \begin{array}{l} \rho_0 \left( \frac{\partial \mathbf{u}_f}{\partial t} + (\mathbf{u}_f \cdot \nabla) \mathbf{u}_f \right) = \nabla \cdot \mathbb{T}(\mathbf{u}_f, p_f) - g\rho_0 [1 - \beta(T_f - T_0)] \mathbf{k}, \\ \nabla \cdot \mathbf{u}_f = 0, \\ \frac{\partial T_f}{\partial t} + \mathbf{u}_f \cdot \nabla T_f = \frac{\kappa_f}{(\rho_0 c_p)_f} \nabla^2 T_f, \end{array} \right. \quad (2.1)$$

where  $\mathbf{u}_f = (u_f, v_f, w_f)$ ,  $p_f$ , and  $T_f$  are the free flow velocity, pressure, and temperature, respectively, with  $g$ ,  $\rho_0$ ,  $\beta$ , and  $T_0$  as acceleration due to gravity, the reference density of the fluid, the coefficient of thermal expansion, and the temperature of the conductive state at the interface, respectively. The stress tensor and rate of strain tensor are defined as  $\mathbb{T}(\mathbf{u}_f, p_f) = 2\mu_0 \mathbb{D}(\mathbf{u}_f) - p_f \mathbb{I}$  and  $\mathbb{D}(\mathbf{u}_f) = \frac{1}{2} (\nabla \mathbf{u}_f + \nabla \mathbf{u}_f^\top)$ , respectively, with  $\mu_0$  as dynamic viscosity and  $\mathbf{k}$  as the upward pointing unit normal. Additionally,  $\kappa_f$ ,  $c_p$ , and  $\lambda_f = \kappa_f / (\rho_0 c_p)_f$  are the thermal conductivity of the fluid, specific heat capacity of the fluid, and thermal diffusivity of the fluid, respectively.

For fluid flow in porous media, the Darcy or Brinkman equations are the prevailing choice in the literature. For porous media with relatively large porosity ( $\chi > .75$ ), Brinkman is more appropriate than Darcy. Darcy is valid under the assumption that the medium has a small porosity [4, 68], generally applicable to geophysical systems. We therefore employ the Darcy system with the advection-diffusion equation for heat:

$$\left\{ \begin{array}{l} \frac{\rho_0}{\chi} \frac{\partial \mathbf{u}_m}{\partial t} + \frac{\mu_0}{\Pi} \mathbf{u}_m = -\nabla p_m - g\rho_0 [1 - \beta (T_m - T_L)] \mathbf{k}, \\ \nabla \cdot \mathbf{u}_m = 0, \\ \frac{(\rho_0 c_p)_m}{(\rho_0 c_p)_f} \frac{\partial T_m}{\partial t} + \mathbf{u}_m \cdot \nabla T_m = \frac{\kappa_m}{(\rho_0 c_p)_f} \nabla^2 T_m, \end{array} \right. \quad (2.2)$$

where  $\mathbf{u}_m = (u_m, v_m, w_m)$ ,  $p_m$ , and  $T_m$  are the velocity, pressure, and temperature in the porous medium respectively,  $\chi$  and  $\Pi$  are the porosity and permeability,  $\lambda_m = \kappa_m / (\rho_0 c_p)_f$  is the thermal diffusivity of the medium, and  $T_L$  is the temperature at the lower boundary of the domain. In this work, we assume the medium to be homogeneous and isotropic so that the permeability  $\Pi$  is constant and scalar-valued. For anisotropic media, the permeability  $\Pi$  would be tensor-valued. The thermal conductivity  $\kappa_m$  and specific heat capacity  $(\rho_0 c_p)_m$  of the porous medium are defined as averages of the fluid and solid components. Many references simply use an arithmetic average [52, 53, 54]  $\phi_m = \chi\phi_f + (1 - \chi)\phi_s$ , where  $\phi$  represents either thermal conductivity or heat capacity. However, we point out that homogenization theory gives the harmonic average,  $\phi_m^{-1} = \chi\phi_f^{-1} + (1 - \chi)\phi_s^{-1}$ . Though we advocate the latter approach, the analysis presented here is independent of which average is used. We also remark that, since we are studying the onset of convection, the thermal conductivity and specific heat are intrinsic values and not effective values which incorporate dispersive effects.

The time derivative  $\partial_t \mathbf{u}_m$  in the first equation of (2.2) is often neglected since it is heuristically small at small Darcy number. Inclusion of this term in Darcy's equation has been debated in the literature [95]. In this paper, we include the time derivative primarily for the benefit of the energy analysis, although a welcome side effect is that this term would allow more accurate description of temporal transitions. Several works concerning linear stability, [18, 27, 28, 67], exclude time derivatives of the Navier-Stokes and/or Darcy equations by invoking the principle of exchange of stabilities. We note that this principle has not been rigorously established for the coupled system, and therefore we do not assume it. Our numerics, however, suggest that the principle seems to hold in practice.

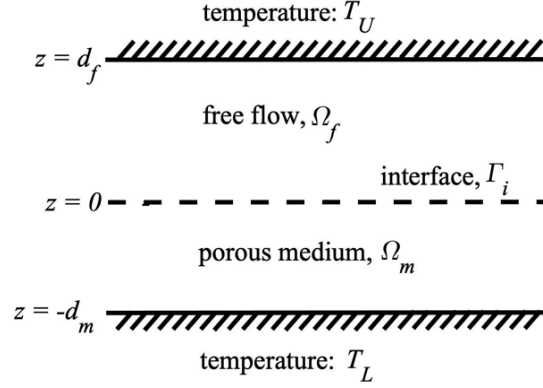


Figure 2.1: Schematic of the domain  $\Omega = \{(x, y) \in \mathbb{R}^2 \times z \in (-d_m, d_f)\}$ , comprised of a free-flow region  $\Omega_f$  and a porous medium  $\Omega_m$ . The two subdomains meet at an interface  $\Gamma_i$ . The upper and lower boundaries are impermeable and held at constant temperatures  $T_U$  and  $T_L$ , respectively, with  $T_L > T_U$ .

### 2.2.2 Boundary and interface conditions

For the domain, shown in Figure 2.1, we assume flat, horizontal, non-penetrable plates at the top and bottom with a non-deforming interface between the two regions,  $\Omega_f = \{(x, y) \in \mathbb{R}^2 \times z \in (0, d_f)\}$  for the free flow and  $\Omega_m = \{(x, y) \in \mathbb{R}^2 \times z \in (-d_m, 0)\}$  for the porous medium. The temperature is held constant at the top and bottom plates. For the flow, we use a free-slip condition at the top and an impermeable condition at the bottom,

$$\begin{cases} T_f = T_U, \mathbf{u}_f \cdot \mathbf{n} = \frac{\partial \mathbf{u}_{f\tau}}{\partial \mathbf{n}} = 0, & \text{at } z = d_f, \\ T_m = T_L, \mathbf{u}_m \cdot \mathbf{n} = 0, & \text{at } z = -d_m, \end{cases} \quad (2.3)$$

where  $\mathbf{u}_{f\tau} = (v_f, w_f)$  denotes the tangential (horizontal) components of the velocity at the top of the domain with  $\mathbf{n}$  as the unit normal vector.

At the interface  $\Gamma_i$  ( $z = 0$ ), we require continuity of temperature, heat flux, and the normal component of velocity:

$$T_f = T_m, \quad (2.4)$$

$$k_f \nabla T_f \cdot \mathbf{n} = k_m \nabla T_m \cdot \mathbf{n}, \quad (2.5)$$

$$\mathbf{u}_f \cdot \mathbf{n} = \mathbf{u}_m \cdot \mathbf{n}. \quad (2.6)$$

The next condition must involve the tangential stress at the interface. The primary condition considered here is the Beavers-Joseph-Saffman-Jones (BJSJ) condition [79], also known as the

Navier-slip condition, which relates the shear stress to the tangential velocity:

$$-\boldsymbol{\tau} \cdot \mathbb{T}(\mathbf{u}_f, p_f) \mathbf{n} = \frac{\mu_0 \alpha}{\sqrt{\Pi}} \boldsymbol{\tau} \cdot \mathbf{u}_f, \quad (2.7)$$

where  $\alpha$  is an empirically determined coefficient and  $\boldsymbol{\tau}$  denotes the unit tangent vectors. Our nonlinear stability analysis will rely on the BJSJ condition. This condition is debated in the literature, and we will therefore consider a few alternatives in the linear analysis, namely the Beavers-Joseph (BJ) condition [5] and the Beavers-Joseph-Jones (BJJ) condition [56]. All three conditions can be represented concisely as

$$\frac{\partial u_{f,\gamma}}{\partial z} + \Psi_J \frac{\partial w_f}{\partial x_\gamma} = \frac{\alpha}{\sqrt{\Pi}} (u_{f,\gamma} - \Psi_S u_{m,\gamma}) \quad \text{for } \gamma = 1, 2,$$

where  $u_{i,\gamma}$  is the  $\gamma$  component of the velocity in  $\Omega_i$ , and  $\Psi_J, \Psi_S \in \{0, 1\}$  are switches associated with the Jones correction and the Saffman approximation terms, respectively. The BJ condition corresponds to  $\Psi_J = 0$  and  $\Psi_S = 1$ , the BJJ condition to  $\Psi_J = 1$  and  $\Psi_S = 1$ , and the BJSJ condition to  $\Psi_J = 1$  and  $\Psi_S = 0$ . The BJJ is considered to be the most physically accurate, as it relates the shear stress to the jump in the tangential velocity across the interface. The BJ condition omits the term  $\partial w_f / \partial x_\gamma$  in the shear stress [21, 26, 27, 28]. Meanwhile, the Saffman approximation drops the Darcy velocity in the right-hand-side, which is relatively small in magnitude as long as the Darcy number is small. Thus, since our nonlinear analysis relies on the BJSJ condition, it will be limited to the physically relevant regime of small Darcy number.

In [83], Straughan compares the BJ and BJJ conditions, showing that the linear marginal stability curves produced by each are almost the same. In section 2.5, we expand upon Straughan's findings by showing that the three interface conditions each produce similar marginal stability curves. Specifically, we show the relative difference between curves produced by the BJSJ condition versus those produced by either BJ or BJJ scales like  $Da$  in the small Darcy number regime.

The last interface condition concerns the balance of force in the normal direction, and there are two options:

$$-\mathbf{n} \cdot \mathbb{T}(\mathbf{u}_f, p_f) \mathbf{n} + \Psi_L \frac{\rho_0}{2} |\mathbf{u}_f|^2 = p_m, \quad (2.8)$$

where  $\Psi_L \in \{0, 1\}$  is a switch for the dynamic pressure term,  $\frac{\rho_0}{2} |\mathbf{u}_f|^2$ . The most common choice in the literature is  $\Psi_L = 0$  which renders Eq. (2.8) linear. For nonlinear analysis, we will choose

$\Psi_L = 1$ , which is known as the *Lions interface condition* [22, 23, 30, 33, 44]. This choice gives rise to an energy law which facilitates the analysis significantly. In the appendix, we show that the dynamic pressure term is order  $Da$  for small Darcy number.

### 2.2.3 Steady-state and perturbed system

First, we introduce the following steady-state solution, known as the conductive state (denoted with an overhead bar):

$$\begin{aligned}\bar{\mathbf{u}}_{\mathbf{f}} &= \bar{\mathbf{u}}_{\mathbf{m}} = \mathbf{0}, \\ \bar{T}_f &= T_0 + z \frac{T_U - T_0}{d_f}, \\ \bar{T}_m &= T_0 + z \frac{T_0 - T_L}{d_m}.\end{aligned}$$

Here,  $T_0$  represents the interface temperature of the conductive solution

$$T_0 = \frac{\kappa_m d_f T_L + \kappa_f d_m T_U}{\kappa_m d_f + \kappa_f d_m}.$$

If  $T_U > T_L$ , the conductive state is stable, but if  $T_L > T_U$ , buoyancy can destabilize the system. In this paper, we consider the latter case. Additionally, we choose  $\bar{p}_f$  and  $\bar{p}_m$  to satisfy

$$\begin{aligned}\nabla \bar{p}_f &= -g\rho_0 (1 - \beta (\bar{T}_f - T_0)) \mathbf{k}, \\ \nabla \bar{p}_m &= -g\rho_0 (1 - \beta (\bar{T}_m - T_L)) \mathbf{k}.\end{aligned}$$

We perturb the steady-state as follows:

$$\begin{aligned}\mathbf{u}_{\mathbf{f}} &= \bar{\mathbf{u}}_{\mathbf{f}} + \mathbf{v}_{\mathbf{f}}, & \mathbf{u}_{\mathbf{m}} &= \bar{\mathbf{u}}_{\mathbf{m}} + \mathbf{v}_{\mathbf{m}}, \\ T_f &= \bar{T}_f + \theta_f, & T_m &= \bar{T}_m + \theta_m, \\ p_f &= \bar{p}_f + \pi_f, & p_m &= \bar{p}_m + \pi_m,\end{aligned}\tag{2.9}$$

where  $\mathbf{v}_j$ ,  $\theta_j$ , and  $\pi_j$  are the perturbation variables. In the linear stability analysis, the perturbations are assumed to be small compared to the background state. However, with the nonlinear analysis, there is no assumption concerning the magnitude of the perturbations. Substituting (2.9) into the

original system produces:

$$\text{In } \Omega_f : \begin{cases} \rho_0 \left( \frac{\partial \mathbf{v}_f}{\partial t_f} + (\mathbf{v}_f \cdot \nabla) \mathbf{v}_f \right) = \nabla \cdot \mathbb{T}(\mathbf{v}_f, \pi_f) + \rho_0 g \beta \theta_f \mathbf{k}, \\ \nabla \cdot \mathbf{v}_f = 0, \\ \varrho \frac{\partial \theta_f}{\partial t_f} + \mathbf{v}_f \cdot \nabla \theta_f = \lambda_f \nabla^2 \theta_f - w_f \left( \frac{T_U - T_0}{d_f} \right), \end{cases}$$

for  $(x, y, z, t) \in \{\mathbb{R}^2 \times (0, d_f) \times (0, \infty)\}$ ,

$$\text{In } \Omega_m : \begin{cases} \frac{\mu_0}{\Pi} \mathbf{v}_m = -\nabla \pi_m + \rho_0 g \beta \theta_m \mathbf{k}, \\ \nabla \cdot \mathbf{v}_m = 0, \\ \varrho \frac{\partial \theta_m}{\partial t_m} + \mathbf{v}_m \cdot \nabla \theta_m = \lambda_m \nabla^2 \theta_m - w_m \left( \frac{T_0 - T_L}{d_m} \right), \end{cases}$$

for  $(x, y, z, t) \in \{\mathbb{R}^2 \times (-d_m, 0) \times (0, \infty)\}$ , and

$$\text{On } \Gamma_i : \begin{cases} \theta_f = \theta_m, \\ \kappa_f \nabla \theta_f \cdot \mathbf{n} = \kappa_m \nabla \theta_m \cdot \mathbf{n}, \\ \mathbf{v}_f \cdot \mathbf{n} = \mathbf{v}_m \cdot \mathbf{n}, \\ \frac{\mu_0 \alpha}{\sqrt{\Pi}} (\boldsymbol{\tau} \cdot \mathbf{v}_f) = -\boldsymbol{\tau} \cdot \mathbb{T}(\mathbf{v}_f, \pi_f) \mathbf{n}, \\ \pi_m = -\mathbf{n} \cdot \mathbb{T}(\mathbf{v}_f, \pi_f) \mathbf{n} + \Psi_L \frac{\rho_0}{2} |\mathbf{v}_f|^2, \end{cases}$$

for  $(x, y, 0, t) \in \{\mathbb{R}^2 \times (z = 0) \times (0, \infty)\}$  with

$$\varrho = \frac{(\rho_0 c_p)_m}{(\rho_0 c_p)_f}.$$

## 2.2.4 Nondimensionalization

We introduce the same scalings as [26, 83] with nondimensional variables denoted by tildes:

$$\begin{aligned} \mathbf{v}_f &= \tilde{\mathbf{v}}_f \frac{\nu}{d_f}, & \mathbf{x}_f &= \tilde{\mathbf{x}}_f d_f, & t_f &= \tilde{t}_f \frac{d_f^2}{\lambda_f}, & \theta_f &= \tilde{\theta}_f \frac{(T_U - T_0) \nu}{\lambda_f}, & \pi_f &= \tilde{\pi}_f \frac{\rho_0 \nu^2}{d_f^2}, \\ \mathbf{v}_m &= \tilde{\mathbf{v}}_m \frac{\nu}{d_m}, & \mathbf{x}_m &= \tilde{\mathbf{x}}_m d_m, & t_m &= \tilde{t}_m \frac{d_m^2}{\lambda_m}, & \theta_m &= \tilde{\theta}_m \frac{(T_0 - T_L) \nu}{\lambda_m}, & \pi_m &= \tilde{\pi}_m \frac{\rho_0 \nu^2}{d_m^2}, \end{aligned}$$

(where  $\nu = \mu_0/\rho_0$  is the kinematic viscosity) which yields the systems (sans tildes):

$$\text{In } \Omega_f : \begin{cases} \frac{1}{\text{Pr}_f} \frac{\partial \mathbf{v}_f}{\partial t_f} + (\mathbf{v}_f \cdot \nabla) \mathbf{v}_f = 2\nabla \cdot \mathbb{D}(\mathbf{v}_f) - \nabla \pi_f - \text{Ra}_f \theta_f \mathbf{k}, \\ \nabla \cdot \mathbf{v}_f = 0, \\ \frac{\partial \theta_f}{\partial t_f} + \text{Pr}_f \mathbf{v}_f \cdot \nabla \theta_f = \nabla^2 \theta_f - w_f, \end{cases} \quad (2.10)$$

for  $(x, y, z, t) \in \{\mathbb{R}^2 \times (0, 1) \times (0, \infty)\}$ ,

$$\text{In } \Omega_m : \begin{cases} \frac{1}{\chi} \frac{\text{Da}}{\text{Pr}_m} \frac{\partial \mathbf{v}_m}{\partial t_m} + \mathbf{v}_m = -\text{Da} \nabla \pi_m - \text{Ra}_m \theta_m \mathbf{k}, \\ \nabla \cdot \mathbf{v}_m = 0, \\ \varrho \frac{\partial \theta_m}{\partial t_m} + \text{Pr}_m \mathbf{v}_m \cdot \nabla \theta_m = \nabla^2 \theta_m - w_m, \end{cases} \quad (2.11)$$

for  $(x, y, z, t) \in \{\mathbb{R}^2 \times (-1, 0) \times (0, \infty)\}$ , and

$$\text{On } \Gamma_i : \begin{cases} \hat{d} \theta_f = \epsilon_T^2 \theta_m, \\ \nabla_f \theta_f \cdot \mathbf{n} = \epsilon_T \nabla_m \theta_m \cdot \mathbf{n}, \\ \mathbf{v}_f \cdot \mathbf{n} = \hat{d} \mathbf{v}_m \cdot \mathbf{n}, \\ \frac{\hat{d} \alpha}{\sqrt{\text{Da}}} (\boldsymbol{\tau} \cdot \mathbf{v}_f) = -\boldsymbol{\tau} \cdot \mathbb{T}(\mathbf{v}_f, \pi_f) \mathbf{n}, \\ \hat{d}^2 \pi_m = -\mathbf{n} \cdot \mathbb{T}(\mathbf{v}_f, \pi_f) \mathbf{n} + \Psi_L \frac{1}{2} |\mathbf{v}_f|^2, \end{cases} \quad (2.12)$$

for  $(x, y, 0, t) \in \{\mathbb{R}^2 \times (z = 0) \times (0, \infty)\}$ . Here, the notation  $\nabla_j$  indicates the gradient with respect to  $\mathbf{x}_j$  where  $j \in \{f, m\}$ .

We have introduced a total of seven dimensionless parameters. The first five are given by

$$\hat{d} = \frac{d_f}{d_m}, \quad \epsilon_T = \frac{\lambda_f}{\lambda_m}, \quad \text{Da} = \frac{\Pi}{d_m^2}, \quad \text{Pr}_f = \frac{\nu}{\lambda_f}, \quad \text{Pr}_m = \frac{\nu}{\lambda_m}.$$

These parameters are, respectively, the depth ratio, the ratio of thermal diffusivities, the Darcy number, and the Prandtl numbers of the free-flow and porous regions. The last two are the Rayleigh numbers of the two regions

$$\text{Ra}_f = \frac{g\beta(T_0 - T_U) d_f^3}{\nu \lambda_f}, \quad \text{Ra}_m = \frac{g\beta(T_L - T_0) \text{Da} d_m^3}{\nu \lambda_m} = \text{Ra}_f \frac{\text{Da} \epsilon_T^2}{\hat{d}^4}. \quad (2.13)$$

## 2.3 Linear stability

In this section, we briefly overview the linear stability analysis of system (2.10)–(2.12). For additional details, the reader is referred to [83], which differs only in the interface condition chosen in Eq. (2.7). Here, we set  $\Psi_J = 1$ ,  $\Psi_S = 0$ , corresponding to the BJSJ condition. The value of  $\Psi_L$  is irrelevant since the dynamic pressure term is nonlinear and hence omitted in linear analysis.

Assuming perturbations to be small eliminates quadratic and higher-order terms from (2.10)–(2.12). With the resulting linear system, we take the double curl to remove the pressure terms and then, considering the third component, we substitute normal mode solutions

$$w_j(\mathbf{x}, t) = F_j(x, y) \tilde{w}_j(z) e^{\sigma_j t} \quad \text{and} \quad \theta_j(\mathbf{x}, t) = F_j(x, y) \tilde{\theta}_j(z) e^{\sigma_j t}, \quad (2.14)$$

for  $j \in \{f, m\}$ . Here,  $F_j(x, y)$  corresponds to a unimodal component of the horizontal planform in each region with corresponding horizontal wavenumber  $a_j$ . That is,

$$a_j^2 F_j(x, y) + \nabla_H^2 F_j(x, y) = 0$$

where  $\nabla_H^2 = \frac{\partial^2}{\partial x^2} + \frac{\partial^2}{\partial y^2}$  is the horizontal Laplacian operator. This modal decomposition defines the structure of the convection cells [21, 37, 85, 87]. With (2.14), the real part of  $\sigma_j$  determines the stability of the flow; if  $\text{Re}(\sigma_j) < 0$  the corresponding normal mode decays in time and if  $\text{Re}(\sigma_j) > 0$  it grows. From our nondimensional scalings, we note the following relationships:

$$a_f = \hat{d} a_m, \quad \sigma_f = \frac{\epsilon_T}{\hat{d}^2} \sigma_m, \quad \text{Ra}_f = \text{Ra}_m \frac{\hat{d}^4}{\text{Da} \epsilon_T^2}. \quad (2.15)$$

Using the notation  $D_f = \frac{d}{dz_f}$  and  $D_m = \frac{d}{dz_m}$  for spatial derivatives in  $\Omega_f$  and  $\Omega_m$ , respectively, we acquire the system: Using the notation  $D_f = \frac{d}{dz_f}$  and  $D_m = \frac{d}{dz_m}$  for spatial derivatives in  $\Omega_f$  and  $\Omega_m$ , respectively, we acquire the system:

$$\text{In } \Omega_f, z \in (0, 1) : \quad \begin{cases} \frac{\sigma_f}{\text{Pr}_f} (D_f^2 - a_f^2) w_f = (D_f^2 - a_f^2)^2 w_f + a_f^2 \text{Ra}_f \theta_f, \\ \sigma_f \theta_f = (D_f^2 - a_f^2) \theta_f - w_f, \end{cases} \quad (2.16)$$

$$\text{In } \Omega_m, z \in (-1, 0) : \quad \begin{cases} \frac{\sigma_m}{\chi} \frac{\text{Da}}{\text{Pr}_m} (D_m^2 - a_m^2) w_m = -(D_m^2 - a_m^2) w_m + a_m^2 \text{Ra}_m \theta_m, \\ \sigma_m \varrho \theta_m = (D_m^2 - a_m^2) \theta_m - w_m, \end{cases} \quad (2.17)$$

$$\text{On } \Gamma_i, z = 0 : \left\{ \begin{array}{l} \hat{d}\theta_f = \epsilon_T^2 \theta_m, \\ D_f \theta_f = \epsilon_T D_m \theta_m, \\ w_f = \hat{d} w_m, \\ \frac{\hat{d}\alpha}{\sqrt{\text{Da}}} D_f w_f = D_f^2 w_f, \\ \frac{\sigma_f}{\text{Pr}_f} D_f w_f - D_f^3 w_f + 3a_f^2 D_f w_f = \frac{\hat{d}^4}{\chi \text{Pr}_m} \sigma_m D_m w_m + \frac{\hat{d}^4}{\text{Da}} D_m w_m, \end{array} \right. \quad (2.18)$$

with the boundary conditions at the top and bottom of the domain:

$$\text{At } z = 1 : \quad w_f = D_f w_f = \theta_f = 0, \quad (2.19)$$

$$\text{At } z = -1 : \quad w_m = \theta_m = 0. \quad (2.20)$$

### 2.3.1 Solving the linear system

System (2.16)–(2.20) constitutes a generalized eigenvalue problem for either  $\sigma_f$  or  $\sigma_m$ , which we solve with the Chebyshev tau-QZ algorithm [36] implemented with the Chebfun package [38]. This algorithm first performs Chebyshev collocation [57, 64, 93] and then solves the resulting linear system with the QZ method [47, 63]. Lastly, we make substitution (2.15) to find the marginal stability curves in the  $(a_m, \text{Ra}_m)$  plane. For each wavenumber  $a_m$ , there is a Rayleigh number  $\text{Ra}_m$  where the flow transitions from stable to unstable (i.e.  $\text{Re}(\sigma_j)$  changes from negative to positive). The marginal stability curves,  $\text{Re}(\sigma_j) = 0$ , shown in section 2.5 delineate the boundary between stable and unstable regimes.

To use the Chebyshev-tau method, we first transform both the fluid system (2.16) from  $z_f \in (0, 1)$  and the porous system (2.17) from  $z_m \in (-1, 0)$  to the Chebyshev domain  $z_c \in (-1, 1)$  with  $z_c = 2z_f - 1$  and  $z_c = -2z_m - 1$ . This allows the outer-boundaries of the physical domain to be mapped to  $z_c = 1$  while both interfaces are mapped to  $z_c = -1$ . The mapping is detailed in Table 2.1.

With  $D$  as the discretized spatial derivative instead of  $D_f$  and  $D_m$  as the derivatives in the fluid and medium and  $A_f$  defined as an independent variable for convenience (in the style of Straughan et al.), we have the linear system to solve (2.16)–(2.18):

Table 2.1: Transformations from the nondimensional domain to the Chebyshev domain.

	Nondimensional Domain	Transformation $\implies$	Chebyshev Domain
Top of fluid region:	$z_f = 1$	$z_c = 2z_f - 1$	$z_c = 1$
Interface (from fluid region):	$z_f = 0$	$\implies$	$z_c = -1$
Interface (from porous medium):	$z_m = 0$	$z_c = -2z_m - 1$	$z_c = -1$
Bottom of porous medium:	$z_m = -1$	$\implies$	$z_c = 1$

$$\text{For } z_c \in (-1, 1) : \left\{ \begin{array}{l} (4D^2 - a_f^2) w_f - A_f = 0, \\ (4D^2 - a_f^2) A_f + a_f^2 \text{Ra}_f \theta_f = \frac{\sigma_f}{\text{Pr}_f} (4D^2 - a_f^2) w_f, \\ (4D^2 - a_f^2) \theta_f - w_f = \sigma_f \theta_f, \\ (4D^2 - a_m^2) w_m - a_m^2 \text{Ra}_m \theta_m = -\frac{\sigma_m}{\chi} \frac{\text{Da}}{\text{Pr}_m} (4D^2 - a_m^2) w_m, \\ (4D^2 - a_m^2) \theta_m - w_m = \sigma_m \rho \theta_m. \end{array} \right.$$

As stated above, we solve this system for the eigenvalue  $\sigma_m$  in the  $(a_m, \text{Ra}_m)$ -plane by exploiting the relationship noted in (2.15), and making the appropriate substitutions for  $a_f, \text{Ra}_f$ , and  $\sigma_f$ . We solve the eigenvalue problem  $A \mathbf{s} = \sigma B \mathbf{s}$ , where  $\mathbf{s}$  is a vector of the independent variables  $(w_f, A_f, \theta_f, w_m, \theta_m)$  as truncated Chebyshev series,  $I$  is the identity matrix, and the spatial derivative  $D$  is now the discretized derivative operator as a matrix. The explicit system  $A \mathbf{s} = \sigma_m B \mathbf{s}$  is written as:

$$\implies \begin{pmatrix} 4D^2 - \hat{d}^2 a_m^2 I & -I & 0 & 0 & 0 \\ 0 & 4D^2 - \hat{d}^2 a_m^2 I & \text{Ra}_m \frac{\hat{d}^6 a_m^2}{\text{Da} \epsilon_T^2} I & 0 & 0 \\ -I & 0 & 4D^2 - \hat{d}^2 a_m^2 I & 0 & 0 \\ 0 & 0 & 0 & 4D^2 - a_m^2 I & -a_m^2 \text{Ra}_m I \\ 0 & 0 & 0 & -I & 4D^2 - a_m^2 I \end{pmatrix} \begin{pmatrix} w_f \\ A_f \\ \theta_f \\ w_m \\ \theta_m \end{pmatrix} =$$

$$\sigma_m \begin{pmatrix} 0 & 0 & 0 & 0 & 0 \\ \frac{1}{\text{Pr}_f} (4D^2 - \hat{d}^2 a_m^2 I) & 0 & 0 & 0 & 0 \\ 0 & 0 & I & 0 & 0 \\ 0 & 0 & 0 & -\frac{\text{Da}}{\chi \text{Pr}_m} (4D^2 - a_m^2 I) & 0 \\ 0 & 0 & 0 & 0 & \rho I \end{pmatrix} \begin{pmatrix} w_f \\ A_f \\ \theta_f \\ w_m \\ \theta_m \end{pmatrix}$$

subject to the boundary conditions at the top and bottom of the Chebyshev domain as:

$$\text{at } z_c = 1 : \quad w_f = Dw_f = \theta_f = w_m = \theta_m = 0,$$

and

$$\text{at } z_c = -1 : \left\{ \begin{array}{l} 0 = \hat{d}\theta_f - \epsilon_T^2 \theta_m, \\ 0 = D\theta_f + \epsilon_T D\theta_m, \\ 0 = w_f - \hat{d}w_m, \\ 0 = 2D^2w_f - \frac{\hat{d}\alpha}{\sqrt{\text{Da}}} Dw_f, \\ 0 = \sigma_m \frac{\hat{d}^4}{\chi \text{Pr}_m} Dw_m + \frac{\hat{d}^4}{\text{Da}} Dw_m + \sigma_m \frac{\epsilon_T}{\text{Pr}_f \hat{d}^2} Dw_f - 4D^3w_f + 3\hat{d}^2 a_m^2 Dw_f. \end{array} \right.$$

With use of the Chebfun package, we solve this system for a given wavenumber  $a_m$  and Rayleigh number  $\text{Ra}_m$  to determine the eigenvalue  $\sigma_m$ . We iterate through the Rayleigh numbers to find the minimum Rayleigh number which provides  $\sigma_m > 0$ . These points in the  $(a_m, \text{Ra}_m)$ -plane denote the marginal stability curves, shown in results section.

In Figure 2.2, we show the eigenvalues found from solving the generalized eigenvalue problem for different Rayleigh numbers. For each of the cases, we use the parameters  $\hat{d} = .2$ ,  $a_m = 10.0$ ,  $\sqrt{\text{Da}} = 5.0 \times 10^{-3}$ ,  $\epsilon_T = .7$ ,  $\alpha = 1.0$ , and the BJSJ condition ( $\Psi_J = 1, \Psi_S = 0$ ). For this wavenumber  $a_m = 10.0$ , we iterate through increasing Rayleigh numbers until we find that the maximum of the real components of eigenvalues becomes positive. In the top plots of Figure 2.2, we show the eigenvalues  $\sigma_m$  for  $\text{Ra}_m = 10$  and  $\text{Ra}_m = 11$ . Neither of these cases have  $\text{Re}(\sigma_m) > 0$ , but they are approaching 0. In the bottom left plot with  $\text{Ra}_m = 12$ , we see the real component of  $\sigma_m > 0$ . So, we would repeat this process of iterating through Rayleigh numbers, between  $\text{Ra}_m = 11$  and  $\text{Ra}_m = 12$  this time to obtain a more precise stability threshold for this wavenumber. These steps help us get a *single point* in the  $(a_m, \text{Ra}_m)$ -plane to construct the marginal stability curves. So, creating marginal stability curves for the coupled case is a time-consuming process.

For the single layer cases of a single layer of fluid or a single layer of a porous medium saturated with a fluid, a principle of exchange of stabilities has been shown stating that if  $\text{Ra} > 0$ , then  $\sigma$  must be real. This allows us to set  $\sigma = 0$  and solve an eigenvalue problem for the  $\text{Ra}$  to determine marginal stability curves. This principle has not been shown for the coupled case. However, we see the results hold in practice. For  $\text{Ra}_m > 0$ , we see that the eigenvalues  $\sigma_m$  lie along the real line in Figure 2.2. Additionally, for  $\text{Ra}_m < 0$  (shown in the bottom right plot of Figure 2.2), we see the

eigenvalues can have imaginary components. These results suggest that the principle of exchange of stabilities may hold for the coupled case. Rigorously proving that the principle holds has yet to be shown though.

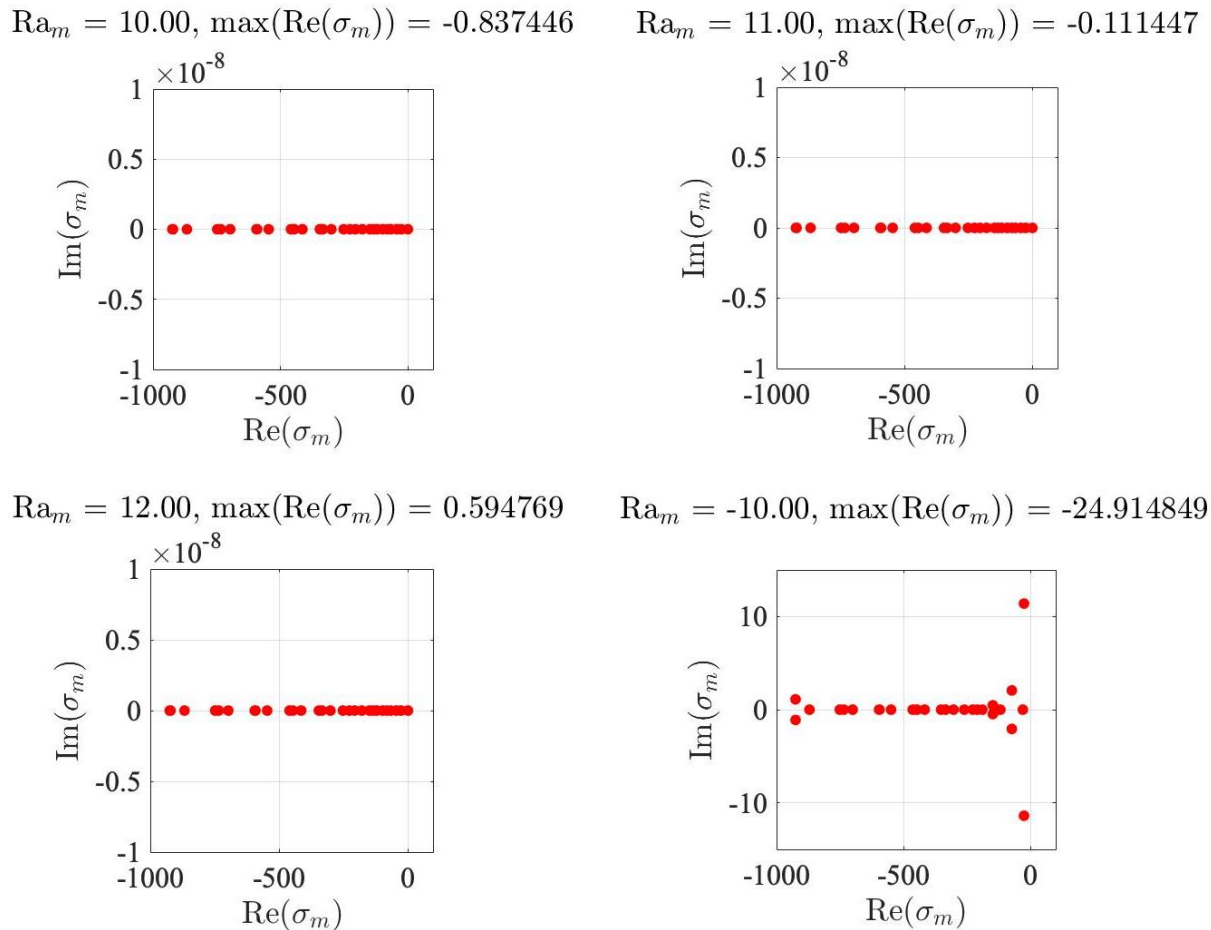


Figure 2.2: Eigenvalues for linear stability, with parameters  $\hat{d} = .2$ ,  $a_m = 10.0$ ,  $\sqrt{\text{Da}} = 5.0 \times 10^{-3}$ ,  $\epsilon_T = .7$ ,  $\alpha = 1.0$ , and the BJSJ condition is used ( $\Psi_J = 1$ ,  $\Psi_S = 0$ ).

## 2.4 Nonlinear stability

In this section, we address nonlinear stability using the energy method. Our analysis builds off of important previous works [52, 53, 54, 71] that examined nonlinear stability of related fluid-porous

systems. Here, we adopt similar techniques, in conjunction with the Lions interface condition, to obtain an energy law and ultimately resolve nonlinear stability of the Navier-Stokes-Darcy system.

Throughout this section we employ the BJSJ condition ( $\Psi_J = 1, \Psi_S = 0$ ) and the Lions condition ( $\Psi_L = 1$ ). We use the following notation for vector-valued functions  $\mathbf{f}$  and  $\mathbf{g}$  and matrix-valued functions  $\mathbf{A}$  and  $\mathbf{B}$ :

$$(\mathbf{f}, \mathbf{g})_j = \int_{\Omega_j} \mathbf{f} \cdot \mathbf{g} \, d\Omega_j, \quad \langle \mathbf{A}, \mathbf{B} \rangle_j = \int_{\Omega_j} \mathbf{A} : \mathbf{B} \, d\Omega_j, \quad \|\mathbf{f}\|_j^2 = (\mathbf{f}, \mathbf{f})_j, \quad |\mathbf{f}|^2 = \mathbf{f} \cdot \mathbf{f},$$

for domains  $j \in \{f, m\}$ . In this section,  $\Omega_f$  and  $\Omega_m$  represent a single period cell in the respective domains. We dot the first equation of (2.10) with  $\mathbf{v}_f$  and integrate over  $\Omega_f$ :

$$\frac{1}{\text{Pr}_f} \left( \frac{\partial \mathbf{v}_f}{\partial t_f}, \mathbf{v}_f \right) + ((\mathbf{v}_f \cdot \nabla) \mathbf{v}_f, \mathbf{v}_f)_f = 2(\nabla \cdot \mathbb{D}(\mathbf{v}_f), \mathbf{v}_f)_f - (\nabla \pi_f, \mathbf{v}_f)_f - \text{Ra}_f (\theta_f \mathbf{k}, \mathbf{v}_f)_f.$$

After integrating by parts, the boundary integrals reduce to integrals along the interface of the fluid region,  $\Gamma_f$ , leaving

$$\begin{aligned} \frac{1}{2 \text{Pr}_f} \frac{d}{dt_f} \|\mathbf{v}_f\|_f^2 &= \frac{1}{2} \int_{\Gamma_f} |\mathbf{v}_f|^2 (\mathbf{v}_f \cdot \mathbf{n}) \, d\Gamma_f - 2 \langle \mathbb{D}(\mathbf{v}_f), \mathbb{D}(\mathbf{v}_f) \rangle_f - 2 \int_{\Gamma_f} \mathbf{n} \cdot \mathbb{D}(\mathbf{v}_f) \mathbf{n} (\mathbf{v}_f \cdot \mathbf{n}) \, d\Gamma_f \\ &\quad - 2 \int_{\Gamma_f} \sum_{i=1}^2 \boldsymbol{\tau}_i \cdot \mathbb{D}(\mathbf{v}_f) \mathbf{n} (\mathbf{v}_f \cdot \boldsymbol{\tau}_i) \, d\Gamma_f + \int_{\Gamma_f} \pi_f (\mathbf{v}_f \cdot \mathbf{n}) \, d\Gamma_f - \text{Ra}_f (\theta_f, w_f)_f, \end{aligned}$$

where  $\boldsymbol{\tau}_i$  are the unit tangents in  $x$  and  $y$  at the interface. Applying the BJSJ and Lions interface conditions from (2.12) gives

$$\begin{aligned} \frac{1}{2 \text{Pr}_f} \frac{d}{dt_f} \|\mathbf{v}_f\|_f^2 &= \frac{1}{2} \int_{\Gamma_f} |\mathbf{v}_f|^2 (\mathbf{v}_f \cdot \mathbf{n}) \, d\Gamma_f - 2 \langle \mathbb{D}(\mathbf{v}_f), \mathbb{D}(\mathbf{v}_f) \rangle_f \\ &\quad + \int_{\Gamma_f} \left[ \hat{d}^2 \pi_m - \pi_f - \frac{1}{2} |\mathbf{v}_f|^2 \right] (\mathbf{v}_f \cdot \mathbf{n}) \, d\Gamma_f - \int_{\Gamma_f} \sum_{i=1}^2 \left[ \frac{\hat{d} \alpha}{\sqrt{\text{Da}}} (\mathbf{v}_f \cdot \boldsymbol{\tau}_i) \right] (\mathbf{v}_f \cdot \boldsymbol{\tau}_i) \, d\Gamma_f \\ &\quad + \int_{\Gamma_f} \pi_f (\mathbf{v}_f \cdot \mathbf{n}) \, d\Gamma_f - \text{Ra}_f (\theta_f, w_f)_f. \end{aligned}$$

We note that the first term on the RHS involving  $\frac{1}{2} |\mathbf{v}_f|^2 (\mathbf{v}_f \cdot \mathbf{n})$  arises from the nonlinear advection. Importantly, the application of the *Lions* interface condition to the expression  $\mathbf{n} \cdot \mathbb{D}(\mathbf{v}_f) \mathbf{n} (\mathbf{v}_f \cdot \mathbf{n})$  produces a similar term with opposite sign that cancels this first term. Without this cancellation, the presence of the sign-indefinite term  $\frac{1}{2} |\mathbf{v}_f|^2 (\mathbf{v}_f \cdot \mathbf{n})$  would hamper energy analysis.

However, with the cancellation, we obtain the following energy law

$$\begin{aligned} \frac{1}{2 \text{Pr}_f} \frac{d}{dt_f} \|\mathbf{v}_f\|_f^2 &= -2 \langle \mathbb{D}(\mathbf{v}_f), \mathbb{D}(\mathbf{v}_f) \rangle_f - \text{Ra}_f (\theta_f, w_f)_f \\ &+ \int_{\Gamma_f} \hat{d}^2 \pi_m (\mathbf{v}_f \cdot \mathbf{n}) d\Gamma_f - \int_{\Gamma_f} \sum_{i=1}^2 \frac{\hat{d} \alpha}{\sqrt{\text{Da}}} (\mathbf{v}_f \cdot \boldsymbol{\tau}_i)^2 d\Gamma_f. \end{aligned} \quad (2.21)$$

Now, we dot the third equation of (2.10), the first equation of (2.11), and the third equation of (2.11) with  $\theta_f$ ,  $\mathbf{v}_m$ , and  $\theta_m$ , respectively, and then integrate over the appropriate domains, producing

$$\frac{1}{2} \frac{d}{dt_f} \|\theta_f\|_f^2 = -\frac{\text{Pr}_f}{2} \int_{\Gamma_f} (\mathbf{v}_f \cdot \mathbf{n}) \theta_f^2 d\Gamma_f + \int_{\Gamma_f} \theta_f (\nabla \theta_f \cdot \mathbf{n}) d\Gamma_f - \|\nabla \theta_f\|_f^2 - (w_f, \theta_f)_f, \quad (2.22)$$

$$\frac{1}{2} \frac{\text{Da}}{\chi \text{Pr}_m} \frac{d}{dt_m} \|\mathbf{v}_m\|_m^2 = -\|\mathbf{v}_m\|_m^2 - \int_{\Gamma_m} \text{Da} \pi_m (\mathbf{v}_m \cdot \mathbf{n}) d\Gamma_m - \text{Ra}_m (\theta_m, w_m)_m, \quad (2.23)$$

$$\frac{\varrho}{2} \frac{d}{dt_m} \|\theta_m\|_m^2 = \frac{\text{Pr}_m}{2} \int_{\Gamma_m} (\mathbf{v}_m \cdot \mathbf{n}) \theta_m^2 d\Gamma_m - \int_{\Gamma_m} \theta_m (\nabla \theta_m \cdot \mathbf{n}) d\Gamma_m - \|\nabla \theta_m\|_m^2 - (w_m, \theta_m)_m, \quad (2.24)$$

where  $\Gamma_m$  denotes the interface of the porous medium. From here, we follow an argument similar to that of Straughan, Carr, and Hill in [53, 54]. We add equations (2.21)–(2.24) together and multiply (2.22), (2.23), (2.24) by coupling parameters  $\lambda_1, \lambda_2, \lambda_3 > 0$ , respectively. The introduction of these parameters permits sharper bounds on the critical Rayleigh numbers than could be obtained otherwise. In addition, we rescale time derivatives in the porous medium by the factor  $\epsilon_T/\hat{d}^2$ , so that we are using the same scale as in the free-flow zone. These manipulations yield the system

$$\begin{aligned} \frac{d}{dt} \left[ \frac{1}{2 \text{Pr}_f} \|\mathbf{v}_f\|_f^2 + \frac{\lambda_2 \epsilon_T}{2 \hat{d}^2} \frac{\text{Da}}{\chi \text{Pr}_m} \|\mathbf{v}_m\|_m^2 + \frac{\lambda_1}{2} \|\theta_f\|_f^2 + \frac{\lambda_3 \varrho \epsilon_T}{2 \hat{d}^2} \|\theta_m\|_m^2 \right] &= \\ -2 \langle \mathbb{D}(\mathbf{v}_f), \mathbb{D}(\mathbf{v}_f) \rangle_f + \int_{\Gamma_f} \hat{d}^2 \pi_m (\mathbf{v}_f \cdot \mathbf{n}) d\Gamma_f - \int_{\Gamma_i} \sum_{i=1}^2 \frac{\hat{d} \alpha}{\sqrt{\text{Da}}} (\mathbf{v}_f \cdot \boldsymbol{\tau}_i)^2 d\Gamma_i - \text{Ra}_f (\theta_f, w_f)_f & \\ + \lambda_1 \left( -\frac{\text{Pr}_f}{2} \int_{\Gamma_f} (\mathbf{v}_f \cdot \mathbf{n}) \theta_f^2 d\Gamma_f + \int_{\Gamma_f} \theta_f (\nabla \theta_f \cdot \mathbf{n}) d\Gamma_f - \|\nabla \theta_f\|_f^2 - (w_f, \theta_f)_f \right) & \\ + \lambda_2 \left( -\|\mathbf{v}_m\|_m^2 - \int_{\Gamma_m} \text{Da} \pi_m (\mathbf{v}_m \cdot \mathbf{n}) d\Gamma_m - \text{Ra}_m (\theta_m, w_m)_m \right) & \\ + \lambda_3 \left( \frac{\text{Pr}_m}{2} \int_{\Gamma_m} (\mathbf{v}_m \cdot \mathbf{n}) \theta_m^2 d\Gamma_m - \int_{\Gamma_m} \theta_m (\nabla \theta_m \cdot \mathbf{n}) d\Gamma_m - \|\nabla \theta_m\|_m^2 - (w_m, \theta_m)_m \right). & \end{aligned}$$

We will next choose the coupling parameters,  $\lambda_1, \lambda_2, \lambda_3$ , to make convenient cancellations with integrals along the interface. First, focusing on  $\lambda_2$ , a change of variables allows us to write

$$\int_{\Gamma_f} \hat{d}^2 \pi_m(\mathbf{v}_f \cdot \mathbf{n}) d\Gamma_f - \lambda_2 \int_{\Gamma_m} \text{Da} \pi_m(\mathbf{v}_m \cdot \mathbf{n}) d\Gamma_m = \left( \hat{d}^2 - \lambda_2 \frac{\text{Da}}{\hat{d}} \right) \int_{\Gamma_f} \pi_m(\mathbf{v}_f \cdot \mathbf{n}) d\Gamma_f.$$

We therefore choose  $\lambda_2 = \hat{d}^3/\text{Da}$  so that the expression on the right-hand-side vanishes. Next, consider the terms associated with  $\lambda_1$  and  $\lambda_3$ :

$$\begin{aligned} -\lambda_1 \frac{\text{Pr}_f}{2} \int_{\Gamma_f} (\mathbf{v}_f \cdot \mathbf{n}) \theta_f^2 d\Gamma_f + \lambda_3 \frac{\text{Pr}_m}{2} \int_{\Gamma_m} (\mathbf{v}_m \cdot \mathbf{n}) \theta_m^2 d\Gamma_m &= \left( -\lambda_1 + \lambda_3 \frac{\hat{d}}{\epsilon_T^3} \right) \int_{\Gamma_f} (\mathbf{v}_f \cdot \mathbf{n}) \theta_f^2 d\Gamma_f, \\ \lambda_1 \int_{\Gamma_f} \theta_f (\nabla \theta_f \cdot \mathbf{n}) d\Gamma_f - \lambda_3 \int_{\Gamma_m} \theta_m (\nabla \theta_m \cdot \mathbf{n}) d\Gamma_m &= \left( \lambda_1 - \lambda_3 \frac{\hat{d}}{\epsilon_T^3} \right) \int_{\Gamma_f} \theta_f (\nabla \theta_f \cdot \mathbf{n}) d\Gamma_f. \end{aligned}$$

Choosing  $\lambda_1 = \lambda_3 \left( \hat{d}/\epsilon_T^3 \right)$  allows both terms on the right-hand-sides to vanish. In summary, we choose  $\lambda_2 = \hat{d}^3/\text{Da}$ ,  $\lambda_1 = \lambda$ , and  $\lambda_3 = \left( \epsilon_T^3/\hat{d} \right) \lambda$ . Importantly, there is now only a single free parameter  $\lambda$ .

With our choices for the coupling parameters and the functional energy

$$2E(t) = \frac{1}{\text{Pr}_f} \|\mathbf{v}_f\|_f^2 + \frac{\hat{d}^3}{\chi \text{Pr}_m} \|\mathbf{v}_m\|_m^2 + \lambda \|\theta_f\|_f^2 + \lambda \frac{\epsilon_T^3}{\hat{d}} \varrho \|\theta_m\|_m^2,$$

we are left with

$$\frac{dE}{dt} = -\mathcal{D} + \mathcal{I} - \int_{\Gamma_i} \sum_{i=1}^2 \frac{\hat{d} \alpha}{\sqrt{\text{Da}}} (\mathbf{v}_f \cdot \boldsymbol{\tau}_i)^2 d\Gamma_f \leq -\mathcal{D} + \mathcal{I}, \quad (2.25)$$

where the definite and indefinite terms,  $\mathcal{D}$  and  $\mathcal{I}$ , respectively, are defined as

$$\begin{aligned} \mathcal{D} &= \|\nabla \mathbf{v}_f\|_f^2 + \frac{\hat{d}^3}{\text{Da}} \|\mathbf{v}_m\|_m^2 + \lambda \|\nabla \theta_f\|_f^2 + \lambda \frac{\epsilon_T^3}{\hat{d}} \|\nabla \theta_m\|_m^2, \\ \mathcal{I} &= -[\text{Ra}_{f,\lambda} + \lambda] (w_f, \theta_f)_f - \left[ \frac{\hat{d}^3}{\text{Da}} \text{Ra}_{m,\lambda} + \lambda \frac{\epsilon_T^3}{\hat{d}} \right] (w_m, \theta_m)_m, \end{aligned}$$

and  $2\langle \mathbb{D}(\mathbf{v}_f), \mathbb{D}(\mathbf{v}_f) \rangle_f = \|\nabla \mathbf{v}_f\|_f^2$ . We are now using the notation  $\text{Ra}_{f,\lambda}$  and  $\text{Ra}_{m,\lambda}$  to indicate dependence on the coupling parameter  $\lambda$ . The change in the total energy of the system is bounded by

$$\frac{dE}{dt} \leq -\mathcal{D} + \mathcal{I} = \mathcal{D} \left( \frac{\mathcal{I}}{\mathcal{D}} - 1 \right) \leq \mathcal{D} \left( \max_{\mathcal{H}} \frac{\mathcal{I}}{\mathcal{D}} - 1 \right) = -\mathcal{D} \left( 1 - \max_{\mathcal{H}} \frac{\mathcal{I}}{\mathcal{D}} \right),$$

where  $\mathcal{H}$  is the set of admissible solutions to equations (2.10) and (2.11) subject to (2.12). Defining  $R_E$  as the maximum of the ratio of energies

$$\frac{1}{R_E} = \max_{\mathcal{H}} \frac{\mathcal{I}}{\mathcal{D}} \quad (2.26)$$

yields

$$\frac{dE}{dt} \leq -\mathcal{D} \left( \frac{R_E - 1}{R_E} \right). \quad (2.27)$$

The Poincaré inequality implies that  $\mathcal{D} \geq cE$  for some constant  $c > 0$  [52, 53, 54]. Then, if  $R_E \geq 1$ , Gronwall's inequality produces at least exponential convergence:

$$E(t) \leq E(0)e^{-\hat{a}t} \rightarrow 0 \text{ as } t \rightarrow \infty \quad (2.28)$$

where  $\hat{a} = c(R_E - 1)/R_E$ . Hence, the system is nonlinearly stable as long as  $R_E \geq 1$ .

$R_E = 1$  corresponds to the sharpest threshold for nonlinear stability that is made possible by (2.28), and hence is the most important case to analyze. Setting  $R_E = 1$  in (2.26) produces an optimization problem,  $\max_{\mathcal{H}}(\mathcal{I}/\mathcal{D}) = 1$ , that can be solved by the Euler-Lagrange equations:

$$z \in (0, 1) : \begin{cases} 2 \nabla^2 \mathbf{v}_f - (\text{Ra}_{f,\lambda} + \lambda) \theta_f \mathbf{k} = \frac{\partial L_f}{\partial \mathbf{x}}, \\ 2\lambda \nabla^2 \theta_f - (\text{Ra}_{f,\lambda} + \lambda) w_f = 0, \end{cases} \quad (2.29)$$

$$z \in (-1, 0) : \begin{cases} 2 \frac{\hat{d}^3}{\text{Da}} \mathbf{v}_m + \left( \frac{\hat{d}^3}{\text{Da}} \text{Ra}_{m,\lambda} + \lambda \frac{\epsilon_T^3}{\hat{d}} \right) \theta_m \mathbf{k} = \frac{\partial L_m}{\partial \mathbf{x}}, \\ 2\lambda \frac{\epsilon_T^3}{\hat{d}} \nabla^2 \theta_m - \left( \frac{\hat{d}^3}{\text{Da}} \text{Ra}_{m,\lambda} + \lambda \frac{\epsilon_T^3}{\hat{d}} \right) w_m = 0, \end{cases} \quad (2.30)$$

where  $L_f, L_m$  are Lagrange multipliers for the fluid region and porous medium, respectively. Taking the double curl of the first equations of (2.29) and (2.30) to remove the Lagrange multipliers and using the normal mode representations once again, we obtain the systems for the fluid layer and porous medium, respectively:

$$z \in (0, 1) : \begin{cases} 2 (D_f^2 - a_f^2)^2 w_f + a_f^2 (\text{Ra}_{f,\lambda} + \lambda) \theta_f = 0, \\ 2\lambda (D_f^2 - a_f^2) \theta_f - (\text{Ra}_{f,\lambda} + \lambda) w_f = 0, \end{cases} \quad (2.31)$$

$$z \in (-1, 0) : \begin{cases} 2 \frac{\hat{d}^3}{\text{Da}} (D_m^2 - a_m^2) w_m - a_m^2 \left( \frac{\hat{d}^3}{\text{Da}} \text{Ra}_{m,\lambda} + \lambda \frac{\epsilon_T^3}{\hat{d}} \right) \theta_m = 0, \\ 2\lambda \frac{\epsilon_T^3}{\hat{d}} (D_m^2 - a_m^2) \theta_m - \left( \frac{\hat{d}^3}{\text{Da}} \text{Ra}_{m,\lambda} + \lambda \frac{\epsilon_T^3}{\hat{d}} \right) w_m = 0. \end{cases} \quad (2.32)$$

For the interface and boundary conditions, we use the same equations as the linear case (2.18)–(2.20) with the exception of the Lions condition (replacing its linear counterpart) given by

$$-\mathbf{n} \cdot \mathbb{T}(\mathbf{v}_f, \pi_f) \mathbf{n} + \frac{1}{2} |\mathbf{v}_f|^2 = \hat{d}^2 \pi_m.$$

Equations (2.31)–(2.32) with the interface/boundary conditions as noted above constitute a generalized eigenvalue problem for  $\text{Ra}_{m,\lambda}$  (recall that  $\text{Ra}_{m,\lambda}$  and  $\text{Ra}_{f,\lambda}$  are related through (2.15)). For given wavenumber  $a_m$ , we solve for  $\text{Ra}_{m,\lambda}$  numerically, once again using the Chebyshev tau-QZ method. We then maximize over  $\lambda$  to obtain the sharpest threshold for nonlinear stability,

$$\text{Ra}_m = \max_{\lambda} \text{Ra}_{m,\lambda}.$$

Once  $\text{Ra}_m$  is found for a range of wavenumbers, we can construct the marginal stability curve  $(a_m, \text{Ra}_m)$ , below which we are guaranteed *nonlinear stability*.

## 2.5 Results and discussion

In this section, we first present the marginal stability curves produced by the linear and nonlinear analysis. Next, we show that the relative difference between linear and nonlinear curves scales like  $\text{Da}^1$  for small Darcy numbers, while the absolute difference scales like  $\text{Da}^2$ . We find similar scalings for the differences between marginal stability curves produced by the BJSJ versus the BJJ or BJ interface conditions. Lastly, we comment on resulting streamline patterns for convection cells occupying the entire domain or remaining solely in the fluid region, and remark on the effect of certain parameters on stability.

### 2.5.1 Marginal stability results

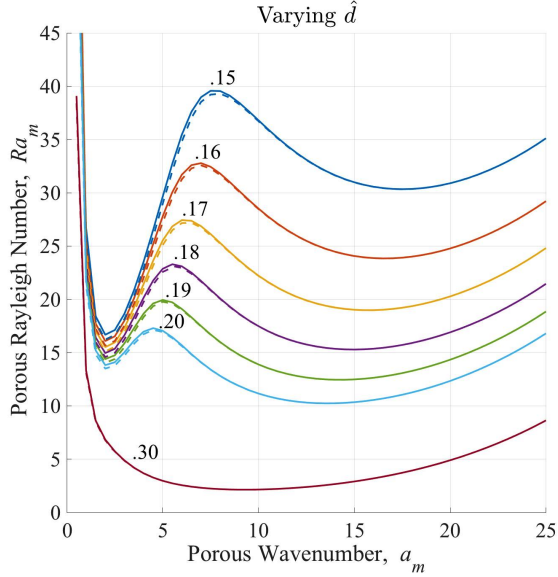
The marginal stability curves in Figure 2.3 show the  $\text{Ra}_m$  values which mark the transition from stability to instability for each wavenumber  $a_m$ . Below the linear marginal stability curves, we are guaranteed *linear* stability, while we are assured unconditional stability below the nonlinear marginal stability curves. In the area between the two curves, nonlinear effects could potentially

destabilize the system even though the background state is linearly stable, i.e. a subcritical instability. However, Figure 2.3 shows that the linear and nonlinear curves follow each other closely, suggesting that the impact of these nonlinear terms is small, at least during the onset of convection. We have explored an extensive range of parameters (not shown here) with similar findings. We therefore conclude that the linear theory accurately describes the onset of convection, and that the region of potential subcritical instabilities is very small. Furthermore, this result implies that the linear stability thresholds, which are generally simpler to compute, actually approximate unconditional or global stability of the system to a high level of accuracy. We remark that the selected energy function  $E(t)$  may not necessarily be the optimal choice. It is conceivable that an improved choice of  $E(t)$  may reduce the gap between the linear and nonlinear curves even further.

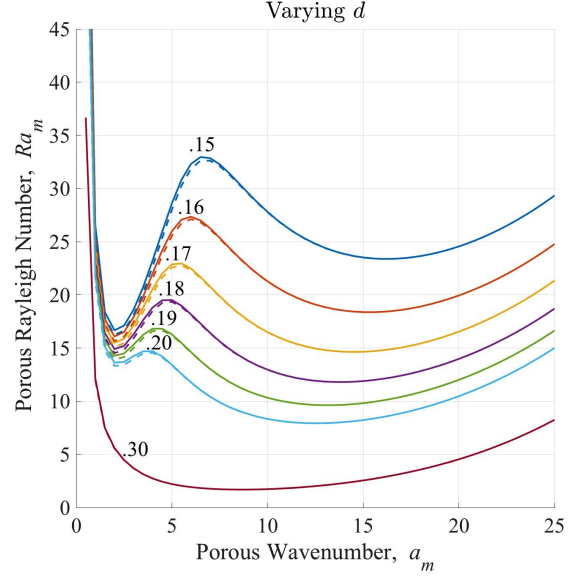
In comparing the linear stability system (2.16)–(2.20) and the nonlinear stability system (2.31)–(2.32), we note the nonlinear stability system loses explicit dependence on the Prandtl number. This loss of Pr-dependence has been observed in a variety of other convective problems [68]. While the linear system does contain Pr terms, they are all associated with the  $\sigma$  eigenvalue terms. In the single layer case, the principle of exchange of stabilities implies that  $\sigma$  is real as long as the Rayleigh number is positive, meaning again that there is no dependence on Pr. In the coupled case, however, exchange of stabilities has not been established rigorously. Our numerics indicate that  $\sigma$  can indeed take complex values. However, we always observe  $\sigma$  to be real whenever the Rayleigh number is positive. This numerical observation suggests that the principle of exchange of stabilities holds in practice, and consequently dependence on Pr is lost. These principles are exhibited in Figure 2.2.

### 2.5.2 Influence of interface conditions

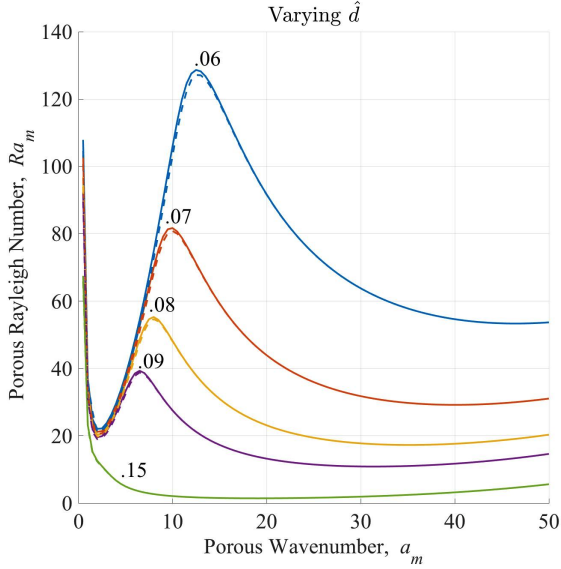
To quantify how closely the linear and nonlinear marginal stability thresholds agree, we examine the relative difference between the respective stability curves. The Lions condition is used to produce the nonlinear thresholds while its linear counterpart is used as the normal interface condition for the linear stability curves. The results are shown in Figure 2.4a. For a fixed  $\hat{d}$  and  $a_m$ , the  $\text{Ra}_m$  values are computed with the linear and nonlinear arguments for various Da values. We then examine the relative difference between the two computed  $\text{Ra}_m$  values. For small Darcy numbers,  $\text{Da} \in [10^{-8}, 10^{-4}]$ , we see the relative difference scales like  $\text{Da}^1$ , as shown with the comparison line. Given that  $\text{Ra}_m \sim \mathcal{O}(\text{Da})$  in the small Darcy limit, the absolute difference scales



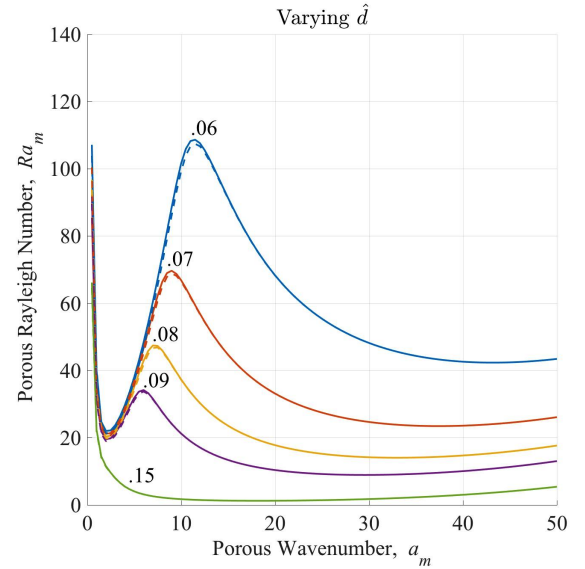
(a)  $\sqrt{\text{Da}} = 5.0 \times 10^{-3}$ ,  $\alpha = 1.0$ .



(b)  $\sqrt{\text{Da}} = 5.0 \times 10^{-3}$ ,  $\alpha = 0.1$ .



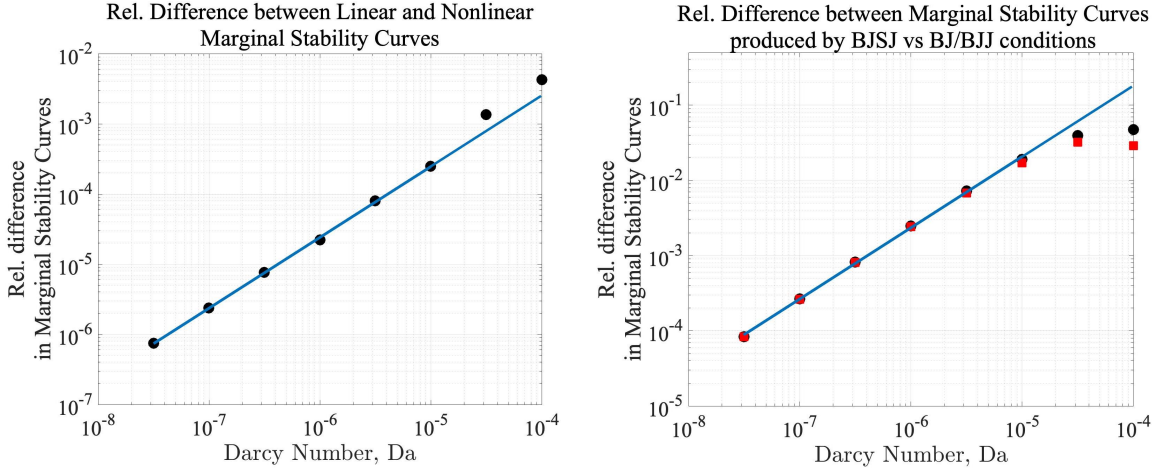
(c)  $\sqrt{\text{Da}} = 1.0 \times 10^{-3}$ ,  $\alpha = 1.0$ .



(d)  $\sqrt{\text{Da}} = 1.0 \times 10^{-3}$ ,  $\alpha = 0.1$ .

Figure 2.3: Marginal stability curves for different values of  $\text{Da}$  and  $\alpha$ , with  $\epsilon_T = .7$  in all cases. Both linear (solid) and nonlinear (dashed) stability results are shown. The two results agree closely with one another in all cases, indicating that the region of potential subcritical instability is very small.

like  $Da^2$ , as is expected from the theory and reflected in the numerical tests. In the appendix, we present an asymptotic argument showing that, while the dynamic pressure term is  $\mathcal{O}(Da)$ , it only begins to affect the solutions at  $\mathcal{O}(Da^2)$ . Though somewhat heuristic, this asymptotic analysis provides guidance for the scaling of stability threshold differences found using the Lions and the linear interface conditions in the small Darcy number regime.



(a) The relative difference between nonlinear and linear marginal stability curves produced with the Lions interface condition and its linear counterpart, respectively (with BJSJ used).

(b) The relative differences between linear marginal stability curves produced with the: BJSJ and Jones interface conditions (black circles), and the BJSJ and Beavers-Joseph conditions (red squares).

Figure 2.4: Relative differences between marginal stability curves for various cases. Parameters:  $\hat{d} = .1$ ,  $a_m = 25.0$ ,  $\epsilon_T = .7$ ,  $\alpha = 1.0$ . Both comparison lines have slope of 1.

Now, we briefly discuss small differences in the tangential interface conditions. In particular, we show in Figure 2.4b, the relative differences in the linear stability curves produced by the BJ, BJJ, and BJSJ interface conditions. The relative differences between BJSJ and BJJ are marked with black circles while BJSJ versus BJ are marked with red squares. Both of the relative differences scale like  $Da^1$  and both absolute differences scale like  $Da^2$ . Thus, using any of the three conditions results in similar qualitative behavior in the marginal stability curves.

An important parameter that enters these tangential interface conditions is the frictional coefficient  $\alpha$ . Looking back at Fig. 2, we vary  $\alpha$  from 1.0 to 0.1 in going from the left columns, (a) and (c), to the right, (b) and (d). We note that although the marginal stability curves are altered, the location of their minima does not change significantly. This minimum value of  $Ra_m$  is known as

the critical Raleigh number

$$\text{Ra}_{m,c} = \min_{a_m^2} \text{Ra}_m, \quad (2.33)$$

which is the smallest Rayleigh number for which an unstable mode exists. Thus, the critical Raleigh number exhibits low sensitivity to  $\alpha$ , as is consistent with previous studies [29].

### 2.5.3 Fluid-dominated versus full convection

An important insight that can be obtained from the marginal stability curves is whether the convection extends throughout the domain or is confined to the fluid region. For this, we examine the wavenumber associated with  $\text{Ra}_{m,c}$ , which offers information on the lengthscale and aspect ratio of this most unstable mode; i.e. smaller wavenumbers correspond to larger convection cells that extend throughout the domain while large wavenumbers correspond to smaller convection cells which arise only in the free-zone. For example, in Figure 2.3a, for  $\hat{d} = [.15, .18]$ , we find the minima of the marginal stability curves all occur around  $a_m = 2.0$ . At  $\hat{d} = .19$  though, the minimum shifts to a higher wavenumber,  $a_m = 14.0$ . At some depth ratio between  $\hat{d} = .18$  and  $\hat{d} = .19$ , the convection cells' aspect ratio suddenly changes from wide cells ( $a_m = 2.0$ ) to thin cells ( $a_m = 14.0$ ). This phenomenon is also observed in [83]. When the convection cells occupy both the porous medium and fluid region, we denote this as *full* convection while we use *fluid-dominated* convection to describe when convection cells lie only in the fluid region. Qualitatively, when the  $\text{Ra}_{m,c}$  occurs at smaller wavenumber, we have full convection, and when  $\text{Ra}_{m,c}$  occurs at larger wavenumber, we have fluid-dominated convection.

To understand which region dominates convection in a more quantitative sense, we examine the resulting streamline and temperature profiles, as well as the Nusselt numbers. Figure 2.5 shows the streamlines in black and the temperature profiles in color for  $\hat{d} = .18$  and  $\hat{d} = .19$  at their critical Rayleigh numbers with:  $\chi = .3$ ,  $\sqrt{\text{Da}} = 5.0 \times 10^{-3}$ ,  $\alpha = 1.0$ ,  $\epsilon_T = .7$ . The streamlines are computed via numerical solution of the linear system (2.16)–(2.20). Both figures are plotted over the same  $x$  range to more effectively show how the small change in the  $\hat{d}$  value (from  $\hat{d} = .18$  to  $.19$ ) drastically alters the convection cells, streamlines, and temperature profiles. For full convection, we see that the temperature and velocity deviations from the steady-state occur throughout the entirety of the domain. For the fluid-dominated convection though, temperature and velocity fluctuations only

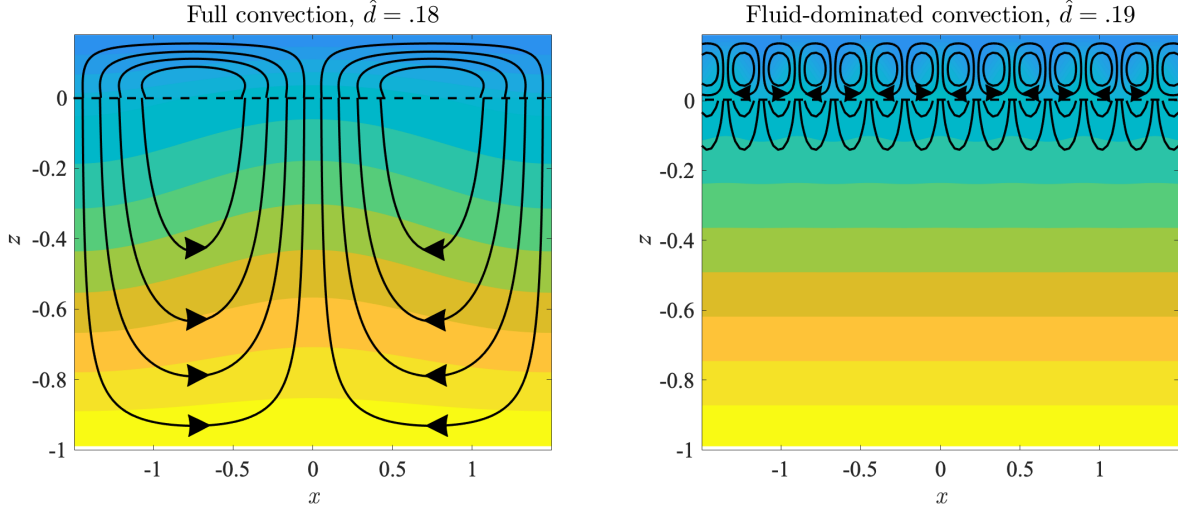


Figure 2.5: Marginally stable flow configurations and temperature profiles (color) for two values of  $\hat{d}$ . (a)  $\hat{d} = .18$  produces convection cells that extend throughout the entire domain, while (b)  $\hat{d} = .19$  produces cells that are confined to the free-flow region. In both cases,  $\sqrt{\text{Da}} = 5.0 \times 10^{-3}$ ,  $\epsilon_T = .7$ ,  $\alpha = 1.0$ , and the BJSJ condition is used ( $\Psi_J = 1, \Psi_S = 0$ ).

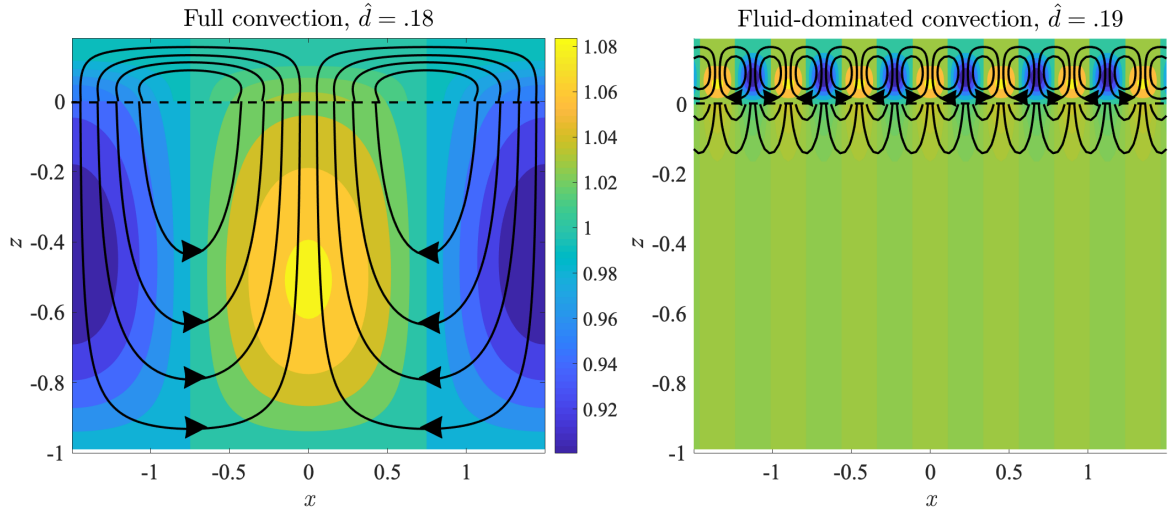


Figure 2.6: Color map of the Nusselt number with streamlines in black for the same two cases shown in Fig. 2.5. In the first case (a), the greatest variations of  $\text{Nu}$  occur in the porous medium, while in the second case (b) the extrema of  $\text{Nu}$  are confined to the free-flow region.

occur in and immediately around the free zone. To further quantify these observations, we analyze

the Nusselt number  $\text{Nu}$ , calculated from the vertical convective and conductive fluxes as

$$\text{Nu} = \frac{J_{\text{cnv}} + J_{\text{cnd}}}{J_{\text{cnd}}} \quad \text{with} \quad J_{\text{cnv}} = w_j T_j \quad \text{and} \quad J_{\text{cnd}} = -\kappa_j \frac{\partial T_j}{\partial z_j}, \quad (2.34)$$

for  $j \in \{f, m\}$ . In Figure 2.6, we show the Nusselt numbers for the same cases  $\hat{d} = .18$  and  $\hat{d} = .19$  with the same streamlines pictured in Figure 2.5. In regions where  $\text{Nu} = 1$ , there is negligible vertical fluid flow and the heat transfer is purely conductive. Wherever  $\text{Nu} > 1$ , the convective flux is upward and it enhances the conductive flux. On the other hand, when  $\text{Nu} < 1$  convective flux is downward which opposes the conductive flux. At the middle of the convection cells and at the top and bottom of the domain, fluid motion is almost purely horizontal and so the Nusselt number is nearly 1. At the edges of the convection cells, we see  $\text{Nu}$  attains its maximum and minimum as the flow is almost solely in the vertical direction, moving upward and downward for the maximum and minimum of  $\text{Nu}$ , respectively. When the Nusselt number achieves its extrema in the fluid region, the convection is fluid-dominated while we have full convection when the Nusselt number varies throughout the whole domain.

With the analysis above, determining which region dominates convection is relatively straightforward. However, determining parameter values where the convection shifts from full to fluid-dominated is more complicated. The region that dominates convection depends on a number of parameters, namely the depth ratio  $\hat{d}$ , the Darcy number  $\text{Da}$ , and the ratio of thermal diffusivities  $\epsilon_T$ . For example, fixing  $\text{Da}$  and  $\epsilon_T$ , one could compute the marginal stability curves for a number of  $\hat{d}$  values to find the depth ratio where the transition in convection occurs. However, this can be a computationally demanding task, since, even producing a single marginal stability curve requires a search over the parameters  $a_m$  and  $\text{Ra}_m$ . We therefore offer a simplified theory to determine whether the onset of convection is full or fluid-dominated. Although the Darcy number  $\text{Da}$  and the ratio of thermal diffusivities  $\epsilon_T$  could also trigger the transition, we focus on the influence of  $\hat{d}$  in this paper.

For the purpose of developing a simplified theory, let us briefly consider the free-flow and porous domains as *uncoupled*. As before, the Rayleigh number in each domain is denoted  $\text{Ra}_m$  and  $\text{Ra}_f$ , with the same relationship as in (2.13):

$$\text{Ra}_m = \text{Ra}_f \frac{\text{Da} \epsilon_T^2}{\hat{d}^4} \quad (2.35)$$

Let  $\text{Ra}_m^*$  and  $\text{Ra}_f^*$  denote the corresponding critical values in the *uncoupled* system. Both of these values are well known,  $\text{Ra}_f^* = 1707$  and  $\text{Ra}_m^* = 4\pi^2$ . Heuristically, the strength of convection in each domain should be proportional to the Rayleigh number scaled by the appropriate critical value. Thus, the transition from full to fluid-dominated convection is expected to occur approximately where the ratios are equal,

$$\frac{\text{Ra}_m}{\text{Ra}_m^*} = \frac{\text{Ra}_f}{\text{Ra}_f^*}.$$

Substituting relationship (2.35) and solving for  $\hat{d}$  gives the predicted transition value

$$\hat{d}^* = \left[ \frac{\text{Ra}_f^*}{\text{Ra}_m^*} \text{Da} \epsilon_T^2 \right]^{1/4}. \quad (2.36)$$

Therefore, by neglecting any coupling between the two regions, we have obtained a simple, approximate formula for the depth ratio at which convection is predicted to transition from full to fluid dominated.

We test this theory with the parameters  $\sqrt{\text{Da}} = 5.0 \times 10^{-3}$  and  $\epsilon_T = 0.7$ . Numerically, the transition occurs around  $\hat{d}^* \approx .181$ , as shown in Figure 2.3a. The value predicted by the simplified theory is

$$\left( \frac{1707}{4\pi^2} (5.0 \times 10^{-3})^2 (.7)^2 \right)^{1/4} \approx .151.$$

which agrees with the numerically computed value to within 16% error. Secondly, we test  $\sqrt{\text{Da}} = 1.0 \times 10^{-3}$  and  $\epsilon_T = 0.7$ , with the result shown in Figure 2.3c. The simple theory predicts the transition to occur at  $\hat{d}^* \approx .067$ , while numerics show the transition to occur around  $\hat{d}^* \approx .079$ , corresponding to an error of 15%.

Table 2.2: Relative error between predicted and actual  $\hat{d}^*$  values for *original* simple theory. Fixed parameters:  $\chi = .3$ ,  $\alpha = 1.0$ .

$\sqrt{\text{Da}}$	$\epsilon_T$	Predicted $\hat{d}^*$	Actual $\hat{d}^*$	Relative error	Figure reference
$5.0 \times 10^{-3}$	0.7	.151	.181	16.5%	2.3a
$1.0 \times 10^{-3}$	0.7	.067	.079	15.1 %	2.3c
$5.0 \times 10^{-3}$	0.5	.128	.155	17.4 %	2.7a
$5.0 \times 10^{-3}$	1.5	.222	.256	13.3 %	2.7b

Table 2.2 compares the predicted and actual values of  $\hat{d}$  for the cases discussed above as well as a few additional cases. For various Da and  $\epsilon_T$  values, we see our theory, numerics, and intuition are all

in agreement. For example, with the last two rows of the table, as the ratio of thermal diffusivities  $\epsilon_T = \lambda_f/\lambda_m$  decreases, convection occurs more easily through the entire domain. Consequently, the transition from full to fluid-dominated convection takes place at a lower depth ratio. Figure 2.7 illustrates this trend with marginal stability curves for  $\epsilon_T$  values of 0.5 and 1.5.

In summary, we find the transition depth  $\hat{d}^*$  heuristically predicted by (2.36) agrees with the true transition value to within about 15% in all cases tested. Thus, while the theory is not extremely accurate, it is a useful first estimate to narrow the parameter range that must be searched to find the transition depth. The theory is perhaps even more accurate than could be expected given that it completely neglects coupling between the two regions. It is a promising first step towards developing a more refined theory to predict the transition, perhaps by accounting for weak coupling between the two regions. We also remark that the simplified theory seems to consistently underpredict the transition depth. Thus, the effect of coupling is to inhibit fluid-dominated convection in favor of full convection.

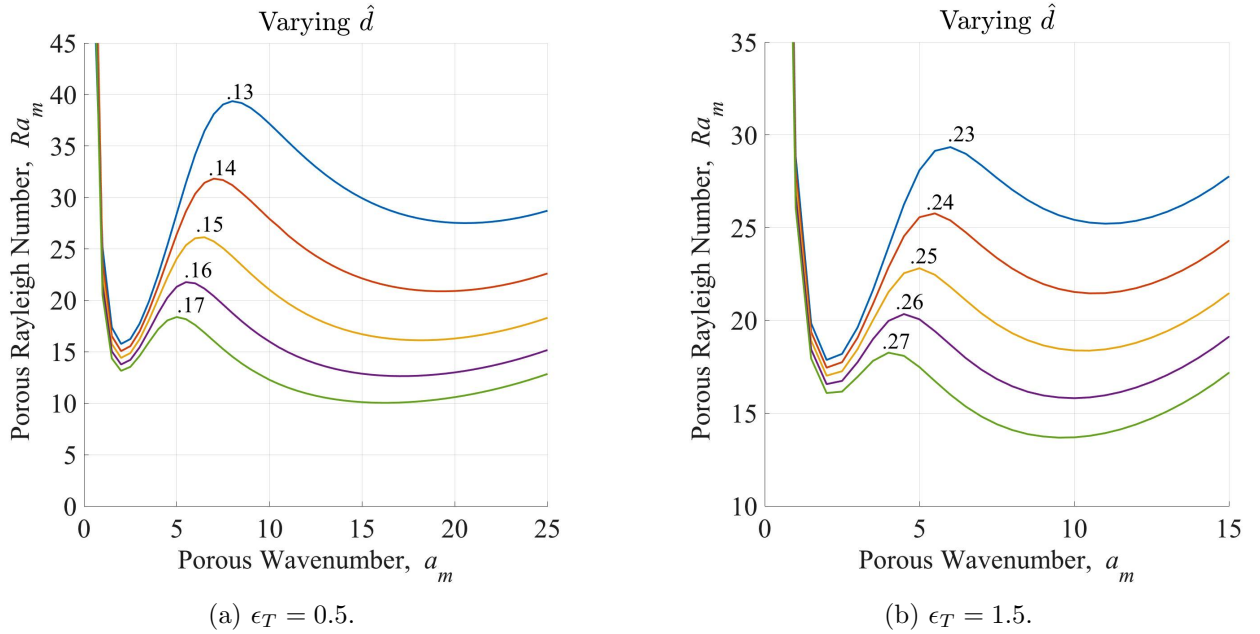


Figure 2.7: Marginal stability curves for varying  $\epsilon_T$ , with  $\sqrt{\text{Da}} = 5.0 \times 10^{-3}$  and  $\alpha = 1.0$  fixed. Linear stability results with the BJSJ interface condition used ( $\Psi_J = 1, \Psi_S = 0$ ).

## 2.6 Conclusions

In this chapter, we presented linear and nonlinear stability results of the coupled Navier-Stokes-Darcy-Boussinesq system that governs convection in a fluid-porous medium system. The main contribution is the newly obtained nonlinear analysis, which relies crucially on the Lions interface condition in order to establish an energy law. We found that the marginal stability curves produced by the nonlinear and linear analysis follow each other closely, suggesting that linear stability is sufficient to describe the onset of convection. The agreement between the linear and nonlinear curves also implies that the more easily obtained linear thresholds indicate unconditional or global stability of the coupled fluid-porous system, at least for relatively small Darcy number. Some additional results concerning convection are related to choosing interface conditions, namely those specifying tangential stress. We showed the three different choices (BJ, BJJ, and BJSJ) are essentially the same, at least in terms of the onset of convection at small Darcy number regime; hence, it makes sense to adopt BJSJ due to the associated mathematical convenience.

We also postulated a simple theory to predict the transition from full to fluid-dominated convection due to changes in the depth ratio, the Darcy number, and the ratio of thermal diffusivities. We find estimated transition depths to agree with the numerically computed values with reasonable accuracy (roughly 15% error). Accurate prediction of this transition could have applications in geophysics and in alloy solidification [58, 59], and further refinement of the theory is an exciting future direction. In addition, while this work considered a flat, stationary interface between the free-zone and porous medium, future work could consider more complex interfaces [2, 50], or boundaries that move or evolve due to natural processes [65, 75, 100].

# CHAPTER 3

## NUMERICS

In the previous chapter, we conducted stability analyses for convection in the coupled fluid-porous media system. In this chapter though, we explore the simpler *single layer* cases— convection in a single layer of fluid, and in a layer of a porous medium saturated with a fluid. With numerical methods in place for convection in the single layers of fluid and porous medium, we are then able to simulate convection for the *coupled* case by combining the two single layer solvers.

With the both of single layer cases, we conduct stability analyses, followed by detailing our numerical methods to simulate these systems. While a generous amount of the chapter is dedicated to the analyses for both the single layer cases, the results from the analyses are extremely important in validating the numerical results. Finally, we return to the coupled case as we implement a numerical method to simulate convection in the Navier-Stokes-Darcy-Boussinesq system.

### 3.1 Single layer of fluid

In this section, we outline the case of convection in a single layer of fluid, conduct a linear stability analysis, detail the numerical method used to simulate the system, and finally, conclude with results.

Much of the analysis in this section concerning a single layer of fluid being heated from below is not new. The linear stability analysis for this phenomenon was by performed by Lord Rayleigh in 1916 [76]. Many researchers followed suite and established rigorous analytical results; for a non-exhaustive list of works containing the linear stability analysis, several of which present the principle of exchange of stabilities, see [24, 37, 73, 77, 87]. These analyses are presented so that we are able to validate our numerical methods and results.

#### 3.1.1 Equations, and linear stability analysis

For the equations governing convection in a single layer of fluid, we have the momentum equation with the addition of the Boussinesq approximation, which takes the form of the Navier-Stokes-

Boussinesq equation. Two other equations needed are the continuity equation, aided by the incompressibility of the fluid, and an advection-diffusion equation (ADE) to describe the evolution of heat in the domain:

$$\left\{ \begin{array}{l} \rho_0 \left( \frac{\partial \mathbf{u}_f}{\partial t_f} + (\mathbf{u}_f \cdot \nabla) \mathbf{u}_f \right) = \nabla \cdot \mathbb{T}(\mathbf{u}_f, p_f) - g\rho_0 [1 - \beta(T_f - T_L)] \mathbf{k}, \\ \nabla \cdot \mathbf{u}_f = 0, \\ \frac{\partial T_f}{\partial t_f} + \mathbf{u}_f \cdot \nabla T_f = \frac{\kappa_f}{(\rho_0 c_p)_f} \nabla^2 T_f, \end{array} \right.$$

with same variables from Chapter 2 of this thesis.

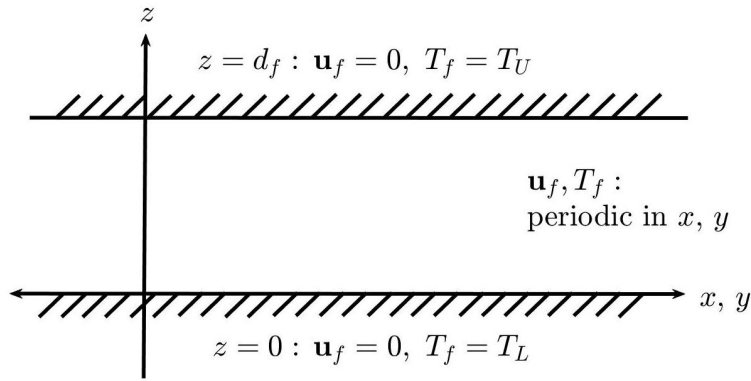


Figure 3.1: Schematic of the domain  $\Omega = \{(x, y) \in \mathbb{R}^2 \times z \in (0, d_f)\}$ . The upper and lower boundaries are impermeable and held at constant temperatures  $T_U$  and  $T_L$ , respectively, with  $T_L > T_U$ .

For the domain, shown in Figure 3.1, we assume flat, horizontal, nonpenetrable plates at the top and bottom,  $\Omega_f = \{(x, y) \in \mathbb{R}^2 \times z \in (0, d_f)\}$ . If the bottom plate is at a higher temperature than the top plate, buoyancy can potentially destabilize the system, resulting in convection; we consider this case. To begin the linear stability analysis, we start by finding the steady-states. These correspond to the conductive states, denoted by an over-bar: no-flow for the fluid, a linear temperature profile, and the pressure gradient needed to satisfy the remainder of the momentum equation:

$$\begin{aligned} \bar{\mathbf{u}}_f &= 0, \\ \bar{T}_f &= T_L + z \frac{T_U - T_L}{d_f}, \\ \nabla \bar{p}_f &= -g\rho_0 (1 - \beta(\bar{T}_f - T_L)) \mathbf{k}. \end{aligned}$$

Next, we perturb the steady-states with  $\mathbf{u}_f = \bar{\mathbf{u}}_f + \mathbf{v}_f$ ,  $T_f = \bar{T}_f + \theta_f$ ,  $p_f = \bar{p}_f + \pi_f$ , and set up a system in terms of the perturbation variables. This yields

$$\left\{ \begin{array}{l} \rho_0 \left( \frac{\partial \mathbf{v}_f}{\partial t_f} + (\mathbf{v}_f \cdot \nabla) \mathbf{v}_f \right) = \nabla \cdot \mathbb{T}(\mathbf{v}_f, \pi_f) + \rho_0 g \beta \theta_f \mathbf{k}, \\ \nabla \cdot \mathbf{v}_f = 0, \\ \frac{\partial \theta_f}{\partial t_f} + \mathbf{v}_f \cdot \nabla \theta_f = \lambda_f \nabla^2 \theta_f - w_f \left( \frac{T_U - T_L}{d_f} \right). \end{array} \right.$$

Our goal is to determine what happens to these perturbations as time evolves. Given a small enough heat difference between the top and the bottom plates, the perturbations damp out and the original system would return to the conductive state. With this case, we say the system is linearly stable to small perturbations. However, if the heat difference is greater than some threshold, the system is linearly unstable and we have non-trivial perturbations to the steady-state. This case is referred to as the convective state.

To nondimensionalize the system, we use the same scalings from Chapter 2 (and [62]):

$$\mathbf{v}_f = \tilde{\mathbf{v}}_f \frac{\nu}{d_f}, \quad \mathbf{x}_f = \tilde{\mathbf{x}}_f d_f, \quad t_f = \tilde{t}_f \frac{d_f^2}{\lambda_f}, \quad \theta_f = \tilde{\theta}_f \frac{(T_L - T_U) \nu}{\lambda_f}, \quad \pi_f = \tilde{\pi}_f \frac{\rho_0 \nu^2}{d_f^2}.$$

We additionally suppose that the perturbations are small, that  $\mathbf{v}_f, \theta_f, \pi_f \sim \mathcal{O}(\varepsilon)$  for some small  $\varepsilon$ . With this assumption, we collect all  $\mathcal{O}(\varepsilon)$  terms and drop all higher-order terms— that is,  $\mathcal{O}(\varepsilon^2)$  or higher terms. This allows us to drop the nonlinear terms of the momentum equation and the advection-diffusion equation. Dropping the tildes yields the nondimensional system for the perturbation variables, now in  $\Omega_f = \{(x, y) \in \mathbb{R}^2 \times z \in (0, 1)\}$ :

$$\left\{ \begin{array}{l} \frac{1}{\text{Pr}_f} \frac{\partial \mathbf{v}_f}{\partial t_f} = 2 \nabla \cdot \mathbb{D}(\mathbf{v}_f) - \nabla \pi_f + \text{Ra}_f \theta_f \mathbf{k}, \\ \nabla \cdot \mathbf{v}_f = 0, \\ \frac{\partial \theta_f}{\partial t_f} = \nabla^2 \theta_f + w_f, \end{array} \right.$$

with  $\text{Pr}_f = \frac{\nu}{\lambda_f}$ ,  $\text{Ra}_f = \frac{g \beta (T_L - T_U) d_f^3}{\nu \lambda_f}$ , and  $w_f$  as the  $z$ -component of the velocity.

We will now start to determine the temperature threshold needed for the transition from the linearly stable to unstable cases. With this in mind, we take the double curl of the momentum equation and use the identity

$$\nabla \times (\nabla \times \mathbf{A}) = \nabla (\nabla \cdot \mathbf{A}) - \nabla^2 \mathbf{A}$$

to obtain:

$$-\frac{1}{\text{Pr}_f} \nabla^2 \frac{\partial \mathbf{v}_f}{\partial t_f} = -\nabla^4 \mathbf{v}_f + \text{Ra}_f \left( \nabla \frac{\partial \theta_f}{\partial z} - \nabla^2 \theta_f \mathbf{k} \right).$$

Then, we look at the  $z$ -component of the equation above coupled with the advection-diffusion equation for  $z \in (0, 1)$ :

$$\begin{cases} \left( \frac{1}{\text{Pr}_f} \frac{\partial}{\partial t_f} - \nabla^2 \right) \nabla^2 w_f = \text{Ra}_f \nabla_H^2 \theta_f, \\ \left( \frac{\partial}{\partial t_f} - \nabla^2 \right) \theta_f = w_f, \end{cases}$$

where  $\nabla_H^2 = \frac{\partial^2}{\partial x^2} + \frac{\partial^2}{\partial y^2}$  is the horizontal Laplacian operator.

At the upper and lower boundaries of the domain, we consider several options for conditions on velocity and temperature. For conditions on the velocity at the top and bottom plates, we require that the boundary is nonpenetrable. That is, the normal component of velocity is 0, or  $w_f = 0$ . For the second condition, we have two options of imposing a no-slip condition or a free-slip condition, corresponding to a rigid surface and a free surface, respectively. The no-slip condition gives  $\frac{\partial w_f}{\partial z} = 0$ , and the free-slip condition gives  $\frac{\partial^2 w_f}{\partial z^2} = 0$ . Both conditions come from manipulating the continuity equation.

For boundary conditions on  $\theta_f$ , we also have two options. We can impose a constant temperature or a constant heat flux, corresponding to a conductive boundary and an insulating boundary, respectively. The constant temperature gives  $\theta_f = 0$ , and the constant heat flux gives  $\frac{\partial \theta_f}{\partial z} = 0$  at the boundary. We will investigate different combinations of the boundary conditions for the velocity and temperature perturbations.

Similar to the analysis in Chapter 2, we now consider the normal modes of  $w_f$  and  $\theta_f$ :

$$w_f(\mathbf{x}, t) = F(x, y) w_f(z) e^{\sigma t}, \quad \theta_f(\mathbf{x}, t) = F(x, y) \theta_f(z) e^{\sigma t}.$$

Here,  $F(x, y)$  corresponds to a unimodal component of the horizontal planform in each region with corresponding horizontal wavenumber  $a$ . That is,

$$a^2 F(x, y) + \nabla_H^2 F(x, y) = 0.$$

The choice of how to define  $F$  dictates the shape of the convection cell. In two dimensions, some variation of sines and/or cosines is traditionally used. For the hexagonal cells observed in three

dimensions, the horizontal wavenumber is defined with the two horizontal components  $a^2 = a_x^2 + a_y^2$ , and more complicated planforms are used. One example noted in [37, 87] is

$$F(x, y) = \cos\left(\frac{a(x\sqrt{3} + y)}{2}\right) + \cos\left(\frac{a(x\sqrt{3} - y)}{2}\right) + \cos(ay).$$

While this modal decomposition defines the structure of the convection cells,  $\sigma$  dictates growth or decay of the perturbations in time. For a given Rayleigh number, or heat difference, if  $\text{Re}(\sigma) < 0$ , the perturbations damp out and the system is stable and if  $\text{Re}(\sigma) > 0$ , the perturbations grow and the system is unstable. With  $D = \frac{\partial}{\partial z}$  for convenience, the coupled system can be written as

$$\begin{cases} \left(\frac{\sigma}{\text{Pr}_f} - (D^2 - a^2)\right) (D^2 - a^2) w_f = -a^2 \text{Ra}_f \theta_f, \\ (\sigma - (D^2 - a^2)) \theta_f = w_f. \end{cases} \quad (3.1)$$

### 3.1.2 Principle of exchange of stabilities

The principle of exchange of stabilities detailed here allows us to set  $\sigma = 0$  in (3.1) to find the Rayleigh number needed for a given wavenumber of the perturbation to become unstable. To show this, we will multiply the equations of (3.1) by the complex conjugates of  $w_f$  and  $\theta_f$ , respectively, and integrate over  $z$  from 0 to 1. Manipulating these equations will allow us to draw conclusions about  $\sigma$  and effectively reduce the system we need to solve to determine marginal stability curves.

With the complex conjugate denoted by a superscript  $*$ , we multiply the first equation of (3.1) by  $w_f^*$  and integrate:

$$\int_0^1 w_f^* \left[ \left(\frac{\sigma}{\text{Pr}_f} - (D^2 - a^2)\right) (D^2 - a^2) \right] w_f dz = -a^2 \text{Ra}_f \int_0^1 w_f^* \theta_f dz.$$

We can now integrate by parts to obtain

$$\begin{aligned} \frac{\sigma}{\text{Pr}_f} \underbrace{\int_0^1 [|Dw_f|^2 + a^2|w_f|^2] dz}_{:=I_1 > 0} + \underbrace{\int_0^1 [|D^2w_f|^2 + 2a^2|Dw_f|^2 + a^4|w_f|^2] dz}_{:=I_2 > 0} &= a^2 \text{Ra}_f \int_0^1 w_f^* \theta_f dz, \\ \Rightarrow \frac{\sigma}{\text{Pr}_f} I_1 + I_2 &= a^2 \text{Ra}_f \int_0^1 w_f^* \theta_f dz. \end{aligned} \quad (3.2)$$

(3.2) holds regardless of the boundary conditions chosen for  $w_f$ , no-slip or free-slip.

We follow a similar argument for the second equation of (3.1), multiplying by  $\theta_f^*$  and then integrating:

$$\int_0^1 \theta_f^* [\sigma - (D^2 - a^2)] \theta_f dz = \int_0^1 \theta_f^* w_f dz.$$

Integrating by parts allows us to find

$$\begin{aligned} \sigma \underbrace{\int_0^1 |\theta_f|^2 dz}_{:=I_3 > 0} + \underbrace{\int_0^1 [|D\theta_f|^2 + a^2|\theta_f|^2] dz}_{:=I_4 > 0} &= \int_0^1 \theta_f^* w_f dz, \\ \Rightarrow \sigma I_3 + I_4 &= \int_0^1 \theta_f^* w_f dz, \end{aligned} \quad (3.3)$$

which once again holds regardless of our choice of the boundary condition for  $\theta_f$ , constant temperature or constant heat flux.

We now explicitly assume that  $\sigma$  has both real and imaginary parts,  $\sigma = \sigma_{re} + i\sigma_{im}$ . Multiplying (3.3) by  $a^2 \text{Ra}_f$  and subtracting off the complex conjugate of (3.2) removes the right-hand sides of these equations, providing

$$a^2 \text{Ra}_f \sigma I_3 + a^2 \text{Ra}_f I_4 - \frac{\sigma^*}{\text{Pr}_f} I_1 - I_2 = 0.$$

Both the real and the imaginary components of the above equation must equal 0. In looking at the imaginary component, we have

$$\sigma_{im} \left( a^2 \text{Ra}_f I_3 + \frac{1}{\text{Pr}_f} I_1 \right) = 0.$$

If the Rayleigh number is positive (that is, the bottom plate is hotter than the top plate), then the expression in parentheses is strictly positive and  $\sigma_{im} = 0$ . So, for  $\text{Ra}_f > 0$ , the imaginary component of  $\sigma$  must be equal to 0. This allows us to set  $\sigma = 0$  to solve for the Rayleigh number needed to trigger the transition from a stable to an unstable configuration. Additionally, in looking at the real component of the equation above, we have

$$\sigma_{re} \left( a^2 \text{Ra}_f I_4 - \frac{1}{\text{Pr}_f} I_1 \right) + a^2 \text{Ra}_f I_4 - I_2 = 0.$$

This implies that if  $\text{Ra}_f < 0$ , then  $\sigma_{re} < 0$  also. This reinforces the notion that the case where the top plate is hotter than the bottom plate is a stable configuration.

### 3.1.3 Marginal stability curves

With the principle of exchange of stabilities, we set  $\sigma = 0$  to obtain the coupled equations:

$$\begin{cases} (D^2 - a^2)^2 w_f = a^2 \text{Ra}_f \theta_f, \\ (D^2 - a^2) \theta_f = -w_f. \end{cases}$$

This system can be written as a generalized eigenvalue problem for  $z \in (0, 1)$ , solving for  $\text{Ra}_f$  to determine marginal stability (with  $I$  as the identity matrix):

$$\begin{pmatrix} D^4 - 2a^2 D^2 + a^4 I & 0 \\ I & D^2 - a^2 I \end{pmatrix} \begin{pmatrix} w_f \\ \theta_f \end{pmatrix} = \text{Ra}_f \begin{pmatrix} 0 & a^2 I \\ 0 & 0 \end{pmatrix} \begin{pmatrix} w_f \\ \theta_f \end{pmatrix}. \quad (3.4)$$

We solve this eigenvalue problem with the Chebyshev tau-QZ algorithm [36], in the same manner as described in Section 2.3.1. With the reduction of the system, we lose dependence on the Prandtl number, implying that the  $\text{Pr}_f$  term does not influence the *onset* of convection. This term may impact convection after the cells begin to form though.

In solving (3.4), we explore different combinations of boundary conditions. One condition we impose for each case is the assumption of an impermeable wall, expressed with  $w_f = 0$ . However, the other conditions vary, and are summed up (with their abbreviations used later):

- no-slip (NO-SL):  $Dw_f = 0$ ,
- free-slip (FREE):  $D^2w_f = 0$ ,
- conducting (COND):  $\theta_f = 0$ ,
- insulating (INSUL):  $D\theta_f = 0$ .

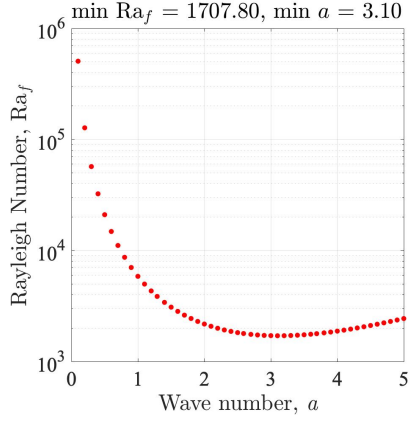
For each value of  $a$ , we solve (3.4) for  $\text{Ra}_f$ , which gives the Rayleigh number needed for that wave-number of the perturbation to become unstable. These points plotted in the  $(a, \text{Ra}_f)$ -plane form marginal stability curves which divide the plane into linearly stable and unstable regions. Figure 3.2 shows the marginal stability curves for several combinations of boundary condition choices. The captions for each plot note the boundary conditions used. The order of the boundary conditions are for:  $w_f$  at  $z = 0$ ,  $w_f$  at  $z = 1$ ,  $\theta_f$  at  $z = 0$ , and  $\theta_f$  at  $z = 1$ .

An important aspect of the marginal stability curves deals with the minimum of these curves—the critical Rayleigh number. The critical Rayleigh number signifies the smallest heat difference

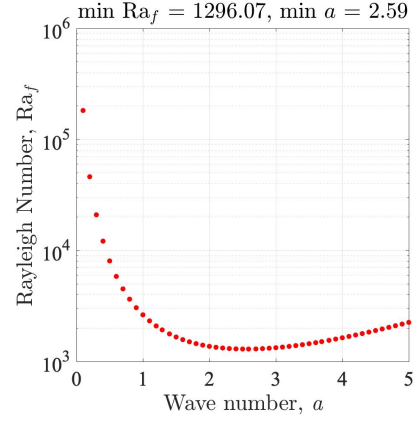
needed for perturbations to grow in time. For  $Ra_f$  less than the critical Rayleigh number, the system will remain stable while  $Ra_f$  values greater than the critical Rayleigh number have the potential to produce instabilities. In Table 3.1, we note the various critical Rayleigh numbers and the wave-number at which they are achieved for different combinations of the boundary conditions. While we investigated different combinations, we will focus on the most practical case for our simulations: no-slip conditions at the top and bottom of the domain with conductive boundaries at the top and bottom.

Table 3.1: Critical Rayleigh numbers for the single fluid layer with different combinations of boundary conditions. The marginal stability curves for 6 of these cases are shown in Figure 3.2.

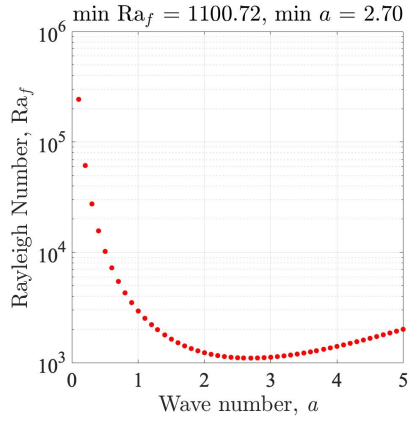
velocity		heat		$Ra_c$	$a_c$
$z = 0$	$z = 1$	$z = 0$	$z = 1$		
NO-SL	NO-SL	COND	COND	1707.8	3.1
NO-SL	NO-SL	COND	INSUL	1296.0	2.6
NO-SL	NO-SL	INSUL	COND	1296.0	2.6
NO-SL	NO-SL	INSUL	INSUL	720.3	0
NO-SL	FREE	COND	COND	1100.7	2.7
NO-SL	FREE	COND	INSUL	669.0	2.1
NO-SL	FREE	INSUL	COND	816.8	2.2
NO-SL	FREE	INSUL	INSUL	320.3	0
FREE	NO-SL	COND	COND	1100.7	2.7
FREE	NO-SL	COND	INSUL	816.8	2.2
FREE	NO-SL	INSUL	COND	669.0	2.1
FREE	NO-SL	INSUL	INSUL	320.3	0
FREE	FREE	COND	COND	657.6	2.2
FREE	FREE	COND	INSUL	384.9	1.8
FREE	FREE	INSUL	COND	384.9	1.8
FREE	FREE	INSUL	INSUL	120.0	0



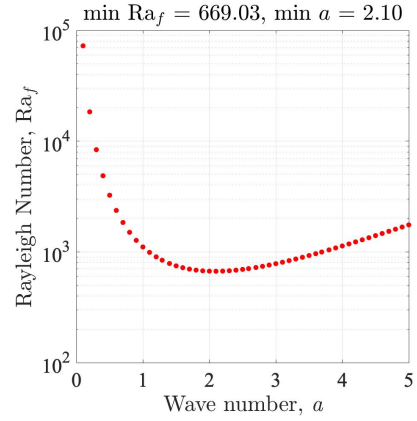
(a) NO-SL, NO-SL, COND, COND.



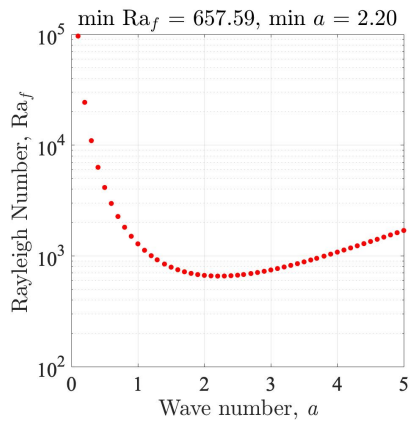
(b) NO-SL, NO-SL, COND, INSUL.



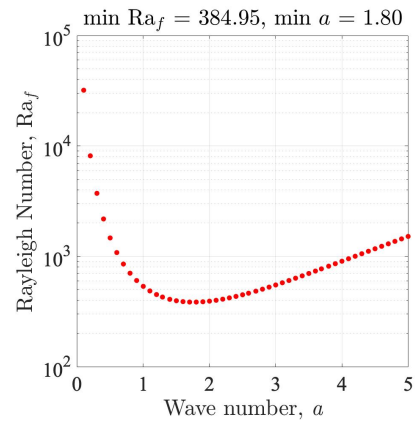
(c) NO-SL, FREE, COND, COND.



(d) NO-SL, FREE, COND, INSUL.



(e) FREE, FREE, COND, COND.



(f) FREE, FREE, COND, INSUL.

Figure 3.2: Marginal stability curves for a single layer of fluid with various boundary conditions, noted beneath each plot. The conditions are for the velocity at  $z = 0$  and  $z = 1$ , respectively, followed by the conditions on  $\theta_f$  at  $z = 0$  and  $z = 1$ .

### 3.1.4 Numerics

To simulate the full system, we return to the original nondimensional system for  $(x, y, z) \in (-L_x, L_x)^2 \times (0, 1)$ :

$$\begin{cases} \frac{1}{\text{Pr}} \frac{\partial \mathbf{u}_f}{\partial t_f} + (\mathbf{u}_f \cdot \nabla) \mathbf{u}_f = \nabla \cdot \mathbb{T}(\mathbf{u}_f, p_f) + \text{Ra}_f T_f \mathbf{k}, \\ \nabla \cdot \mathbf{u}_f = 0, \\ \frac{\partial T_f}{\partial t_f} + \mathbf{u}_f \cdot \nabla T_f = \nabla^2 T_f, \end{cases}$$

which agrees with [97] as a quick sanity check. We consider horizontal, rigid, non-penetrable plates at the top and bottom of our domain; that is, we have no-slip conditions for the velocity at the top and bottom of the domain with periodic boundary conditions at the left- and right-sides. For temperature, we consider conductive boundary conditions at the upper and lower boundaries of the domain held at constant temperatures,  $T_U$  and  $T_L$ , respectively. For convection to be possible, we will only investigate cases with  $T_U < T_L$ . Also, we require the temperature be periodic at the left and right of the domain. A schematic of the domain is shown in Figure 3.1, and a schematic of the mesh is shown in Figure 3.3.

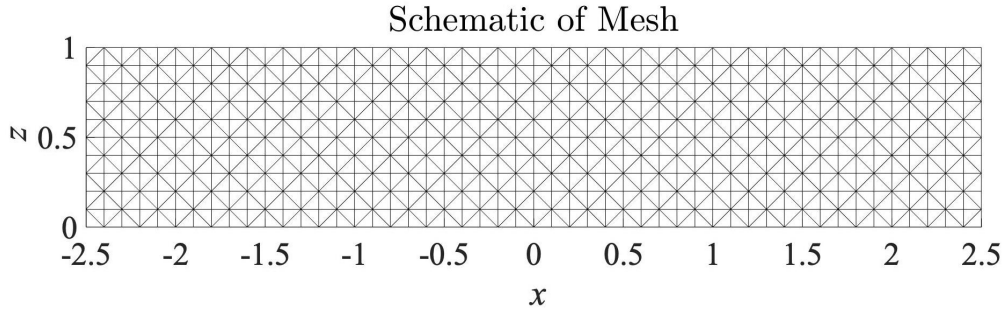


Figure 3.3: Schematic of the discretized domain for a single layer of fluid. For simulations, more elements are used.

To conduct our simulations, we use the Finite Element Method (FEM). Many of the details of implementing this are referenced in Appendix B; we include descriptions of how the problems are formulated in the FEM, how line- and surface-integrals are approximated with numerical quadrature, and how periodic boundary conditions are implemented, along with examples of each. In this section (and for the other sections with numerical simulations), we will only show the variational

forms of our problems; we will not write out the linear systems or matrices for the sake of brevity. For example, with the variational forms shown, all of the integrals over the domain will be decomposed into the sum of integrals over the elements comprising the domain, where the integrals will be approximated with numerical quadrature. So that these details do not need to be repeated in each section, we recommend reading through the discussions in Appendix B before continuing on in this section.

With the following finite element (FE) spaces:

- $V = \{\mathbf{v} \in [H^1(\Omega)]^2 : \mathbf{v} = \mathbf{0} \text{ at top and bottom} + \text{periodic on left and right}\},$
- $Q = \{q \in L^2(\Omega) : \int_{\Omega} q \, d\mathbf{x} = 0 + \text{periodic on left and right}\} = L_0^2(\Omega),$
- $\Psi = \{\psi \in H^1(\Omega) : \psi = 1 \text{ on bottom, } \psi = 0 \text{ on top} + \text{periodic on left and right}\}.$

With the conductive state as the initial condition, we perturb the steady-state with a seeded random perturbation field of magnitude  $\epsilon_{mag} := \epsilon_{mag}(\mathbf{x})$ , set at  $1.0 \times 10^{-8}$ ; we start with

$$\left(\mathbf{u}_f^{(0)}, T_f^{(0)}\right) = (\mathbf{0}, 1.0 - y) + \epsilon_{mag}.$$

Given  $\left(\mathbf{u}_f^{(n)}, T_f^{(n)}\right) \in V \times \Psi$ , we find  $\left(\mathbf{u}_f^{(n+1)}, p_f^{(n+1)}, T_f^{(n+1)}\right) \in V \times Q \times \Psi$  such that

$$\begin{aligned} & \frac{1}{\text{Pr}_f} \int_{\Omega} \frac{\partial \mathbf{u}_f^{(n+1)}}{\partial t_f} \cdot \mathbf{v} \, d\mathbf{x} + \int_{\Omega} \left(\mathbf{u}_f^{(n)} \cdot \nabla\right) \mathbf{u}_f^{(n+1)} \cdot \mathbf{v} \, d\mathbf{x} + 2 \int_{\Omega} \mathbb{D} \left(\mathbf{u}_f^{(n+1)}\right) : \mathbb{D}(\mathbf{v}) \, d\mathbf{x} \\ & - \int_{\Omega} \left(\nabla \cdot \mathbf{u}_f^{(n+1)}\right) \cdot q \, d\mathbf{x} - \int_{\Omega} (\nabla \cdot \mathbf{v}) \cdot p_f^{(n+1)} \, d\mathbf{x} - \int_{\Omega} \text{Ra}_f T_f^{(n)} \mathbf{k} \cdot \mathbf{v} \, d\mathbf{x} = 0 \end{aligned} \quad (3.5)$$

for all test functions  $\mathbf{v} \in V$  and  $q \in Q$ , and

$$\int_{\Omega} \frac{\partial T_f^{(n+1)}}{\partial t_f} \psi \, d\mathbf{x} + \int_{\Omega} \mathbf{u}_f^{(n+1)} \cdot \nabla T_f^{(n+1)} \psi \, d\mathbf{x} + \int_{\Omega} \nabla T_f^{(n+1)} \cdot \nabla \psi \, d\mathbf{x} = 0 \quad (3.6)$$

for all test functions  $\psi \in \Psi$ . With the way we have the Navier-Stokes problem defined in (3.5), we see that it is linear due to partially lagging the nonlinear convection term, as done in [99] among other works. With the linear problem, we are able to use more computationally efficient

solvers. Additionally, by lagging the temperature term in Navier-Stokes and the velocity term of the advection-diffusion equation, the Navier-Stokes-Heat system is decoupled. The decoupled nature of the problem is extremely desirable; it allows us to more easily verify that the independent solvers are working correctly, and it also allows for parallelization of the code. (We did not parallelize the code for this thesis though.) For efficiently handling the convective terms in Navier-Stokes and the ADE, we use a Characteristic Galerkin method (see [46]) implemented with FreeFem [51].

We can also find the stream function  $\phi$ , solving

$$\int_{\Omega} \left[ \nabla \phi^{(n+1)} \cdot \nabla \varphi - \varphi \left( \nabla \times \mathbf{u}_f^{(n+1)} \right) \right] d\mathbf{x} = 0 \quad (3.7)$$

for all test functions  $\varphi \in \Phi$ , with the FE space:

- $\Phi = \{\varphi \in H^1(\Omega) : \varphi = 0 \text{ on top and bottom} + \text{periodic on left and right}\}$ .

With our simulations, we use the algorithm:

---

**Algorithm 1:** Solving Navier-Stokes-Heat system

---

**Result:**  $\mathbf{u}_f^{(N)}, p_f^{(N)}, T_f^{(N)}, \phi^{(N)}$ .  
 Use initial conditions:  $(\mathbf{u}_f^{(0)}, T_f^{(0)}) = (\mathbf{0}, 1 - y) + \epsilon_{mag}$ .  
**for**  $n = 0; n < N; n++$   
**do**  
     With  $\mathbf{u}_f^{(n)}, T_f^{(n)}$ , solve (3.5) for  $\mathbf{u}_f^{(n+1)}, p_f^{(n+1)}$ .  
     With  $\mathbf{u}_f^{(n+1)}, T_f^{(n)}$ , solve (3.6) for  $T_f^{(n+1)}$ .  
     With  $\mathbf{u}_f^{(n+1)}$ , solve (3.7) for  $\phi^{(n+1)}$ .  
**end**

---

In solving (3.5), we tested the fluid solver with convergence tests and timing with different kinds of elements and linear solvers to see which combination would be best for our simulations. For velocity and temperature element choices, we tried  $\mathcal{P}_2$  elements (with 6 nodes along the boundary of our triangular elements) and  $\mathcal{P}_1$  elements (with 3 nodes along the boundary of each element). For the linear solver, we needed a method that works for potentially non-symmetric, sparse matrices;

the coupled problem later will take this form. Two methods that work well for this class of problem, and also easily implemented on FreeFem, are the generalized minimal residual method (GMRES) and the Unsymmetric MultiFrontal method (UMFPACK).

For *brief* explanations of the linear solvers, GMRES is an iterative solver that approximates a solution by the vector in a Krylov subspace with minimal residual. For a better description of GMRES (as well as other iterative solvers for sparse systems), we recommend [78]. On the other hand, UMFPACK is categorized as a direct solver, but uses iterative techniques. The main idea behind this method is to compute an LU factorization (with  $A = PR^{-1}AQ = LU$  where  $P, Q$  are permutation matrices and  $R$  is a diagonal matrix) and then use forward/backward substitution to form an approximate solution. This solution is then improved by iterative refinement. For the technical report on UMFPACK, see [32]. These two linear solvers are designed to efficiently solve sparse matrices, and are already in a variety of languages' built-in libraries. We call them both with FreeFem for our simulations.

To test the 2D solver (in  $x, z$ -plane), we begin by looking at the steady Stokes problem, written in variational form below. Given a fixed  $T_f$ , we solve for  $(\mathbf{u}_f, p_f) \in V \times Q$  such that

$$2 \int_{\Omega} \mathbb{D}(\mathbf{u}_f) : \mathbb{D}(\mathbf{v}) \, d\mathbf{x} - \int_{\Omega} (\nabla \cdot \mathbf{u}_f) \cdot q \, d\mathbf{x} - \int_{\Omega} (\nabla \cdot \mathbf{v}) \cdot p_f \, d\mathbf{x} - \int_{\Omega} T_f \mathbf{k} \cdot \mathbf{v} \, d\mathbf{x} = 0 \quad (3.8)$$

for all  $\mathbf{v} \in V$  and  $q \in Q$ . With this reduced problem, we use the method of manufactured solutions to verify our code and quantify how accurate the approximations are. We start with the 'exact' solutions:

$$\mathbf{u}_f^{ex} = \left( \cos(\beta x), z \beta \sin(\beta x) \right), \quad \beta = \frac{\pi}{2},$$

where  $\beta$  is chosen so that solutions are periodic in  $x$ . This solution satisfies  $\nabla \cdot \mathbf{u}_f^{ex} = 0$ . Given a temperature profile of  $T_f = z \beta^3 \sin(\beta x)$ , we are able to determine the pressure gradient, and the pressure up to a constant, that helps satisfy (3.8):  $p_f^{ex} = -\beta \sin(\beta x)$ . Then, we impose  $\mathbf{u}_f = \mathbf{u}_f^{ex}$ ,  $p_f = p_f^{ex}$  at the boundaries and solve (3.8) for  $\mathbf{u}_f$  and  $p_f$ . We compare the solutions to the exact solution with the  $L^2$  norm:

$$\text{error}^2 = \int_{\Omega} |\mathbf{u}_f - \mathbf{u}_f^{ex}|^2 \, d\mathbf{x}.$$

We solve this problem with different elements,  $\mathcal{P}_1$  and  $\mathcal{P}_2$ , and different linear solvers, UMFPACK and GMRES. The velocity and vorticity for this test case are shown in Figure 3.4.

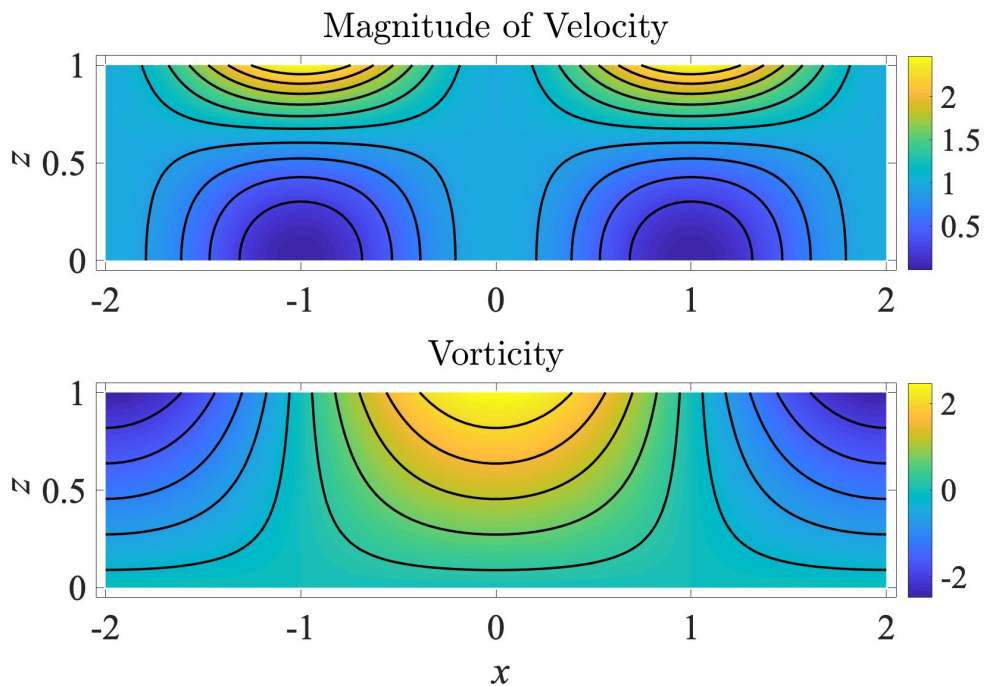


Figure 3.4: Approximate velocity and vorticity from solving the steady Stokes equation (3.8).

In Figure 3.5, we plot the  $L^2$  error against the number of elements per unit distance on the mesh, labelled  $N$ . We see that for the  $\mathcal{P}_1$  elements, both UMFPACK and GMRES are second-order in space; that is, as we halve the max element edge distance on our uniform mesh, the error decreases by a factor of 4. This is evident with the slope of 2 with the  $L^2$  errors for the  $\mathcal{P}_1$  cases. For the  $\mathcal{P}_2$  cases though, we see the method is third-order in space with the slope of 3 with the  $L^2$  errors. This means that halving the max element edge distance on our mesh causes the error to decrease by a factor of 8. Strictly based on convergence rates of  $L^2$  errors, the  $\mathcal{P}_2$  elements clearly outperform their  $\mathcal{P}_1$  counterparts, regardless of the linear solver used.

However, the UMFPACK cases run more quickly than the GMRES ones, as evident in the plot from Figure 3.6. For example, with  $\mathcal{P}_2$  elements and  $2^{15}$  elements (the case for the most refined

mesh shown in Figure 3.6), the UMFPACK solve took 8.6 seconds while the GMRES case took 645 seconds, about 80 times as long. With the comparison lines having slopes of 1 and 3/2 for the UMFPACK and GMRES linear solvers, respectively, the computational times of these methods are  $\mathcal{O}(N^1)$  and  $\mathcal{O}(N^{3/2})$  with  $N$  as the total number of elements in the mesh. Even though UMFPACK computes an LU factorization, the algorithm exploits the sparse structure of the matrix to reduce the number of operations needed to solve the system. Additionally, the factorization does not need to be computed each step, further reducing the computational storage and time for running simulations. Figure 3.6 also helps illustrate an issue with the GMRES solver: with the most refined mesh,  $2^{15}$  elements, the GMRES solver does not converge with the  $\mathcal{P}_1$  elements. As the number elements increases and  $\Delta x$  gets smaller, the system becomes more ill-conditioned. As a result, the GMRES iterations may not converge—this is the case for the case with  $\mathcal{P}_1$  and  $2^{15}$  elements, evident in the two ‘missing’ data points in Figures 3.5 and 3.6.

Taking into account the  $L^2$  error convergence rates and time per solve, using  $\mathcal{P}_2$  elements for velocity in our simulations seems to be the best choice with UMFPACK to solve the linear systems. While the  $\mathcal{P}_1$  cases would take less time to run, the better errors and convergence rates associated with the  $\mathcal{P}_2$  elements are worth the extra time spent solving the additional degrees of freedom.

The type of element used for the pressure terms has yet to be discussed though. Despite  $\mathcal{P}_2$  elements having better error convergence rates compared to  $\mathcal{P}_1$  elements, we will choose to put pressure on  $\mathcal{P}_1$  elements with velocity on  $\mathcal{P}_2$  elements. These mixed element choices are referred to the Taylor-Hood elements. Numerous convergence studies and analyses have been performed with this choice of elements (see: [14, 42, 43, 49, 91]) proving the convergence rates using the  $\mathcal{P}_2$ - $\mathcal{P}_1$  Taylor-Hood elements are

$$\|\mathbf{u}_f^{ex} - \mathbf{u}_f\|_{L^2} \sim \mathcal{O}(\Delta x^3), \quad \|p_f^{ex} - p_f\|_{L^2} \sim \mathcal{O}(\Delta x^2),$$

where  $\Delta x$  corresponds to the length of the largest element of the mesh. We see these convergence rates hold in practice with Figure 3.7.

With all of the above information, we will use the mixed FE Taylor-Hood elements for our simulations with the UMFPACK linear solver.

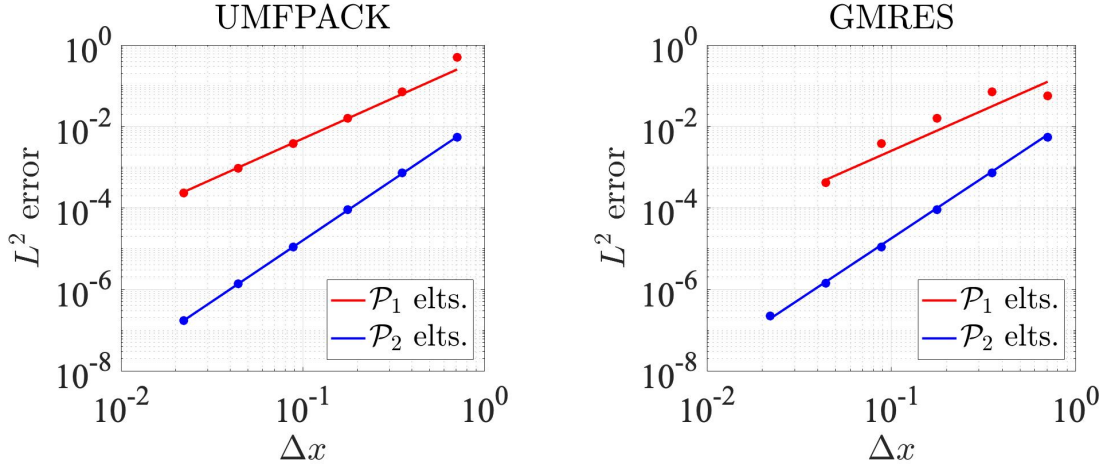


Figure 3.5: Convergence for the steady Stokes problem with  $\mathcal{P}_1$  and  $\mathcal{P}_2$  elements with UMFPACK and GMRES linear solvers. The  $L^2$  error of velocity is plotted as the max edge size,  $\Delta x$  on the mesh, is varied. The comparison lines in each plot have slopes of 2 for the blue line ( $\mathcal{P}_1$  elts.) and 3 for the red line ( $\mathcal{P}_2$  elts.).

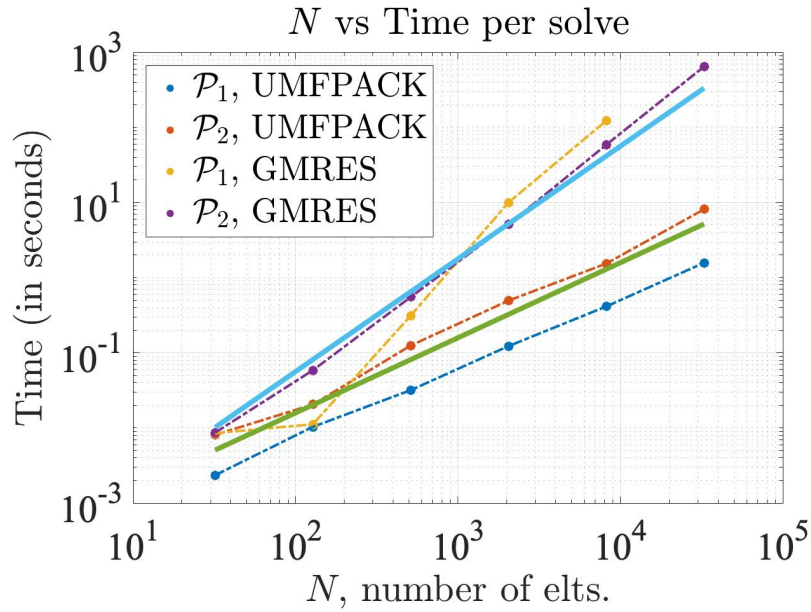


Figure 3.6: Time per solve for the steady Stokes problem with  $\mathcal{P}_1$  and  $\mathcal{P}_2$  elements with UMFPACK and GMRES linear solvers. The green comparison line has a slope of 1, the blue line has a slope of  $3/2$ .

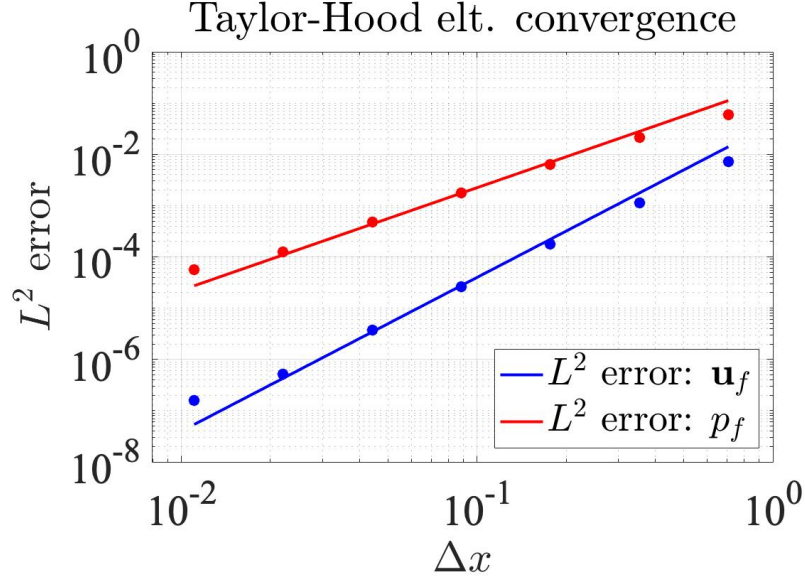


Figure 3.7: Convergence with  $L^2$  errors of  $\mathbf{u}_f$  and  $p_f$  with the steady Stokes problem using the Taylor-Hood  $\mathcal{P}_2\text{-}\mathcal{P}_1$  elements with UMFPAK as the linear solver. The red comparison line has a slope of 2, and the blue has a slope of 3.

### 3.1.5 Quantifying convection

To quantify the effectiveness of heat transfer and the onset of convection, we use two primary measurements: the (non-physical) energy of the system, and the Nusselt number. While we defined the energy of the system ourselves and it does not have an innate physical meaning, our analyses were conducted with the energy in mind. These analyses were then used to determine the Rayleigh number needed for the onset of convection with the marginal stability curves. A more traditional measurement in quantifying convection is the Nusselt number, which describes the ratio of convective to conductive heat transfer at the boundary of a fluid. Both of these measurements are described in more detail below.

For the energy analysis, we return to the system of perturbations to the steady-state,  $\mathbf{v}_f$ ,  $\pi_f$ ,  $\theta_f$  (perturbations to velocity, pressure, and temperature, respectively):

$$\begin{cases} \frac{1}{\text{Pr}} \frac{\partial \mathbf{v}_f}{\partial t_f} + (\mathbf{v}_f \cdot \nabla) \mathbf{v}_f = \nabla \cdot \mathbb{T}(\mathbf{v}_f, \pi_f) + \text{Ra}_f \theta_f \mathbf{k}, \\ \frac{\partial \theta_f}{\partial t_f} + \mathbf{v}_f \cdot \nabla \theta_f = \nabla^2 \theta_f + w_f, \end{cases}$$

then take the inner product of the two equations above with  $\mathbf{v}$  and  $\theta_f$ , respectively. We integrate by parts and apply the boundary conditions to arrive at the energies of each equation<sup>1</sup>:

$$\begin{cases} \frac{1}{2\text{Pr}} \frac{d}{dt_f} \|\mathbf{v}_f\|^2 = -\|\nabla \mathbf{v}_f\|^2 + \text{Ra}_f \int_{\Omega} \theta_f \mathbf{k} \cdot \mathbf{v}_f d\mathbf{x}, \\ \frac{1}{2} \frac{d}{dt_f} \|\theta_f\|^2 = -\|\nabla \theta_f\|^2 + \int_{\Omega} \theta_f w_f d\mathbf{x}. \end{cases}$$

We define the energy of the system as the sum of the two left-hand sides of the equations above (without the time derivative):

$$2E(t_f) = \frac{1}{\text{Pr}} \|\mathbf{v}_f\|^2 + \|\theta_f\|^2. \quad (3.9)$$

Then, the change in energy is

$$\frac{dE}{dt_f} = -\mathcal{D} + \mathcal{I} \quad (3.10)$$

where the definite and indefinite terms,  $\mathcal{D}$  and  $\mathcal{I}$ , are

$$\begin{aligned} \mathcal{D} &= \|\nabla \mathbf{v}_f\|^2 + \|\nabla \theta_f\|^2, \\ \mathcal{I} &= (\text{Ra}_f + 1) \int_{\Omega} \theta_f w_f d\mathbf{x}. \end{aligned}$$

With (3.9) and (3.10) governing the energy and change in energy, we could follow an argument similar to that in Chapter 2 to determine nonlinear stability curves; however, the equations would reduce to those used in the linear analysis. Here, (3.9) and (3.10) are only being used here to quantify the energy of the system.

One other quantitative benchmark with many works on convection is the Nusselt number. The Nusselt number  $\text{Nu}$  is the ratio of convective to conductive heat transfer at the boundary of a fluid, as seen in Chapter 2 with (2.34). In Chapter 2 though, the Nusselt number was viewed as a field; in this chapter, we view the Nusselt number as a *scalar* quantifying the ratio of convective to conductive heat transfer. Many seminal works in the fields of convection, turbulence, and geophysical fluid dynamics make use of the Nusselt number to quantify heat transfer. For a non-exhaustive list of works concerning the Nusselt number in a variety of settings with convection in fluids, see [16, 31, 34, 35, 48, 55, 69, 82, 97].

---

<sup>1</sup>The resulting equations are the same regardless of the choice of no-slip or free-slip boundary conditions on the top and bottom plates.

We have various ways to define the Nusselt number  $\text{Nu}$ ; despite appearances, all the definitions are equivalent with the divergence theorem and/or integration by parts. To define  $\text{Nu}$ , we use the following notation:

$$\bar{f} := \bar{f}(z) = \frac{1}{2L_x} \int_{-L_x}^{L_x} f \, dx \text{ (horizontal average),} \quad \langle f \rangle = \frac{1}{d} \int_0^d \bar{f} \, dz \text{ (vertical average).}$$

Then, the Nusselt number can be defined by any of these statements

$$\text{Nu}(t) = 1 + \langle w T \rangle \tag{3.11}$$

$$= \langle |\nabla T|^2 \rangle \tag{3.12}$$

$$= \frac{\int_{\Omega} w T \, d\mathbf{x} + \int_{\Omega} -\frac{\partial T}{\partial z} \, d\mathbf{x}}{\int_{\Omega} -\frac{\partial T}{\partial z} \, d\mathbf{x}} \tag{3.13}$$

$$= 1 - \left. \frac{\partial \theta}{\partial z} \right|_{z=1} \tag{3.14}$$

where  $T$  is the temperature field,  $\theta$  is the deviation of the temperature from the conductive state, and  $w$  is the vertical component of the velocity. Doering et al. and Howard showed that (3.11), (3.12), and (3.13) were all equivalent in [34, 35, 55].

Traditionally, the Nusselt number is defined as the time-average of  $\text{Nu}(t)$ . We plot how the Nusselt number varies in time though since it is related to the energy of the system. With a scaled version of the Nusselt number and the energy of the system

$$\widetilde{\text{Nu}} = \frac{\text{Nu} - 1}{\max(\text{Nu} - 1)}, \quad \widetilde{E} = \frac{E}{\max E}, \tag{3.15}$$

we will show how closely these two measurements align. Effectively, the non-physical energy of the system  $E(t)$  is closely related to the physically-motivated Nusselt number by  $\widetilde{\text{Nu}}(t) \approx \widetilde{E}(t)$ , which we show in the Results section below.

### 3.1.6 Results

With the simulations, we discretize the domain into the mesh. A schematic of the mesh is shown in Figure 3.3, which has 10 elements per unit distance. For our simulations in this chapter, we use a mesh over  $(x, z) \in [-2.5, 2.5] \times [0, 1]$  with 20 elements per unit distance.

While verifying our results, one obvious aspect to investigate is the critical Rayleigh number. A healthy amount of this chapter is dedicated to determining the critical Rayleigh numbers for

various boundary conditions, after all. With our simulations, we consider no-slip conditions for velocity and conductive conditions for temperature at the top/bottom of the domain with periodic boundary conditions at the left and right. Earlier, we determined that the critical Rayleigh number corresponding to this case is 1708. So, choosing a Rayleigh number below that threshold should result in the conductive state, while choosing one above 1708 should produce convection cells.

Additionally, we can relate the choice of the Rayleigh number to the energy of the system from (3.9). For  $Ra_f < 1708$ , the energy of the system, as well as the change in energy, will stay at 0 for the duration of the simulation. For  $Ra_f$  values above 1708 though, the energy of the system will grow and then plateau at the saturation energy. While the energy is growing, the convection cells are beginning to form. Once the cells have completely formed and the system has achieved its saturation energy, the system is at its new steady-state, evident with  $dE/dt = 0$  at this point in the simulations. We plot the energy and change in energy for simulations of various Rayleigh numbers, shown in Figure 3.8. These results are in agreement with the stability analyses conducted earlier in this chapter.

We also plot the Nusselt number in Figure 3.8. Values of  $Nu > 1$  correspond to convection, while  $Nu = 1$  corresponds to the conductive state. This directly correlates to  $E(t) > 0$  signifying that convection cells will arise and  $E(t) = 0$  for the initial ‘no-flow’ steady state. Similar to the energy of the system, higher Rayleigh numbers are related to higher Nusselt numbers. Determining the relationship between the Rayleigh number and the Nusselt number is an active research area, especially in the high Rayleigh number regime. For higher Rayleigh numbers, there are many relationships (some more complicated than others) describing how  $Nu$  and  $Ra$  can be related. For example, in [35], Doering et al. determined the bound

$$Nu \leq 0.644 \times Ra^{1/3} [\ln(Ra)]^{1/3}$$

in the asymptotic limit of  $Ra \rightarrow \infty$ . Many other papers have been dedicated to determining relationships and bounds like this for large, but finite, Rayleigh numbers as well.

Without looking at the scales of the vertical axis, we note the similarities in profiles for  $E(t)$  and  $Nu(t)$ . This prompted us to normalize both profiles, scaling them by their max and shifting the Nusselt number downward to have a minimum of 0. These scaled profiles are shown in Figure 3.9. These results suggest that the energy of the system has a more prominent role in convection

than we initially figured; while it is defined as a non-physical measure of the mathematical energy of the system, it also is closely related to the Nusselt number. So, many of the results we show with the energy can be directly extrapolated to results with the Nusselt number. We will limit these relationships to ‘lower’ Rayleigh number regimes though.

With the Figures 3.10 and 3.11, we run simulations with  $Ra_f = 2500$  and  $Ra_f = 10000$ . As the Rayleigh number increases, the velocity of the convection cells increases (as noted with the larger values of the isolines in the streamline graphs) and the temperature profile begins to develop more “plume-like” shapes. With the increase in  $Ra_f$ , the energy of the system increases as well; this is shown with Figures 3.10b and 3.11b. In the case with  $Ra_f = 2500$ , the convection cells develop gradually over  $t \in (5, 7)$ . With  $Ra_f = 10000$  though, the convection cells develop much more rapidly. The fluid velocity gains momentum and the system overshoots the saturation energy. The cells then lose some velocity to settle down at steady convection cells as  $E(t)$  and  $dE/dt$  level out.

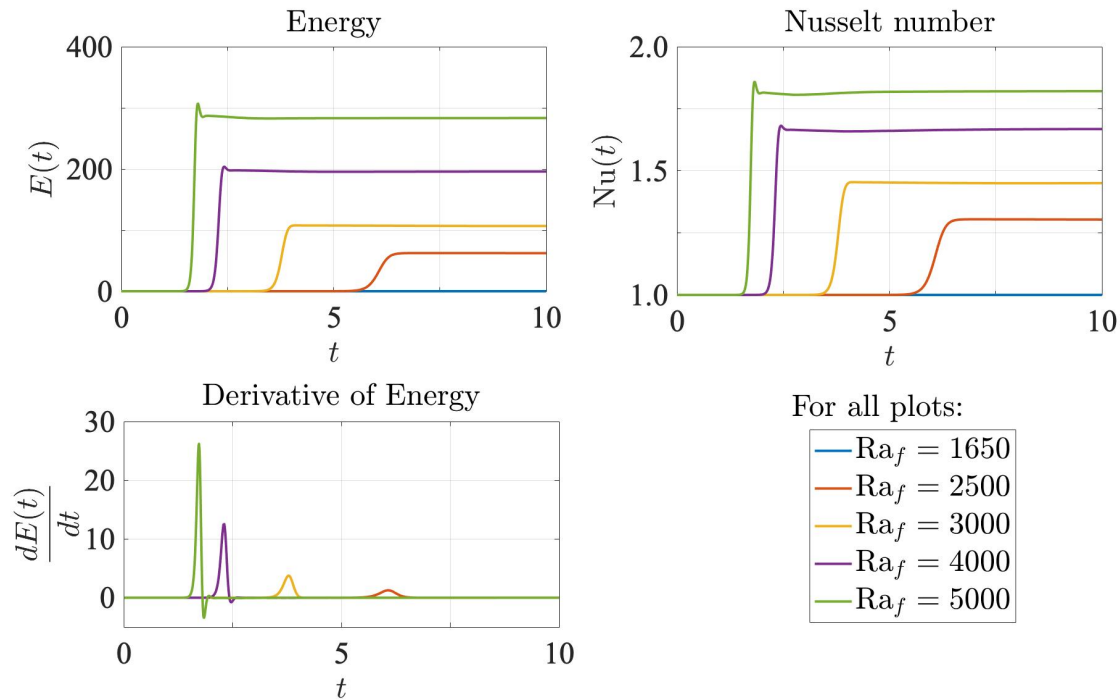


Figure 3.8: Energy of the systems and the change in energy for various  $Ra_f$  values. The mesh is on  $(x, z) \in [-2.5, 2.5] \times [0, 1]$  with 20 elements/unit distance on the mesh, and  $\Delta t = .01$ ,  $Pr_f = .7$ .

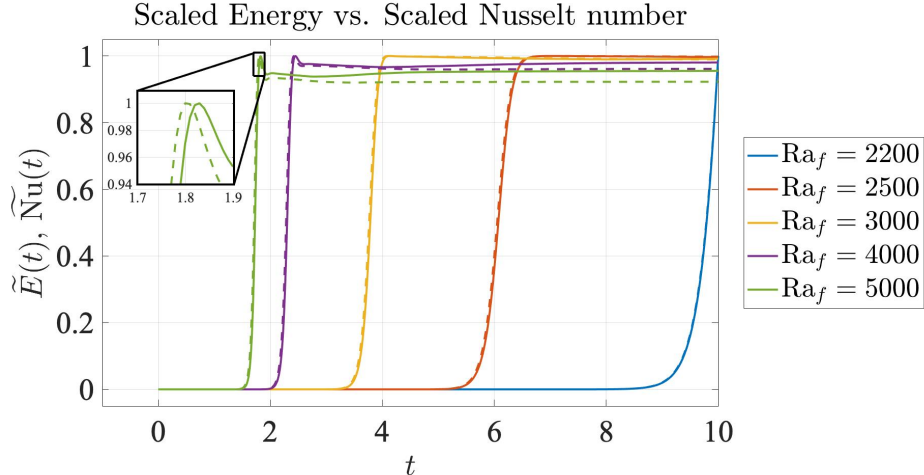


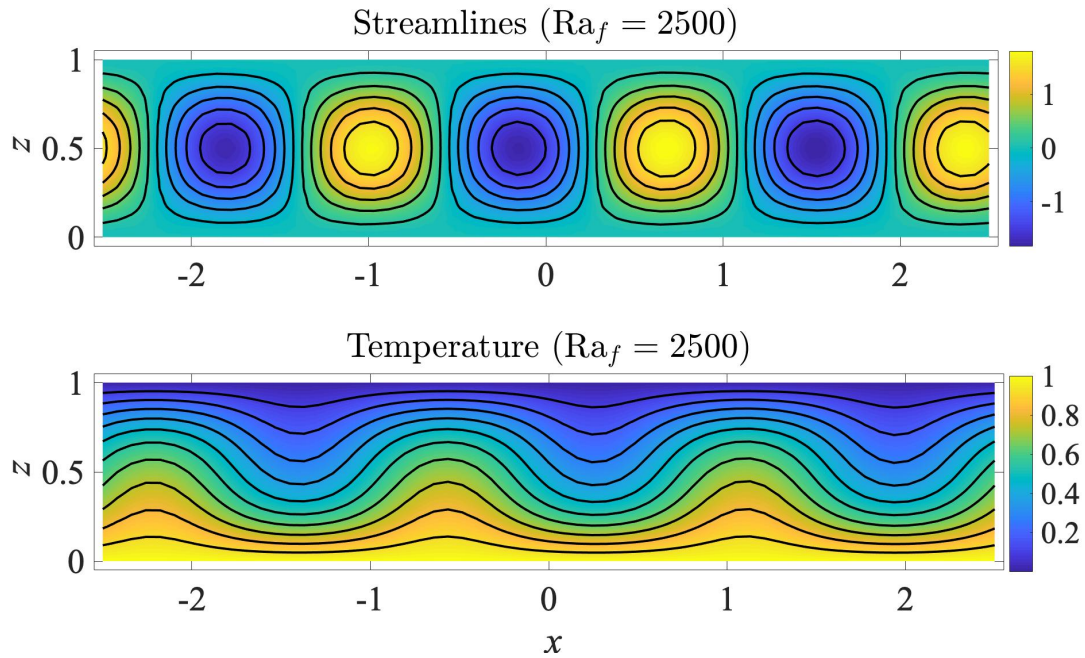
Figure 3.9: Scaled energy and scaled Nusselt number of the systems for various  $Ra_f$  values. The solid lines represent the scaled Nusselt number, the dashed are the scaled energy. The mesh is on  $(x, z) \in [-2.5, 2.5] \times [0, 1]$  with 20 elements/unit distance on the mesh, and  $\Delta t = .01$ ,  $Pr_f = .7$ .

When the systems achieve their steady-state, we can determine the saturation energy. For various Rayleigh numbers, we plot the saturation energy versus  $Ra_f$  in Figure 3.12. With these results, we see once again that the critical Rayleigh number is around 1708; this is evident with the saturation energy at 0 until  $Ra_f \approx 1708$ . Additionally, we fit the data with the red line shown in the figure:

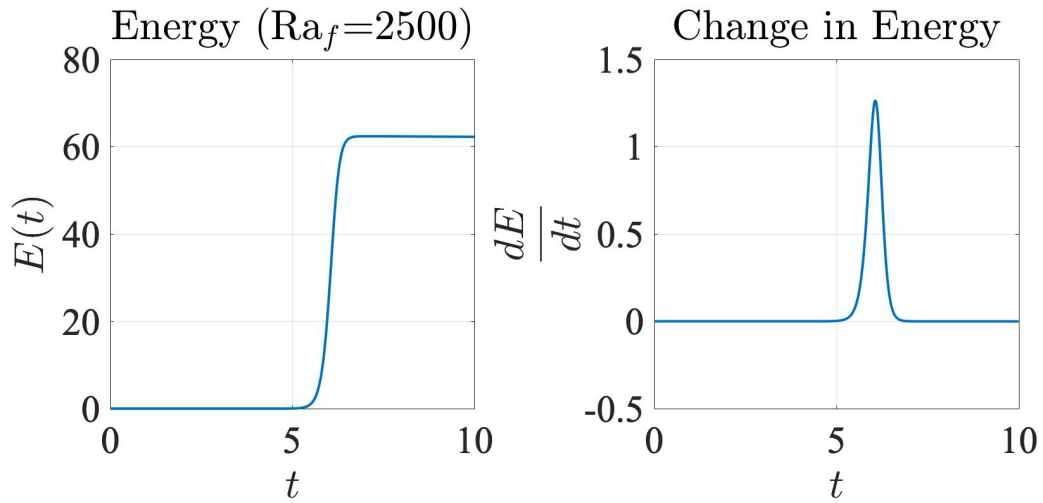
$$E_{fit} = .084 \cdot Ra_f - 143.5.$$

This suggests a linear relationship between the Rayleigh number and saturation energy. Furthermore, with the predicted saturation energy, inputting  $Ra_f = 1708$  into the equation yields  $E_{fit} = -.028 \approx 0$ , verifying the critical Rayleigh number yet again. This method has the potential to be used with the coupled case to verify the critical Rayleigh numbers found with our linear and nonlinear stability analyses. We postulate these results are only valid in non-turbulent parameter regimes.

With the simulations for Figure 3.12, we stay in a parameter regime where steady-states can be achieved. If the Rayleigh number is increased to  $Ra_f \sim \mathcal{O}(10^6 - 10^7)$ , we enter a turbulent regime. While turbulence in these scenarios is still a very active research problem, turbulence adds another facet to the convection problem and is beyond the scope of the work we conduct in this thesis. As a result, we only consider ‘nice’ parameter regimes which do not result in turbulence. Figure

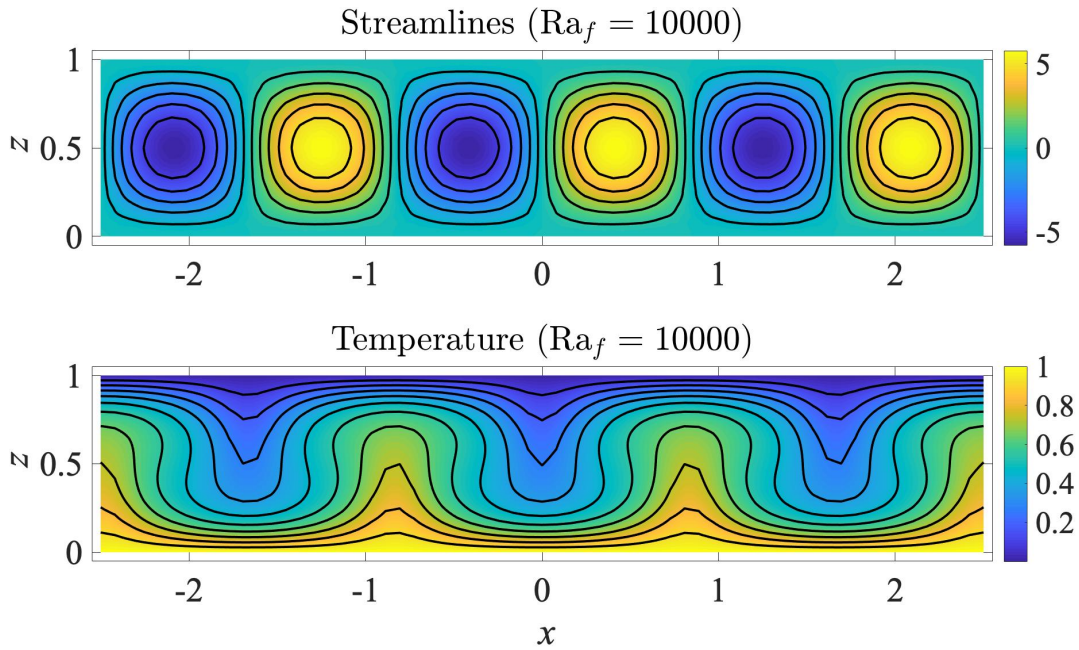


(a) Streamlines and temperature profiles at  $t = 10$ . Positive isolines circulate in the positive direction with negative isolines circulating in the negative direction.

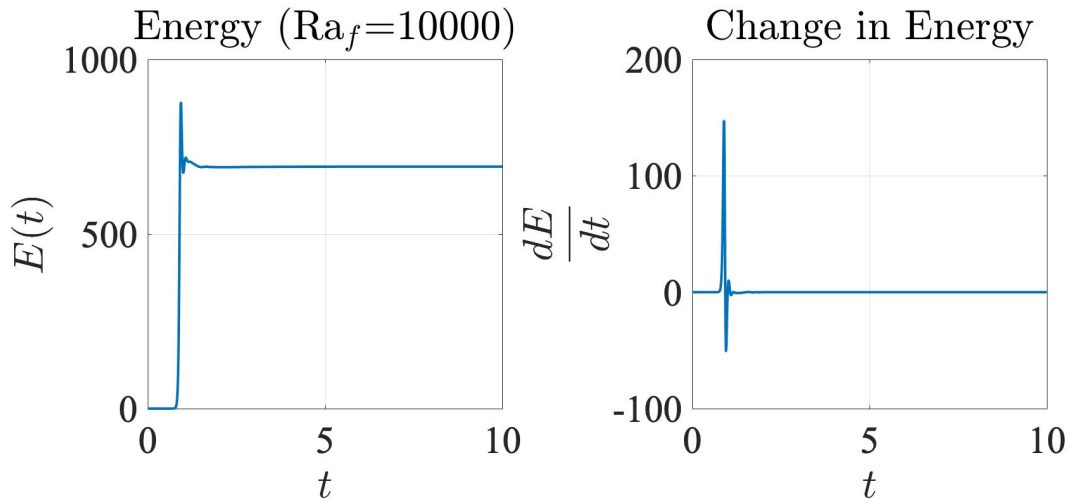


(b) Energy and change in energy.

Figure 3.10: Simulation with  $Ra_f = 2500$ . The mesh is on  $(x, z) \in [-2.5, 2.5] \times [0, 1]$  with 20 elements/unit distance on the mesh, and  $\Delta t = .01$ ,  $Pr_f = .7$ .



(a) Streamlines and temperature profiles at  $t = 10$ . Positive isolines circulate in the positive direction with negative isolines circulating in the negative direction.



(b) Energy and change in energy.

Figure 3.11: Simulation with  $Ra_f = 10000$ . The mesh is on  $(x, z) \in [-2.5, 2.5] \times [0, 1]$  with 20 elements/unit distance on the mesh, and  $\Delta t = .01$ ,  $Pr_f = .7$ .

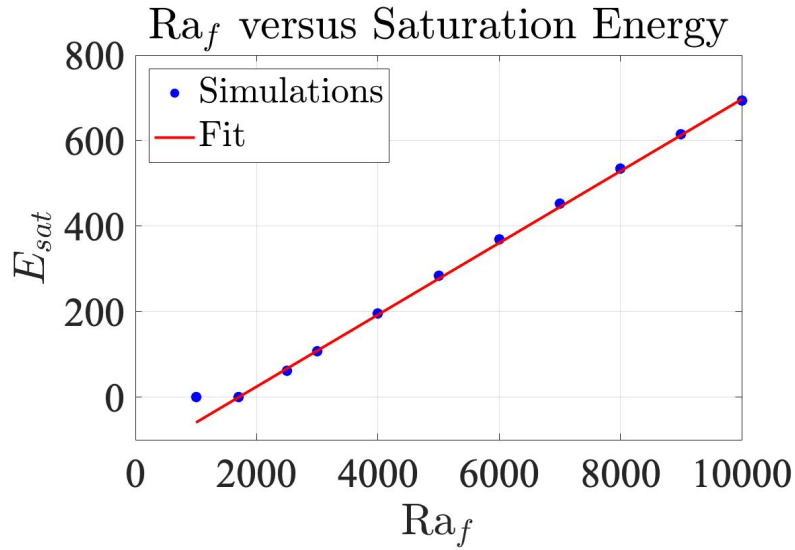


Figure 3.12:  $Ra_f$  versus saturation energy for a single layer of fluid.

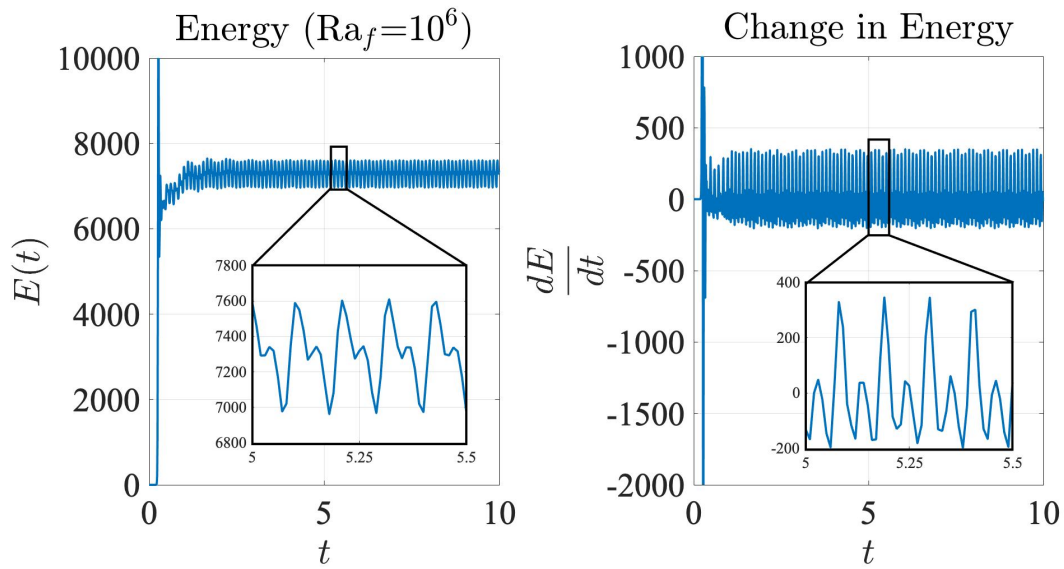


Figure 3.13: Energy and the change in energy for  $Ra_f = 10^6$ , in a ‘turbulent’ system. The mesh is on  $(x, z) \in [-2.5, 2.5] \times [0, 1]$  with 20 elements/unit distance on the mesh, and  $\Delta t = .01$ ,  $Pr_f = .7$ .

3.13 shows the energy and change in energy for a ‘weakly turbulent’ case with  $Ra_f = 10^6$ ; we note neither the energy nor the change in energy of the system settle down.

## 3.2 Single layer of a porous medium saturated with fluid

This section focuses on the phenomenon of convection in a single layer of a porous medium saturated with fluid. Here, we outline the linear stability analysis, our numerical method to simulate the system, and related results. Many of the arguments made in this section are similar to those discussed in the previous section. The linear stability analyses here are not novel; the same arguments are presented in popular survey texts concerning convection in porous media [68, 86].

### 3.2.1 Equations, and linear stability analysis

With fluid flow in a porous medium, the Darcy system or the Brinkman equations are the most appropriate choices. However, for media with small porosities, Darcy is the most well-accepted model governing fluid behavior. With the temperature component, the Boussinesq approximation is included with Darcy, and we add an advection-diffusion equation into the system as well. For  $\Omega = \{(x, y, z) \in \mathbb{R}^2 \times (-d_m, 0)\}$ , we have:

$$\begin{cases} \frac{\rho_0}{\chi} \frac{\partial \mathbf{u}_m}{\partial t_m} + \frac{\mu_0}{\Pi} \mathbf{u}_m = \nabla p_m - g\rho_0 [1 - \beta (T_m - T_L)] \mathbf{k}, \\ \nabla \cdot \mathbf{u}_m = 0, \\ \frac{\partial T_m}{\partial t_m} + \mathbf{u}_m \cdot \nabla T_m = \lambda_m \nabla^2 T_m, \end{cases}$$

with  $\lambda_m = \kappa_m / (\rho_0 c_p)_f$ . A schematic of the domain is shown in Figure 3.14.

To begin the linear stability analysis, we find the steady-states. Like the case of the single layer of fluid, the steady-states are zero fluid flow and a linear temperature profile with the pressure gradient selected to satisfy the remainder of the Darcy-Boussinesq equation. The steady-states are denoted by an overbar:

$$\begin{aligned} \bar{\mathbf{u}}_m &= 0, \\ \bar{T}_m &= T_U + z \frac{T_U - T_L}{d_m}, \\ \nabla \bar{p}_m &= -g\rho_0 (1 - \beta (\bar{T}_m - T_L)) \mathbf{k}. \end{aligned}$$

We perturb the steady-states with the perturbation variables

$$\mathbf{u}_m = \bar{\mathbf{u}}_m + \mathbf{v}_m, \quad T_m = \bar{T}_m + \theta_m, \quad p_m = \bar{p}_m + \pi_m,$$

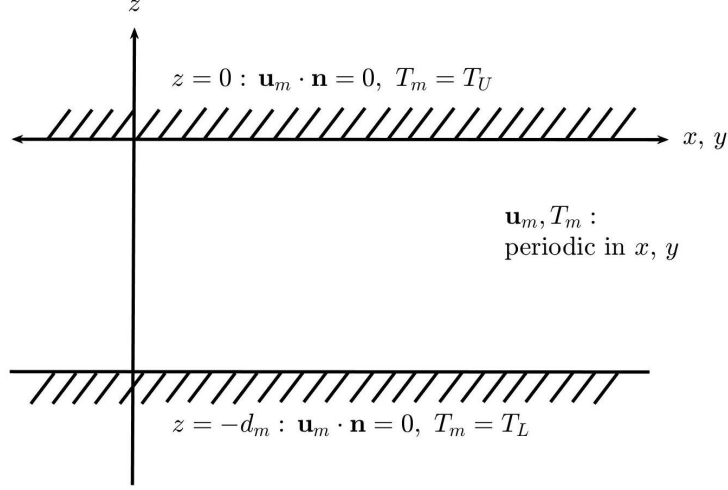


Figure 3.14: Schematic of the domain  $\Omega = \{(x, y) \in \mathbb{R}^2 \times z \in (-d_m, 0)\}$ . The upper and lower boundaries are impermeable and held at constant temperatures  $T_U$  and  $T_L$ , respectively, with  $T_L > T_U$ .

which yields the system:

$$\begin{cases} \frac{\rho_0}{\chi} \frac{\partial \mathbf{v}_{\mathbf{m}}}{\partial t_m} + \frac{\mu_0}{\Pi} \mathbf{v}_{\mathbf{m}} = -\nabla \pi_m + \rho_0 g \beta \theta_m \mathbf{k}, \\ \nabla \cdot \mathbf{v}_{\mathbf{m}} = 0, \\ \frac{\partial \theta_m}{\partial t_m} + \mathbf{v}_{\mathbf{m}} \cdot \nabla \theta_m = \lambda_m \nabla^2 \theta_m - w_m \left( \frac{T_U - T_L}{d_m} \right). \end{cases}$$

We nondimensionalize the system with the following scalings:

$$\mathbf{v}_{\mathbf{m}} = \tilde{\mathbf{v}}_m \frac{\nu}{d_m}, \quad \mathbf{x}_m = \tilde{\mathbf{x}}_m d_m, \quad t_m = \tilde{t}_m \frac{d_m^2}{\lambda_m}, \quad \theta_m = \tilde{\theta}_m \frac{(T_L - T_U) \nu}{\lambda_m}, \quad \pi_m = \tilde{\pi}_m \frac{\rho_0 \nu^2}{d_m^2},$$

and assuming that the perturbations are small, we find the linear, nondimensional system for the perturbation variables:

$$\begin{cases} \frac{1}{\chi} \frac{\text{Da}}{\text{Pr}_m} \frac{\partial \mathbf{v}_{\mathbf{m}}}{\partial t_m} + \mathbf{v}_{\mathbf{m}} = -\text{Da} \nabla \pi_m + \text{Ra}_m \theta_m \mathbf{k}, \\ \nabla \cdot \mathbf{v}_{\mathbf{m}} = 0, \\ \frac{\partial \theta_m}{\partial t_m} = \nabla^2 \theta_m + w_m, \end{cases}$$

$$\text{with } \text{Pr}_m = \frac{\nu}{\lambda_m} \quad \text{Da} = \frac{\Pi}{d_m^2}, \quad \text{and } \text{Ra}_m = \frac{g \beta (T_L - T_U) \text{Da} d_m^3}{\nu \lambda_m}.$$

After taking the double curl of the Darcy-Boussinesq equation and looking the  $z$ -component of the resulting equation, we find the coupled system for  $z \in (-1, 0)$  :

$$\begin{cases} \left( \frac{1}{\chi} \frac{\text{Da}}{\text{Pr}_m} \frac{\partial}{\partial t_m} + 1 \right) \nabla^2 w_m = \text{Ra}_m \nabla_H^2 \theta_m, \\ \left( \frac{\partial}{\partial t_m} - \nabla^2 \right) \theta_m = w_m, \end{cases} \quad (3.16)$$

For boundary conditions, we have various options to enforce at the top and bottom plates of the domain. For velocity, we can enforce an impermeable boundary or an ‘open boundary.’ An impermeable boundary would correspond to a rigid plate and  $w_m = 0$  on the boundary. Alternatively, an ‘open boundary’ would refer to a free surface or a “boundary at a constant pressure, [as in] a medium bounded by a fluid” [68]. Tyvand stated this condition is equivalent to requiring that the surrounding fluid is hydrostatic [94]. Tyvand also noted that just as impermeable boundary is expressed with  $\mathbf{u} \cdot \mathbf{n} = 0$ , the condition describing an open boundary is  $\mathbf{u} \times \mathbf{n} = 0$ . With our variables, the free surface condition is then written as  $\frac{\partial w_m}{\partial z} = 0$ . This condition follows from an argument that assumes a fluid at hydrostatic equilibrium is outside the porous medium, and is derived in detail in [94].

For boundary conditions on the temperature perturbation, we have a two choices yet again. The first assumes that the boundary is perfectly conductive, and as a result, the perturbation to the steady-state would be 0 at the boundary— that is,  $\theta_m = 0$ . A second option assumes a constant heat flux, or an insulating boundary, with  $\frac{\partial \theta_m}{\partial z} = 0$ .

Now, we take normal modes of the perturbations

$$w_m(\mathbf{x}, t) = F(x, y) w_m(z) e^{\sigma t}, \quad \theta_m(\mathbf{x}, t) = F(x, y) \theta_m(z) e^{\sigma t},$$

and substitute them into (3.16), which gives:

$$\begin{cases} \left( \frac{1}{\chi} \frac{\text{Da}}{\text{Pr}_m} \sigma + 1 \right) (D^2 - a^2) w_m = -a^2 \text{Ra}_m \theta_m, \\ (\sigma - (D^2 - a^2)) \theta_m = w_m. \end{cases} \quad (3.17)$$

### 3.2.2 Principle of exchange of stabilities

Like the single layer of fluid case, the principle of exchange of stabilities holds for a single layer of a porous medium regardless of which combination of boundary conditions we choose to enforce. To

show that this principle holds, we multiply the two equations of (3.17) by  $w_m^*$  and  $\theta_m^*$ , respectively, and integrate over the domain. Then, with integration by parts, we can manipulate the equations to show that setting  $\sigma = 0$  suffices for determining marginal stability.

With the first equation of (3.17), we have

$$\left(\frac{1}{\chi} \frac{\text{Da}}{\text{Pr}_m} \sigma + 1\right) \int_{-1}^0 w_m^* (D^2 - a^2) w_m dz = -a^2 \text{Ra}_m \int_{-1}^0 w_m^* \theta_m dz.$$

Now, we can integrate by parts to find

$$\begin{aligned} \left(\frac{1}{\chi} \frac{\text{Da}}{\text{Pr}_m} \sigma + 1\right) \underbrace{\int_{-1}^0 |Dw_m|^2 + a^2 |w_m|^2 dz}_{:=I_1 > 0} &= a^2 \text{Ra}_m \int_{-1}^0 w_m^* \theta_m dz, \\ \Rightarrow \left(\frac{1}{\chi} \frac{\text{Da}}{\text{Pr}_m} \sigma + 1\right) I_1 &= a^2 \text{Ra}_m \int_{-1}^0 w_m^* \theta_m dz. \end{aligned} \quad (3.18)$$

We follow a similar procedure with the second equation of (3.17), multiplying by  $\theta_m^*$

$$\int_{-1}^0 \theta_m^* (\sigma - (D^2 - a^2)) \theta_m dz = \int_{-1}^0 \theta_m^* w_m dz,$$

and then integrating by parts

$$\begin{aligned} \sigma \underbrace{\int_{-1}^0 |\theta_m|^2 dz}_{:=I_2 > 0} + \underbrace{\int_{-1}^0 |D\theta_m|^2 + a^2 |\theta_m|^2 dz}_{:=I_3 > 0} &= \int_{-1}^0 \theta_m^* w_m dz, \\ \Rightarrow \sigma I_2 + I_3 &= \int_{-1}^0 \theta_m^* w_m dz. \end{aligned} \quad (3.19)$$

We take  $a^2 \text{Ra}_m$  times (3.19) and subtract off (3.18) to eliminate the right-hand sides of the equations, yielding

$$a^2 \text{Ra}_m \sigma I_2 + a^2 \text{Ra}_m I_3 - \left(\frac{1}{\chi} \frac{\text{Da}}{\text{Pr}_m} \sigma^* + 1\right) I_1 = 0.$$

We assume  $\sigma = \sigma_{re} + i \sigma_{im}$  and collect the real and imaginary components of the above equation, each of which should be equal to zero. With the imaginary component, we have

$$\sigma_{im} \left( a^2 \text{Ra}_m I_2 + \frac{1}{\chi} \frac{\text{Da}}{\text{Pr}_m} I_1 \right) = 0,$$

implying that for  $\text{Ra}_m > 0$ , we must have  $\sigma_{im} = 0$ . So, when the bottom plate of the domain is hotter than the top plate (i.e.,  $\text{Ra}_m > 0$ ), the  $\sigma$  values of the perturbation have no imaginary component. This allows us to set  $\sigma = 0$  in (3.17) to solve for the marginal stability curves.

With the real part of the equation, we have

$$\sigma_{re} \left( a^2 \text{Ra}_m I_2 - \frac{1}{\chi} \frac{\text{Da}}{\text{Pr}_m} I_1 \right) + a^2 \text{Ra}_m I_3 - I_1 = 0.$$

For  $\text{Ra}_m < 0$ , we must also have  $\sigma_{re} < 0$ . The assumption of  $\text{Ra}_m < 0$  corresponds to the top plate having a higher temperature than the bottom plate and the conclusion of  $\sigma_{re} < 0$  indicates the perturbations damps out and the configuration is stable.

### 3.2.3 Marginal stability curves

Evoking the principle of exchange of stabilities allows us to set  $\sigma = 0$  and solve a generalized eigenvalue problem for Ra to determine marginal stability:

$$\begin{cases} (D^2 - a^2) w_m = -a^2 \text{Ra}_m \theta_m, \\ (D^2 - a^2) \theta_m = -w_m. \end{cases}$$

Once again, we lose dependence on the Prandtl number. We also notice that the porosity  $\chi$  is also not explicitly represented in the equations above; however, it is interwoven into the  $\text{Ra}_m$  term with the permeability. The generalized eigenvalue problem takes the form:

$$\begin{pmatrix} D^2 - a^2 I & 0 \\ I & D^2 - a^2 I \end{pmatrix} \begin{pmatrix} w_m \\ \theta_m \end{pmatrix} = \text{Ra}_m \begin{pmatrix} 0 & a^2 I \\ 0 & 0 \end{pmatrix} \begin{pmatrix} w_m \\ \theta_m \end{pmatrix}, \quad (3.20)$$

which we solve with the Chebyshev tau-QZ algorithm [36] using a mixture of boundary conditions (with their respective abbreviations used in Figure 3.15):

- impermeable (IMPR):  $w_m = 0$ ,
- “free-slip” (FREE):  $Dw_m = 0$ ,
- conducting (COND):  $\theta_m = 0$ ,
- insulating (INSUL):  $D\theta_m = 0$ .

Table 3.2 notes the critical Rayleigh numbers we find for different combinations of the boundary conditions. Each of the values present are in agreement with the work conducted by Nield and Bejan in [68]. We also plot several marginal stability curves in Figure 3.15.

The marginal stability curves reveal some interesting behavior. The first four panels of Figure 3.15, (a) through (d), resemble stability curves from the free flow region. However, the last two curves shown in panels (e) and (f) have their respective minima at a wavenumber of  $a = 0.0$ . This tells us that long-wave perturbations are the most unstable. An unstable perturbation with a wavenumber of  $a = 0$  would not allow a convection cell to form since a perturbation with wavenumber  $a = 0$  would correspond to a convection cell with infinite width. In practice, the length of a domain would help provide a lower-bound on wavenumbers producing instabilities. For example, in a physical domain of length 5, no perturbations with a width of more than 5 can be present; there physically is not space for those cells to form.

Additionally, we note a trend observed with the free flow marginal stability results; as we relax the boundary conditions (from an impenetrable boundary to free-slip, or from a conductive to an insulating condition), the critical Ra value decreases too. In fact, a system with “free-slip” and insulating conditions at the top and bottom of the domain (i.e., the most relaxed combination of boundary conditions possible) has a critical Raleigh number of  $Ra_m = 0$ , which is achieved at wavenumber  $a = 0$ . This implies that *any* positive Rayleigh number will produce an instability.

Table 3.2: Critical Rayleigh numbers for the single porous layer with different combinations of boundary conditions.

velocity		heat		$Ra_c$	$a_c$
$z = -1$	$z = 0$	$z = -1$	$z = 0$		
IMPR	IMPR	COND	COND	39.4	3.1
IMPR	IMPR	COND	INSUL	27.1	2.3
IMPR	IMPR	INSUL	COND	27.1	2.3
IMPR	IMPR	INSUL	INSUL	12.0	0
IMPR	FREE	COND	COND	27.1	2.3
IMPR	FREE	COND	INSUL	9.8	1.6
IMPR	FREE	INSUL	COND	17.6	1.8
IMPR	FREE	INSUL	INSUL	3.0	0
FREE	IMPR	COND	COND	27.1	2.3
FREE	IMPR	COND	INSUL	17.6	1.8
FREE	IMPR	INSUL	COND	9.8	1.6
FREE	IMPR	INSUL	INSUL	3.0	0
FREE	FREE	COND	COND	12.0	0
FREE	FREE	COND	INSUL	3.0	0
FREE	FREE	INSUL	COND	3.0	0
FREE	FREE	INSUL	INSUL	0.0	0

### 3.2.4 Numerics

For simulations, we return to the original variables in the nondimensional system  $(x, y, z) \in (-L_x, L_x)^2 \times (-1, 0)$ :

$$\begin{cases} \frac{\text{Da}}{\chi \text{Pr}_m} \frac{\partial \mathbf{u}_m}{\partial t_m} + \mathbf{u}_m = -\text{Da} \nabla p_m + \text{Ra}_m T_m \mathbf{k}, \\ \nabla \cdot \mathbf{u}_m = 0, \\ \frac{\partial T_m}{\partial t_m} + \mathbf{u}_m \cdot \nabla T_m = \nabla^2 T_m. \end{cases}$$

Here, the Rayleigh number is the still ‘Rayleigh-Darcy’ number:

$$\text{Ra}_m = \frac{g\beta (T_L - T_U) \text{Da} d_m^3}{\nu \lambda_m} = \frac{g\beta (T_L - T_U) \Pi d_m}{\nu \lambda_m}.$$

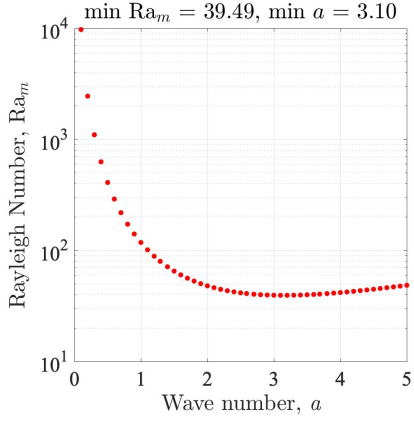
For boundary conditions, we consider conductive, impermeable plates at the top and bottom of the domain (shown in Figure 3.14) with periodic conditions at the left- and right-sides. These conditions correspond to  $\mathbf{u}_m \cdot \mathbf{n} = 0$  and  $T_m = T_U$  at the upper plate with  $\mathbf{u}_m \cdot \mathbf{n} = 0$  and  $T_m = T_L$  at the lower boundary. Once again, we consider  $T_U < T_L$  so that convection is possible. One difference between these conditions and those used in the single layer of fluid case deals with the conditions on the fluid velocity. With Navier-Stokes, we have a second-order equation in space for the velocity; this allows us to enforce two conditions on the velocity at each boundary, namely  $\mathbf{u}_f \cdot \mathbf{n} = 0$  and  $\mathbf{u}_f \cdot \boldsymbol{\tau} = 0$ , written succinctly as  $\mathbf{u}_f = 0$ . However, with the porous medium case, Darcy is a first order equation in space and as a result, we are only able to impose one condition on the velocity. So, we require  $\mathbf{u}_m \cdot \mathbf{n} = 0$ , corresponding to no fluid flowing in the normal direction at the boundary (i.e., no fluid flowing into or through the boundary).

With these conditions, we introduce the FE spaces:

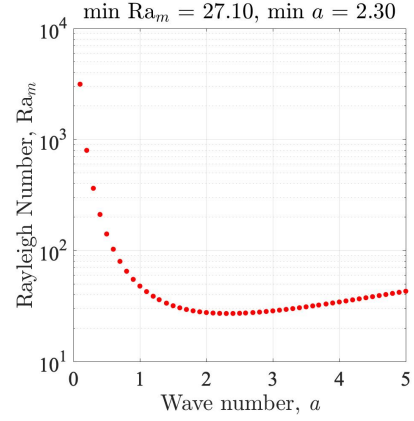
- $V = \{\mathbf{v} \in [H^1(\Omega)]^2 : \mathbf{v} \cdot \mathbf{n} = 0 \text{ at top and bottom} + \text{periodic on left and right}\},$
- $Q = \{q \in L^2(\Omega) : \int_{\Omega} q \, d\mathbf{x} = 0 + \text{periodic on left and right}\} = L_0^2(\Omega),$
- $\Psi = \{\psi \in H^1(\Omega) : \psi = 1 \text{ on bottom, } \psi = 0 \text{ on top} + \text{periodic on left and right}\}.$

To get the variational form to solve Darcy, we take the divergence of both sides of the equation:

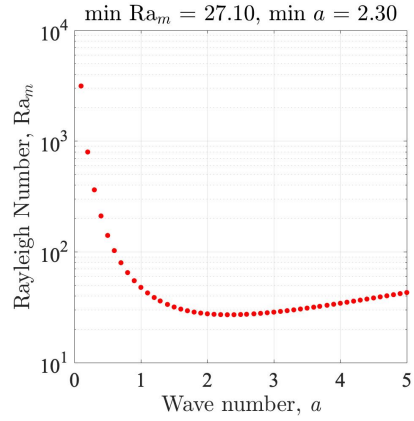
$$\nabla \cdot \left[ \frac{\text{Da}}{\chi \text{Pr}_m} \frac{\partial \mathbf{u}_m}{\partial t_m} + \mathbf{u}_m \right] = -\nabla \cdot [\text{Da} \nabla p_m + \text{Ra}_m T_m \mathbf{k}].$$



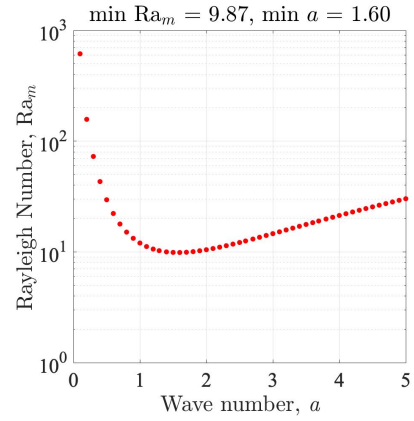
(a) IMPR, IMPR, COND, COND.



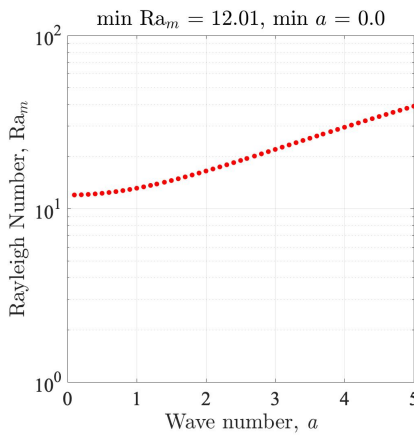
(b) IMPR, IMPR, COND, INSUL.



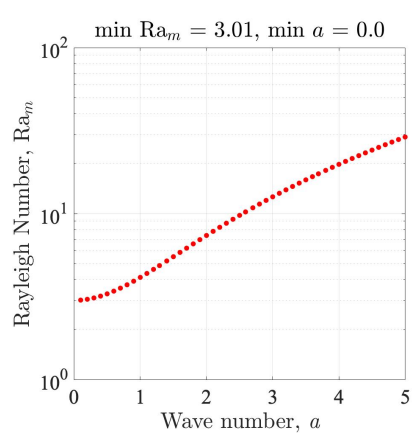
(c) IMPR, FREE, COND, COND.



(d) IMPR, FREE, COND, INSUL.



(e) FREE, FREE, COND, COND.



(f) FREE, FREE, COND, INSUL.

Figure 3.15: Marginal stability curves for a single layer of a porous medium with various boundary conditions, noted beneath each plot. The conditions are for the velocity at  $z = -1$  and  $z = 0$ , followed by the conditions on  $\theta_m$  at  $z = -1$  and  $z = 0$ .

The LHS goes to zero with the incompressibility condition  $\nabla \cdot \mathbf{u}_m = 0$ , and we are left with the right-hand side only,

$$0 = -\nabla \cdot [\text{Da} \nabla p_m + \text{Ra}_m T_m \mathbf{k}] .$$

In this form, we multiply by the test function  $q \in Q$  and integrate over the domain. Integration by parts allows us to rewrite this as:

$$\int_{\Omega} \text{Da} \nabla p_m \cdot \nabla q \, d\mathbf{x} + \int_{\partial\Omega} (-\text{Da} \nabla p_m \cdot \mathbf{n}) q \, dS - \int_{\Omega} (\text{Ra}_m T_m \mathbf{k}) \cdot \nabla q \, d\mathbf{x} + \int_{\partial\Omega} (\text{Ra}_m T_m \mathbf{k} \cdot \mathbf{n}) q \, dS = 0 .$$

We combine the boundary terms, and make the substitution noted:

$$\int_{\Omega} \text{Da} \nabla p_m \cdot \nabla q \, d\mathbf{x} - \int_{\Omega} (\text{Ra}_m T_m \mathbf{k}) \cdot \nabla q \, d\mathbf{x} + \int_{\partial\Omega} \underbrace{(-\text{Da} \nabla p_m + \text{Ra}_m T_m \mathbf{k}) \cdot \mathbf{n}}_{= \frac{\text{Da}}{\chi \text{Pr}_m} \frac{\partial \mathbf{u}_m}{\partial t_m} + \mathbf{u}_m} q \, dS = 0 .$$

Since  $\mathbf{u}_m \cdot \mathbf{n} = 0$  on the top and bottom boundaries and we enforce periodic at the left and right of the domain, the boundary integral goes to zero. This leaves us with the variational form below, where we solve for  $p_m \in V$  (given a  $T_m \in \Psi$ ):

$$\int_{\Omega} \text{Da} \nabla p_m \cdot \nabla q \, d\mathbf{x} - \int_{\Omega} (\text{Ra}_m T_m \mathbf{k}) \cdot \nabla q \, d\mathbf{x} = 0 \quad \forall q \in Q .$$

Then, we can then find the velocity  $\mathbf{u}_m^{(n+1)}$  using the previous velocity  $\mathbf{u}_m^{(n)}$  and the just-solved-for pressure  $p_m^{(n+1)}$ :

$$\begin{aligned} \frac{\text{Da}}{\text{Pr}_m \chi} \frac{\mathbf{u}_m^{(n+1)} - \mathbf{u}_m^{(n)}}{\Delta t} + \mathbf{u}_m^{(n+1)} &= -\text{Da} \nabla p_m^{(n+1)} + \text{Ra}_m T_m^{(n)} \mathbf{k} , \\ \implies \mathbf{u}_m^{(n+1)} &= \left[ -\text{Da} \nabla p_m^{(n+1)} + \text{Ra}_m T_m^{(n)} \mathbf{k} + \frac{\text{Da}}{\text{Pr}_m \chi \Delta t} \mathbf{u}_m^{(n)} \right] \left( \frac{\text{Pr}_m \chi \Delta t}{\text{Da} + \text{Pr}_m \chi \Delta t} \right) . \end{aligned} \quad (3.21)$$

using Backward Euler for the time-derivative. Backward Euler is the simplest choice of time-integrators; however, we could substitute in a higher-order integrator if needed.

To simulate the system, we begin by perturbing the conductive temperature with seeded white-noise  $\epsilon_{mag} := \epsilon_{mag}(\mathbf{x})$  (the magnitude of this perturbation is set at  $1.0 \times 10^{-8}$ ):

$$\left( \mathbf{u}_m^{(0)}, T_m^{(0)} \right) = (\mathbf{0}, -y) + \epsilon_{mag} .$$

We note that perturbing the pressure is not necessary since the variational form to solve for pressure does not require a previous pressure value.

So, given  $T_m^{(n)} \in \Psi$ , we find  $(p_m^{(n+1)}, T_m^{(n+1)}) \in Q \times \Psi$  such that

$$\int_{\Omega} \text{Da} \nabla p_m^{(n+1)} \cdot \nabla q \, d\mathbf{x} - \int_{\Omega} \left( \text{Ra}_m T_m^{(n)} \mathbf{k} \right) \cdot \nabla q \, d\mathbf{x} = 0, \quad (3.22)$$

for all  $q \in Q$ , and

$$\int_{\Omega} \frac{\partial T_m^{(n+1)}}{\partial t_m} \psi \, d\mathbf{x} + \int_{\Omega} \mathbf{u}_{\mathbf{m}}^{(n+1)} \cdot \nabla T_m^{(n+1)} \psi \, d\mathbf{x} + \int_{\Omega} \nabla T_m^{(n+1)} \cdot \nabla \psi \, d\mathbf{x} = 0 \quad (3.23)$$

for all  $\psi \in \Psi$ , where the velocity  $\mathbf{u}_{\mathbf{m}}^{(n+1)}$  is found with (3.21) *before* solving for  $T_m^{(n+1)}$ .

Like the fluid case, we write these problems in a form so that they are uncoupled and may be solved sequentially. This allows us to use linear methods to solve the systems rather than using more computationally expensive methods to solve the coupled problem. Additionally, the uncoupled nature of our problem does not require us to create any ‘new’ code to simulate the fluid-temperature system; we can use a Darcy solver for the velocity and a temperature solver for the advection-diffusion equation, both with some minor adjustments.

Similar to the fluid case as well, we are able to find the stream function  $\phi$ , solving

$$\int_{\Omega} \left[ \nabla \phi^{(n+1)} \cdot \nabla \varphi - \varphi \left( \nabla \times \mathbf{u}_{\mathbf{m}}^{(n+1)} \right) \right] d\mathbf{x} = 0 \quad (3.24)$$

for all  $\varphi \in \Phi$ , where

- $\Phi = \{ \varphi \in H^1(\Omega) : \varphi = 0 \text{ on top and bottom} + \text{periodic on left and right} \}$ .

With our simulations, we have the algorithm:

---

**Algorithm 2:** Solving Darcy-Heat system

---

**Result:**  $\mathbf{u}_m^{(N)}, p_m^{(N)}, T_m^{(N)}, \phi^{(N)}$ .

Use initial conditions:  $(\mathbf{u}_m^{(0)}, T_m^{(0)}) = (\mathbf{0}, -y) + \epsilon_{mag}$ .

**for**  $n = 0; n < N; n++$

**do**

With  $T_m^{(n)}$ , solve (3.22) for  $p_m^{(n+1)}$ .

With  $p_m^{(n+1)}, T_m^{(n)}, \mathbf{u}_m^{(n)}$ , update  $\mathbf{u}_m^{(n+1)}$  with (3.21).

With  $\mathbf{u}_m^{(n+1)}$ , solve (3.23) for  $T_m^{(n+1)}$ .

With  $\mathbf{u}_m^{(n+1)}$ , solve (3.24) for  $\phi^{(n+1)}$ .

**end**

---

Unlike the simulations with the single layer of fluid, we use  $\mathcal{P}_2$  elements for pressure in the Darcy-Heat solver since pressure plays a larger role in convection here. With the velocity as a by-product of the pressure, any errors in the pressure immediately propagate to the velocity. To remedy this potential issue, using  $\mathcal{P}_2$  elements is a natural solution by increasing the degrees of freedom, and hopefully, giving more accurate approximations to  $p_m$  and  $\mathbf{u}_m$ . Also, our choice of element-type for velocity is almost inconsequential since we never solve a system for  $\mathbf{u}_m$ ; the velocity is only used in solving for the temperature field and streamlines.

To validate our Darcy solver, we perform a convergence study. Once again, we use the method of manufactured solutions with

$$\mathbf{u}_m^{ex} = \left( \cos(\beta x), z \beta \sin(\beta x) \right), \quad p_m^{ex} = -\frac{1}{\beta} \sin(\beta x) + \cos(\pi(2z - 1)),$$

where  $\beta = \pi/2$  enforces periodic solutions in  $x$  and temperature profile is chosen to be

$$T_m = z \beta \sin(\beta x) - 2\pi \sin(\pi(2z - 1)).$$

Instead of the dynamic equations, we consider the steady-state Darcy equation (without the Darcy number or Rayleigh number since their value should not affect implementing the code) and its variational form:

$$\mathbf{u}_m = -\nabla p_m + T_m \mathbf{k} \implies \int_{\Omega} [\nabla p_m - T_m \mathbf{k}] \cdot \nabla q \, d\mathbf{x} = 0 \quad \forall q \in Q.$$

At the boundaries of  $\Omega$ , we enforce  $p_m = p_m^{ex}$ . Then, solving for  $p_m$  allows us to determine the Darcy velocity  $\mathbf{u}_m = -\nabla p_m + T_m \mathbf{k}$ .

To quantify the errors, we plot the  $L^2$  error of each quantity with  $\mathcal{P}_2$  elements for pressure and then  $\mathcal{P}_1$  and  $\mathcal{P}_2$  elements for velocity. Above, we noted that the choice of element-type for velocity was inconsequential; our plot in Figure 3.16 confirms this. The error for velocity as  $\mathcal{P}_1$  and  $\mathcal{P}_2$  elements has the same slope of 2 in the log-log plot in addition to similar timing for each case. With these slopes, we have

$$\|\mathbf{u}_m^{ex} - \mathbf{u}_m\|_{L^2} \sim \mathcal{O}(\Delta x^2), \quad \|p_m^{ex} - p_m\|_{L^2} \sim \mathcal{O}(\Delta x^3),$$

where  $\Delta x$  corresponds to the length of the largest element of the mesh. This result holds for  $\mathcal{P}_2$  elements for pressure and both  $\mathcal{P}_1$  and  $\mathcal{P}_2$  elements for velocity.

The results in Figure 3.16 are almost the opposite of those we found for the single layer of fluid case with Figures 3.6 and 3.7 where the  $L^2$  error for  $\mathbf{u}_f$  had slope 3 and the error for  $p_f$  had slope 2. However, this is expected. In solving Navier-Stokes, we solved for  $\mathbf{u}_f$  and found  $p_f$  as a by-product of the velocity. With our Darcy solver, we are solving for the pressure  $p_m$  while the velocity  $\mathbf{u}_m$  is now the by-product of the pressure. With our FEM simulations and our choice of element types, the variable we solve for has third-order convergence while the variable we find as a by-product has second-order convergence.

For our simulations of convection with fluid in a single layer of a porous medium, we will use  $\mathcal{P}_2$  elements for both velocity and pressure. While the choice between  $\mathcal{P}_1$  and  $\mathcal{P}_2$  elements for velocity in this single layer case does not matter, the choice *will* matter in the coupled case.

### 3.2.5 Quantifying convection

To analyze the energy of the system, we look to the system of the perturbed variables,  $\mathbf{v}_m$ ,  $\pi_m$ ,  $\theta_m$  (perturbations to velocity, pressure, and temperature, respectively):

$$\begin{cases} \frac{\text{Da}}{\chi \text{Pr}_m} \frac{\partial \mathbf{v}_m}{\partial t_m} + \mathbf{v}_m = -\text{Da} \nabla \pi_m + \text{Ra}_m \theta_m \mathbf{k}, \\ \nabla \cdot \mathbf{v}_m = 0, \\ \frac{\partial \theta_m}{\partial t_m} + \mathbf{v}_m \cdot \nabla \theta_m = \nabla^2 \theta_m + w_m. \end{cases}$$

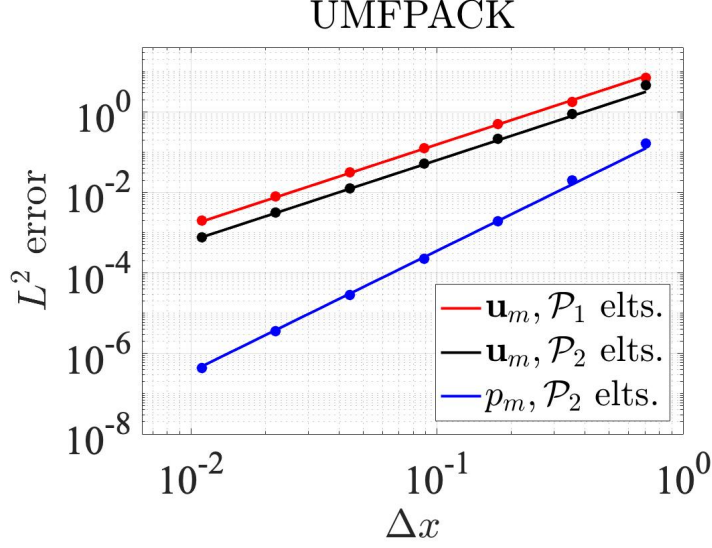


Figure 3.16: Convergence for the steady Darcy problem with  $\mathcal{P}_2$  elements for pressure,  $\mathcal{P}_1$  and  $\mathcal{P}_2$  for the velocity, and UMFPACK as the linear solver. The  $L^2$  errors are plotted as the max edge size,  $\Delta x$  on the mesh, is varied. The comparison lines in each plot have slopes of 2 for the red and black lines (for velocity) and 3 for the blue line (for pressure).

We then take the inner product of the Darcy and advection-diffusion equations with  $\mathbf{v}$  and  $\theta_f$ , respectively. We integrate by parts and apply the boundary conditions to arrive at the energies of each equation:

$$\begin{cases} \frac{1}{2\chi \text{Pr}_m} \frac{d}{dt_m} \|\mathbf{v}_m\|^2 = -\frac{1}{\text{Da}} \|\mathbf{v}_m\|^2 + \frac{\text{Ra}_m}{\text{Da}} \int_{\Omega} \theta_m \mathbf{k} \cdot \mathbf{v}_m \, d\mathbf{x}, \\ \frac{1}{2} \frac{d}{dt_m} \|\theta_m\|^2 = -\|\nabla \theta_m\|^2 + \int_{\Omega} \theta_m w_m \, d\mathbf{x}, \end{cases}$$

where  $\text{Ra}_m$  is still the ‘Rayleigh-Darcy’ number defined above.

To quantify the energy of the system, we define the energy as:

$$2E_m(t_m) = \frac{1}{\chi \text{Pr}_m} \|\mathbf{v}_m\|^2 + \|\theta_m\|^2,$$

with the change in energy as

$$\frac{dE_m}{dt_m} = -\mathcal{D} + \mathcal{I}$$

where the definite and indefinite terms,  $\mathcal{D}$  and  $\mathcal{I}$ , are

$$\mathcal{D} = \frac{1}{\text{Da}} \|\mathbf{v}_m\|^2 + \|\nabla\theta_m\|^2,$$

$$\mathcal{I} = \left( \frac{\text{Ra}_m}{\text{Da}} + 1 \right) \int_{\Omega} \theta_m w_m d\mathbf{x}.$$

Similar to the previous section dedicated to the single layer of fluid, we are also interested in determining the Nusselt number in these simulations as well. The definitions of Nu from (3.11)–(3.14) and the scaled versions of the energy and Nusselt number from (3.15) still apply in this section as well. While the energy was derived as a non-physical quantity, we once again show in the results section that the energy and Nusselt number approximate each other nicely when scaled appropriately.

### 3.2.6 Results

For the discretized domain, we use a mesh similar to the one used in the fluid case shown with the schematic in Figure 3.3, albeit on  $z \in (-1, 0)$  instead of  $z \in (0, 1)$ . Additionally, instead of the 10 elements/ unit distance as shown in the schematic, we use 20 elements/ unit distance for our simulations.

In Figure 3.17, we plot the energy and change in energy of systems with various Darcy numbers. For the combination of boundary conditions chosen, the critical Rayleigh number is 39.4. With the  $\text{Ra}_m = 35$  simulation, we see the perturbations damp to 0, as  $E_m(t_m)$  and  $dE_m/dt_m$  are zero for the entirety of the simulation. For simulations run with  $\text{Ra}_m > 39.4$ , we see convection cells form, evident in the energy of the system growing, and achieve a steady-state, evident with  $dE_m/dt_m$  returning to 0 after a spike. We also note the close agreement with the Nusselt number and the energy, observed in Figure 3.17 and then with their scaled counterparts in Figure 3.18. The scaled Nusselt and energy profiles for the porous medium are much closer than the results obtained from the single layer of fluid. While we have no definitive conclusion about why this occurs, we speculate it is related to the nonlinearities present in governing system for the fluid layer or perhaps a serendipitous choice of parameter regimes.

We also plot the streamlines and temperature profile for a cases run with  $\text{Ra}_m = 50$  and  $\text{Ra}_m = 75$ , shown in Figures 3.19 and 3.20. With these simulations, we note that as the Rayleigh number is increased, the temperature profiles develop a more ‘plume-like’ shape (also noted in the fluid case) as well as an increase in the energy of the system.

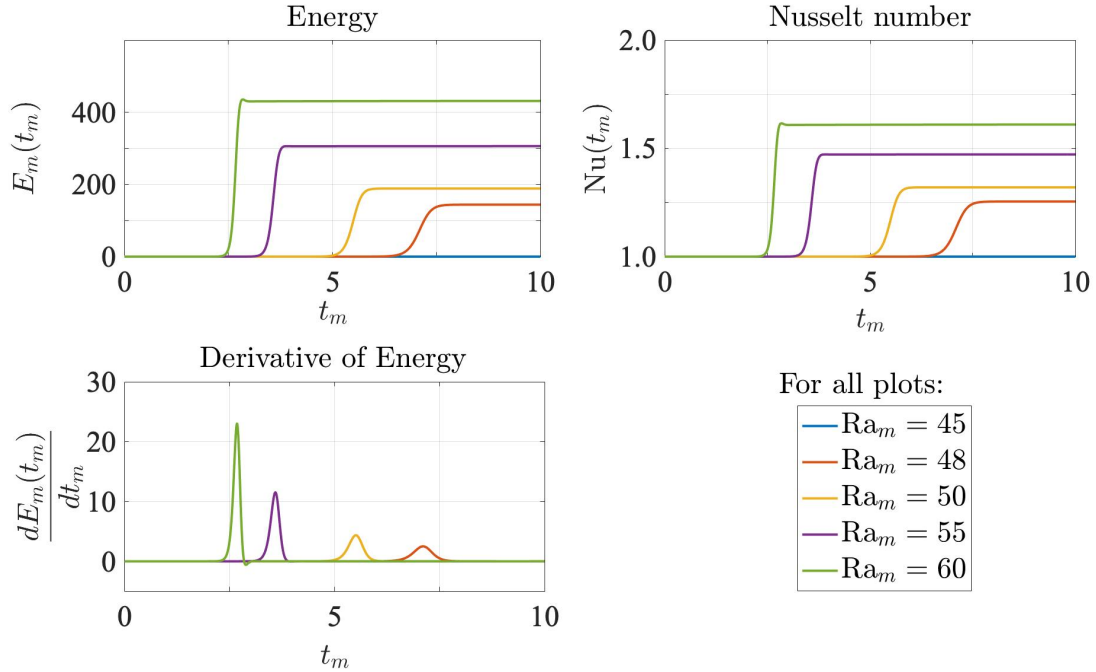


Figure 3.17: Energy of the systems and the change in energy for various  $Ra_m$  values. The mesh is on  $(x, z) \in [-2.5, 2.5] \times [-1, 0]$  with 20 elements/unit distance on the mesh, and  $Da = 10^{-5}$ ,  $\Delta t = .01$ ,  $Pr_m = .7$ ,  $\chi = .3$ .

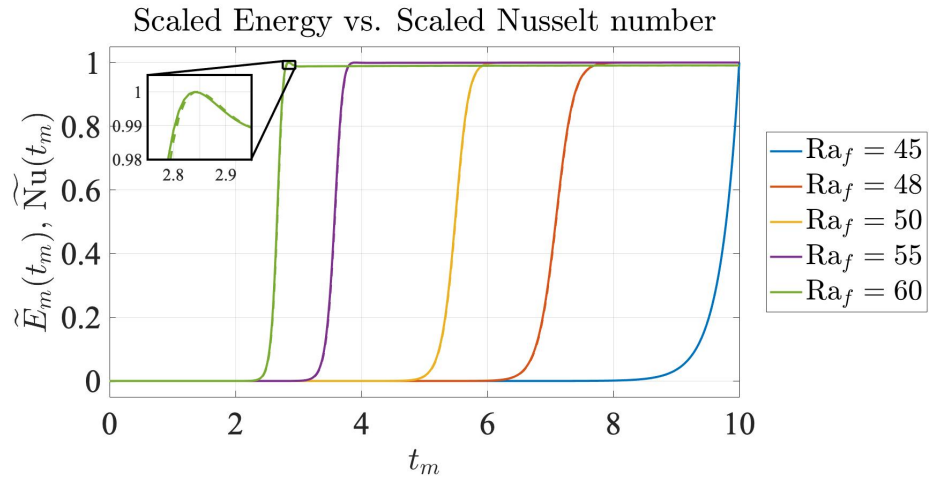
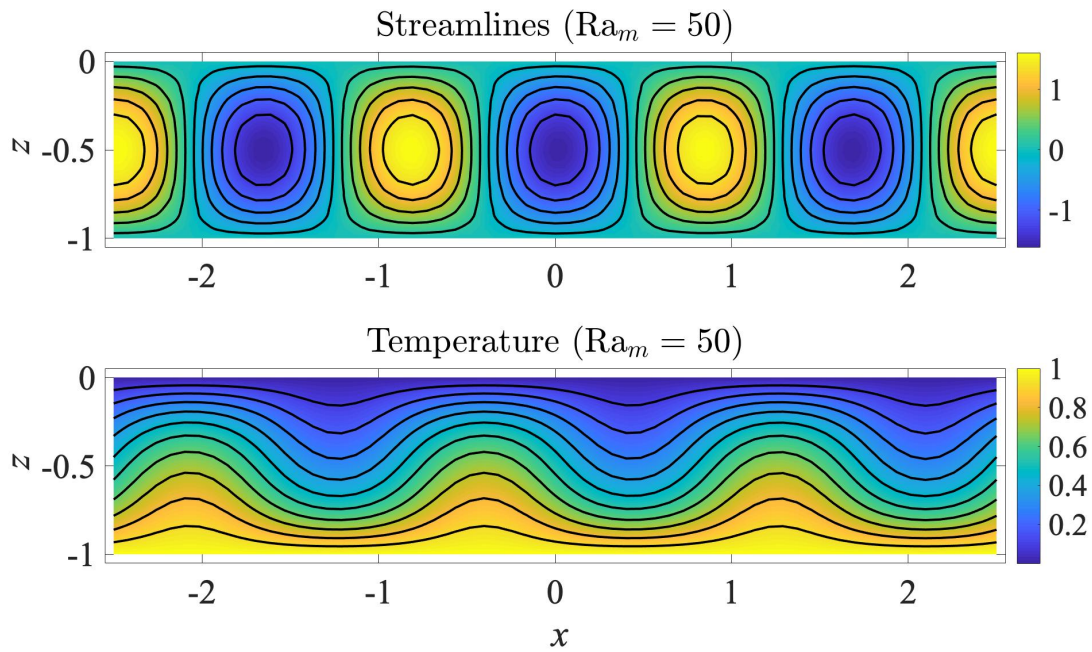
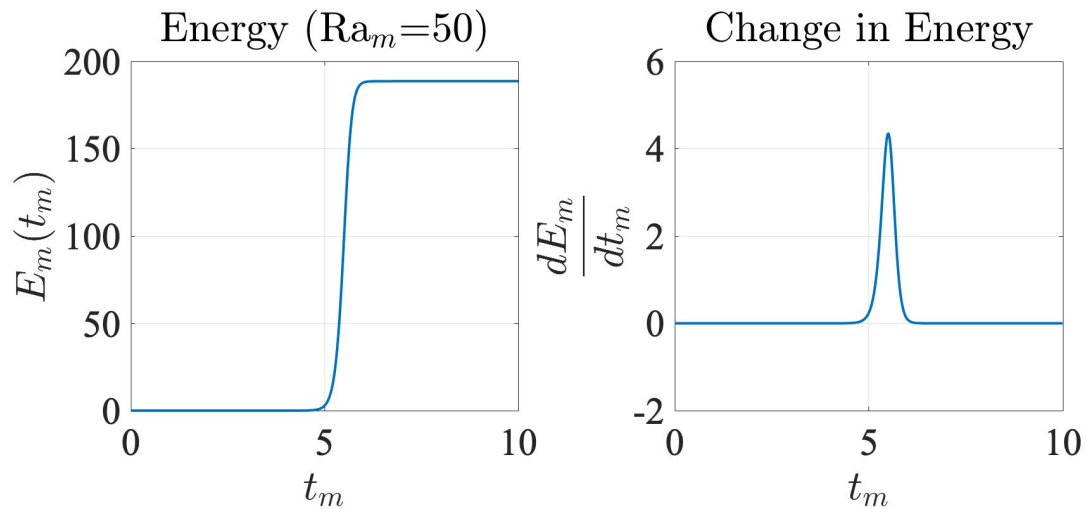


Figure 3.18: Scaled energy and scaled Nusselt number of the systems for various  $Ra_m$  values. The solid lines represent the scaled Nusselt number, the dashed are the scaled energy. The mesh is on  $(x, z) \in [-2.5, 2.5] \times [-1, 0]$  with 20 elements/unit distance on the mesh, and  $Da = 10^{-5}$ ,  $\Delta t = .01$ ,  $Pr_m = .7$ ,  $\chi = .3$ .

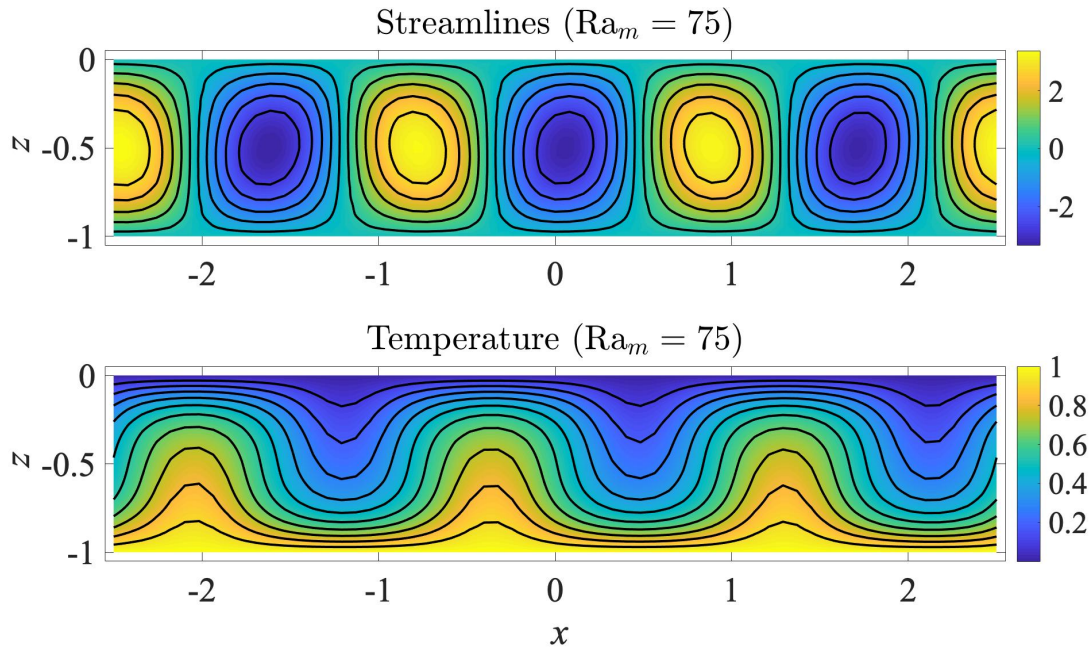


(a) Streamlines and temperature profiles at  $t = 10$ . Positive isolines circulate in the positive direction with negative isolines circulating in the negative direction.

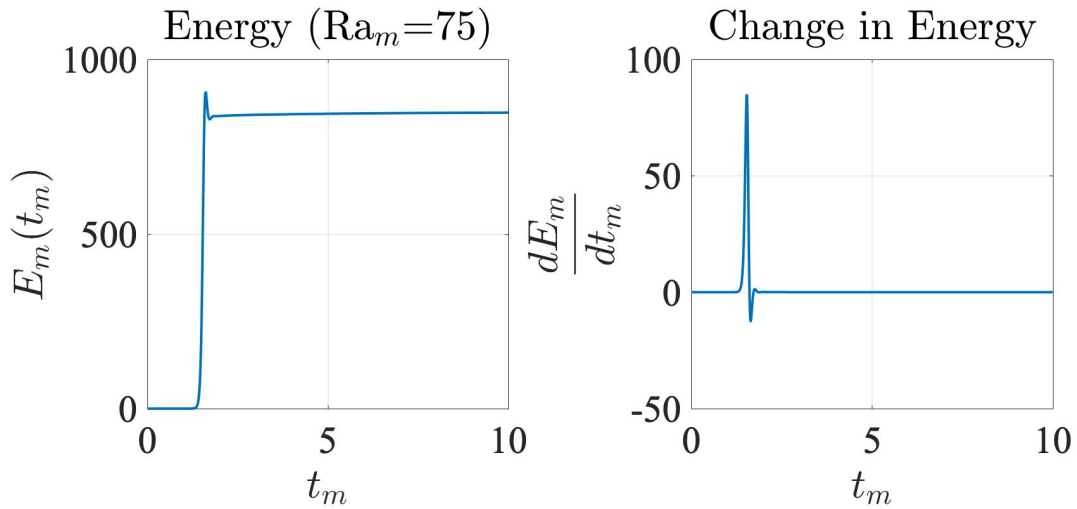


(b) Energy and change in energy.

Figure 3.19: Simulation with  $Ra_m = 50$ . The mesh is on  $(x, z) \in [-2.5, 2.5] \times [-1, 0]$  with 20 elements/unit distance on the mesh, and  $Da = 10^{-5}$ ,  $\Delta t = .01$ ,  $Pr_m = .7$ ,  $\chi = .3$ .



(a) Streamlines and temperature profiles at  $t = 10$ . Positive isolines circulate in the positive direction with negative isolines circulating in the negative direction.



(b) Energy and change in energy.

Figure 3.20: Simulation with  $Ra_m = 75$ . The mesh is on  $(x, z) \in [-2.5, 2.5] \times [-1, 0]$  with 20 elements/unit distance on the mesh, and  $Da = 10^{-5}$ ,  $\Delta t = .01$ ,  $Pr_m = .7$ ,  $\chi = .3$ .

### 3.3 Coupled numerics

In Chapter 2, we conducted linear and nonlinear stability analyses for convection in a fluid overlying a saturated porous medium. Although we discussed the onset of convection in detail there, our streamlines and temperature profiles were found using eigenvalues only— there were no numerical simulations run. Now, armed with numerical methods to simulate convection in the two *single layer cases* (from the past two sections), we create a method to simulate convection in the *coupled case*.

As of now, there has yet to be a numerical investigation of the evolutionary Navier-Stokes-Darcy-Boussinesq system— i.e., Navier-Stokes, Darcy, and the advection-diffusion equations with the inclusion of their time derivatives, all coupled together. A very recent article [101] by Zhang, Shan, and Hou used a FEM to study the stationary system and investigated the well-posedness of their Finite Element approximation. Other works have used numerical methods as well to study convection in superposed fluid-porous layers [1, 90, 96], albeit with Brinkman instead of Darcy, or Stokes instead of its nonlinear counterpart. So, to the best of our knowledge, we are the first to simulate the evolutionary coupled system, and as a result, we present a novel numerical scheme in this section.

With the full system (i.e., not the perturbations to the steady-state), we have the nondimensional system and interface conditions obtained with nondimensional scalings and numbers taken from the *porous medium scalings* from Chapter 2:

$$\left\{ \begin{array}{l} \frac{1}{\text{Pr}_m} \frac{\partial \mathbf{u}_f}{\partial t} + (\mathbf{u}_f \cdot \nabla) \mathbf{u}_f = \nabla \cdot \mathbb{T}(\mathbf{u}_f, p_f) + \frac{\text{Ra}_m}{\text{Da}} (T_f - T_0) \mathbf{k}, \\ \nabla \cdot \mathbf{u}_f = 0, \\ \frac{\partial T_f}{\partial t} + \text{Pr}_m \mathbf{u}_f \cdot \nabla T_f = \epsilon_T \nabla^2 T_f, \end{array} \right.$$

for  $(x, y, z, t) \in \{\mathbb{R}^2 \times (0, d_f/d_m) \times (0, \infty)\}$ ,

$$\left\{ \begin{array}{l} \frac{\text{Da}}{\text{Pr}_m \chi} \frac{\partial \mathbf{u}_m}{\partial t} + \mathbf{u}_m = -\text{Da} \nabla p_m + \text{Ra}_m (T_m - T_L) \mathbf{k}, \\ \nabla \cdot \mathbf{u}_m = 0, \\ \varrho \frac{\partial T_m}{\partial t} + \text{Pr}_m \mathbf{u}_m \cdot \nabla T_m = \nabla^2 T_m, \end{array} \right.$$

for  $(x, y, z, t) \in \{\mathbb{R}^2 \times (-1, 0) \times (0, \infty)\}$ , and

$$\left\{ \begin{array}{l} T_f = T_m, \\ \epsilon_T \nabla T_f \cdot \mathbf{n} = \nabla T_m \cdot \mathbf{n}, \\ \mathbf{u}_f \cdot \mathbf{n} = \mathbf{u}_m \cdot \mathbf{n}, \\ -\boldsymbol{\tau} \cdot \mathbb{T}(\mathbf{u}_f, p_f) \mathbf{n} = \frac{\alpha_{BJSJ}}{\sqrt{Da}} (\boldsymbol{\tau} \cdot \mathbf{u}_f), \\ -\mathbf{n} \cdot \mathbb{T}(\mathbf{u}_f, p_f) \mathbf{n} + \Psi_L |\mathbf{u}_f|^2 = p_m, \end{array} \right.$$

for  $(x, y, 0, t) \in \{\mathbb{R}^2 \times (z = 0) \times (0, \infty)\}$ .

Similar to the single layer cases, we will decouple the equations and create linear systems to solve by lagging certain terms; these terms will be noted as they are presented. Next, we detail how the variational forms are obtained. Additionally, with this section, we return to the following notation for vector-valued functions  $\mathbf{f}$  and  $\mathbf{g}$  and matrix-valued functions  $\mathbf{A}$  and  $\mathbf{B}$ :

$$(\mathbf{f}, \mathbf{g})_j = \int_{\Omega_j} \mathbf{f} \cdot \mathbf{g} d\Omega_j, \quad \langle \mathbf{A}, \mathbf{B} \rangle_j = \int_{\Omega_j} \mathbf{A} : \mathbf{B} d\Omega_j, \quad \|\mathbf{f}\|_j^2 = (\mathbf{f}, \mathbf{f})_j, \quad |\mathbf{f}|^2 = \mathbf{f} \cdot \mathbf{f},$$

for domains  $j \in \{f, m\}$  when we take inner-products below.

### 3.3.1 Heat

First, we deal with the advection-diffusion equations (ADEs). In their respective domains, they are:

$$\begin{aligned} \text{in } \Omega_f : \quad & \frac{\partial T_f}{\partial t} + \text{Pr}_m \mathbf{u}_f \cdot \nabla T_f = \epsilon_T \nabla^2 T_f, \\ \text{in } \Omega_m : \quad & \varrho \frac{\partial T_m}{\partial t} + \text{Pr}_m \mathbf{u}_m \cdot \nabla T_m = \nabla^2 T_m. \end{aligned}$$

With how similar they look, we choose to write them as a single equation, governing how the temperature of the entire domain evolves:

$$\text{in } \Omega : \quad \delta_1 \frac{\partial T}{\partial t} + \text{Pr}_m \mathbf{u} \cdot \nabla T = \delta_2 \nabla^2 T$$

where  $T$  is the temperature for the whole domain,  $\mathbf{u}$  is the velocity field for the entire domain, and  $\delta_i$  are the domain-based constants:

$$\delta_1 = \begin{cases} 1 & \text{in } \Omega_f \\ \varrho & \text{in } \Omega_m \end{cases}, \quad \delta_2 = \begin{cases} \epsilon_T & \text{in } \Omega_f \\ 1 & \text{in } \Omega_m \end{cases}. \quad (3.25)$$

These constants are chosen to recover their respective equations in the sub-domains *and* enforce the interface conditions. By writing the two ADEs as a single equation, we do not have to describe the interface at all; the interface is taken care of with how we have  $\delta_1, \delta_2$  defined. And although there can be discontinuities in the  $\delta_i$  coefficients (discontinuities occur if  $\varrho \neq 1$  or  $\epsilon_T \neq 1$ ) at the interface, there is no discontinuity in the temperature profiles across the interface, as the  $\delta_i$  coefficients help enforce continuity of temperature and heat flux at the interface.

With  $\psi$  as a test function in a currently undefined FE space  $\Psi$ , the variational form of the ADE is:

$$\left( \delta_1 \frac{\partial T}{\partial t}, \psi \right)_{\Omega} + \text{Pr}_m (\mathbf{u} \cdot \nabla T, \psi)_{\Omega} + (\delta_2 \nabla T, \nabla \psi)_{\Omega} = 0 \quad \forall \psi \in \Psi.$$

Once we have all the variational forms, we will introduce the appropriate FE spaces.

### 3.3.2 Fluid region

In the fluid layer, we have the weak form of Navier-Stokes with the test function  $\mathbf{v}_f \in V$ :

$$\left( \frac{1}{\text{Pr}_m} \frac{\partial \mathbf{u}_f}{\partial t} + (\mathbf{u}_f \cdot \nabla) \mathbf{u}_f, \mathbf{v}_f \right)_f - \left( 2 \nabla \cdot \mathbb{D}(\mathbf{u}_f) - \nabla p_f + \frac{\text{Ra}_m}{\text{Da}} (T_f - T_0) \mathbf{k}, \mathbf{v}_f \right)_f = 0 \quad \forall \mathbf{v}_f \in V.$$

Next, we use integration by parts, as well as the decomposition  $\mathbf{v}_f = (\mathbf{v}_f \cdot \mathbf{n}) \mathbf{n} + (\mathbf{v}_f \cdot \boldsymbol{\tau}) \boldsymbol{\tau}$ , to obtain:

$$\begin{aligned} & \left( \frac{1}{\text{Pr}_m} \frac{\partial \mathbf{u}_f}{\partial t} + (\mathbf{u}_f \cdot \nabla) \mathbf{u}_f, \mathbf{v}_f \right)_f + 2 \langle \mathbb{D}(\mathbf{u}_f), \mathbb{D}(\mathbf{v}_f) \rangle_f - (p_f, \nabla \cdot \mathbf{v}_f)_f + \frac{\text{Ra}_m}{\text{Da}} (T_f - T_0, \mathbf{v}_f \cdot \mathbf{k})_f \\ & + \int_{\Gamma_i} p_f \mathbf{v}_f \cdot \mathbf{n} \, d\Gamma_i - \int_{\Gamma_i} 2 \mathbf{n} \cdot \mathbb{D}(\mathbf{u}_f) \mathbf{n} (\mathbf{v}_f \cdot \mathbf{n}) \, d\Gamma_i - \int_{\Gamma_i} 2 \boldsymbol{\tau} \cdot \mathbb{D}(\mathbf{u}_f) \mathbf{n} (\mathbf{v}_f \cdot \boldsymbol{\tau}) \, d\Gamma_i = 0. \end{aligned}$$

We then combine the interface conditions with terms involving  $\mathbf{v}_f \cdot \mathbf{n}$ , which allows us to apply the interface conditions, producing the variational form (now with the incompressibility condition):

$$\begin{aligned} & \left( \frac{1}{\text{Pr}_m} \frac{\partial \mathbf{u}_f}{\partial t} + (\mathbf{u}_f \cdot \nabla) \mathbf{u}_f, \mathbf{v}_f \right)_f + 2 \langle \mathbb{D}(\mathbf{u}_f), \mathbb{D}(\mathbf{v}_f) \rangle_f - (p_f, \nabla \cdot \mathbf{v}_f)_f + (\nabla \cdot \mathbf{u}_f, q_f)_f \\ & + \frac{\text{Ra}_m}{\text{Da}} (T_f - T_0, \mathbf{v}_f \cdot \mathbf{k})_f + \int_{\Gamma_i} p_m (\mathbf{v}_f \cdot \mathbf{n}) \, d\Gamma_i + \int_{\Gamma_i} \frac{\alpha_{BJSJ}}{\sqrt{\text{Da}}} (\mathbf{u}_f \cdot \boldsymbol{\tau}) (\mathbf{v}_f \cdot \boldsymbol{\tau}) \, d\Gamma_i = 0. \end{aligned}$$

The interface conditions here allow the porous medium to exert its influence on the fluid region via the  $p_m$  term.

### 3.3.3 Porous region

For the fluid in the porous medium, we begin in a similar manner to the single layer case, but taking the divergence of Darcy, which yields

$$0 = \nabla \cdot (-\text{Da} \nabla p_m + \text{Ra}_m (T_m - T_L) \mathbf{k}).$$

We take the inner-product of the above equation with the test function  $q_m$  and integrate by parts:

$$\begin{aligned} & \text{Da} (\nabla p_m, \nabla q_m)_m - \text{Ra}_m ((T_m - T_L) \mathbf{k}, \nabla q_m)_m \\ & + \int_{\Gamma_i} (-\text{Da} \nabla p_m + \text{Ra}_m (T_m - T_L) \mathbf{k}) \cdot \mathbf{n} q_m d\Gamma_i \quad \forall q_m \in Q. \end{aligned}$$

From here, we note that the term inside the parentheses of the integral along interface is the RHS of Darcy. We substitute in the LHS of Darcy for it, and apply the interface condition  $\mathbf{u}_f \cdot \mathbf{n} = \mathbf{u}_m \cdot \mathbf{n}$ . This gives us the variational form:

$$\text{Da} (\nabla p_m, \nabla q_m)_m - \text{Ra}_m ((T_m - T_L) \mathbf{k}, \nabla q_m)_m + \int_{\Gamma_i} \left[ \frac{\text{Da}}{\text{Pr}_m \chi} \frac{\partial \mathbf{u}_f}{\partial t} + \mathbf{u}_f \right] \cdot \mathbf{n} q_m d\Gamma_i = 0.$$

With the above equation, we solve for  $p_m$ . With  $p_m$  and  $T_m$ , we are able to determine the Darcy velocity  $\mathbf{u}_m$ .

### 3.3.4 Simulations with the Finite Element Method

We introduce the following FE spaces:

- $V_f = \{\mathbf{v}_f \in [H^1(\Omega_f)]^2 : \mathbf{v}_f = \mathbf{0} \text{ at top} + \text{periodic on left and right}\},$
- $Q_f = \{q_f \in L^2(\Omega_f) : \int_{\Omega_f} q_f d\mathbf{x} = 0 + \text{periodic on left and right}\} = L_0^2(\Omega_f),$
- $V_m = \{\mathbf{v}_m \in [H^1(\Omega_m)]^2 : \mathbf{v}_m \cdot \mathbf{n} = 0 \text{ at bottom} + \text{periodic on left and right}\},$
- $Q_m = \{q_m \in L^2(\Omega_m) : \int_{\Omega_m} q_m d\mathbf{x} = 0 + \text{periodic on left and right}\} = L_0^2(\Omega_m),$
- $V = \{\mathbf{v} \in [H^1(\Omega)]^2 : \mathbf{v} = \mathbf{0} \text{ at top}, \mathbf{v} \cdot \mathbf{n} = 0 \text{ at bottom} + \text{periodic on left and right}\},$
- $\Psi = \{\psi \in H^1(\Omega) : \psi = 1 \text{ on bottom}, \psi = 0 \text{ on top} + \text{periodic on left and right}\}.$

These all resemble their single layer counterparts with the exception of restrictions on the interface of the domain; we no longer require  $\mathbf{v}_f = \mathbf{0}$  in  $V_f$  or  $\mathbf{v}_m \cdot \mathbf{n} = 0$  in  $V_m$  at the interface since those restrictions have been lifted from  $\mathbf{u}_f, \mathbf{u}_m$  thanks to the interface conditions. Also, we have two spaces spanning the entire domain,  $V$  and  $\Psi$ . The  $V$  space will be reserved for the velocity field of the entire domain, and the space  $\Psi$  is for the temperature field over  $\Omega$  since we now have it written as a problem over the whole domain.

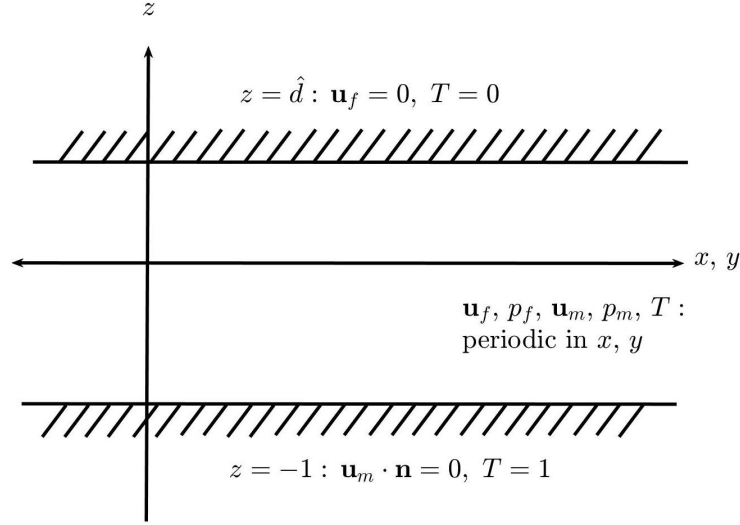


Figure 3.21: Schematic of the domain  $\Omega = \{(x, y) \in \mathbb{R}^2 \times z \in (-1, d_f/d_m)\}$ . The upper and lower boundaries are impermeable and held at constant temperatures  $T_U = 0$  and  $T_L = 1$ .

With the schematic of the domain shown in Figure 3.21, we have the initial conditions from the conductive state:

$$\begin{aligned} \mathbf{u}_f^{(0)} &= \mathbf{u}_m^{(0)} = \mathbf{0}, \\ T^{(0)} &= \begin{cases} T_0 (1 - z/\hat{d}) & \text{for } z \geq 0 \\ T_0 (1 + z) - z & \text{for } z \leq 0 \end{cases}, \end{aligned} \quad (3.26)$$

with  $T_0$  as the initial interface temperature:

$$T_0 = \frac{\kappa_m \hat{d}}{\kappa_m \hat{d} + \kappa_f} = \frac{\hat{d}}{\hat{d} + \epsilon_T}.$$

Then, we begin solving the variational problems. First, given  $(\mathbf{u}_f^{(n)}, T^{(n)}) \in V_f \times \Psi$ , we find  $p_m^{(n+1)} \in Q_m$  with

$$\begin{aligned} & \text{Da} \left( \nabla p_m^{(n+1)}, \nabla q_m \right)_m - \text{Ra}_m \left( (T^{(n)} - 1) \mathbf{k}, \nabla q_m \right)_m \\ & + \int_{\Gamma_i} \left[ \frac{\text{Da}}{\text{Pr}_m \chi} \frac{\partial \mathbf{u}_f^{(n)}}{\partial t} + \mathbf{u}_f^{(n)} \right] \cdot \mathbf{n} q_m d\Gamma_i = 0 \quad \forall q_m \in Q_m. \end{aligned} \quad (3.27)$$

To decouple the problems, we use the previous  $\mathbf{u}_f$  values in the integral along the interface. With  $p_m^{(n+1)}$  solved for, we can use the previous Darcy velocity  $\mathbf{u}_m^{(n)}$  to find the updated velocity  $\mathbf{u}_m^{(n+1)}$  using Backward Euler for the time derivative, we have

$$\frac{\text{Da}}{\text{Pr}_m \chi} \frac{\mathbf{u}_m^{(n+1)} - \mathbf{u}_m^{(n)}}{\Delta t} + \mathbf{u}_m^{(n+1)} = -\text{Da} \nabla p_m^{(n+1)} + \text{Ra}_m (T^{(n)} - 1) \mathbf{k},$$

which we can solve for  $\mathbf{u}_m^{(n+1)}$  with

$$\mathbf{u}_m^{(n+1)} = \left[ -\text{Da} \nabla p_m + \text{Ra}_m (T^{(n)} - 1) \mathbf{k} + \frac{\text{Da}}{\text{Pr}_m \chi \Delta t} \mathbf{u}_m^{(n)} \right] \left( \frac{\text{Pr}_m \chi \Delta t}{\text{Da} + \text{Pr}_m \chi \Delta t} \right). \quad (3.28)$$

Once again, the time-integrator can be swapped for a higher-order integrator.

Next, with  $(\mathbf{u}_f^{(n)}, p_m^{(n+1)}, T^{(n)}) \in V_f \times Q_m \times \Psi$ , we are able find  $(\mathbf{u}_f^{(n+1)}, p_f^{(n+1)}) \in V_f \times Q_f$  by solving

$$\begin{aligned} & \left( \frac{1}{\text{Pr}_m} \frac{\partial \mathbf{u}_f^{(n+1)}}{\partial t} + (\mathbf{u}_f^{(n)} \cdot \nabla) \mathbf{u}_f^{(n+1)}, \mathbf{v}_f \right)_f + 2 \left\langle \mathbb{D}(\mathbf{u}_f^{(n+1)}), \mathbb{D}(\mathbf{v}_f) \right\rangle_f \\ & - \left( p_f^{(n+1)}, \nabla \cdot \mathbf{v}_f \right)_f + \left( \nabla \cdot \mathbf{u}_f^{(n+1)}, q_f \right)_f + \frac{\text{Ra}_m}{\text{Da}} \left( T^{(n)} - T_0, \mathbf{v}_f \cdot \mathbf{k} \right)_f \\ & + \int_{\Gamma_i} p_m^{(n+1)} (\mathbf{v}_f \cdot \mathbf{n}) d\Gamma_i + \int_{\Gamma_i} \frac{\alpha_{BJSJ}}{\sqrt{\text{Da}}} \left( \mathbf{u}_f^{(n+1)} \cdot \boldsymbol{\tau} \right) (\mathbf{v}_f \cdot \boldsymbol{\tau}) d\Gamma_i = 0 \quad \forall \mathbf{v}_f \in V_f, q_f \in Q_f. \end{aligned} \quad (3.29)$$

We use the previously found  $p_m^{(n+1)}$  for the interface integral as well as the previous temperature  $T^{(n)}$ . Also, we partially lag the velocity  $\mathbf{u}_f$  in the nonlinear term to linearize the problem. Now

that we have the velocity in both sub-domains, we can write them as a single, updated velocity field,  $\mathbf{u}^{(n+1)} = \mathbf{u}_f^{(n+1)} + \mathbf{u}_m^{(n+1)}$ .

With  $(\mathbf{u}^{(n+1)}, T^{(n)}) \in V \times \Psi$ , we solve for  $T^{(n+1)} \in \Psi$  with

$$\left( \delta_1 \frac{\partial T^{(n+1)}}{\partial t}, \psi \right)_{\Omega} + \text{Pr}_m \left( \mathbf{u}^{(n+1)} \cdot \nabla T^{(n+1)}, \psi \right)_{\Omega} + \left( \delta_2 \nabla T^{(n+1)}, \nabla \psi \right)_{\Omega} = 0 \quad \forall \psi \in \Psi, \quad (3.30)$$

where  $\delta_i$  are defined in (3.25). The previous temperature  $T^{(n)}$  is used with the time-derivative term. With the updated velocity field over the entire domain, we are also able to solve for the streamlines  $\phi$ :

$$\left( \nabla \phi^{(n+1)}, \nabla \varphi \right)_{\Omega} - \left( \nabla \times \mathbf{u}^{(n+1)}, \varphi \right)_{\Omega} = 0 \quad (3.31)$$

for all  $\varphi \in \Phi$ , where

- $\Phi = \{\varphi \in H^1(\Omega) : \varphi = 0 \text{ on top and bottom} + \text{periodic on left and right}\}$ .

For our simulations, we use the algorithm:

---

**Algorithm 3:** Solving Navier-Stokes-Darcy-Boussinesq system

---

**Result:**  $\mathbf{u}_f^{(N)}, p_f^{(N)}, \mathbf{u}_m^{(N)}, p_m^{(N)}, T^{(N)}, \phi^{(N)}$ .

Use initial conditions from (3.26):  $(\mathbf{u}_f^{(0)}, \mathbf{u}_m^{(0)}, T^{(0)}) = (\mathbf{u}_f^{(0)}, \mathbf{u}_m^{(0)}, T^{(0)}) + \epsilon_{mag}$ .

**for**  $n = 0; n < N; n++$

**do**

    With  $\mathbf{u}_f^{(n)}, T^{(n)}$ , solve (3.27) for  $p_m^{(n+1)}$ .

    With  $\mathbf{u}_m^{(n)}, p_m^{(n+1)}, T_m^{(n)}$ , update  $\mathbf{u}_m^{(n+1)}$  with (3.28).

    With  $\mathbf{u}_f^{(n)}, p_m^{(n+1)}, T^{(n)}$ , solve (3.29) for  $\mathbf{u}_f^{(n+1)}$ .

    With  $\mathbf{u}_f^{(n+1)}, \mathbf{u}_m^{(n+1)}$ , update velocity field  $\mathbf{u}^{(n+1)} = \mathbf{u}_f^{(n+1)} + \mathbf{u}_m^{(n+1)}$ .

    With  $\mathbf{u}^{(n+1)}$ , solve (3.30) for  $T^{(n+1)}$ .

    With  $\mathbf{u}^{(n+1)}$ , solve (3.31) for  $\phi^{(n+1)}$ .

**end**

---

Four our simulations, we have three meshes: one for the fluid layer, one for the porous medium, and one for the entire domain. In the fluid region, we have the velocity  $\mathbf{u}_f$  and pressure  $p_f$  with the Taylor-Hood elements:  $\mathcal{P}_2$  elements for velocity and  $\mathcal{P}_1$  elements for pressure. With the convergence properties referenced in Figure 3.7 in Section 3.1, the Taylor-Hood elements are a natural choice. For the porous medium, we choose  $\mathcal{P}_2$  elements for both velocity and pressure. Although the velocity is a by-product of the pressure and using  $\mathcal{P}_1$  elements would result in the same convergence rates, we use  $\mathcal{P}_2$  elements for the velocity of the medium so that the velocity field over the entire domain will be  $\mathcal{P}_2$  when we combine the velocities with  $\mathbf{u} = \mathbf{u}_f + \mathbf{u}_m$ . This velocity,  $\mathbf{u}$ , is on the mesh over the whole domain along with the temperature,  $T$ . Additionally, we use  $\mathcal{P}_2$  elements for the temperature. These are all summed up with:

- Fluid region,  $\Omega_f$ :  $\mathbf{u}_f$  is  $\mathcal{P}_2$ ,  $p_f$  is  $\mathcal{P}_1$ ,
- Porous medium,  $\Omega_m$ :  $\mathbf{u}_m$  is  $\mathcal{P}_2$ ,  $p_m$  is  $\mathcal{P}_2$ ,
- Entire domain,  $\Omega$ :  $\mathbf{u}$  is  $\mathcal{P}_2$ ,  $T$  is  $\mathcal{P}_2$ .

### 3.3.5 Verifying numerics

The one component we have yet to validate in our numerical simulations is temperature solver. In the single layer cases, solving the advection-diffusion equation is relatively straightforward; however, in the coupled case, care must be taken with this solver due to the interface, especially since we treat the temperature across the entire domain, not sub-domains like for the pressures and velocities. We test the solver with the stationary variational form:

$$(\mathbf{u} \cdot \nabla T, \psi)_\Omega + (\delta_2 \nabla T, \nabla \psi)_\Omega = 0 \quad \forall \psi \in \Psi, \quad (3.32)$$

where  $\Psi$  is the FE space defined above and  $\delta_2$  is piecewise-constant,  $\delta_2 = \begin{cases} \epsilon_T & \text{in } \Omega_f \\ 1 & \text{in } \Omega_m \end{cases}$ . For the interface conditions, we require continuity of the temperature across the interface, as well as condition for the heat flux:  $\epsilon_T \nabla T_f = \nabla T_m$ . Since we will be considering a single temperature field, and not separate ones, the temperature across the interface should satisfy the interface condition:  $\epsilon_T \nabla T|_{\Omega_f} = \nabla T|_{\Omega_m}$ .

Using the method of manufactured solutions over the domain of  $(x, z) \in [-1, 1] \times [-1, 1]$ , we define the exact solution

$$T^{ex} = \delta_3 e^{-x^2} z \quad \text{with } \mathbf{u}^{ex} = \delta_2 (-2x, -2y) \quad \text{and} \quad \delta_3 = \begin{cases} 1 & \text{in } \Omega_f \\ \epsilon_T & \text{in } \Omega_m \end{cases}.$$

The exact solution in this case mimics the temperature of our case with convection in that they both have a domain-dependent parameter,  $\delta_2$ , which changes at the interface, and we require continuity of the temperature and a scaled heat-flux. In both cases, the different values of  $\epsilon_T$  dictate how easily the heat diffuses in the medium compared to the fluid region. For low values of  $\epsilon_T$ , the heat more readily advects in the free-flow, shown in Figure 3.22 with the temperature fields from the convergence study.

The potential issue with convergence of this solver deals with these domain-dependent coefficients. For  $\epsilon_T = 1$ , there is no discontinuity at the interface; as a result, there are no issues with convergence since everything is continuous in the problem and with the solution. However, for  $\epsilon_T \neq 1$ , there is a discontinuity in several coefficients across the interface. While these discontinuities affect how those parameters are defined in the problem, since the *solution* is continuous (and differentiable at least once) across the interface, we do get convergence with our FEM approximations as  $\Delta x \rightarrow 0$ .

Since we are considering the temperature across the entire domain, there is no clear definition for  $\delta_2$  at the interface;  $\delta_2$  cannot be both 1 and  $\epsilon_T$  at the interface. To compromise, we define these domain-dependent constants with the arithmetic average:

$$\delta_2 = \begin{cases} \epsilon_T & \text{in } z > 0 \\ (\epsilon_T + 1)/2 & \text{at } z = 0 \\ 1 & \text{in } z < 0. \end{cases}, \quad \delta_3 = \begin{cases} 1 & \text{in } z > 0 \\ (\epsilon_T + 1)/2 & \text{at } z = 0 \\ \epsilon_T & \text{in } z < 0. \end{cases}.$$

So, at any nodes which are exactly along the interface, these constants are defined; they do not have to compete between two values.

Additionally, with our ‘single-domain’ approach, we do not have *explicitly* state, or enforce, the interface conditions for temperature. These conditions are *implicitly enforced* with our definitions of the  $\delta_i$  coefficients, since these coefficients have been chosen such that the interface conditions hold. Even with these (relatively) lax conditions, we still get third-order convergence in space using UMFPACK to solve the linear system. This is evident with the comparison line of slope 3 shown

in Figure 3.23, which plots the  $L^2$  error of the temperature from the stationary problem defined in (3.32). To ensure that convergence holds with discontinuities in the domain-dependent parameters, we test various  $\epsilon_T$  values.

Another way to implement the single-domain approach could be with a level set method. Since the interface is stationary, the level set method would be relatively easy to implement, as it would be equivalent to creating a ‘fuzzy interface’ between the two subdomains. This method would probably be the most appropriate one to use if we considered an interface that evolved in time. Determining how the interface changes though would add a more difficult element to the problem, as well as introducing non-trivial numerical issues associated with advancing the level set function.

Temperature field with various  $\epsilon_T$  values

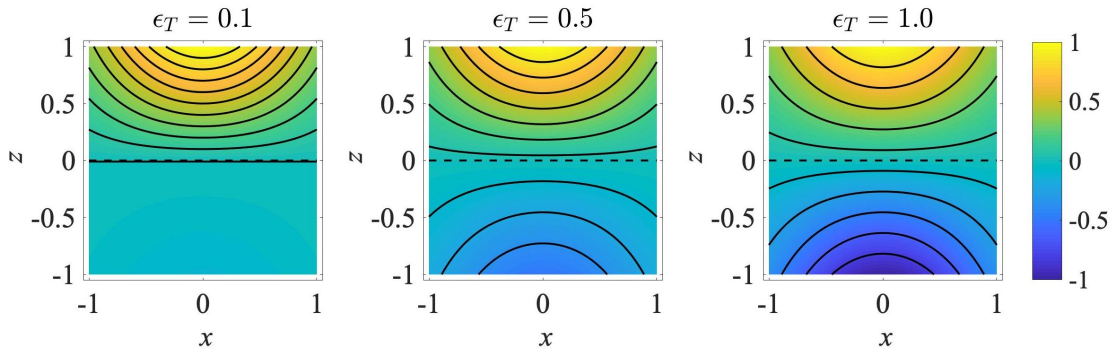


Figure 3.22: Temperature fields for various values of  $\epsilon_T$  in solving the steady ADE (3.32).

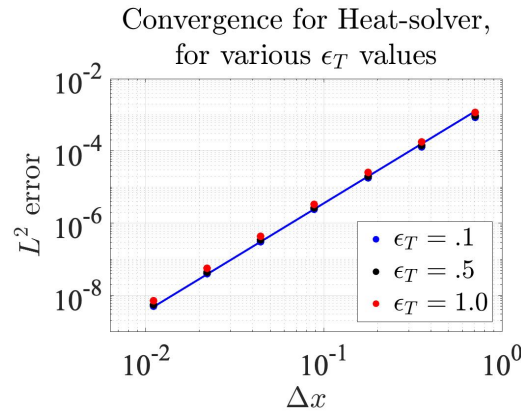


Figure 3.23:  $L^2$  error of the temperature field over the entire domain,  $\Omega$ , for various  $\epsilon_T$  values. The blue comparison line has a slope of 3.

### 3.4 Results

Similar to our energy definition in Chapter 2, we define the functional energy  $E(t)$  as:

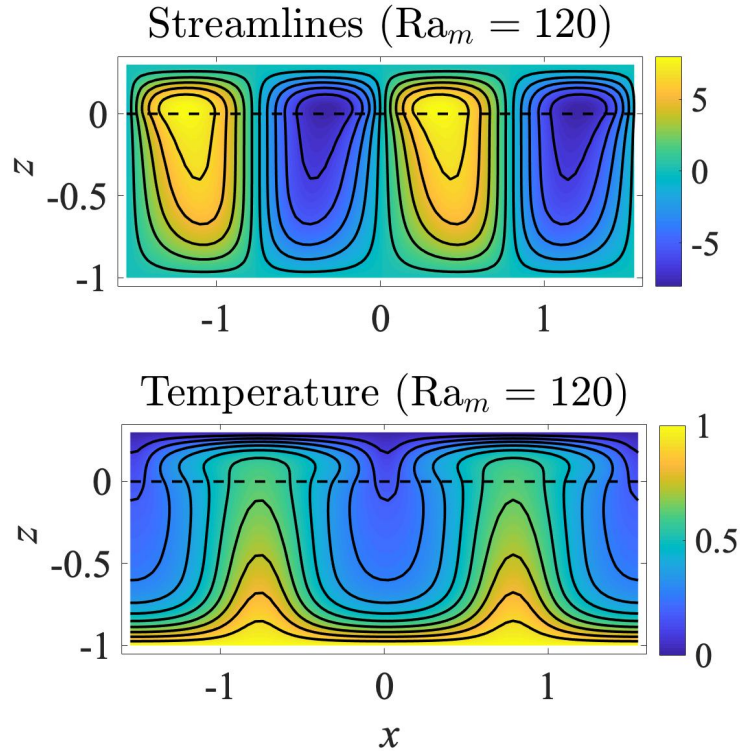
$$2\text{Pr}_m E(t) = \|\mathbf{u}\|^2 + \delta_1 \|T - T^{(0)}\|_f^2,$$

where  $\delta_1$  is defined in (3.25). This differs from Chapter 2 in that we use the velocity and temperature over the entire domain instead of their single layer counterparts. Additionally, almost all of the cumbersome constants have vanished with nondimensionalizing by the porous medium scalings.

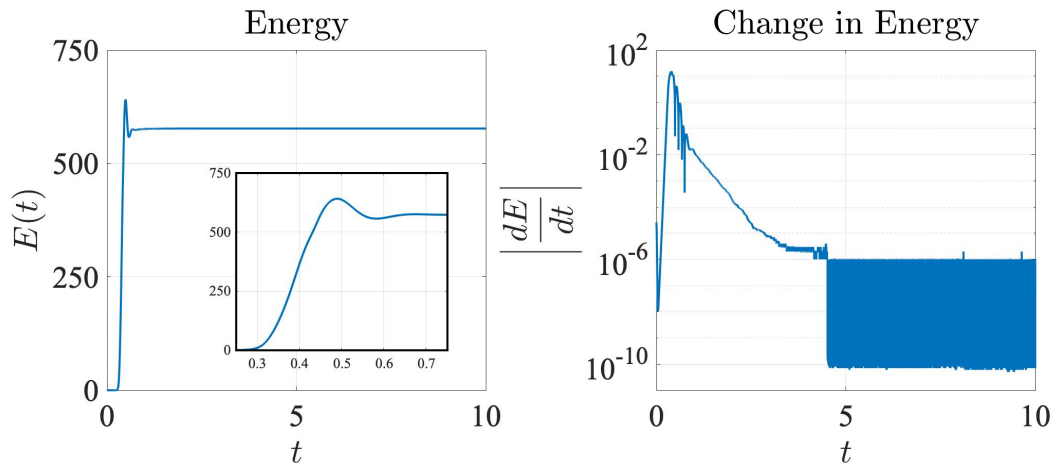
A few results from simulations are shown in Figures 3.24 and 3.25. With Figure 3.24a, the streamline and temperature profiles are shown for  $\text{Ra} = 120$  at  $t = 10$  of the simulation. Figure 3.24b notes the energy and the change in energy of the system, showing the formation of the convection cells and the steady-state. The formation is noted with the spike in the energy profile, and achieving a steady-state is indicated by the derivative of the energy taking on a value of zero. Due to perturbing the system, the absolute value of the derivative fluctuating around single-precision zero is ‘zero’ for all intents and purposes. These results will be referred to in the next section for a comparison as to how boundary conditions can affect convection.

In Figure 3.25, we see the influence of the Darcy number on convection cells, with our results in agreement with the analyses conducted in Chapter 2. For  $\text{Da} = 10^{-3}$ , we see full convection, while decreasing the Darcy number to  $\text{Da} = 10^{-4}$  inhibits flow in the porous medium, resulting in fluid-dominated convection. Since all other parameters are held constant for these simulations, our results suggest that there is some critical Darcy number in between  $\text{Da} = 10^{-4}$  and  $\text{Da} = 10^{-3}$  that marks the transition from fluid-dominated to full convection. An accurate theory for predicting a critical Darcy number for this transition (or a theory for predicting a critical depth ratio) could be utilized in a number of industrial applications. Developing a theory like this is the main focus on the next chapter.

One item of note with these simulations is the time-scale for convection to occur and the time-step restrictions for (numerical) stability. With Figure 3.25a, the simulation took until  $t = 2.0$  to fully form the convection cells, while the cells formed by  $t = .2$  in Figure 3.25b. Additionally, with  $\text{Da} = 10^{-3}$ , we had a time-step of  $\Delta t = 1.25 \times 10^{-3}$  for stability and the case with  $\text{Da} = 10^{-4}$  needed a time-step of  $\Delta t = 1.25 \times 10^{-4}$  to be stable. Based on these results (and many other test cases), we obtain a *non-rigorous* requirement for numerical stability:  $\Delta t \sim \mathcal{O}(\text{Da})$ .

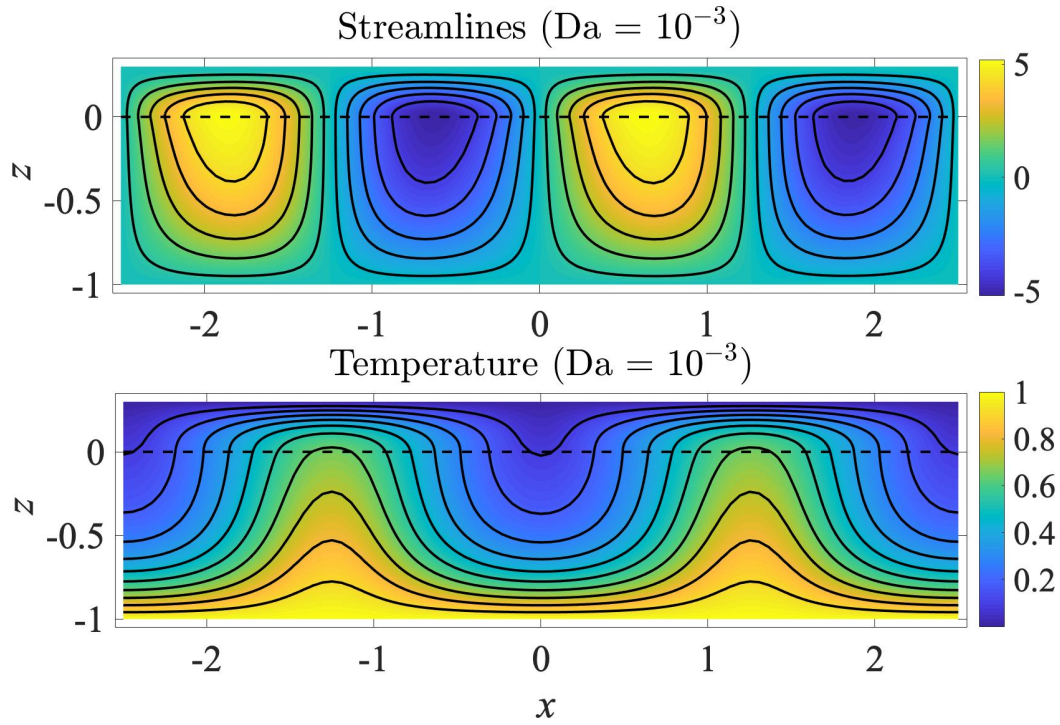


(a) Streamlines and temperature profiles at  $t = 10$ . Positive isolines circulate in the positive direction with negative isolines circulating in the negative direction.

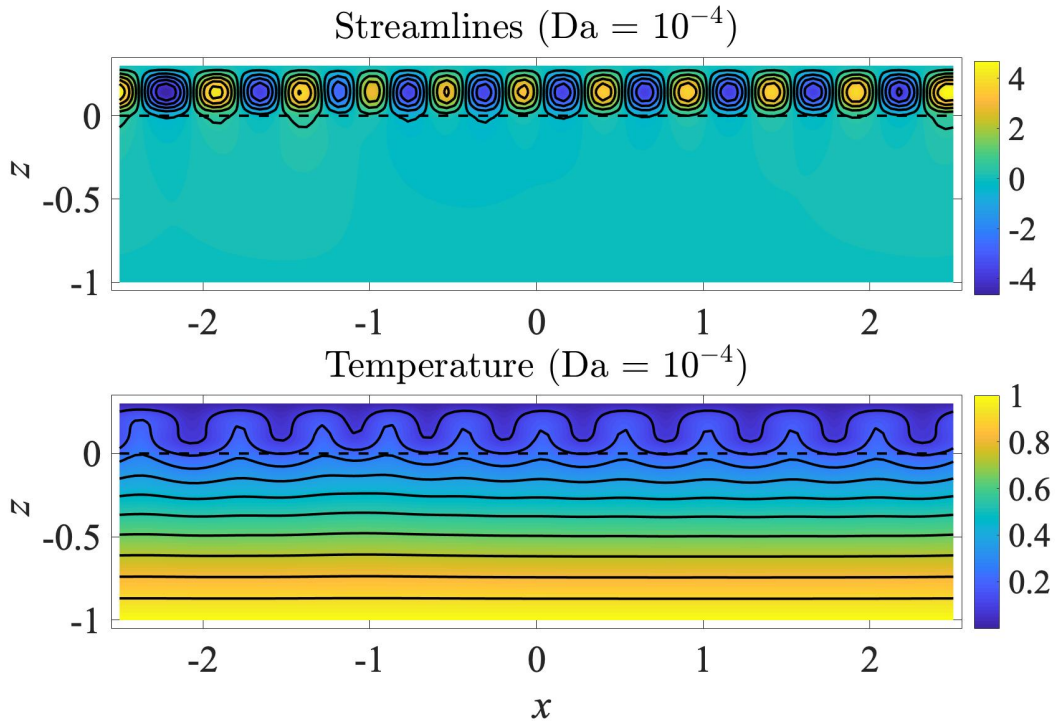


(b) Energy and change in energy.

Figure 3.24: Simulation with  $Ra_m = 120$  at  $t = 10$ . The mesh is on  $(x, z) \in [-1.55, 1.55] \times [-1, .3]$  with 25 elements/unit distance on the mesh, and  $Da = 10^{-3}$ ,  $\Delta t = 1.25 \times 10^{-3}$ ,  $\hat{d} = .3$ ,  $Pr_m = \epsilon_T = \varrho = .7$ ,  $\chi = .3$ .



(a) Full convection at  $t = 2.0$  with  $Da = 10^{-3}$ ,  $\Delta t = 1.25 \times 10^{-3}$ .



(b) Fluid-dominated convection at  $t = 0.2$  with  $Da = 10^{-4}$ ,  $\Delta t = 1.25 \times 10^{-4}$ .

Figure 3.25: Full- versus fluid-dominated convection at  $Da = 10^{-3}$  and  $Da = 10^{-4}$  with  $Ra_m = 50$ . All other parameters held constant:  $\hat{d} = .3$ ,  $Pr_m = \epsilon_T = \rho = .7$ ,  $\chi = .3$ .

With the previous figures, the parameter regimes were carefully and painstakingly curated so that everything worked out nicely— the steady-states were achieved relatively early in the simulations and the convection was clearly full- or fluid-dominated. Alternatively, parameters can also be chosen to achieve the opposite goal: steady-states are not easily attained and convection cells do not exist solely in the fluid-region or occupy the entire domain. The case in Figures 3.26 and 3.27 presents results to this effect.

With the parameters chosen in Figures 3.26 and 3.27, the onset of convection is fluid-dominated between  $t \approx .1-.3$ ; this is shown in the top left panel of Figure 3.27. Unlike cases presented so far in this dissertation, the convection does not stay fluid-dominated for the duration of the simulation. The convection cells in the fluid-region begin to coalesce as time progresses and expand into the porous medium, with the ‘bulk’ of the convection cells remaining in the fluid region. Eventually, two cells remain and the system achieves a steady-state. We do not have qualitative definition for the kind of convection we see in examining the streamlines at  $t = 5.0$ . When we have seen full convection in the past (see Figures 3.24a and 3.25a), the cells extended throughout the domain and the extrema of the streamlines occurred *across* the interface. In this parameter regime, the cells occupy the whole domain but the extrema of the streamlines exist solely in the fluid region. Future work could involve an in-depth exploration into quantifying this kind of convection.

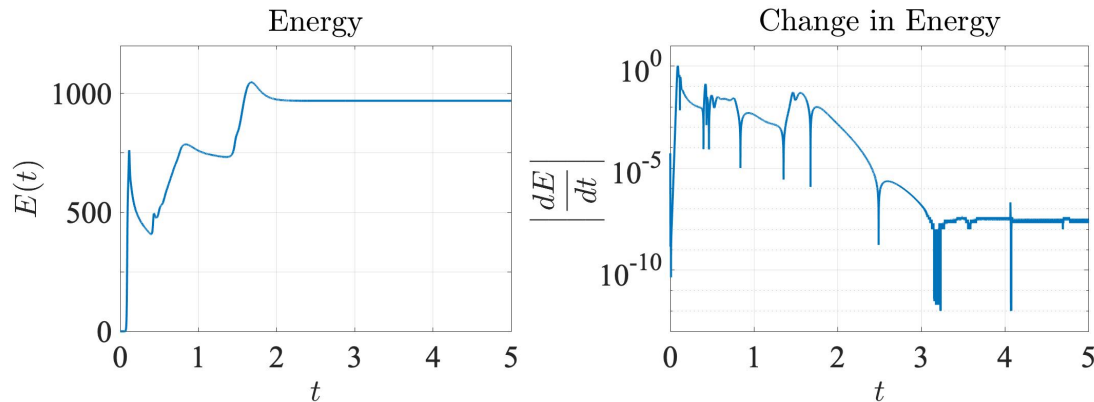


Figure 3.26: Energy and change in energy for simulation with  $Ra_m = 50$ ,  $Da = 10^{-4}$  and periodic left/right boundaries. The mesh is on  $(x, z) \in [-1.55, 1.55] \times [-1, .3]$  with 25 elements/unit distance on the mesh, and  $\Delta t = 2.5 \times 10^{-4}$ ,  $\hat{d} = .3$ ,  $Pr_m = \epsilon_T = \varrho = .7$ ,  $\chi = .3$ .

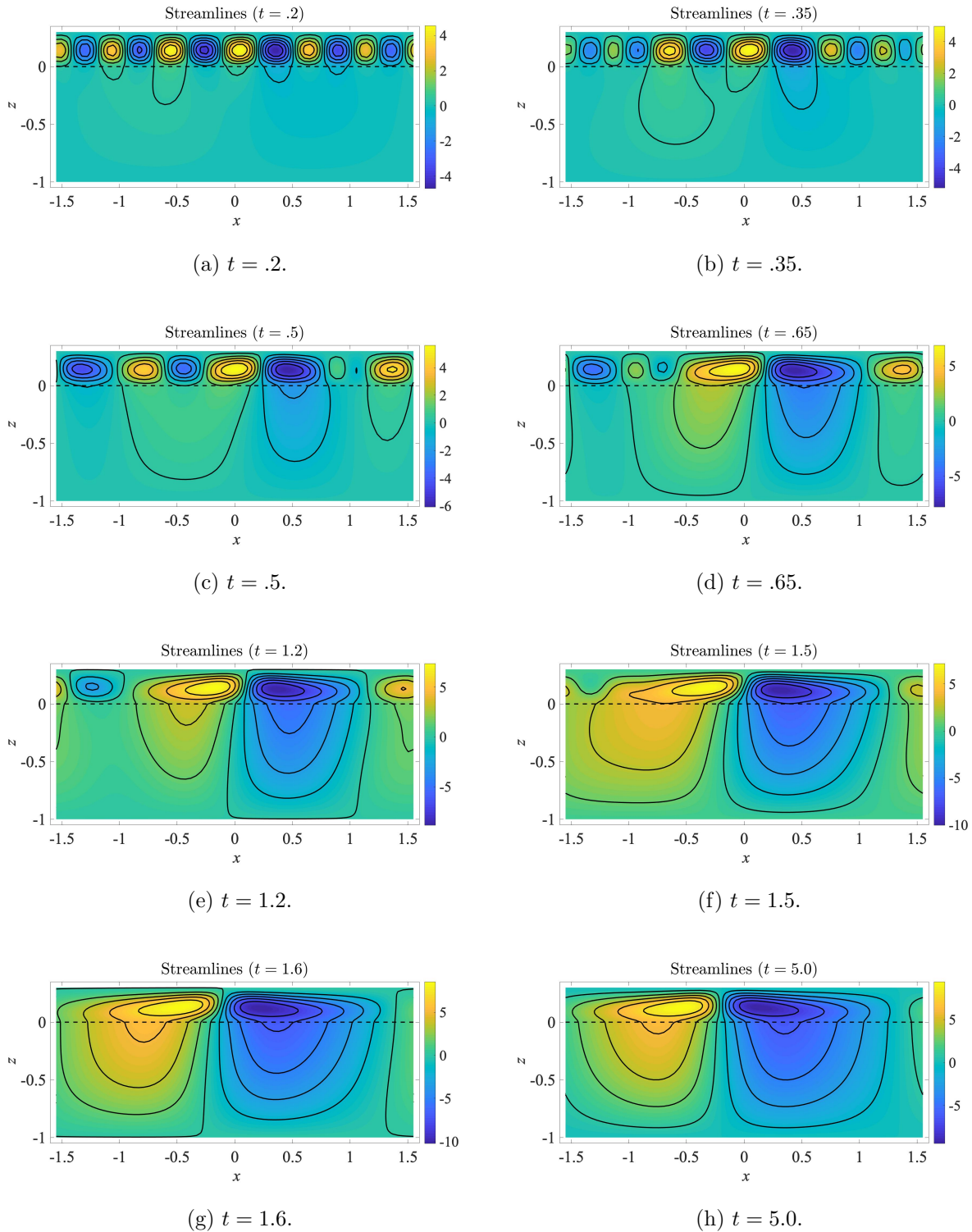


Figure 3.27: Streamlines for  $Ra_m = 50$ ,  $Da = 10^{-4}$  and periodic left/right boundaries. The mesh is on  $(x, z) \in [-1.55, 1.55] \times [-1, .3]$  with 25 elements/unit distance on the mesh, and  $\Delta t = 2.5 \times 10^{-4}$ ,  $\hat{d} = .3$ ,  $Pr_m = \epsilon_T = \rho = .7$ ,  $\chi = .3$ .

### 3.4.1 Influence of boundary conditions

In more realistic geophysical settings, one of the basic assumption from our previous numerical simulations and analyses must to be modified: the periodic boundary conditions at the left and right of the domain. While the periodicity allows our analyses to be conducted, these conditions are not appropriate while modelling ‘real-world’ scenarios. As a result, we implement the following boundary conditions on the left and the right of the domain:

$$\mathbf{u} \cdot \mathbf{n} = \frac{\partial T}{\partial \mathbf{n}} = 0,$$

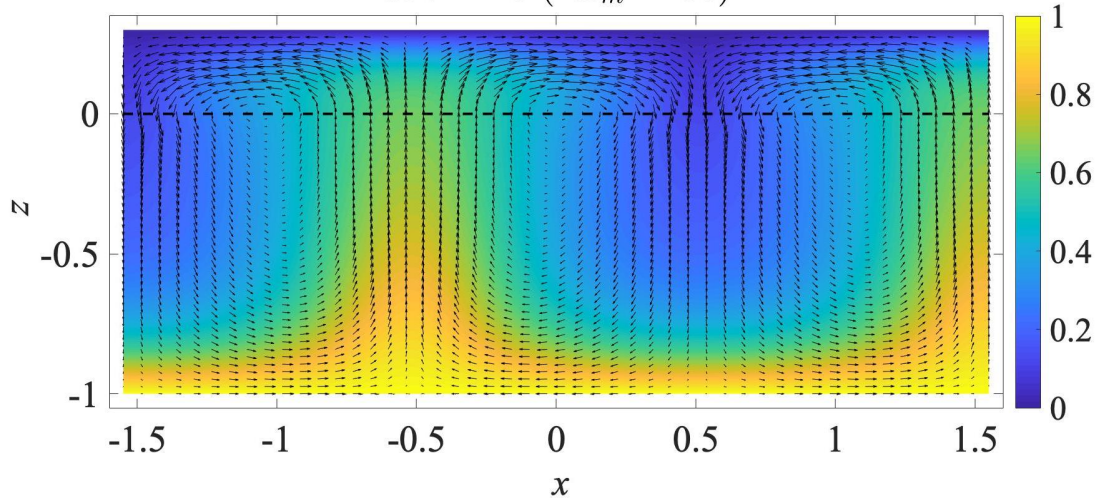
which correspond to a free-slip condition for velocity and a Neumann condition for temperature. With the periodic assumption, if convection cells form, then they do so at their preferred wave-length almost immediately. However, choosing to enforce the conditions noted above instead of periodic conditions can allow– or force– convection cells to alter their wave-length so that they are evenly distributed across the domain. These conditions also constrain the system in that the convection cells must begin and end at the left and right boundaries, respectively. While these conditions are seemingly innocuous, they can produce drastically different profiles than results obtained with the periodic assumptions.

Figure 3.28 shows the velocity fields and temperature profiles for two coupled cases with the free-slip and Neumann conditions at the left and right boundaries for the velocity and temperature, respectively. Three and four convection cells are present for these cases, respectively, evident with the vector fields showing the velocity and color noting the temperature. For these parameter choices, the convection cells will stay at these wave-lengths for the duration of the simulation; the total energy of the system levels out as time progresses. Their energy profiles are shown in 3.29.

The other energy profiles in both plots of Figure 3.29 are produced with various Rayleigh numbers, and we draw attention to the saturation energy– i.e., the energy of the system at its convective steady-state. The profiles in Figure 3.29a have a monotonically increasing relationship between the Rayleigh number and the saturation energy. This makes intuitive sense; the energy of the system increases with an increase in the Rayleigh number, which signifies the energy being ‘pumped into’ the system via heating the bottom plate. However, in looking at the profiles in Figure 3.29b, we see that relationship does not always hold.

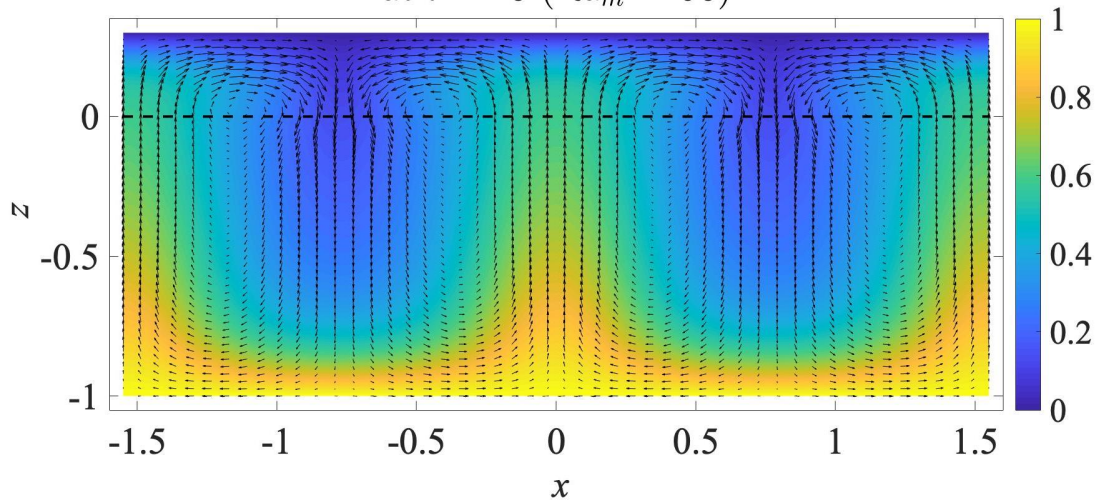
Using the free-slip/Neumann conditions instead of their periodic counterparts can alter the monotonically increasing relationship between saturation energy and the Rayleigh number. In

Velocity field, temperature  
at  $t = 10$  ( $\text{Ra}_m = 80$ )



(a) Simulation with  $\text{Ra}_m = 80$ .

Velocity field, temperature  
at  $t = 10$  ( $\text{Ra}_m = 90$ )



(b) Simulation with  $\text{Ra}_m = 90$ .

Figure 3.28: Streamlines and temperature profiles at  $t = 10$  with  $\text{Ra}_m = 80$  in (a) and  $\text{Ra}_m = 90$  in (b) with solid left/right boundaries. The mesh is on  $(x, z) \in [-1.55, 1.55] \times [-1, .3]$  with 25 elements/unit distance on the mesh, and  $\text{Da} = 10^{-3}$ ,  $\Delta t = 1.25 \times 10^{-3}$ ,  $\hat{d} = .3$ ,  $\text{Pr}_m = \epsilon_T = \varrho = .7$ ,  $\chi = .3$ .

Figure 3.29b, we see that for ‘higher’ Rayleigh numbers, the relationship is gone. The lowest to highest saturation energies correspond to  $Ra_m = 90, 80, 120, 100, 130, 110$ , in that order. Initially, this was extremely puzzling. After viewing the simulations though, the culprit was revealed. For  $Ra_m = 80$  at its steady convection state shown in Figure 3.28a, there are three cells present, while the case with  $Ra_m = 90$  (shown in Figure 3.28b) has four convection cells. With the additional convection cell for the  $Ra_m = 90$  case, the velocity and temperature have more flexibility in dissipation, resulting in a lower saturation energy than the case with  $Ra_m = 80$ .

To help illustrate this, we plot the Rayleigh number against the saturation energy in Figure 3.30 for a selection of Rayleigh numbers, spanning  $Ra_m = 55$  to  $Ra_m = 110$  by increments of 5. Between  $Ra_m = 85$  and  $Ra_m = 90$ , there is a shift in the number of convection cells at the steady-state, from three cells to four cells, shown with the drop in the right plot of Figure 3.30. As the Rayleigh number continues to increase past the cases we tested, there will be another drop in our curve when the shift from four to five convection cells are present at the steady-state, and so on.

One other interesting aspect about Figure 3.30 deals with the  $Ra_m = 110$  case (shown with top energy profile, the green line). We see the curve reaches a local maximum around  $t = .5$ , decreases for short period, and then increases again before leveling off. The dubious behavior this case

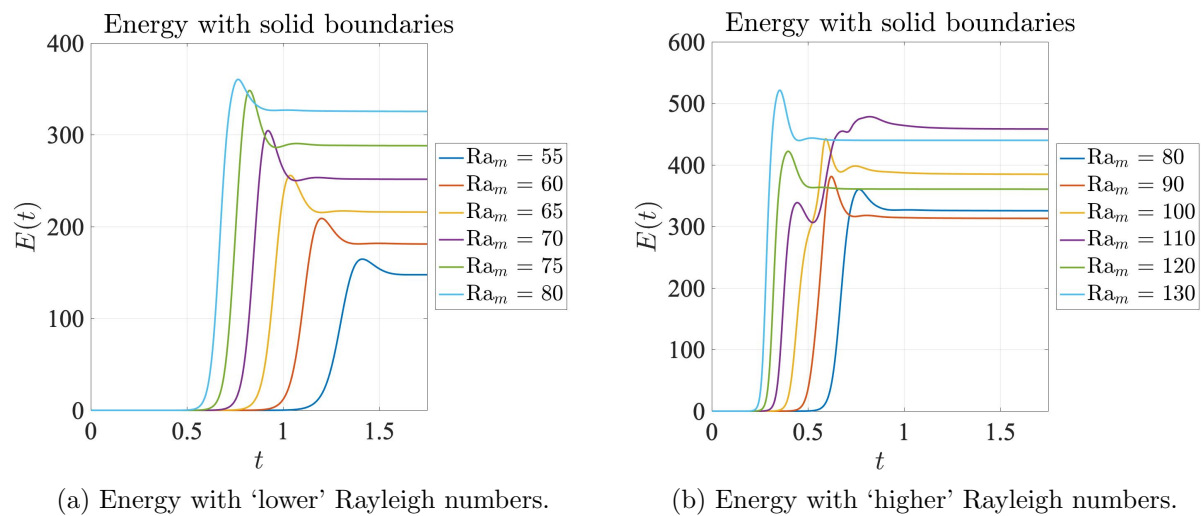


Figure 3.29: Energy of the coupled system with various Rayleigh numbers and solid left/right boundaries. The mesh is on  $(x, z) \in [-1.55, 1.55] \times [-1, .3]$  with 25 elements/unit distance on the mesh, and  $Da = 10^{-3}$ ,  $\Delta t = 1.25 \times 10^{-3}$ ,  $\hat{d} = .3$ ,  $Pr_m = \epsilon_T = \varrho = .7$ ,  $\chi = .3$ .

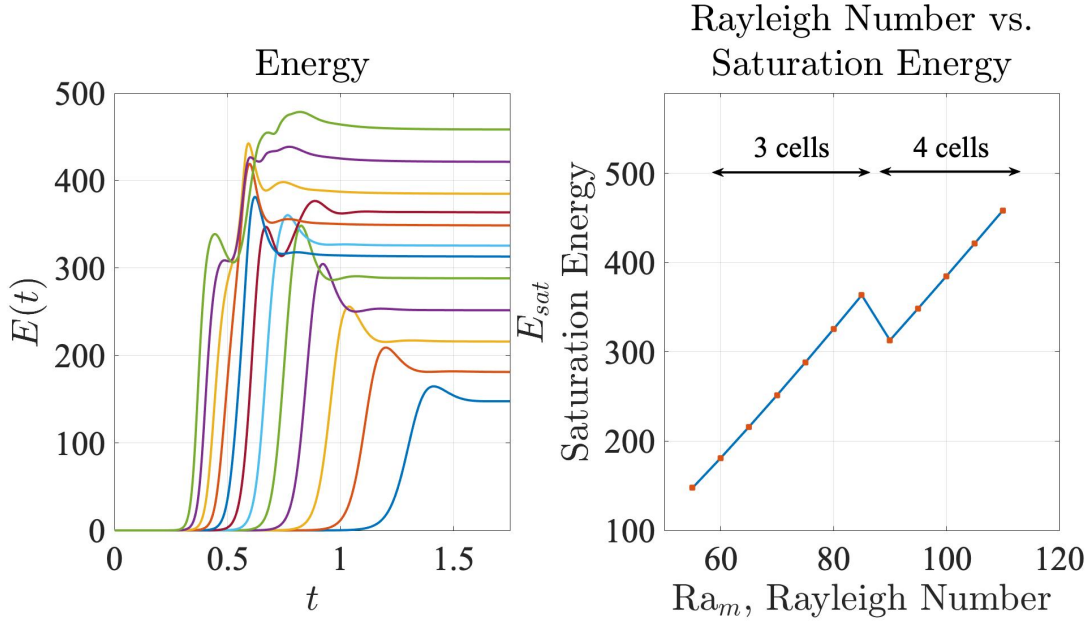


Figure 3.30: (Left) Energy profiles of various Rayleigh numbers ( $Ra_m = 55$  to  $Ra_m = 110$ , by increments of 5) and solid left/right boundaries. (Right) The relationship between  $Ra_m$  and saturation energy, where the data points come from the simulated energy profiles. The mesh is on  $(x, z) \in [-1.55, 1.55] \times [-1, .3]$  with 25 elements/unit distance on the mesh, and  $Da = 10^{-3}$ ,  $\hat{d} = .3$ ,  $Pr_m = \epsilon_T = \rho = .7$ ,  $\chi = .3$ .

exhibits is a result of the system attempting to form six convection cells at the onset of convection. (Even if we did not have the data from  $Ra_m = 110$  in the right panel of Figure 3.30, we could infer that six convection cells at the steady-state is probably not the preferred state; this would require a very abrupt jump from four to six cells in the relationship we found between the Rayleigh number and saturation energy.) As time progresses though, the two outer-most cells collapse into their neighboring cells, producing a total of four fully-developed cells at the system's steady-state. The reduction from six to four convection cells gives each cell more room in the domain, allowing for the cells' circulation velocity to increase; the more physical space each cell has, the higher their velocities can be. Since the energy of the system is closely related to the velocity of each cell, a lower Rayleigh number with fewer cells/higher circulation velocity can produce a greater saturation energy than a higher Rayleigh number with more cells/slower circulation. With the case of  $Ra_m = 110$ , the formation, collapse, and subsequent steadying occurs between  $t \approx .5$  and  $t \approx 1.0$  with the jump in its energy profile shown in the left panel of Figure 3.30.

The strange behavior from that case prompted another investigation, presenting a new quandary for us to explore. This investigation consisted of running cases for longer times and looking at their energy profiles. One of these results is shown in Figure 3.32 with  $Ra_m = 120$ , presenting characteristics related to metastability, or potentially hysteresis. With the energy profile, we see the energy peaks early in the simulation and then quickly levels out until around  $t \approx 5$ , signifying the convection cells are at ‘steady-state.’ Although the cells are visibly unchanging, the derivative of the energy is increasing from  $\sim 10^{-4}$  to  $\sim 10^{-2}$ ; this tells us that the system is not at a true steady-state. Between  $t \approx 5$  and  $t \approx 6$ , the left-most convection cell collapses and is absorbed into its neighboring cell, creating a spike in the energy between  $t = 6$  and  $t = 6.5$ . The cells stabilize again, and the energy levels off; this time though, the derivative of the energy profile hovers around 0 with single-precision white noise.

Metastability is characterized by a system shifting from one steady-state to another, like with the example notes above. This occurs when more than one stable solution exists and the ‘preferred’ steady-state is the one with the lowest energy (not necessarily the same energy we have defined here though). The schematic in Figure 3.31 helps illustrate this concept. Considering a ball on a hill with two valleys, the bottom of both valleys are ‘stable solutions’ in that once the ball is there, small perturbations will not affect its position. However, the ball at position 1 can be perturbed enough so that it rolls down to position 2. Metastability describes the transition from position 1 to position 2, both stable steady-states. Similar metastable systems have been observed in a variety of fluid settings with convection: in chemical applications [70], geophysical applications [17, 89], meteorological and astrophysical applications [11, 17], and in more general fluid settings [41, 61, 74, 81]. Transitioning from one steady-state to another can also be described by hysteresis. Hysteresis differs from metastability in that with hysteresis, both forward and backward transitions are possible while only one-way transitions are possible with metastability. We hypothesize that these systems are exhibiting metastability, although hysteresis can not be definitively ruled out without a more thorough analysis.

The velocity fields and temperatures at various times throughout the simulation are shown in the six panels of Figures 3.33 and 3.34. At the beginning of the simulation (panels one and two of Figure 3.33), the systems settles into six convection cells and appears to be at a steady-state. At the left side boundary though, the temperature can be seen slowly creeping up the wall, evident

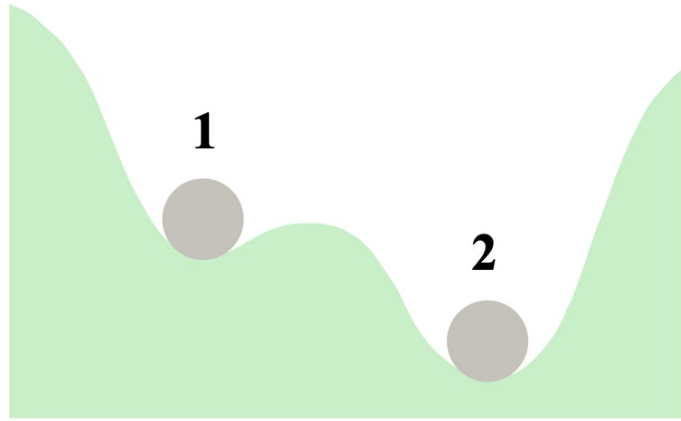


Figure 3.31: Schematic for metastability, showing two stable solutions. Position 2 is the ‘preferred’ solution, as it has a lower energy than position 1.

with the temperature’s height difference between panels one and three. In the first panel of Figure 3.34, the left-most convection cell has collapsed into its neighbor. This can be seen with the large convection cell and the nonuniform temperature distribution. The size of the convection cells then even out as the system achieves its actual steady-state in panels two and three of Figure 3.34.

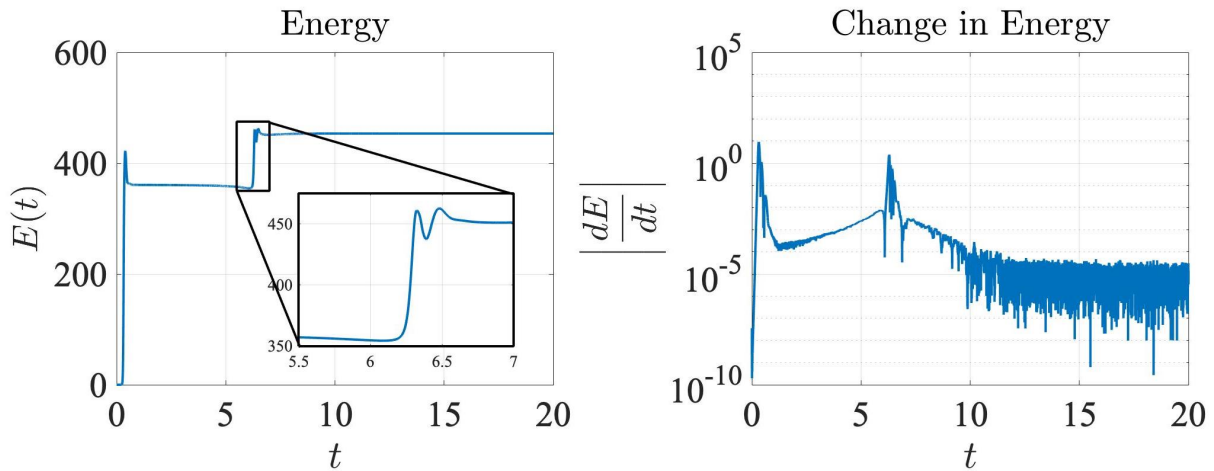


Figure 3.32: Energy and change in energy of the coupled system with  $Ra_m = 120$  and solid left/right boundaries. The mesh is on  $(x, z) \in [-1.55, 1.55] \times [-1, .3]$  with 25 elements/unit distance on the mesh, and  $Da = 10^{-3}$ ,  $\hat{d} = .3$ ,  $Pr_m = \epsilon_T = \varrho = .7$ ,  $\chi = .3$ .

With the jump from the ‘pseudo-steady-state’ achieved between  $t \approx 0$  to  $t \approx 5$  to the ‘actual

steady-state' from  $t \approx 6$  onward, something like hysteresis is coming into play. Exploring hysteresis in convection could be a future direction of this project. We speculate though that this jump from a pseudo- to an actual steady-state is occurring due to the solid left/right boundaries.

Results obtained with the periodic boundary conditions are shown with Figure 3.24, which we can compare directly to Figure 3.32; the *only* difference in these simulations is the boundary conditions. With periodic conditions at the left/right boundaries, the cells form at their preferred wave-length and tend to achieve a steady-state almost immediately after the onset of convection, observable with the energy profile from Figure 3.24b. We also see that the periodic conditions result in a higher saturation energy than the case run with solid left/right boundaries. Despite the same amount of energy being pumped into the system (since both cases have the same Rayleigh number), the periodic boundary condition produce a higher saturation energy, which is seemingly contrary to intuition. Upon closer inspection, we observe the following: the steady-state for the periodic boundary conditions has four cells while the solid left/right boundary yields five convection cells. With fewer cells, each cell occupies more physical space of the domain and the extra room allows for the cells to circulate faster. This increase in the velocity amplifies the energy profile of the system. Although the periodic conditions may not *always* have a higher saturation energy than their counterparts with solid left/right boundaries, this case shows that is it *possible* for the two cases to have different saturation energies.

Finally, one last observation from implementing solid boundaries deals with similarity solutions. In certain parameter regimes, the energy profiles are incredibly similar looking. This prompted us to scale the time of the simulations by the time it takes to achieve the maximum energy of the system, and scaling the energy by its maximum as well. Figure 3.35 shows the energy profiles  $E$  as a function of time  $t$ , and the scaled energy profiles  $\tilde{E}$  as a function of the scaled time  $\tilde{t}$  for various Rayleigh numbers,  $Ra_m = 120 - 150$  increasing by increments of 5. The data collapsing on itself this nicely suggests that similarity solutions may be able to be found for energy profiles in certain parameter regimes, which could be a direction for future research.

The solid left/right boundaries produce more unpredictable cell patterns; we do not have a theory yet for predicting how many cells will be present in a system or how they will be organized. Refining theories, analyses, and predictions for solid boundaries could be the topic of a future research project and is definitely of interest for industrial applications.

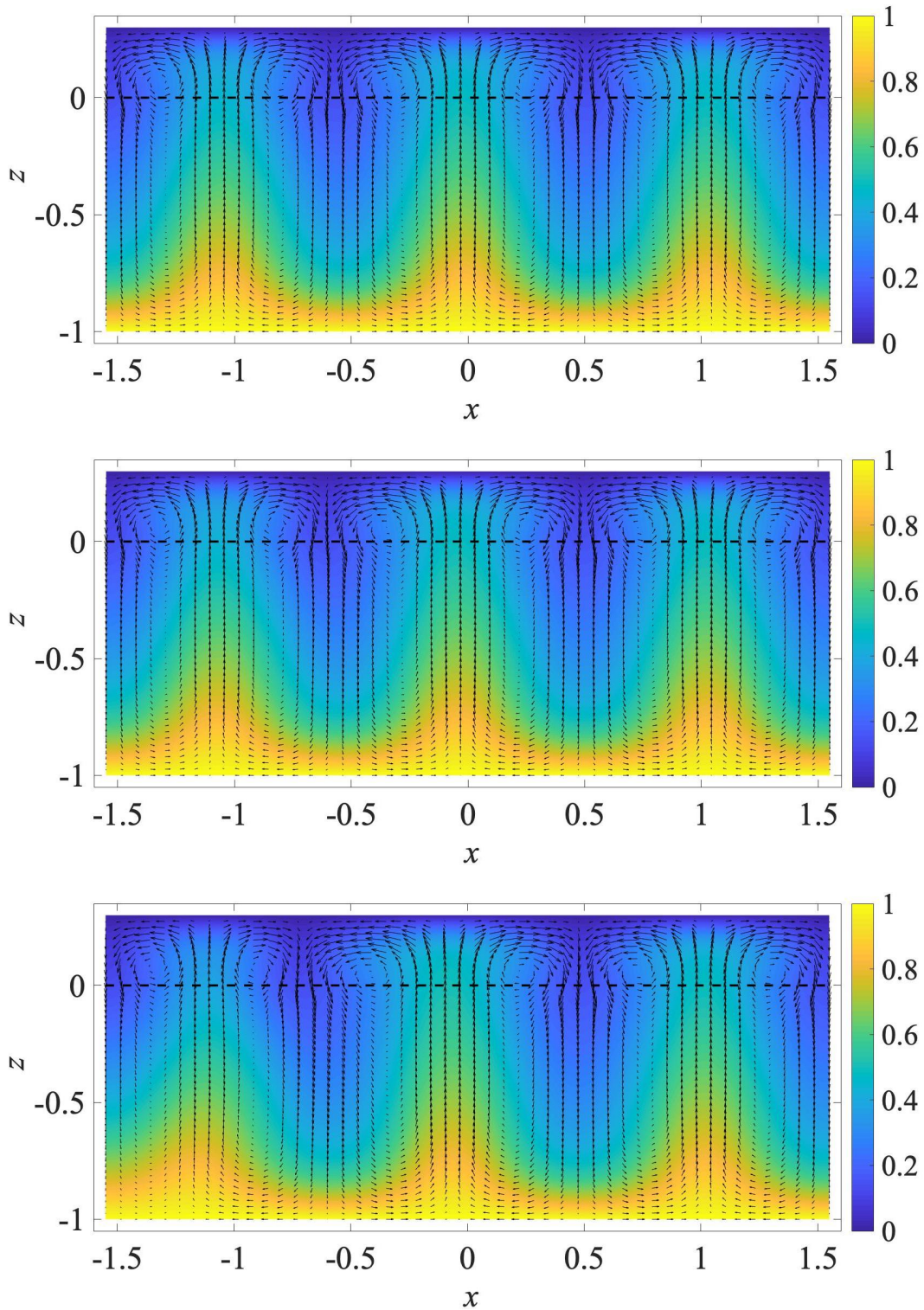


Figure 3.33: Simulation with solid left and right boundaries and the parameters:  $Ra_m = 120$ ,  $Da = 10^{-3}$ ,  $\hat{d} = .3$ ,  $Pr_m = \epsilon_T = \varrho = .7$ ,  $\chi = .3$ ,  $\Delta t = 1.25 \times 10^{-3}$ . Velocity is shown with the vector field, temperature is with color. From top to bottom, the panels are at  $t = 1.0, 5.5, 6.0$ .

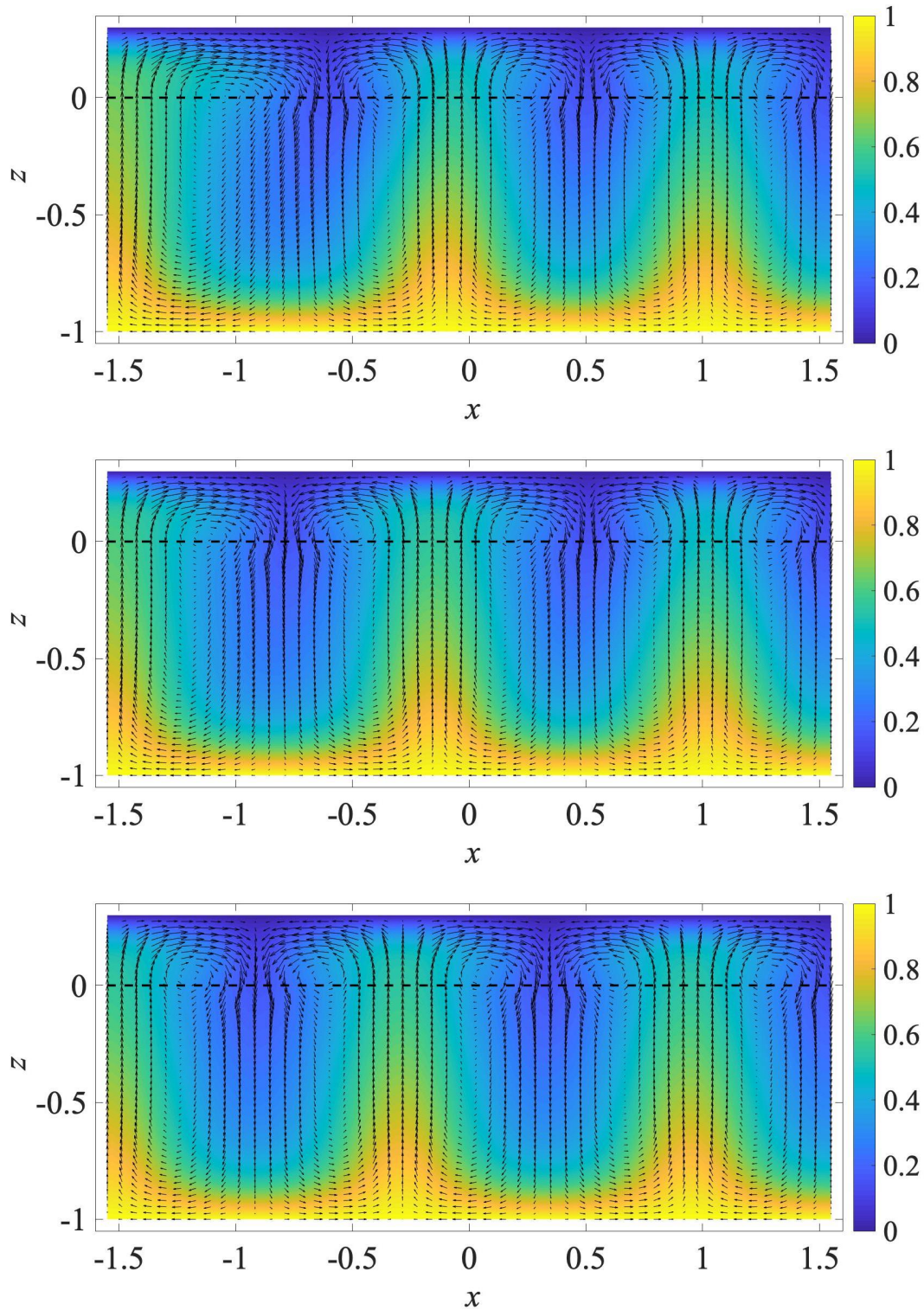


Figure 3.34: Continued results from Figure 3.33. Simulation with solid left and right boundaries and the parameters:  $Ra_m = 120$ ,  $Da = 10^{-3}$ ,  $\hat{d} = .3$ ,  $Pr_m = \epsilon_T = \varrho = .7$ ,  $\chi = .3$ ,  $\Delta t = 1.25 \times 10^{-3}$ . Velocity is shown with the vector field, temperature is with color. From top to bottom, the panels are at  $t = 6.5, 7.0, 10.0$ .

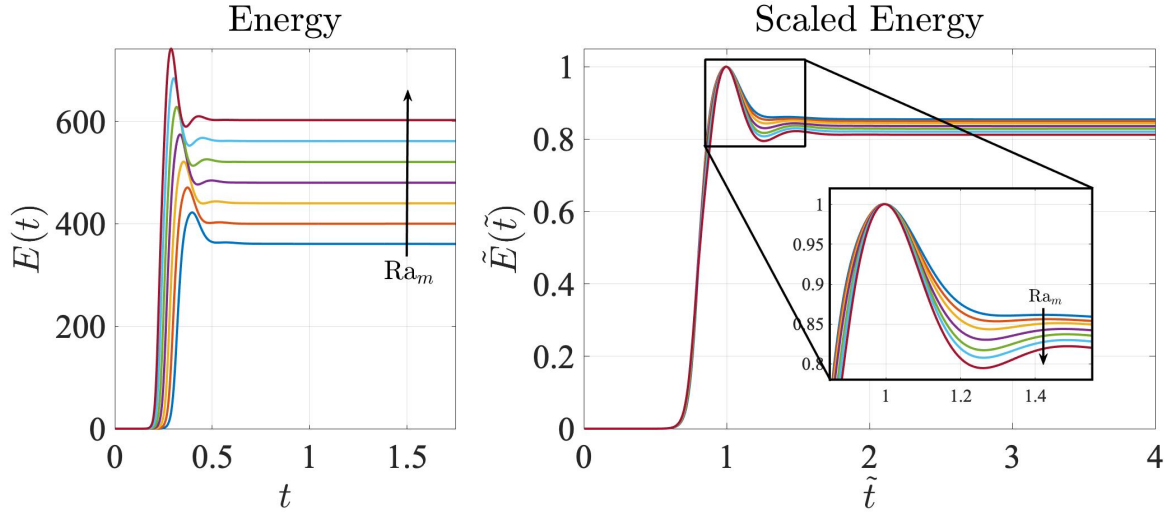


Figure 3.35: (Left) Energy profiles of various Rayleigh numbers ( $Ra_m = 120$  to  $Ra_m = 150$ , by increments of 5) and solid left/right boundaries. (Right) The mesh is on  $(x, z) \in [-1.55, 1.55] \times [-1, .3]$  with 25 elements/unit distance on the mesh, and  $Da = 10^{-3}$ ,  $\hat{d} = .3$ ,  $Pr_m = \epsilon_T = \varrho = .7$ ,  $\chi = .3$ .

### 3.5 Conclusions

This chapter began with consideration given to the respective single layers. We conducted linear stability analyses and showed how the principle of exchange of stabilities held with each case. These results allowed us to calculate marginal stability curves and critical Rayleigh numbers for various combinations of boundary conditions. Next, we detailed the numerical methods used to simulate the single layer systems via the finite element method. Special attention was paid to constructing the variational forms and noting where the boundary conditions were applied. With our numerics, we investigated convergence properties and showed our results were in agreement with the analysis.

Once the single layer numerical simulations were validated, we shifted our focus to simulating the coupled system. This consisted of combining our single layer cases while altering their boundary conditions to account for the interface between the two subdomains. The variational forms of our system were similar to work conducted Chapter 2 and earlier in this section with the separate cases. Implementing periodic boundary conditions with our numerical simulations allowed us to make direct comparisons to the analytical results we determined with the stability bounds. We also implemented solid left/right boundaries so that our code can potentially be used for industrial

simulations. Both sets of boundary conditions were explored via a number of simulations, each of which presented new and interesting characteristics that had yet to be documented prior to our work.

The most important result from this chapter deals with the agreement we see between our stability analyses from Chapter 2 and our numerical simulations. The strong agreement we observe helps validate the numerical simulations based on the theory we developed and rigorously proved in the previous chapter. Without this validation, we could only *speculate* that our simulations were producing appropriate results. Now, we can be certain in stating our numerical methods are working and being implemented properly.

### 3.5.1 Remark

The astute reader would note that the Nusselt number is not referenced in this section's results, due to time constraints. With the single layer Nusselt results though, we showed the defined energy  $E$  was a good proxy for the Nusselt number. Consequently, all of the results in this section with the energy of the system could likely be extrapolated to results with the Nusselt number for non-turbulent parameter regimes (the Rayleigh numbers we consider in this dissertation). The Nusselt profiles will be found for these cases though, and are to be published in a forthcoming paper.

# CHAPTER 4

## HEURISTIC PHASE TRANSITION THEORY

In Chapter 2, we postulated a simple theory with (2.36) to predict the critical depth ratio  $\hat{d}^*$  needed for the transition from full- to fluid-dominated convection. With that theory, we noted that the *best* case scenario had around 13% relative error. While that theory was still promising, especially since it neglected any kind of coupling between the domains, we noted that the introduction of weak coupling could produce a more refined theory. In this chapter, we introduce a more accurate theory which, for the parameter regimes explored, has a *worst* case scenario of 13% relative error in predicting the  $\hat{d}^*$  value that demarcates full- and fluid-dominated convection.

### 4.1 Simple theory, revisited

For the simple theory from Chapter 2, we began with the  $\text{Ra}_m$ - $\text{Ra}_f$  relationship from our nondimensionalization, and solved for the depth ratio:

$$\text{Ra}_m = \text{Ra}_f \frac{\text{Da} \epsilon_T^2}{\hat{d}^4} \quad \Rightarrow \quad \hat{d} = \left[ \frac{\text{Ra}_f \text{Da} \epsilon_T^2}{\text{Ra}_m} \right]^{1/4}.$$

We then substituted in the critical Rayleigh numbers,  $\text{Ra}_f^*$  and  $\text{Ra}_m^*$ , respectively, to predict the critical depth ratio,  $\hat{d}^*$ :

$$\hat{d}^* = \left[ \frac{\text{Ra}_f^*}{\text{Ra}_m^*} \text{Da} \epsilon_T^2 \right]^{1/4}. \quad (4.1)$$

Then, with the critical Rayleigh numbers of the *uncoupled* cases as  $\text{Ra}_f^* = 1707$  and  $\text{Ra}_m^* = 4\pi^2$ , we were able to predict (to varying degrees of success) the critical depth ratio as a function of the Darcy number and ratio of thermal diffusivities:

$$\hat{d}^* = \left[ \frac{1707}{4\pi^2} \text{Da} \epsilon_T^2 \right]^{1/4}. \quad (4.2)$$

We used marginal stability curves to determine the ‘true’ values of the critical depth ratios, and in comparing those to the predictions from (4.2), we had between 13-17% relative error as shown

in Table 2.2. While this theory did not produce extremely accurate predictions, it was useful in narrowing the parameter regime for determining where the actual transition occurs.

The key assumption in this theory was that the transition occurs when the Rayleigh numbers of the two regions are equivalent in some sense, which prompted substituting in the critical Rayleigh numbers of each region. However, both of the critical Rayleigh numbers used ( $\text{Ra}_f^* = 1707$  and  $\text{Ra}_m^* = 4\pi^2$ ) are for the respective regions with no-slip boundaries at the top and bottom of the domain. These conditions completely neglect interaction between the free flow and porous medium; therefore, a more accurate theory would incorporate some sort of coupling between the regions. With this in mind, we revisit the boundary conditions imposed to determine the critical Rayleigh numbers of the two regions in hopes of finding more appropriate choices for  $\text{Ra}_f^*$ ,  $\text{Ra}_m^*$  and a more refined approximation.

## 4.2 Heuristic theory

In Appendix A, we conduct an asymptotic analysis for the coupled Navier-Stokes-Darcy-Boussinesq system as the Darcy number goes to zero. One of the main results from the analysis is that at leading order, fluid does not flow into the porous medium (since the Darcy system is degenerate in the limit of  $\text{Da} \rightarrow 0$ ). This provides rationale that the boundary conditions for the *uncoupled* free flow region should have no-slip at both the top and bottom of the domain, allowing us to continue using  $\text{Ra}_f^* = 1707$  as the critical Rayleigh number.

To determine an appropriate critical Rayleigh number for the porous medium though, no-slip at the top and bottom are not physically realistic for mimicking the behavior of the coupled system. At the bottom of the domain, no-slip is a suitable choice. However, at the interface of the coupled system (i.e., the top of the porous medium), a free-slip condition is more congruous with the fluid behavior from the porous medium's domain. So, using no-slip at the bottom and a free-slip condition at the top of the *uncoupled* porous medium gives the critical Rayleigh number of  $\text{Ra}_m^* = 27.1$  (as calculated in Table 3.2).

With these critical Rayleigh numbers, we obtain the new theory for predicting the critical depth ratio:

$$\hat{d}^* = \left[ \frac{1707.8}{27.1} \text{Da} \epsilon_T^2 \right]^{1/4}. \quad (4.3)$$

While the rationale behind these boundary conditions and the corresponding Rayleigh numbers are seemingly heuristic, the results produced with this theory are increasingly accurate in the small Darcy limit. Since our intuition in choosing boundary conditions came from the asymptotic limit as  $Da \rightarrow 0$ , the theory being accurate for small Darcy numbers makes sense. Our theory is further reinforced by the fact that the critical Rayleigh numbers obtained from the linear stability analyses approach the critical Rayleigh numbers used in our heuristic theory from (4.3),  $Ra_f^* = 1707$  and  $Ra_m^* = 27.1$  in the limit of the Darcy number approaching zero. Data for these claims are shown in Figure 4.1 and Tables 4.1–4.3.

Figure 4.1 shows data for three different  $\epsilon_T$  values while varying  $Da$ , since our theory is a function of these two variables. In the left plot of each case, we have the critical depth ratio predicted from the heuristic theory compared to the actual critical depth ratio obtained from the linear stability analysis. Additionally, with our coupled numerical simulations, we were able to obtain a bound in the depth ratio for where the transition from full- to fluid-dominated convection occurred; these data points are shown for ‘larger’ Darcy numbers in our plots.<sup>1</sup>

In the right plots of each case, we present the relative and maximum errors between the predicted and actual  $\hat{d}^*$  values. We see that as the Darcy number goes to zero, the theory gets more accurate—both in terms of the relative and maximum errors. With the original theory from Chapter 2, the best prediction had a relative error of 13%. With the heuristic theory, our *worst* case prediction has 13% relative error with the best prediction (in the parameter regimes explored) having a relative error of  $< .1\%$ .

The data from the plots of Figure 4.1 are shown in Tables 4.1–4.3. These tables note the actual  $\hat{d}^*$  values as well as the critical Rayleigh numbers at these depth ratios. Here, we easily see the Rayleigh numbers of the free flow and porous medium approaching the *uncoupled* critical Rayleigh numbers used in developing our theory.

For future work, this theory could be especially applicable to heat sinks and controlling heat dissipation via choosing appropriate material properties, like the height or porosity of the medium. Additionally, we will see if the Nusselt profiles can be of any use in predicting transition parameter regimes or the type of convection (full- versus fluid-dominated convection).

---

<sup>1</sup>For numerical stability with smaller Darcy numbers,  $Da \sim \mathcal{O}(10^{-8} - 10^{-5})$ , the simulations require a time-step too small to feasibly run on a personal laptop without parallelized, or optimized, code.

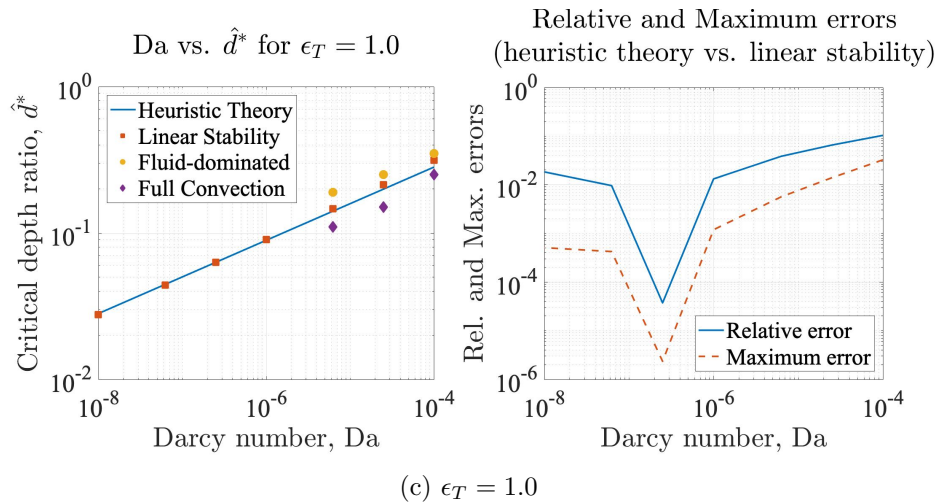
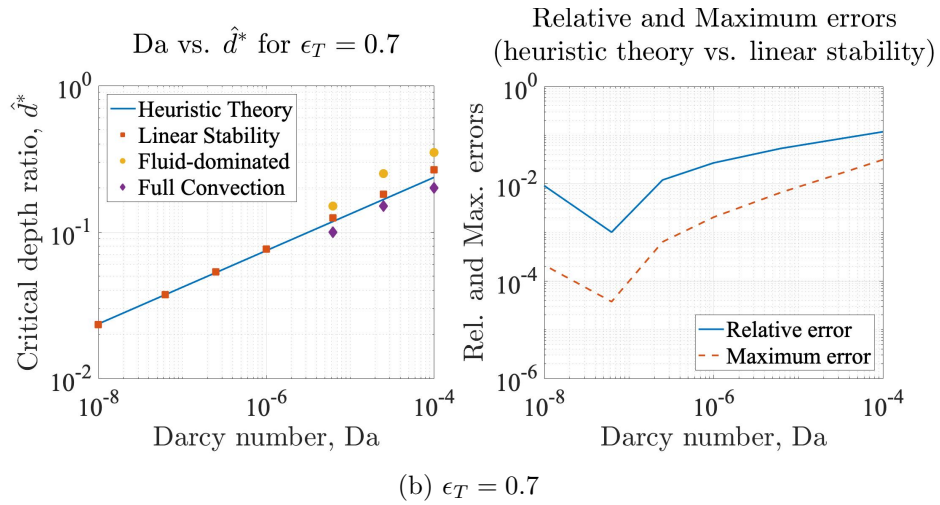
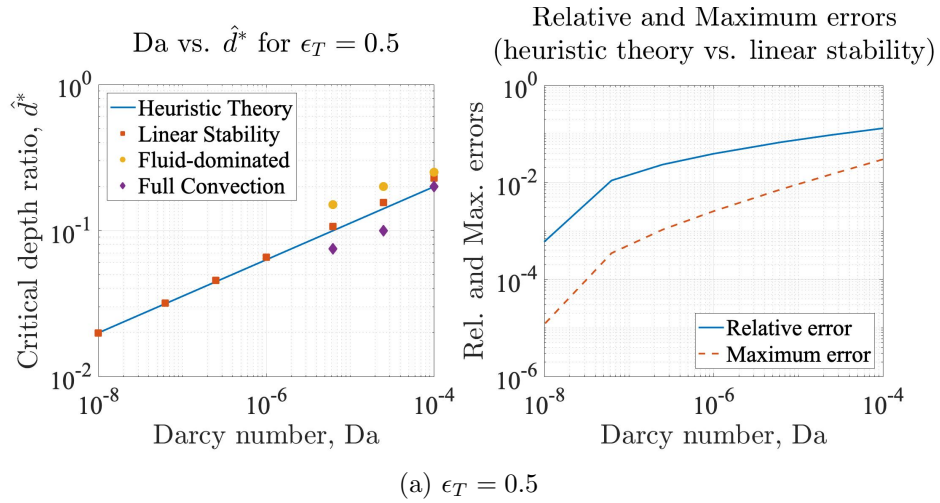


Figure 4.1: Critical depth ratios for various values of  $\epsilon_T$ . The blue line represents the predicted critical depth ratio  $\hat{d}^*$  from the heuristic theory, and the red squares are the  $\hat{d}^*$  from the marginal stability curves from the linear stability analysis. The yellow circles and purple diamonds are points from our numerical simulations.

Table 4.1: With  $\epsilon_T = 0.5$ , actual  $\hat{d}^*$  values from the marginal stability curves along with the two minima of the curve and their associated wavenumbers, Rayleigh numbers. Additionally, predicted  $\hat{d}^*$  values from the heuristic theory, and the relative error between the heuristic  $\hat{d}^*$  values and those from the linear stability.

$\sqrt{\text{Da}}$	actual $\hat{d}^*$	$a_{m,1}^*$	$\text{Ra}_m^*$	$a_{m,2}^* \Rightarrow a_f^*$	$\text{Ra}_f^*$	predicted $\hat{d}^*$	rel. error
$1.0 \times 10^{-2}$	.229	2.1	11.04	11.4 2.6	1214.4	.199	13.1%
$5.0 \times 10^{-3}$	.1557	2.1	14.05	17.6 2.6	1321.1	.141	9.4%
$2.5 \times 10^{-3}$	.1068	2.1	16.75	26.2 2.8	1394.7	.0996	6.7%
$1.0 \times 10^{-3}$	.06555	2.1	19.76	43.5 2.9	1459.3	.06300	3.9%
$5.0 \times 10^{-4}$	.04561	2.2	21.55	63.0 2.9	1492.1	.04455	2.3%
$2.5 \times 10^{-4}$	.03185	2.2	22.98	90.7 2.9	1513.4	.03150	1.1%
$1.0 \times 10^{-4}$	.019911	2.3	24.37	145.7 2.9	1532.1	.019923	.06%

Table 4.2: With  $\epsilon_T = 0.7$ , actual  $\hat{d}^*$  values from the marginal stability curves along with the two minima of the curve and their associated wavenumbers, Rayleigh numbers. Additionally, predicted  $\hat{d}^*$  values from the heuristic theory, and the relative error between the heuristic  $\hat{d}^*$  values and those from the linear stability.

$\sqrt{\text{Da}}$	actual $\hat{d}^*$	$a_{m,1}^*$	$\text{Ra}_m^*$	$a_{m,2}^* \Rightarrow a_f^*$	$\text{Ra}_f^*$	predicted $\hat{d}^*$	rel. error
$1.0 \times 10^{-2}$	.267	2.1	11.66	9.6 2.6	1209.3	.236	11.6%
$5.0 \times 10^{-3}$	.181	2.1	14.85	14.8 2.7	1301.1	.167	7.7%
$2.5 \times 10^{-3}$	.1245	2.1	17.60	22.2 2.8	1380.7	.1179	5.3%
$1.0 \times 10^{-3}$	.0766	2.2	20.50	36.7 2.8	1440.4	.0745	2.7%
$5.0 \times 10^{-4}$	.05335	2.2	22.20	53.1 2.8	1468.1	.05271	1.2%
$2.5 \times 10^{-4}$	.03731	2.2	23.49	76.2 2.8	1486.3	.03727	0.1%
$1.0 \times 10^{-4}$	.02336	2.3	24.74	122.1 2.9	1503.5	.02357	0.9%

Table 4.3: With  $\epsilon_T = 1.0$ , actual  $\hat{d}^*$  values from the marginal stability curves along with the two minima of the curve and their associated wavenumbers, Rayleigh numbers. Additionally, predicted  $\hat{d}^*$  values from the heuristic theory, and the relative error between the heuristic  $\hat{d}^*$  values and those from the linear stability.

$\sqrt{\text{Da}}$	actual $\hat{d}^*$	$a_{m,1}^*$	$\text{Ra}_m^*$	$a_{m,2}^* \Rightarrow a_f^*$	$\text{Ra}_f^*$	predicted $\hat{d}^*$	rel. error
$1.0 \times 10^{-2}$	.3143	2.1	12.34	7.9 2.5	1204.2	.2818	10.3%
$5.0 \times 10^{-3}$	.2132	2.1	15.72	12.4 2.6	1299.2	.1992	6.5%
$2.5 \times 10^{-3}$	.1465	2.1	18.50	18.5 2.7	1363.5	.1409	3.8%
$1.0 \times 10^{-3}$	.09029	2.2	21.28	30.6 2.8	1414.3	.08910	1.3%
$5.0 \times 10^{-4}$	.063004	2.2	22.83	44.1 2.8	1438.9	.06300	0.1%
$2.5 \times 10^{-4}$	.044125	2.2	24.00	63.3 2.8	1455.7	.044549	0.9%
$1.0 \times 10^{-4}$	.027666	2.3	25.09	101.3 2.8	1469.9	.028180	1.8%

### 4.2.1 Choosing $\epsilon_T$ values

The three  $\epsilon_T$  values chosen represent physically relevant parameter values in geophysical applications. The value of  $\epsilon_T$  corresponds to the ratio of thermal conductivity values between the fluid region and the porous medium. Thermal conductivity, usually denoted  $\kappa$  in the literature and measured in terms of watts per meter Kelvin, tells us how easily heat will transfer in a material. If  $\kappa = 1$ , then  $1 \text{ m}^3$  of material will transfer heat at a rate of 1 W for every degree Kelvin difference between opposite faces of the material. Materials with higher  $\kappa$  values transfer heat more easily than materials with lower  $\kappa$  values.

From Table 4.4, we see that extrema of thermal conductivity values are .6 and 4.0. To obtain a bound for relevant  $\epsilon_T$  values, we can look at our definition of  $\epsilon_T = \frac{\kappa \text{ for water}}{\kappa \text{ for medium}}$  and then substitute in the extreme values of  $\kappa$  for the relevant media:

$$.15 = \frac{.6}{4.0} \leq \epsilon_T \leq \frac{.6}{.6} = 1.$$

So, a range for  $\epsilon_T$  in geophysical applications is  $[.15, 1.0]$ .

Table 4.4: Thermal conductivity values of materials found in geophysical applications taken at  $25^\circ\text{C}/77^\circ\text{F}$ , taken from [92].

Material	$\kappa$ in W/(mK)
Water	.6
Soil, clay	1.1
Soil, saturated	.6 – 4.0
Ground, or soil	...
→ moist	1.0
→ very moist	1.4
Clay, saturated	.6 – 2.5
Limestone	1.26 – 1.33
Granite	1.7 – 4.0

# CHAPTER 5

## CONCLUSIONS

In this dissertation, we performed linear and nonlinear analyses for convection in superposed fluid-porous media systems. With the coupled Navier-Stokes-Darcy-Boussinesq system, nonlinear stability thresholds had yet to be rigorously proven due to a sign-indefinite term in the energy analysis arising from the nonlinear term of Navier-Stokes. However, using the Lions interface condition (with its dynamic pressure term) allowed for a bound on the typically uncooperative term, which permitted us to obtain nonlinear stability for the system. The good agreement found when comparing the linear and nonlinear stability results provided one of the centerpieces of this work: in the physically-relevant small Darcy limit, the linear theory accurately describes the onset of convection. Further, outside of the small Darcy parameter regime, we quantified the differences that exist between the two theories via analysis of variants of interface conditions. Our arguments were supported by numerical evidence and asymptotic results as the Darcy number approaches zero.

One of the other noteworthy results from investigating stability thresholds dealt with which region of the coupled system dominated the convection. In analyzing the convection patterns formed with our marginal stability results, we came across cases where a small change in one parameter, specifically the depth ratio, drastically altered the behavior of the system. This drastic behavior consisted of a transition from full convection to fluid-dominated convection, or vice versa. Our observations prompted the development of a theory to accurately predict the critical depth ratio needed to trigger this transition as a function of the Rayleigh number, Darcy number, and ratio of thermal diffusivities. The first attempt at creating a theory, presented in Chapter 2, showed promise as it provided predictions on the correct order of magnitude, allowing us to narrow down a parameter regime for where the ‘actual’ transition occurred. However, this theory was refined, and a new theory was detailed in Chapter 4. The improved theory was based on another asymptotic argument, albeit less rigorously than the asymptotics from Chapter 2. Despite some heuristic reasoning, the improved theory’s predictions were increasingly accurate in the small Darcy limit.

To prepare for conducting numerical simulations of the coupled system, we first began by simulating the single layer cases with a finite element method. This consisted of detailing the variational forms, outlining the numerical methods, and providing results to show our simulations were in agreement with the theory. Following the single layer cases, we then performed similar work with the coupled system, which encapsulates the remaining novel work conducted in this dissertation. Simulating the evolutionary coupled system had yet to be done prior to this; many works used the Stokes in lieu of Navier-Stokes, Brinkman instead of Darcy, and/or chose not to include time derivatives. Armed with our numerical method, we validated the analyses and heuristic theory from earlier in the dissertation. Additionally, we offered commentary on energy profiles for the coupled systems and how the choice of boundary conditions can affect the system's behavior.

# APPENDIX A

## SMALL DARCY ASYMPTOTICS

The dynamic pressure term of the Lions interface condition specifying the balance of force in the normal direction is small. As a result, the difference between solutions produced with the Lions interface condition and its linear counterpart is heuristically small as well. However, this claim has been speculative until now. With a formal asymptotic argument, we show that the size of the dynamic pressure term is  $\mathcal{O}(\text{Da})$  in the limit as the small Darcy number limit. Additionally, we find that this term begins to affect solutions to the perturbed systems at  $\mathcal{O}(\text{Da}^2)$

With  $\text{Da} = \varepsilon^2 \rightarrow 0$  (and all other constants held constant), we employ the ansatz that our solutions take the form:

$$\begin{aligned}\mathbf{v}_j^\varepsilon &= \mathbf{v}_j^{(0)} + \varepsilon \mathbf{v}_j^{(1)} + \varepsilon^2 \mathbf{v}_j^{(2)} + \dots, \\ \pi_j^\varepsilon &= \pi_j^{(0)} + \varepsilon \pi_j^{(1)} + \varepsilon^2 \pi_j^{(2)} + \dots, \\ \theta_j^\varepsilon &= \theta_j^{(0)} + \varepsilon \theta_j^{(1)} + \varepsilon^2 \theta_j^{(2)} + \dots,\end{aligned}$$

for  $j \in \{f, m\}$ . We have the components of  $\mathbf{v}_f^\varepsilon = (u_f^\varepsilon, v_f^\varepsilon, w_f^\varepsilon)$  where

$$u_f^\varepsilon = u_f^{(0)} + \varepsilon u_f^{(1)} + \varepsilon^2 u_f^{(2)} + \dots,$$

with the components of  $\mathbf{v}_m^\varepsilon$  defined in the same fashion. Substituting our ansatz into systems (2.10), (2.11), (2.12):

In  $\Omega_f$ :

$$\left\{ \begin{aligned} & \frac{1}{\text{Pr}_f} \frac{\partial}{\partial t} \left[ \mathbf{v}_f^{(0)} + \varepsilon \mathbf{v}_f^{(1)} + \dots \right] + \left[ \mathbf{v}_f^{(0)} + \varepsilon \mathbf{v}_f^{(1)} + \dots \right] \cdot \nabla \left[ \mathbf{v}_f^{(0)} + \varepsilon \mathbf{v}_f^{(1)} + \dots \right] \\ & \quad = \nabla^2 \left[ \mathbf{v}_f^{(0)} + \varepsilon \mathbf{v}_f^{(1)} + \dots \right] - \nabla \left[ \pi_f^{(0)} + \varepsilon \pi_f^{(1)} + \dots \right] \\ & \quad \quad - \text{Ra}_f \left[ \theta_f^{(0)} + \varepsilon \theta_f^{(1)} + \dots \right] \mathbf{k}, \\ & \nabla \cdot \left[ \mathbf{v}_f^{(0)} + \varepsilon \mathbf{v}_f^{(1)} + \dots \right] = 0, \\ & \frac{\partial}{\partial t} \left[ \theta_f^{(0)} + \varepsilon \theta_f^{(1)} + \dots \right] + \text{Pr}_f \left[ \mathbf{v}_f^{(0)} + \varepsilon \mathbf{v}_f^{(1)} + \dots \right] \cdot \nabla \left[ \theta_f^{(0)} + \varepsilon \theta_f^{(1)} + \dots \right] \\ & \quad = \nabla^2 \left[ \theta_f^{(0)} + \varepsilon \theta_f^{(1)} + \dots \right] - \left[ w_f^{(0)} + \varepsilon w_f^{(1)} + \dots \right]. \end{aligned} \right.$$

In  $\Omega_m$ :

$$\left\{ \begin{array}{l} \frac{1}{\chi} \frac{\varepsilon^2}{\text{Pr}_m} \frac{\partial}{\partial t} \left[ \mathbf{v}_m^{(0)} + \varepsilon \mathbf{v}_m^{(1)} + \dots \right] + \left[ \mathbf{v}_m^{(0)} + \varepsilon \mathbf{v}_m^{(1)} + \dots \right] \\ \quad = -\frac{\varepsilon^2}{\hat{d}^2} \nabla \left[ \pi_m^{(0)} + \varepsilon \pi_m^{(1)} + \dots \right] - \varepsilon^2 \text{Ra}_f \frac{\varepsilon_T^2}{\hat{d}^4} \left[ \theta_m^{(0)} + \varepsilon \theta_m^{(1)} + \dots \right] \mathbf{k}, \\ \nabla \cdot \left[ \mathbf{v}_m^{(0)} + \varepsilon \mathbf{v}_m^{(1)} + \dots \right] = 0, \\ \varrho \frac{\partial}{\partial t} \left[ \theta_m^{(0)} + \varepsilon \theta_m^{(1)} + \dots \right] + \text{Pr}_m \left[ \mathbf{v}_m^{(0)} + \varepsilon \mathbf{v}_m^{(1)} + \dots \right] \cdot \nabla \left[ \theta_m^{(0)} + \varepsilon \theta_m^{(1)} + \dots \right] \\ \quad = \nabla^2 \left[ \theta_m^{(0)} + \varepsilon \theta_m^{(1)} + \dots \right] - \left[ w_m^{(0)} + \varepsilon w_m^{(1)} + \dots \right]. \end{array} \right.$$

On  $\Gamma_j$ :

$$\left\{ \begin{array}{l} \hat{d} \left[ \theta_f^{(0)} + \varepsilon \theta_f^{(1)} + \dots \right] = \varepsilon_T^2 \left[ \theta_m^{(0)} + \varepsilon \theta_m^{(1)} + \dots \right], \\ \nabla \left[ \theta_f^{(0)} + \varepsilon \theta_f^{(1)} + \dots \right] \cdot \mathbf{n} = \varepsilon_T \nabla \left[ \theta_m^{(0)} + \varepsilon \theta_m^{(1)} + \dots \right] \cdot \mathbf{n}, \\ \left[ \mathbf{v}_f^{(0)} + \varepsilon \mathbf{v}_f^{(1)} + \dots \right] \cdot \mathbf{n} = \left[ \mathbf{v}_m^{(0)} + \varepsilon \mathbf{v}_m^{(1)} + \dots \right] \cdot \mathbf{n}, \\ \varepsilon \boldsymbol{\tau} \cdot \mathbb{T} \left( \mathbf{v}_f^{(0)} + \varepsilon \mathbf{v}_f^{(1)} + \dots, \pi_m^{(0)} + \varepsilon \pi_m^{(1)} + \dots \right) \mathbf{n} \\ \quad = \alpha \left( \boldsymbol{\tau} \cdot \left[ \mathbf{v}_f^{(0)} + \varepsilon \mathbf{v}_f^{(1)} + \dots \right] \right) \text{ for } \gamma = 1, 2, \\ -\mathbf{n} \cdot \mathbb{T} \left( \mathbf{v}_f^{(0)} + \varepsilon \mathbf{v}_f^{(1)} + \dots, \pi_f^{(0)} + \varepsilon \pi_f^{(1)} + \dots \right) \mathbf{n} = \hat{d}^2 \left[ \pi_m^{(0)} + \varepsilon \pi_m^{(1)} + \dots \right], \\ \text{or } -\mathbf{n} \cdot \mathbb{T} \left( \mathbf{v}_f^{(0)} + \varepsilon \mathbf{v}_f^{(1)} + \dots, \pi_f^{(0)} + \varepsilon \pi_f^{(1)} + \dots \right) \mathbf{n} + \frac{1}{2} \left| \mathbf{v}_f^{(0)} + \varepsilon \mathbf{v}_f^{(1)} + \dots \right|^2 \\ \quad = \hat{d}^2 \left[ \pi_m^{(0)} + \varepsilon \pi_m^{(1)} + \dots \right]. \end{array} \right.$$

Balancing  $\mathcal{O}(1)$

$$\text{In } \Omega_f : \left\{ \begin{array}{l} \frac{1}{\text{Pr}_f} \frac{\partial \mathbf{v}_f^{(0)}}{\partial t} + \mathbf{v}_f^{(0)} \cdot \nabla \mathbf{v}_f^{(0)} = \nabla^2 \mathbf{v}_f^{(0)} - \nabla \pi_f^{(0)} - \text{Ra}_f \theta_f^{(0)} \mathbf{k}, \\ \nabla \cdot \mathbf{v}_f^{(0)} = 0, \\ \frac{\partial \theta_f^{(0)}}{\partial t} + \text{Pr}_f \mathbf{v}_f^{(0)} \cdot \nabla \theta_f^{(0)} = \nabla^2 \theta_f^{(0)} - w_f^{(0)}, \end{array} \right.$$

$$\text{In } \Omega_m : \left\{ \begin{array}{l} \mathbf{v}_m^{(0)} = 0, \\ \varrho \frac{\partial \theta_m^{(0)}}{\partial t} = \nabla^2 \theta_m^{(0)} \quad (\text{since } \mathbf{v}_m^{(0)} = 0), \end{array} \right.$$

$$\mathcal{O}(1) \text{ On } \Gamma_i : \begin{cases} \hat{d}\theta_f^{(0)} = \epsilon_T^2 \theta_m^{(0)}, \\ \nabla\theta_f^{(0)} \cdot \mathbf{n} = \epsilon_T \nabla\theta_m^{(0)} \cdot \mathbf{n}, \\ \mathbf{v}_f^{(0)} \cdot \mathbf{n} = \hat{d}\mathbf{v}_m^{(0)} \cdot \mathbf{n}, \\ 0 = u_{f,\gamma}^{(0)} \text{ for } \gamma = 1, 2, \\ -\mathbf{n} \cdot \mathbb{T}(\mathbf{v}_f^{(0)}, \pi_f^{(0)}) \mathbf{n} = \hat{d}^2 \pi_m^{(0)}. \end{cases}$$

We notice that  $\mathbf{v}_m^{(0)} \equiv 0$  and the interface conditions reduce to

$$\text{On } \Gamma_i : \begin{cases} \mathbf{v}_f^{(0)} = 0, \\ \hat{d}\theta_f^{(0)} = \epsilon_T^2 \theta_m^{(0)}, \\ \nabla\theta_f^{(0)} \cdot \mathbf{n} = \epsilon_T \nabla\theta_m^{(0)} \cdot \mathbf{n}, \\ -\mathbf{n} \cdot \mathbb{T}(\mathbf{v}_f^{(0)}, \pi_f^{(0)}) \mathbf{n} = \hat{d}^2 \pi_m^{(0)}. \end{cases}$$

The  $\mathcal{O}(1)$  dynamic pressure term  $\frac{1}{2}|\mathbf{v}_f^{(0)} \cdot \mathbf{v}_f^{(0)}|$  will be equal to zero at this order since  $\mathbf{v}_f^{(0)} = 0$  at the interface, and the nonlinear Lions interface condition matches its linear counterpart.

**Balancing  $\mathcal{O}(\varepsilon)$**

$$\text{In } \Omega_f : \begin{cases} \frac{1}{\text{Pr}_f} \frac{\partial \mathbf{v}_f^{(1)}}{\partial t} + [\mathbf{v}_f^{(0)} \cdot \nabla \mathbf{v}_f^{(1)} + \mathbf{v}_f^{(1)} \cdot \nabla \mathbf{v}_f^{(0)}] = \nabla^2 \mathbf{v}_f^{(1)} - \nabla \pi_f^{(1)} - \text{Ra}_f \theta_f^{(1)} \mathbf{k}, \\ \nabla \cdot \mathbf{v}_f^{(1)} = 0, \\ \frac{\partial \theta_f^{(1)}}{\partial t} + \text{Pr}_f [\mathbf{v}_f^{(0)} \cdot \nabla \theta_f^{(1)} + \mathbf{v}_f^{(1)} \cdot \nabla \theta_f^{(0)}] = \nabla^2 \theta_f^{(1)} - w_f^{(1)}, \end{cases}$$

$$\text{In } \Omega_m : \begin{cases} \mathbf{v}_m^{(1)} = 0, \\ \varrho \frac{\partial \theta_m^{(1)}}{\partial t} = \nabla^2 \theta_m^{(1)}, \end{cases}$$

$$\text{On } \Gamma_i : \begin{cases} \hat{d}\theta_f^{(1)} = \epsilon_T^2 \theta_m^{(1)}, \\ \nabla\theta_f^{(1)} \cdot \mathbf{n} = \epsilon_T \nabla\theta_m^{(1)} \cdot \mathbf{n}, \\ \mathbf{v}_f^{(1)} \cdot \mathbf{n} = 0, \\ -\boldsymbol{\tau} \cdot \mathbb{T}(\mathbf{v}_f^{(0)}, \pi_m^{(0)}) \mathbf{n} = \alpha u_{f,\gamma}^{(1)} \text{ for } \gamma = 1, 2, \\ -\mathbf{n} \cdot \mathbb{T}(\mathbf{v}_f^{(1)}, \pi_f^{(1)}) \mathbf{n} = \hat{d}^2 \pi_m^{(1)}. \end{cases}$$

The  $\mathcal{O}(\varepsilon)$  dynamic pressure term  $\frac{1}{2}|\mathbf{v}_f^{(0)} \cdot \mathbf{v}_f^{(1)}|$  will equal zero at this order also (since  $\mathbf{v}_f^{(0)} = 0$  on  $\Gamma_i$ ), and the nonlinear Lions interface condition is still equal to its linear counterpart.

**Balancing  $\mathcal{O}(\varepsilon^2)$**

$$\begin{aligned} \text{In } \Omega_f : & \left\{ \begin{aligned} \frac{1}{\text{Pr}_f} \frac{\partial \mathbf{v}_f^{(2)}}{\partial t} + \left[ \mathbf{v}_f^{(1)} \cdot \nabla \mathbf{v}_f^{(1)} + \mathbf{v}_f^{(2)} \cdot \nabla \mathbf{v}_f^{(0)} + \mathbf{v}_f^{(0)} \cdot \nabla \mathbf{v}_f^{(2)} \right] \\ &= \nabla^2 \mathbf{v}_f^{(2)} - \nabla \pi_f^{(2)} - \text{Ra}_f \theta_f^{(2)} \mathbf{k}, \\ \nabla \cdot \mathbf{v}_f^{(2)} &= 0, \\ \frac{\partial \theta_f^{(2)}}{\partial t} + \text{Pr}_f \left[ \mathbf{v}_f^{(1)} \cdot \nabla \theta_f^{(1)} + \mathbf{v}_f^{(2)} \cdot \nabla \theta_f^{(0)} + \mathbf{v}_f^{(0)} \cdot \nabla \theta_f^{(2)} \right] &= \nabla^2 \theta_f^{(2)} - w_f^{(2)}, \end{aligned} \right. \\ \text{In } \Omega_m : & \left\{ \begin{aligned} \frac{1}{\chi} \frac{1}{\text{Pr}_m} \frac{\partial \mathbf{v}_m^{(0)}}{\partial t} + \mathbf{v}_m^{(2)} &= -\frac{1}{\hat{d}^2} \nabla \pi_m^{(0)} - \text{Ra}_f \frac{\epsilon_T^2}{\hat{d}^4} \theta_m^{(0)} \mathbf{k}, \\ \nabla \cdot \mathbf{v}_m^{(2)} &= 0, \\ \varrho \frac{\partial \theta_m^{(2)}}{\partial t} + \text{Pr}_m \mathbf{v}_m^{(2)} \cdot \nabla \theta_m^{(0)} &= \nabla^2 \theta_m^{(2)} - w_m^{(2)}, \end{aligned} \right. \\ \text{On } \Gamma_i : & \left\{ \begin{aligned} \hat{d} \theta_f^{(2)} &= \epsilon_T^2 \theta_m^{(2)}, \\ \nabla \theta_f^{(2)} \cdot \mathbf{n} &= \epsilon_T \nabla \theta_m^{(2)} \cdot \mathbf{n}, \\ \mathbf{v}_f^{(2)} \cdot \mathbf{n} &= \hat{d} \mathbf{v}_m^{(2)} \cdot \mathbf{n}, \\ -\boldsymbol{\tau} \cdot \mathbb{T} \left( \mathbf{v}_f^{(1)}, \pi_m^{(1)} \right) \mathbf{n} &= \alpha u_{f,\gamma}^{(2)} \text{ for } \gamma = 1, 2, \\ -\mathbf{n} \cdot \mathbb{T} \left( \mathbf{v}_f^{(2)}, \pi_f^{(2)} \right) \mathbf{n} &= \hat{d}^2 \pi_m^{(2)}, \\ \text{or } -\mathbf{n} \cdot \mathbb{T} \left( \mathbf{v}_f^{(2)}, \pi_f^{(2)} \right) \mathbf{n} + \frac{1}{2} \left| \mathbf{v}_f^{(1)} \right|^2 &= \hat{d}^2 \pi_m^{(2)}. \end{aligned} \right. \end{aligned}$$

So, at  $\mathcal{O}(\varepsilon^2)$ , the dynamic pressure term finally contributes to the Lions interface condition, which does not match its linear counterpart since  $\mathbf{v}_f^{(1)} \neq 0$  on  $\Gamma_i$ . The first time the dynamic pressure term influences solutions,  $\mathbf{v}_f$  or  $\mathbf{v}_m$ , is at  $\mathcal{O}(\varepsilon^4)$  though. The Lions interface condition and its linear equivalent give a boundary condition for the  $\pi_m^{(2)}$  term, which first shows up at  $\mathcal{O}(\varepsilon^4)$  in  $\Omega_m$  with Darcy's equation to solve for  $\mathbf{v}_m^{(4)}$ :

$$\frac{1}{\chi} \frac{1}{\text{Pr}_m} \frac{\partial \mathbf{v}_m^{(2)}}{\partial t} + \mathbf{v}_m^{(4)} = -\frac{1}{\hat{d}^2} \nabla \pi_m^{(2)} - \text{Ra}_f \frac{\epsilon_T^2}{\hat{d}^4} \theta_m^{(2)} \mathbf{k}.$$

Thus,  $\mathbf{v}_m^{(4)}$  affects interface conditions for the  $\mathcal{O}(\varepsilon^4)$  solution,  $\mathbf{v}_f^{(4)}$ .

# APPENDIX B

## IMPLEMENTING THE FINITE ELEMENT METHOD

In this appendix, we detail how to solve equations with the Finite Element Method (FEM). We discuss how to formulate the problem, how to use numerical quadrature to approximate the line- and surface-integrals arising from the problem formulation, and how to implement the periodic boundary conditions used in the simulations from this thesis. Many of the topics presented here have examples to help demonstrate the ideas.

### Finite Element Formulation

In this section, we work through an example to solve the reaction-diffusion equation with the FEM to illustrate the process. We have the reaction-diffusion equation as:

$$\begin{cases} -\nabla^2 u + cu = f & \text{in } \Omega, \\ u = g_D & \text{on } \Gamma_D, \\ \nabla u \cdot \mathbf{n} = g_N & \text{on } \Gamma_N, \end{cases}$$

where  $u = u(x, y)$  is an unknown scalar function,  $c > 0$  is a constant, and  $f, g_D, g_N$  are given functions for the forcing and boundary terms. For seemingly unknown reasons (right now), to begin solving this equation, we multiply by some function  $v$ , integrate over the domain, and integrate by parts, which leaves us the problem in *variational form*:

$$\int_{\Omega} \nabla u \cdot \nabla v \, d\mathbf{x} + c \int_{\Omega} u v \, d\mathbf{x} = \int_{\Omega} f v \, d\mathbf{x} + \int_{\Gamma_N} g_N v \, dS + \int_{\Gamma_D} (\nabla u \cdot \mathbf{n}) v \, dS.$$

This is also referred to as the *weak form* of the equation. Since we have no form for  $\nabla u \cdot \mathbf{n}$  on  $\Gamma_D$ , we will require  $v = 0$  on  $\Gamma_D$  so that the last term of the equation above vanishes. This leaves us with

$$\int_{\Omega} \nabla u \cdot \nabla v \, d\mathbf{x} + c \int_{\Omega} u v \, d\mathbf{x} = \int_{\Omega} f v \, d\mathbf{x} + \int_{\Gamma_N} g_N v \, dS.$$

To help describe the functions we are using and looking for, we introduce the function spaces

- $L^2(\Omega) = \{f : \Omega \rightarrow \mathbb{R} : \int_{\Omega} |f| dx < \infty\}$ ,
- $L_0^2(\Omega) = \{f \in L^2(\Omega) : \int_{\Omega} f dx = 0\}$ ,
- $H^1(\Omega) = \{u \in L^2(\Omega) : \frac{\partial u}{\partial x}, \frac{\partial u}{\partial y} \in L^2(\Omega)\}$ ,
- $H_{\Gamma_D}^1(\Omega) = \{v \in H^1(\Omega) : v = 0 \text{ on } \Gamma_D\}$ .

So, our problem is to find  $u \in H^1(\Omega)$  such that

$$u = g_D \quad \text{on } \Gamma_D,$$

$$\text{and } \int_{\Omega} \nabla u \cdot \nabla v d\mathbf{x} + c \int_{\Omega} u v d\mathbf{x} = \int_{\Omega} f v d\mathbf{x} + \int_{\Gamma_N} g_N v dS \quad \forall v \in H_{\Gamma_D}^1(\Omega).$$

We discretize the mesh into triangular elements,  $\omega^k$ , with  $N$  nodes,  $\mathbf{n}_i$ . We also introduce another function space; we have  $V_h$  as the space of functions that are linear on each element ( $\omega^k$ ) and globally continuous over the discretized mesh ( $\Omega^k$ ). The dimension of this space is the number of nodes in the mesh,  $N$ . (Later, we will consider functions that are quadratic on the element.)

We introduce the set of basis function  $\phi_i$ , where

$$\phi_i(\mathbf{n}_j) = \begin{cases} 1, & i = j, \\ 0, & i \neq j. \end{cases}$$

Then, we can approximate  $u$  with  $u_h \in V_h$ :

$$u \approx u_h = \sum_{i=1}^N u(\mathbf{n}_i) \phi_i = \sum_{i=1}^N u_i \phi_i.$$

We introduce yet another space,  $V_h^{\Gamma_D} = V_h \cap H_{\Gamma_D}^1 = \{v_h \in V_h : v_h = 0 \text{ on } \Gamma_D\}$ . This lets us define the discrete variational form of the problem; our goal is to find  $u_h \in V_h$  such that  $u_h(\mathbf{n}_i) = g_D(\mathbf{n}_i)$  for nodes on  $\Gamma_D$  and

$$u_h(\mathbf{n}_i) = g_D(\mathbf{n}_i) \text{ for nodes on } \Gamma_D,$$

$$\text{and } \int_{\Omega} \nabla u_h \cdot \nabla v_h d\mathbf{x} + c \int_{\Omega} u_h v_h d\mathbf{x} = \int_{\Omega} f v_h d\mathbf{x} + \int_{\Gamma_N} g_N v_h dS \quad \forall v_h \in V_h^{\Gamma_D}.$$

Now, we let  $v_h = \phi_i \in V_h^{\Gamma_D}$ , and our problem is written as

$$\int_{\Omega} \nabla u_h \cdot \nabla \phi_i d\mathbf{x} + c \int_{\Omega} u_h \phi_i d\mathbf{x} = \int_{\Omega} f \phi_i d\mathbf{x} + \int_{\Gamma_N} g_N \phi_i dS \quad \forall \mathbf{n}_i \in \Omega^k \setminus \Gamma_D.$$

We can decompose  $u_h$  into the parts of  $u_h$  inside the domain and on the portion of the boundary where Dirichlet conditions are imposed:

$$\begin{aligned} u_h &= \sum_{\mathbf{n}_i \in \Omega^k \setminus \Gamma_D} u_i \phi_i + \sum_{\mathbf{n}_i \in \Gamma_D} u_i \phi_i \\ &= \sum_{\mathbf{n}_i \in \Omega^k \setminus \Gamma_D} u_i \phi_i + \sum_{\mathbf{n}_i \in \Gamma_D} g_D(\mathbf{n}_i) \phi_i, \end{aligned}$$

which allows us to write the problem as

$$\begin{aligned} &\sum_{\mathbf{n}_i \in \Omega^k \setminus \Gamma_D} \left[ \int_{\Omega} u_i \nabla \phi_i \cdot \nabla \phi_j \, d\mathbf{x} + c \int_{\Omega} u_i \phi_i \phi_j \, d\mathbf{x} \right] \\ &= \int_{\Omega} f \phi_j \, d\mathbf{x} + \int_{\Gamma_N} g_N \phi_j \, dS - \sum_{\mathbf{n}_i \in \Omega^k \setminus \Gamma_D} g_D(\mathbf{n}_i) \left[ \int_{\Omega} \nabla \phi_i \cdot \nabla \phi_j \, d\mathbf{x} + c \int_{\Omega} \phi_i \phi_j \, d\mathbf{x} \right]. \end{aligned}$$

We can define the stiffness and mass matrices as

$$W_{j,i} = \int_{\Omega} \nabla \phi_i \cdot \nabla \phi_j \, d\mathbf{x}, \quad M_{j,i} = \int_{\Omega} \phi_i \phi_j \, d\mathbf{x}.$$

The stiffness matrix is symmetric, and the mass matrix is symmetric positive-definite. So, the problem can be written in matrix form as

$$\sum_i [W_{j,i} + c M_{j,i}] u_i = b_j - \sum_{\mathbf{n}_i \in \Gamma_D} g_D(\mathbf{n}_i) [W_{j,i} + c M_{j,i}] \text{ for } \mathbf{n}_i \in \Omega^k \setminus \Gamma_D,$$

where

$$b_j = \int_{\Omega} f \phi_j \, d\mathbf{x} + \int_{\Gamma_N} g_N \phi_j \, dS.$$

The entire RHS of the equation is known; all of the terms come from the forcing term  $f$  or the boundary conditions. We are left to solve for the  $u_i$  coefficients on the left-hand side.

As of now, we have not discussed how to integrate the terms of the equation above. Approximating line- and surface-integrals with numerical quadrature is discussed in-depth shortly. However, we will mention here that the integrals can be written as the sum of integrals over the elements  $\omega^k$ .

## Choosing Elements

The triangular elements of the mesh are either  $\mathcal{P}_1$  or  $\mathcal{P}_2$ , meaning the basis functions are either piecewise-linear basis functions or piecewise-quadratic. The differences in the elements deal with the number of nodes on each boundary of the element. With  $\mathcal{P}_1$  elements (schematic shown in

Figure B.1), we have three vertices labelled  $\mathbf{v}_i^k$ , the vertex is the  $i$ th vertex on the  $k$ th element, and the basis functions are shown in Figure B.2. For a  $\mathcal{P}_2$  element shown in Figure B.1, we have 6 nodes along the boundary of the element so that quadratic basis functions can be used, shown in Figure B.3.

With  $\mathcal{P}_1$  elements, the FEM method is second-order accurate in space. With  $\mathcal{P}_2$  elements (and an increase in the degrees of freedom!), the method becomes third-order. These have been briefly discussed in Section 3.1.4 and shown with Figures 3.5 and 3.7.

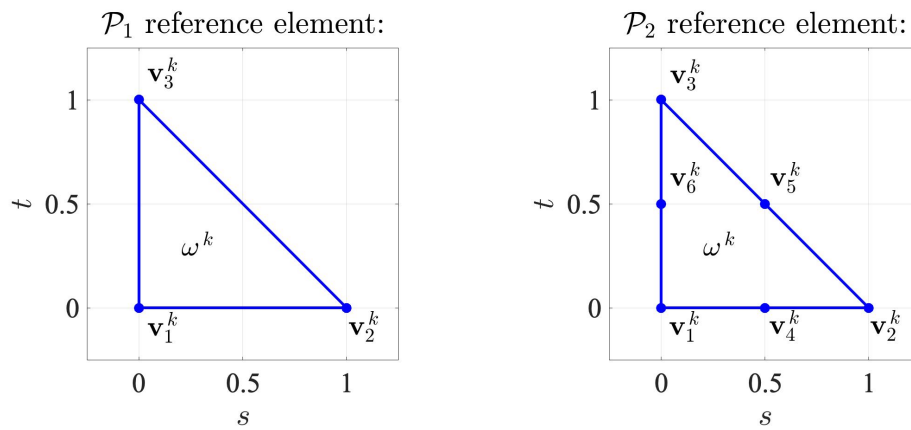


Figure B.1: Schematic of  $\mathcal{P}_1$  and  $\mathcal{P}_2$  reference elements, labelled  $\omega^k$ , in the reference  $(s, t)$ -domain.

Basis Functions for  $\mathcal{P}_1$  elements on reference triangle:

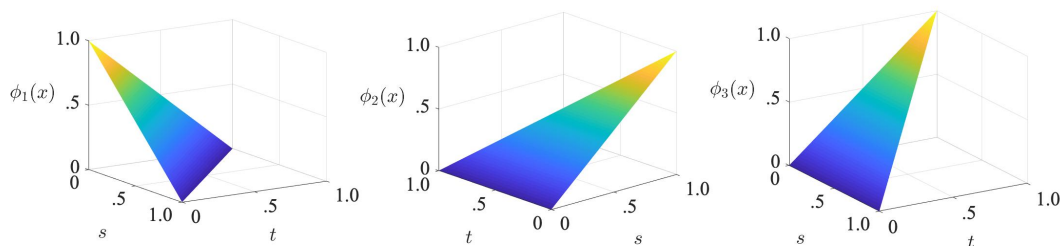


Figure B.2: Basis functions for  $\mathcal{P}_1$  elements in the reference  $(s, t)$ -domain.

### Basis Functions for $\mathcal{P}_2$ elements on reference triangle:

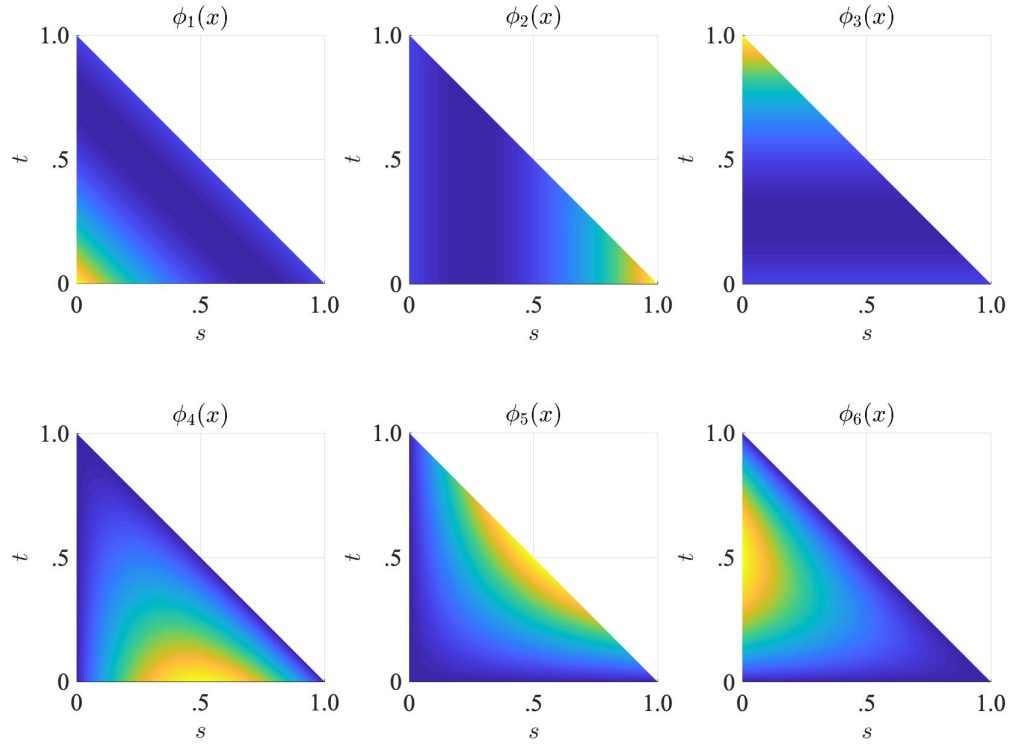


Figure B.3: Quadratic basis functions for  $\mathcal{P}_2$  elements in the reference  $(s, t)$ -domain. The color corresponds to the value of  $\phi_i(x)$ .

### Numerical Quadrature

In this section, we detail how to solve the integrals presented in the FE formulation of the problem. The two kinds of integrals seen there are line-integrals, for integrals along the boundary of our domain, and surface-integrals over the elements of the mesh.

For line integrals on  $C$  from  $\mathbf{x}_0$  to  $\mathbf{x}_1$ , with  $|C|$  as the distance between points, we can discretize the line with  $\mathbf{x}(t) = \mathbf{x}_0(1-t) + \mathbf{x}_1 t$  and then map that to a ‘reference line’ with  $t \in [0, 1]$ . With the change of variables  $f(\mathbf{x}) = g(t)$ , we can approximate the integral with Gauss-Legendre quadrature

formulas of various orders:

-Second-order: (exact for polynomials of degree 1 or less)

$$\int_C f(\mathbf{x}) dS \approx |C| \cdot g\left(\frac{1}{2}\right),$$

-Fourth-order: (exact for polynomials of degree 3 or less)

$$\int_C f(\mathbf{x}) dS \approx \frac{|C|}{2} \cdot \left[ g\left(\frac{1-1/\sqrt{3}}{2}\right) + g\left(\frac{1+1/\sqrt{3}}{2}\right) \right],$$

-Sixth-order: (exact for polynomials of degree 5 or less)

$$\int_C f(\mathbf{x}) dS \approx \frac{|C|}{18} \cdot \left[ 5g\left(\frac{1-\sqrt{3/5}}{2}\right) + 8g\left(\frac{1}{2}\right) + 5g\left(\frac{1+\sqrt{3/5}}{2}\right) \right].$$

These quadrature formulas place points along the reference line from  $t = 0$  to  $t = 1$ , we convert those points back to the original domain, and evaluate the function  $f$  at those points to approximate the integral. The number of points we place along the reference line and their position dictate the order of accuracy obtained with the quadrature approximation. With the formulas listed, we have second-order quadrature formula which places one point in the reference domain to approximate the integral. For the fourth-order formula, we have two points in the domain to approximate the integral, and so on.

This kind of integration– line integrals– is used along boundaries of a domain, stemming from integration by parts; for example, we use it at the interface of the coupled domain. With the flexibility FreeFem [51] provides, we are able to use built-in integrators (only needing to specify the order of the quadrature formula), or we can define our our points along the reference line and their respective weights. For the simulations conducted in this thesis, we use the sixth-order quadrature formula.

Everything stated so far has been for a line integral along the boundary of a single element. We can add more elements along the boundary if needed to further refine the mesh and (hopefully) improve our approximations. In Figure B.4, we show the different quadrature points needed for one, two, and three elements on the reference domain with various quadrature formulas. To improve approximations, we need to balance refining the mesh by adding more elements with increasing the order of the quadrature formula used. For example, using one element with the sixth-order quadrature formula requires three total quadrature points; therefore, we need to evaluate a function

at three points to approximate the integral. However, using three elements with a second-order quadrature formula on each element also yields three total quadrature points.

In Figure B.5, we show the influence of the order of the quadrature formulas against their errors for different numbers of elements to approximate the integral

$$\int_C 2 \sin^2(\pi x) dS = 5, \quad (\text{B.1})$$

where  $C$  is the line from  $(1,0)$  to  $(4,4)$ . To answer the question posed above about increasing the number of elements or the order of the quadrature formula, we see that using an eighth-order quadrature formula on 4 elements produces a better approximation (for this case!) than using a second-order formula on 32 elements—each approximation uses 32 quadrature points. In a perfect world, we could use a high-order quadrature formula and as many elements as needed to get the approximation within some tolerance of the actual integral. Until we develop technology that allows for that though, we will need to balance mesh refinement and order of quadrature to get the best approximation for the available computational power.

For surface integrals over our triangular elements, we map the element in  $(x, y)$  to a reference triangle in  $(s, t)$ , with a visual of the transformation shown in Figure B.6. With the  $x$ - and  $y$ -coordinates of the  $\mathbf{v}_i$  vertex as  $(x_i, y_i)$  mapping to the vertices of the reference triangle in  $(s, t)$  at  $(0, 0)$ ,  $(1, 0)$ ,  $(0, 1)$  we have the transformation and inverse transformation:

$$\begin{aligned} \begin{pmatrix} x \\ y \end{pmatrix} &= \begin{pmatrix} x_1 \\ y_1 \end{pmatrix} + \begin{pmatrix} x_2 - x_1 & x_3 - x_1 \\ y_2 - y_1 & y_3 - y_1 \end{pmatrix} \begin{pmatrix} s \\ t \end{pmatrix}, \\ \begin{pmatrix} s \\ t \end{pmatrix} &= \frac{1}{\det} \begin{pmatrix} y_3 - y_1 & -(x_3 - x_1) \\ -(y_2 - y_1) & x_2 - x_1 \end{pmatrix} \begin{pmatrix} x - x_1 \\ y - y_1 \end{pmatrix}, \end{aligned}$$

where  $\det = (x_2 - x_1)(y_3 - y_1) - (x_3 - x_1)(y_2 - y_1)$ .

With the example shown in Figure B.6, we map the points  $(0, 1)$ ,  $(3, 0)$ ,  $(1, 3)$  to  $(0, 0)$ ,  $(1, 0)$ ,  $(0, 1)$  with the transformations:

$$\begin{aligned} \begin{pmatrix} x \\ y \end{pmatrix} &= \begin{pmatrix} 0 \\ 1 \end{pmatrix} + \begin{pmatrix} 3 & 1 \\ -1 & 2 \end{pmatrix} \begin{pmatrix} s \\ t \end{pmatrix}, \\ \begin{pmatrix} s \\ t \end{pmatrix} &= \frac{1}{8} \begin{pmatrix} 2 & -1 \\ 1 & 3 \end{pmatrix} \begin{pmatrix} x \\ y - 1 \end{pmatrix}. \end{aligned}$$

Similar to the case with line integrals, we introduce a change of variables for surface integrals as well. Using  $f(x, y) = g(s, t)$  to approximate the surface integrals over the triangular element  $\omega$ ,

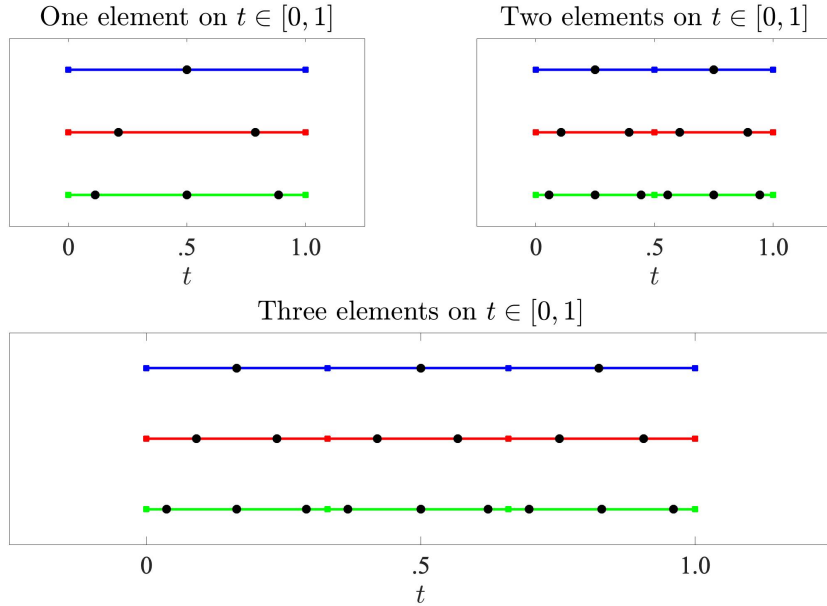


Figure B.4: Schematic showing effect of mesh refinement with 1D quadrature points for various orders of quadrature formulas with one, two, and three elements along the reference line. In each plot, the second-order formula is shown on top in blue, fourth-order in the middle with red, and sixth-order at the bottom in green. Colored squares denote the edges of the element while black circles show the quadrature points.

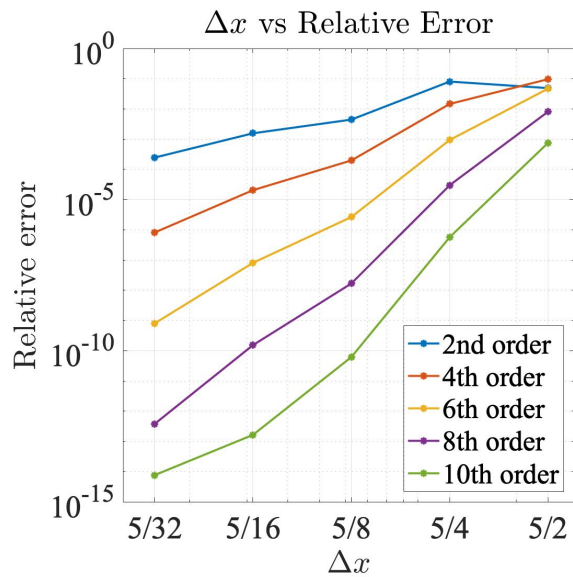


Figure B.5: Log-log plot of the relative error versus  $\Delta x$  for various orders of quadrature formulas (with line-integrals) to approximate (B.1).

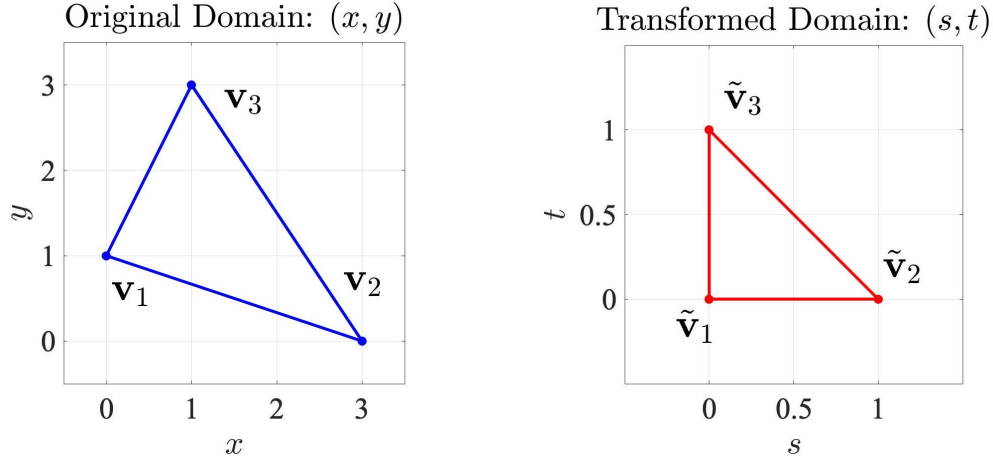


Figure B.6: Mapping from an element  $\omega$  in the original domain to the reference element  $\tilde{\omega}$  in the transformed domain.

we have different order quadrature formulas:

-Second-order: (exact for polynomials of degree 1 or less)

$$\int_{\omega} f(\mathbf{x}) d\mathbf{x} \approx A \cdot g\left(\frac{1}{3}, \frac{1}{3}\right),$$

-Third-order: (exact for polynomials of degree 2 or less)

$$\int_{\omega} f(\mathbf{x}) d\mathbf{x} \approx \frac{A}{3} \cdot \left[ g\left(\frac{1}{2}, 0\right) + g\left(0, \frac{1}{2}\right) + g\left(\frac{1}{2}, \frac{1}{2}\right) \right],$$

-Third-order also: (but! only exact for polynomials of degree 1 or less)

$$\int_{\omega} f(\mathbf{x}) d\mathbf{x} \approx \frac{A}{3} \cdot [g(1, 0) + g(0, 1) + g(0, 0)],$$

where  $A$  is the area of  $\omega$  which can be represented by the determinant

$$A = \begin{vmatrix} 1 & x_1 & y_1 \\ 1 & x_2 & y_2 \\ 1 & x_3 & y_3 \end{vmatrix}.$$

As we see with the two third-order formulas, the location of the quadrature points on the reference triangle ultimately dictates the degree of exactness of the approximation. (Since the second third-order equation above is not as good as the first one, we will not reference it again.) In Figure B.7, we plot the quadrature points used for second-, third-, and sixth-order quadrature formulas for integration over the example element  $\omega$  shown in the first graph of Figure B.6.

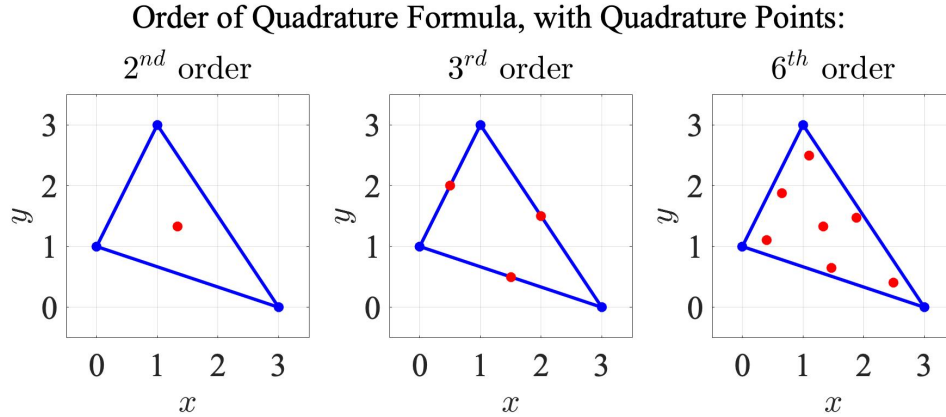


Figure B.7: Second-, third-, and sixth-order quadrature points from the example element shown in the first graph of Figure B.6.

For a test case with surface integrals, we consider

$$\int_0^\pi \int_0^\pi \sin(x) \sin(y) dx dy = 4. \quad (\text{B.2})$$

We show the influence of the order of the quadrature formulas against their errors for different numbers of elements to approximate (B.2) in Figure B.8 with examples of mesh refinements in Figure B.9. As shown with the mesh refinements, each time we increase the number of elements per side, the total number of elements increases with  $2n^2$ , where  $n$  is the number of elements per side. With the nonlinear increase of total elements in the mesh as we increase the number of elements per side, we see that using a higher-order quadrature formula on less elements does not (usually) produce as accurate of an approximation as using a lower-order quadrature formula with more elements.

## Meshes

The uniform meshes shown in this thesis (see Figures 3.3, B.9) are easy to build in FreeFem. However, non-uniform meshes are also relatively easy to implement. We use uniform meshes in this thesis though because they're easier to replicate than non-uniform ones.

## Time-Integrator

Backward Euler is the time-integrator of choice for all the work done in thesis. All of the code is robust enough to easily substitute in a different time-integrator if desired though.

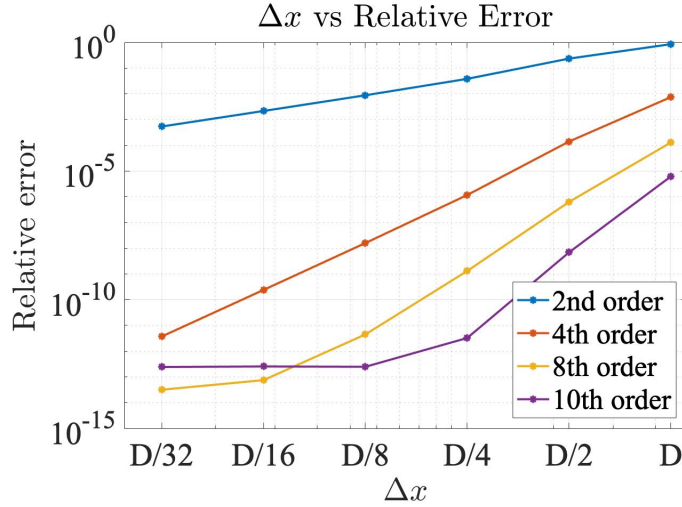


Figure B.8: Log-log plot of the relative error versus  $\Delta x$  for various orders of quadrature formulas for surface-integrals in approximating (B.2). Here,  $D = \pi\sqrt{2}$  is the max edge length of the least refined mesh, with the mesh refinements are shown in Figure B.9.

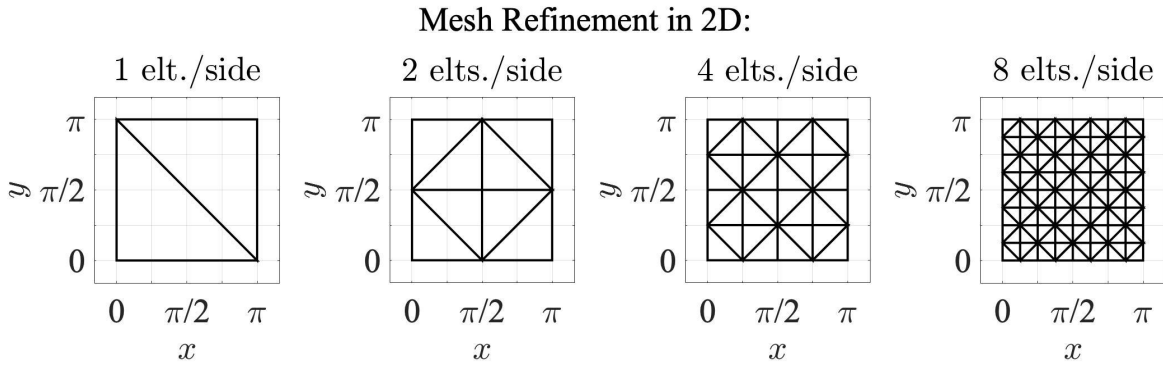


Figure B.9: Mesh refinements used to approximate (B.2). Figure B.8 shows the convergence rates for quadrature formulas of different orders with the mesh refinements shown here.

## Periodic Boundary Conditions

To implement the periodic boundary conditions, we implement an idea like the one shown in Figure B.10. In theory, we replace nodes along the right boundary of the mesh with their counterparts from the left boundary of the domain. With this strategy, care must be taken when setting up the mesh if a non-uniform mesh is used! In practice, we will not be physically removing any nodes— we will be replacing the right nodes with the ones from the left in our problem formation

though. To solve for the value of a function  $u$  at the nodes  $\mathbf{x}_i$  with the problem  $\mathbf{A}\mathbf{u} = \mathbf{f}$ , we will first decompose the problem, explicitly writing everything in terms of the left and right sides of the boundary (with subscripts  $l$  and  $r$ ) as well as the interior of the domain (with subscript  $i$ ). The matrix  $\mathbf{A}$  is split up into  $A_{j,k}$  for  $j, k \in \{l, r, i\}$ , which relates how the  $j$  and  $k$  components of the domain are related with the operator  $\mathbf{A}$ . The values of  $\mathbf{u}$  are split into  $u_l, u_r, u_i$ , with  $\mathbf{f}$  decomposed in a similar fashion. Then, the problem  $\mathbf{A}\mathbf{u} = \mathbf{f}$  can be written as:

$$\begin{pmatrix} A_{i,i} & A_{i,l} & A_{i,r} \\ A_{l,i} & A_{l,l} & A_{l,r} \\ A_{r,i} & A_{r,l} & A_{r,r} \end{pmatrix} \begin{pmatrix} u_i \\ u_l \\ u_r \end{pmatrix} = \begin{pmatrix} f_i \\ f_l \\ f_r \end{pmatrix},$$

following the notation and work in [80]. Then, we make the substitution  $u_l \leftarrow u_r$ , which assigns  $u_l$  to nodes at both the left and the right boundaries, and solve the linear system:

$$\begin{aligned} & \begin{pmatrix} A_{i,i} & A_{i,l} & A_{i,r} \\ A_{l,i} & A_{l,l} & A_{l,r} \\ A_{r,i} & A_{r,l} & A_{r,r} \end{pmatrix} \begin{pmatrix} u_i \\ u_l \\ u_l \end{pmatrix} = \begin{pmatrix} f_i \\ f_l \\ f_r \end{pmatrix}, \\ \Rightarrow & \begin{pmatrix} A_{i,i} & (A_{i,l} + A_{i,r}) \\ (A_{l,i} + A_{r,i}) & (A_{l,l} + A_{l,r} + A_{r,l} + A_{r,r}) \end{pmatrix} \begin{pmatrix} u_i \\ u_l \end{pmatrix} = \begin{pmatrix} f_i \\ f_l + f_r \end{pmatrix}. \end{aligned}$$

This allows whatever actions *would* have been acting on the right of the domain (with the last column of any of the matrices above, and  $f_r$  on the RHS) to still be accounted for in the problem. This implementation scheme can be thought of as the domain wrapping around and attaching back to itself; there are left or right boundaries at all, just an infinite loop.

All of the problems in this thesis (that we simulate numerically) have been written in a linear fashion. So, implementing periodic boundary conditions is relatively straightforward once all the organization is taken care of. FreeFem has the features and flexibility available to allow for periodic conditions to be implemented easily, as long as the boundary nodes align where periodic conditions are to be enforced. With the diagrams shown in Figure B.10, we show the theory for how implementing periodic boundary conditions looks. The idea is to join the left and right boundaries of the domain, leaving the mesh as a cylinder. To do this without leaving an obvious ‘seam’ in the cylinder, we remove nodes along the the right boundary and replace them with nodes from the left boundary. This removes degrees of freedom since we ‘lose’ the vertices/edges along the right edge of the mesh. However, those degrees of freedom are spent helping enforce periodicity.

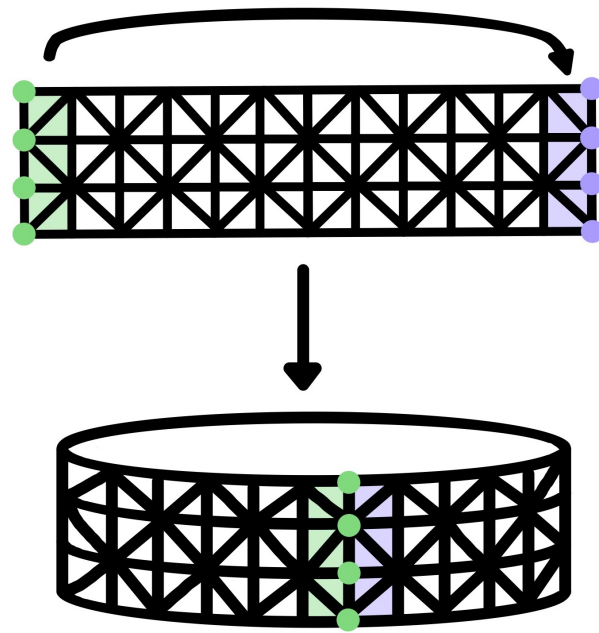


Figure B.10: Theory for implementing periodic boundary conditions. The purple nodes at the right boundary of the top mesh are removed. The left and right boundaries are then connected, using the green nodes to join the edges. The new mesh resembles the surface of a cylinder.

## REFERENCES

- [1] A. M. J. AL-ZAMILY, *Analysis of natural convection and entropy generation in a cavity filled with multi-layers of porous medium and nanofluid with a heat generation*, International Journal of Heat and Mass Transfer, 106 (2017), pp. 1218–1231, <https://doi.org/10.1016/j.ijheatmasstransfer.2016.10.102>.
- [2] M. B. ALLEN, *Collocation Techniques for Modeling Compositional Flows in Oil Reservoirs*, Springer, Verlag Berlin Heidelberg, 1984, <https://doi.org/10.1007/978-3-642-82213-1>.
- [3] M. B. ALLEN, A. BEHIE, AND J. A. TRANGENSTEIN, *Multiphase Flow in Porous Media: Mechanics, Mathematics, and Numerics*, Springer, Verlag New York, 1988, <https://doi.org/10.1007/978-1-4613-9598-0>.
- [4] J. BEAR, *Dynamics of Fluids in Porous Media*, Dover Publications Inc, New York, NY, 1972.
- [5] G. S. BEAVERS AND D. D. JOSEPH, *Boundary conditions at a naturally permeable wall*, Journal of Fluid Mechanics, 30 (1967), pp. 197–207, <https://doi.org/10.1017/S0022112067001375>.
- [6] H. BÉNARD, *Etude expérimentale du mouvement des liquides propageant de la chaleur par convection. Régime permanent: tourbillons cellulaires*, Compte-rendus de l'Académie des sciences, 130 (1900), pp. 1004–1007.
- [7] H. BÉNARD, *Mouvements tourbillonnaires à structure cellulaire. étude optique de la surface*, Compte-rendus de l'Académie des Sciences, 130 (1900), pp. 1065–1068.
- [8] H. BÉNARD, *Tourbillons cellulaires dans une nappe liquide: Pt. I, Description générale des phénomènes; Pt. II, Precedes mecaniques et optiques d'examen; lois numeriques des phenomenes*, Rev. Gen. Sci. Pure Appl, 11 (1900), pp. 1261–1309.
- [9] H. BÉNARD, *Les tourbillons cellulaires dans une nappe liquide propageant de la chaleur par convection: en régime permanent*, Gauthier-Villars, 1901.
- [10] H. BÉNARD, *Les tourbillons cellulaires dans une nappe liquide propageant de la chaleur par convection en régime permanent*, Annales de Chimie et de Physique, (1901).
- [11] H. BÉNARD AND D. AVSEC, *Travaux récents sur les tourbillons cellulaires et les tourbillons en bandes. Applications à l'astrophysique et à la météorologie*, (1938), <https://doi.org/10.1051/jphysrad:01938009011048600>.
- [12] M. J. BLOCK, *Surface tension as the cause of Bénard cells and surface deformation in a liquid film*, Nature, 178 (1956), p. 650, <https://doi.org/10.1038/178650a0>.

- [13] F. BOANO, J. W. HARVEY, A. MARION, A. I. PACKMAN, R. REVELLI, L. RIDOLFI, AND A. WÖRMAN, *Hyporheic flow and transport processes: Mechanisms, models, and biogeochemical implications*, *Reviews of Geophysics*, 52 (2014), pp. 603–679, <https://doi.org/10.1002/2012RG000417>.
- [14] F. BREZZI AND M. FORTIN, *Mixed and hybrid finite element methods*, vol. 15, Springer Science & Business Media, 2012, <https://doi.org/10.1007/978-1-4612-3172-1>.
- [15] S. BUSS AND ET AL, *The hyporheic handbook: a handbook on the groundwater-surfacewater interface and hyporheic zone for environmental managers*, Environment Agency, Bristol, UK, 2009.
- [16] F. BUSSE, *Fundamentals of thermal convection*, *Mantle Convection: Plate Tectonics and Global Dynamics*, 4 (1989), pp. 23–95.
- [17] F. H. BUSSE, *Bénard convection and geophysical applications*, in *Dynamics of Spatio-Temporal Cellular Structures*, Springer, 2006, pp. 103–125, [https://doi.org/10.1007/978-0-387-25111-0\\_6](https://doi.org/10.1007/978-0-387-25111-0_6).
- [18] R. CAMASSA, R. M. MCCLAUGHLIN, M. N. J. MOORE, AND K. YU, *Stratified flows with vertical layering of density: experimental and theoretical study of flow configurations and their stability*, *Journal of Fluid Mechanics*, 690 (2012), pp. 571–606, <https://doi.org/10.1017/jfm.2011.476>.
- [19] M. B. CARDENAS, *Hyporheic zone hydrologic science: A historical account of its emergence and a prospectus*, *Water Resources Research*, 51 (2015), pp. 3601–3616, <https://doi.org/10.1002/2015WR017028>.
- [20] M. CARR, *Penetrative convection in a superposed porous-medium–fluid layer via internal heating*, *Journal of Fluid Mechanics*, 509 (2004), pp. 305–329, <https://doi.org/10.1017/S0022112004009413>.
- [21] M. CARR AND B. STRAUGHAN, *Penetrative convection in a fluid overlying a porous layer*, *Advances in Water Resources*, 26 (2003), pp. 263–276, [https://doi.org/10.1016/S0309-1708\(02\)00086-6](https://doi.org/10.1016/S0309-1708(02)00086-6).
- [22] A. ÇEŞMELIOĞLU AND B. RIVIERE, *Analysis of time-dependent Navier–Stokes flow coupled with Darcy flow*, *Journal of Numerical Mathematics*, 16 (2008), pp. 249–280, <https://doi.org/10.1515/JNUM.2008.012>.
- [23] A. ÇEŞMELIOĞLU AND B. RIVIÈRE, *Primal discontinuous Galerkin methods for time-dependent coupled surface and subsurface flow*, *Journal of Scientific Computing*, 40 (2009), pp. 115–140, <https://doi.org/10.1007/s10915-009-9274-4>.
- [24] S. CHANDRASEKHAR, *Hydrodynamic and hydromagnetic stability*, Courier Corporation, 2013.

- [25] B. CHEN, A. B. CUNNINGHAM, R. EWING, R. PERALTA, AND E. J. VISSER, *Two-dimensional modeling of microscale transport and biotransformation in porous media*, Numerical Methods for Partial Differential Equations, 10 (1994), pp. 65–83, <https://doi.org/10.1002/num.1690100105>.
- [26] F. CHEN AND C. F. CHEN, *Onset of finger convection in a horizontal porous layer underlying a fluid layer*, Journal of Heat Transfer, 110 (1988), pp. 403–409, <https://doi.org/10.1115/1.3250499>.
- [27] F. CHEN AND L. HSU, *Onset of thermal convection in an anisotropic and inhomogeneous porous layer underlying a fluid layer*, Journal of Applied Physics, 69 (1991), pp. 6289–6301, <https://doi.org/10.1063/1.348827>.
- [28] F. CHEN AND J. LU, *Variable viscosity effects on convective instability in superposed fluid and porous layers*, Physics of Fluids A: Fluid Dynamics, 4 (1992), pp. 1936–1944, <https://doi.org/10.1063/1.858363>.
- [29] N. CHEN, M. GUNZBURGER, AND X. WANG, *Asymptotic analysis of the differences between the Stokes–Darcy system with different interface conditions and the Stokes–Brinkman system*, J. Math. Anal. Appl., 368 (2010), pp. 658–676, <https://doi.org/10.1016/j.jmaa.2010.02.022>.
- [30] P. CHIDYAGWAI AND B. RIVIERE, *A weak solution and a multinumercs solution of the coupled Navier–Stokes and Darcy equations*, IMA Journal of Numerical Analysis, (2007).
- [31] P. CONSTANTIN AND C. R. DOERING, *Infinite Prandtl number convection*, Journal of Statistical Physics, 94 (1999), pp. 159–172, <https://doi.org/10.1023/A:1004511312885>.
- [32] T. A. DAVIS, *Algorithm 832: UMFPACK v4.3 - an unsymmetric-pattern multifrontal method.*, ACM Trans. Math. Softw., 30 (2004), pp. 196–199, <https://doi.org/10.1145/992200.992206>.
- [33] M. DISCACCIATI AND A. QUARTERONI, *Navier-Stokes/Darcy coupling: modeling, analysis, and numerical approximation*, Revista Matemática Complutense, (2009), [https://doi.org/10.5209/rev\\_REMA.2009.v22.n2.16263](https://doi.org/10.5209/rev_REMA.2009.v22.n2.16263).
- [34] C. R. DOERING AND P. CONSTANTIN, *Variational bounds on energy dissipation in incompressible flows. III. Convection*, Physical Review E, 53 (1996), p. 5957, <https://doi.org/10.1103/PhysRevE.53.5957>.
- [35] C. R. DOERING, F. OTTO, AND M. G. REZNIKOFF, *Bounds on vertical heat transport for infinite-Prandtl-number Rayleigh–Bénard convection*, Journal of Fluid Mechanics, 560 (2006), p. 229, <https://doi.org/10.1017/S0022112006000097>.

- [36] J. J. DONGARRA, B. STRAUGHAN, AND D. W. WALKER, *Chebyshev tau-QZ algorithm methods for calculating spectra of hydrodynamic stability problems*, Applied Numerical Mathematics, 22 (1996), pp. 399–435, [https://doi.org/10.1016/S0168-9274\(96\)00049-9](https://doi.org/10.1016/S0168-9274(96)00049-9).
- [37] P. G. DRAZIN AND W. H. REID, *Hydrodynamic stability*, Cambridge university press, 2004, <https://doi.org/10.1017/CB09780511616938>.
- [38] T. A. DRISCOLL, N. HALE, AND L. N. TREFETHEN, *Chebfun guide*, 2014.
- [39] R. E. EWING, *The need for multidisciplinary involvement in groundwater contaminant simulations*, in Proceedings of the Next Generation Environmental Models and Computational Methods, SIAM, Philadelphia, PA, 1997, pp. 227–245.
- [40] R. E. EWING AND S. WEEKES, *Numerical methods for contaminant transport in porous media*, in Advances in Computational Mathematics, Z. Chen, Y. Li, C. Micchelli, and Y. Xu, eds., Marcel Dekker, Inc., New York, NY, 1998, pp. 75–95.
- [41] S. FAUVE, *Henri Bénard and pattern-forming instabilities*, Comptes Rendus Physique, 18 (2017), pp. 531–543, <https://doi.org/10.1016/j.crhy.2017.11.002>.
- [42] T. GANTUMUR, *On the convergence theory of adaptive mixed finite element methods for the Stokes problem*, arXiv preprint arXiv:1403.0895, (2014), <https://arxiv.org/pdf/1403.0895.pdf>.
- [43] V. GIRAULT AND P.-A. RAVIART, *Finite element methods for Navier-Stokes equations: theory and algorithms*, vol. 5, Springer Science & Business Media, 2012, <https://doi.org/10.1007/978-3-642-61623-5>.
- [44] V. GIRAULT AND B. RIVIÈRE, *DG approximation of coupled Navier–Stokes and Darcy equations by Beaver–Joseph–Saffman interface condition*, SIAM Journal on Numerical Analysis, 47 (2009), pp. 2052–2089, <https://doi.org/10.1137/070686081>.
- [45] P. H. GLEICK, *Water and Conflict: Fresh Water Resources and International Security*, International Security, 18 (1993), pp. 79–112, <https://doi.org/10.2307/2539033>.
- [46] R. GLOWINSKI AND O. PIRONNEAU, *Finite element methods for Navier-Stokes equations*, Annual Review of Fluid Mechanics, 24 (1992), pp. 167–204, <https://doi.org/10.1146/annurev.fl.24.010192.001123>.
- [47] G. H. GOLUB AND C. F. VAN LOAN, *Matrix computations*, vol. 3, JHU Press, 2012.
- [48] S. GROSSMANN AND D. LOHSE, *Scaling in thermal convection: a unifying theory*, Journal of Fluid Mechanics, 407 (2000), pp. 27–56, <https://doi.org/10.1017/S0022112099007545>.

- [49] M. GUNZBURGER, *Finite element methods for viscous incompressible flows: a guide to theory, practice, and algorithms*, Academic Press, 1989, <https://doi.org/10.1016/C2009-0-22263-X>.
- [50] D. HAN AND X. WANG, *Decoupled energy-law preserving numerical schemes for the Cahn-Hilliard-Darcy system*, Numerical Methods for Partial Differential Equations, 32 (2016), pp. 936–954, <https://doi.org/10.1002/num.22036>.
- [51] F. HECHT, *New development in FreeFem++*, J. Numer. Math., 20 (2012), pp. 251–265, <https://freefem.org/>.
- [52] A. HILL AND M. CARR, *Nonlinear stability of the one-domain approach to modelling convection in superposed fluid and porous layers*, Proceedings of the Royal Society A, 466 (2010), pp. 2695–2705, <https://doi.org/10.1098/rspa.2010.0014>.
- [53] A. HILL AND M. CARR, *Sharp global nonlinear stability for a fluid overlying a highly porous material*, Proceedings of the Royal Society A, 466 (2010), pp. 127–140, <https://doi.org/10.1098/rspa.2009.0322>.
- [54] A. HILL AND B. STRAUGHAN, *Global stability for thermal convection in a fluid overlying a highly porous material*, Proceedings of the Royal Society A, 465 (2009), pp. 207–217, <https://doi.org/10.1098/rspa.2008.0303>.
- [55] L. N. HOWARD, *Heat transport by turbulent convection*, Journal of Fluid Mechanics, 17 (1963), pp. 405–432, <https://doi.org/10.1017/S0022112063001427>.
- [56] I. P. JONES, *Low reynolds number flow past a porous spherical shell*, Proceedings of the Cambridge Philosophical Society, 73 (1973), pp. 231–238, <https://doi.org/10.1017/S0305004100047642>.
- [57] D. A. KOPRIVA, *A staggered-grid multidomain spectral method for the compressible Navier–Stokes equations*, Journal of Computational Physics, 143 (1998), pp. 125–158, <https://doi.org/10.1006/jcph.1998.5956>.
- [58] M. LE BARS AND M. G. WORSTER, *Interfacial conditions between a pure fluid and a porous medium: implications for binary alloy solidification*, Journal of Fluid Mechanics, 550 (2006), pp. 149–173, <https://doi.org/10.1017/S0022112005007998>.
- [59] M. LE BARS AND M. G. WORSTER, *Solidification of a binary alloy: Finite-element, single-domain simulation and new benchmark solutions*, Journal of Computational Physics, 216 (2006), pp. 247–263, <https://doi.org/10.1016/j.jcp.2005.12.002>.
- [60] L. LEFEBVRE, J. BANHART, AND D. DUNAND, *Porous metals and metallic foams: Current status and recent developments*, Advanced Engineering Materials, 10 (2008), pp. 775–787, <https://doi.org/10.1002/adem.200800241>.

- [61] E. LUKASHEV, E. RADKEVICH, N. YAKOVLEV, AND O. VASIL'TEVA, *On the Rayleigh–Bénard instability as the nonequilibrium phase transition*, in AIP Conference Proceedings, 2017, p. 020017, <https://doi.org/10.1063/1.5013954>.
- [62] M. MCCURDY, N. MOORE, AND X. WANG, *Convection in a coupled free flow-porous media system*, SIAM Journal on Applied Mathematics, 79 (2019), pp. 2313–2339, <https://doi.org/10.1137/19M1238095>.
- [63] C. B. MOLER AND G. W. STEWART, *An algorithm for generalized matrix eigenvalue problems*, SIAM Journal on Numerical Analysis, 10 (1973), pp. 241–256, <https://doi.org/10.1137/0710024>.
- [64] M. N. J. MOORE, *A fast Chebyshev method for simulating flexible-wing propulsion*, Journal of Computational Physics, 345 (2017), pp. 792–817, <https://doi.org/10.1016/j.jcp.2017.05.052>.
- [65] M. N. J. MOORE, *Riemann-Hilbert problems for the shapes formed by bodies dissolving, melting, and eroding in fluid flows*, Communications on Pure and Applied Mathematics, 70 (2017), pp. 1810–1831, <https://doi.org/10.1002/cpa.21689>.
- [66] D. NIELD, *Onset of convection in a fluid layer overlying a layer of a porous medium*, Journal of Fluid Mechanics., 81 (1977), pp. 513–522, <https://doi.org/10.1017/S0022112077002195>.
- [67] D. NIELD, *The effect of temperature-dependent viscosity on the onset of convection in a saturated porous medium*, Journal of Heat Transfer, 118 (1996), pp. 803–805, <https://doi.org/10.1115/1.2822705>.
- [68] D. NIELD AND A. BEJAN, *Convection in Porous Media*, Springer International Publishing, Cham, Switzerland, 5 ed., 2017, <https://doi.org/10.1007/978-3-319-49562-0>.
- [69] F. OTTO AND C. SEIS, *Rayleigh–bénard convection: improved bounds on the Nusselt number*, Journal of mathematical physics, 52 (2011), <https://doi.org/10.1063/1.3623417>.
- [70] I. PALYMSKIY, V. PALYMSKIY, AND P. FOMIN, *Rayleigh–Bénard convection in a chemically active gas in the chemical equilibrium state*, Combustion, Explosion, and Shock Waves, 53 (2017), pp. 123–133, <https://doi.org/10.1134/S0010508217020010>.
- [71] L. PAYNE AND B. STRAUGHAN, *Analysis of the boundary condition at the interface between a viscous fluid and a porous medium and related modelling questions*, Journal de mathématiques pures et appliquées, 77 (1998), pp. 317–354, [https://doi.org/10.1016/S0021-7824\(98\)80102-5](https://doi.org/10.1016/S0021-7824(98)80102-5).
- [72] J. PEARSON, *On convection cells induced by surface tension*, Journal of fluid mechanics, 4 (1958), pp. 489–500, <https://doi.org/10.1017/S0022112058000616>.

- [73] A. PELLEW AND R. V. SOUTHWELL, *On maintained convective motion in a fluid heated from below*, Proceedings of the Royal Society of London. Series A. Mathematical and Physical Sciences, 176 (1940), pp. 312–343, <https://doi.org/10.1098/rspa.1940.0092>.
- [74] Y. POMEAU, *Front motion, metastability and subcritical bifurcations in hydrodynamics*, Physica D: Nonlinear Phenomena, 23 (1986), pp. 3–11, [https://doi.org/10.1016/0167-2789\(86\)90104-1](https://doi.org/10.1016/0167-2789(86)90104-1).
- [75] B. D. QUAIFFE AND M. N. J. MOORE, *A boundary-integral framework to simulate viscous erosion of a porous medium*, Journal of Computational Physics, 375 (2018), pp. 1 – 21, <https://doi.org/https://doi.org/10.1016/j.jcp.2018.07.037>.
- [76] L. RAYLEIGH, *On convection currents in a horizontal layer of fluid, when the higher temperature is on the under side*, Philosophical Magazine and Journal of Science (Sixth Series), 32 (1916), pp. 529–546, <https://doi.org/10.1080/14786441608635602>.
- [77] W. REID AND D. HARRIS, *Some further results on the Bénard problem*, The Physics of fluids, 1 (1958), pp. 102–110, <https://doi.org/10.1063/1.1705871>.
- [78] Y. SAAD, *Iterative Methods for Sparse Linear Systems*, SIAM, second ed., 2003, <https://doi.org/10.1137/1.9780898718003>.
- [79] P. SAFFMAN, *On the boundary condition at the interface of a porous medium*, Stud. Appl. Math., 1 (1971), pp. 77–84, <https://doi.org/10.1002/sapm197150293>.
- [80] G. SEGAL, K. VUIK, AND K. KASSELS, *On the implementation of symmetric and anti-symmetric periodic boundary conditions for incompressible flow*, International Journal for Numerical Methods in Fluids, 18 (1994), pp. 1153–1165, <https://doi.org/10.1002/flid.1650181203>.
- [81] A. SERGENT AND P. LE QUÉRÉ, *Large-Scale Patterns in a Rectangular Rayleigh–Bénard Cell*, in Direct and Large-Eddy Simulation VII, Springer, 2010, pp. 415–418, [https://doi.org/10.1007/978-90-481-3652-0\\_61](https://doi.org/10.1007/978-90-481-3652-0_61).
- [82] E. A. SPIEGEL, *Convection in stars I. Basic Boussinesq convection*, Annual review of astronomy and astrophysics, 9 (1971), pp. 323–352, <https://doi.org/10.1146/annurev.aa.09.090171.001543>.
- [83] B. STRAUGHAN, *Effect of property variation and modelling on convection in a fluid overlying a porous layer*, International Journal for Numerical and Analytical Methods in Geomechanics, 26 (2002), pp. 75–97, <https://doi.org/10.1002/nag.193>.
- [84] B. STRAUGHAN, *Sharp global nonlinear stability for temperature-dependent viscosity convection*, Proceedings of the Royal Society of London. Series A: Mathematical, Physical and Engineering Sciences, 458 (2002), pp. 1773–1782, <https://doi.org/10.1098/rspa.2001.0945>.

- [85] B. STRAUGHAN, *Resonant porous penetrative convection*, Proceedings of the Royal Society of London. Series A: Mathematical, Physical and Engineering Sciences, 460 (2004), pp. 2913–2927, <https://doi.org/10.1098/rspa.2004.1292>.
- [86] B. STRAUGHAN, *Stability and wave motion in porous media*, vol. 165, Springer Science & Business Media, 2008, <https://doi.org/10.1007/978-0-387-76543-3>.
- [87] B. STRAUGHAN, *The energy method, stability, and nonlinear convection*, vol. 91, Springer Science & Business Media, 2013, <https://doi.org/10.1007/978-1-4757-2194-2>.
- [88] B. J. SUCHOMEL, B. M. CHEN, AND M. B. ALLEN, *Network model of flow, transport and biofilm effects in porous media*, Transport in Porous Media, 30 (1998), pp. 1–23, <https://doi.org/10.1023/A:1006560705680>.
- [89] E. TAN AND M. GURNIS, *Metastable superplumes and mantle compressibility*, Geophysical Research Letters, 32 (2005), <https://doi.org/10.1029/2005GL024190>.
- [90] N. TATSUO, T. TORU, S. MITSUHIRO, K. YUJI, AND O. HIROYUKI, *Numerical analysis of natural convection in a rectangular enclosure horizontally divided into fluid and porous regions*, International Journal of Heat and Mass Transfer, 29 (1986), pp. 889–898, [https://doi.org/10.1016/0017-9310\(86\)90184-5](https://doi.org/10.1016/0017-9310(86)90184-5).
- [91] C. TAYLOR AND P. HOOD, *A numerical solution of the Navier-Stokes equations using the finite element technique*, Computers & Fluids, 1 (1973), pp. 73–100, [https://doi.org/10.1016/0045-7930\(73\)90027-3](https://doi.org/10.1016/0045-7930(73)90027-3).
- [92] Y. TOULOUKIAN, R. POWELL, C. HO, AND P. KLEMENS, *Thermophysical properties of matter— the TPRC data series, Volume 2: Thermal conductivity-nonmetallic solids*, tech. report, Thermophysical and Electronic Properties Information Analysis Center, Lafayette, IN, 1971.
- [93] L. N. TREFETHEN, *Approximation theory and approximation practice*, SIAM, 2013.
- [94] P. TYVAND, *Onset of Rayleigh-Bénard Convection in Porous Bodies*, in Transport Phenomena in Porous Media II, D. B. Ingham and I. Pop, eds., Pergamon, Oxford, 2002, pp. 82–112, <https://doi.org/10.1016/B978-008043965-5/50005-2>.
- [95] K. VAFAI, *Handbook of Porous Media*, CRC Press, 2005, <https://doi.org/10.1201/9780415876384>.
- [96] J. VALENCIA-LOPEZ AND J. OCHOA-TAPIA, *A study of buoyancy-driven flow in a confined fluid overlying a porous layer*, International Journal of Heat and Mass Transfer, 44 (2001), pp. 4725–4736, [https://doi.org/10.1016/S0017-9310\(01\)00105-3](https://doi.org/10.1016/S0017-9310(01)00105-3).

- [97] X. WANG, *Infinite Prandtl number limit of Rayleigh-Bénard convection*, Communications on Pure and Applied Mathematics, 57 (2004), pp. 1265–1282, <https://doi.org/10.1002/cpa.3047>.
- [98] WWAP (UNITED NATIONS WORLD WATER ASSESSMENT PROGRAMME), *The United Nations World Water Development Report 2018: Nature-based solutions for water*, 2018.
- [99] D. XUE AND Y. HOU, *Numerical analysis of a second order algorithm for a non-stationary Navier–Stokes/Darcy model*, Journal of Computational and Applied Mathematics, 369 (2020), p. 112579, <https://doi.org/10.1016/j.cam.2019.112579>.
- [100] J. ZHANG AND A. LIBCHABER, *Periodic boundary motion in thermal turbulence*, Physical Review Letters, 84 (2000), p. 4361, <https://doi.org/10.1103/PhysRevLett.84.4361>.
- [101] Y. ZHANG, L. SHAN, AND Y. HOU, *Well-posedness and Finite Element approximation for the convection model in superposed fluid and porous layers*, SIAM Journal on Numerical Analysis, 58 (2020), pp. 541–564, <https://doi.org/10.1137/19M1241532>.

## BIOGRAPHICAL SKETCH

Matthew McCurdy was born and raised outside of Memphis, TN. In 2011, he ventured up to the delightfully folksy Danville, KY to begin his undergraduate career at Centre College. There, he studied math and education, earning his B.S. in mathematics in the spring of 2015. The summer before his senior year, Matt worked under Dr. Ellen Swanson on a fluid dynamics research project which culminated in a publication and solidified his desire to pursue a graduate degree in applied math. While at Centre, he was a member of the cross-country and track and field teams, earning numerous All-Conference, All-Region, and All-Academic nods as well as contributing to five conference team titles. Matthew was an active member of Alpha Phi Omega, serving as the chapter's co-president and chair of a national committee during his senior year. Throughout Matt's undergraduate years, math began taking him around the world; he travelled to Rio de Janeiro in the summer of 2013 to teach mathematics, and later, went to Peru to take the course 'Mathematics and Architecture in ancient Peru.'

In 2015, Matt headed to Tallahassee, FL to pursue a Ph.D. in applied and computational mathematics at Florida State University. He taught a number of courses: Pre-Calculus, Calculus, Ordinary Differential Equations, and Applied Linear Algebra. Matthew's love for teaching was recognized in 2020, as he was named a Distinguished Graduate Teaching Assistant. For his service on the Graduate Student Council and work in organizing various events for the department, Matthew was earned the Bettina Zoeller Richmond Award in 2018. The trend of world-travel continued throughout graduate school, as math conferences and talks took him across the country and the globe; memorable trips include the APS Division of Fluid Dynamics conference in Seattle and a trip to China with one advisor, Dr. Moore, to visit the other, Dr. Wang.

In the fall, Matthew will head north to Hartford, CT to teach at Trinity College as a Harold L. Dorwart Visiting Assistant Professor.